Mathematical Models of Fluid Flows in the Human Eye

By

MARIIA DVORIASHYNA

UNIVERSITÀ DEGLI STUDI
DI GENOVA

Department of Civil, Chemical and Environmental Engineering
UNIVERSITY OF GENOA

Advisor: RODOLFO REPETTO

MARCH 2019

In memory of my beloved brother Andrey

ACKNOWLEDGEMENTS

First and foremost I would like to express the deepest gratitude to my supervisor, Prof. Rodolfo Repetto, who provided the scientific and moral support for me during past four years. His genuine interest to problems in biomechanics inspired me to start the research in the field and his careful guidance allowed me to carry on with it. Prof. Repetto has taught me most of the mechanistic modelling I know, from the model setup to careful ways of checking and interpreting the results. But most of all, I would like to thank Prof. Repetto for supporting and encouraging my ambitious ideas. From long-term visit of the University of Oxford to organising European Study Group of Mathematics in Industry and departmental group meetings, Prof. Repetto has always been reassuring and helpful. Without this support I wouldn't have been able to accomplish even half of the things I have done during my PhD. His encouragement really stimulated me to grow scientifically and personally, for which I am extremely grateful.

My sincere appreciation also goes to Prof. Eamonn Gaffney, for co-supervising me during the RPE research. Prof. Gaffney was patiently guiding me throughout the project and provided many very useful insights in mathematical biology. I would also like to thank Prof. Gaffney for supporting my initiatives to visit Mathematical Institute, to join WCMB and Brasenose, which allowed me to attend various events within the department and the college.

I would like to offer my special thanks to Dr. Jennifer Tweedy for co-supervising me during our projects on aqueous humour flow. Within our collaboration I had pleasure to visit Imperial College several times and had the most wonderful working (and birdwatching) time in Shapwick. Dr. Tweedy has also inspired me to always attempt finding analytical solutions for the problems.

The RPE project has been possible thanks to the support of Macular Society and UK Fluids Network. Among the collaborators in this project I would like to acknowledge Prof. Alexander Foss, who initiated the problem and was closely following the model development, providing most useful insights from the clinical point of view, particularly over a pint in Eagle and Child. I am also grateful to Prof. Oliver Jensen for helpful suggestions during the project and for the 'solution from the train' after our first meeting in Oxford, that served as a basis for our RPE work.

Within the projects on aqueous flow I would like to thank Dr. Paolo Soleri, Fred Wassenburg and Ophtec BV for introducing interesting problems and providing most useful comments. I also wish to acknowledge the help provided by Prof. Mario Romano, who guided the iridotomy problem from the medical side and provided ultrasound scans of the posterior chamber.

My PhD wouldn't have been possible without the scholarship kindly provided by the Univer-

sity of Genoa. My department has been like a second home to me, owing to the nice atmosphere and friendly people. I would like to acknowledge Profs. Stocchino and Besio for hosting so many European projects in the department that one never felt hungry, and for kindly allowing me to use their clusters for my simulations. Profs. Mazzino and Blondeaux gave very useful comments for the work in eye rotations, for which I am very grateful. I would like to thank as well Profs. Bottaro and Pralits for the enthusiasm in biological fluid mechanics and for regularly attending and providing useful insights during group meetings. I am also thankful to Prof. Pralits for contributing significantly to my education during the first year of my PhD. Special thanks goes to Prof. Vittori and Prof. Repetto for being very attentive and caring coordinators of the PhD program. I am also grateful to Gaetano Porcile, Rossella Luchi and Nicoletta Tambroni for patiently sharing the office with me for almost three years and to my colleagues: Francesco Enrile, Francesco Ferrari, Francesco De Leo, Stefano Putzu, Peyman Davvalo Khongar, Annalisa De Leo, Giulia Cremonini, Krystyna Isakova, Masoud Ghaderi Zefreh, Daniele Lagomarsino and Edoardo Alinovi.

Tolerating long working hours was possible thanks to people who inspired and supported me in Genoa during these years. I thus thank Quinten Akkerman, Emma de Cecco, Mohsen Shiee, Eva Strohmaier, Lucija Kristiane and Joel Pattison for all the amazing hikes, trips, international dinners and board game nights. I am thankful to Irene Nepita, who would always listen to my doubts and give most valuable advises. I also thank Prof. Repetto again, for saving me with beer and salamini during the darkest of times and to Prof. Federica Grillo for drawing beautiful pictures for our papers and for cooking delicious dinners.

During my time in Maths Institute, I have met lots amazing and inspiring people. I am particularly grateful to Ousman Kodio, James Kwiecinski and Andrew Krause for most interesting discussions about science. I would also like to thank all my friends in Oxford, especially Nadia Ishnazarova for saving my life with wine and russian antibiotics when I got sick, Rasa Giniunaite for introducing me to the world of Lindy Hop and to Victoria Ponce for the contagious passion towards mathematical biology.

I am extremely thankful to my friends, especially to Mariia Koroliuk for motivating me to keep improving, inspiring me to travel more and to Miriam Srokova, who have bravely fought my fear and incapability of camping trips. I am grateful to my MathMods friends and l'Aquila family for all the fun time during various trips. I also thank Yaroslava Gerfanova, Mariia Burchevskaia, Olga Pugacheva and my dearest godson Lev for all the love and support.

Last, but certainly not least, I am very grateful to my family. Their belief and encouragement, even from far away, meant the world to me. My parents' patience must be unlimited, as in the moments of sorrow and joy, they have always supported and encouraged me.

PhD is not an easy time, but if taken four years back, I would certainly choose to do it again. I wish to all fellow PhD students to take the best out of it, to learn as much as possible, to challenge yourself, to take every opportunity to participate in conferences, workshops and summer schools and, most of all, to enjoy the outcomes of the research.

SUMMARY

Fluids in the eye have many important functions, such as regulating the intraocular pressure, delivering nutrients to the avascular intraocular tissue of the cornea and the lens, and contributing to adhesion forces between the sensory retina and the retinal pigment epithelium. Failure of these functions may lead to a number of pathological conditions. Studying fluid flows in the eye is therefore relevant to improve our understanding of the physiology of the organ and to prevent or treat certain eye diseases.

This thesis consists of two main parts. In the first part we propose mathematical models of the dynamics of the aqueous humour in the anterior segment of the eye. The problems considered are in the area of fluid mechanics and our approaches are based on the use of lubrication theory that is applicable for flows in thin domains. The second part is related to fluid transport across the retinal pigment epithelium and it concerns a multiphysics problem, which couples fluid and ion transport. Each part consists of several chapters, which address various projects within these two topics and are briefly summarised below.

Part I. Aqueous flow in the anterior part of the eye

The anterior segment of the eye consists of the anterior (the region between the cornea and the iris) and the posterior (the region between the iris and the lens) chambers (AC and PC), which are connected to each other through a very thin iris–lens channel. These chambers are filled with aqueous humour, a transparent fluid that has properties similar to those of water. Aqueous humour is produced by the ciliary body at an approximately constant rate, it flows through the PC, exits through the pupil into the AC, where it is drained into the trabecular meshwork. The balance between aqueous production and resistance to drainage governs the intraocular pressure (IOP). Elevated IOP is closely associated with glaucoma, a world leading cause of blindness. Aqueous humor is also responsible for delivering nutrients to the cornea and the lens. Mathematical modelling of aqueous flow can help understanding the mechanisms for IOP regulation and nutrient transport in physiological and pathological conditions. In chapter 1 we review the modelling literature concerning AH flow.

In chapter 2 we address one of possible pathological states of the eye that occurs when the iris and lens touch at the pupil (pupillary block). This leads to a pressure build up in the PC, peripheral axial shallowing of the AC and possible angle-closure glaucoma, i.e. blockage of the AH outflow path through the trabecular meshwork. This can cause blindness, which may be prevented by surgically creating an iridotomy, i.e. a hole through the iris, aimed at creating an additional outflow from the PC to the AC, thus reducing the pressure in the PC. The aim of this project is to use mathematical modelling to investigate the ideal size and location of an iridotomy.

The model is semianalytical and is based on the assumption that the PC is a thin region. This allows us to simplify the Navier-Stokes equations that govern fluid flow, using lubrication theory.

In our model the iridotomy is treated as a point sink and we assume that the flow through the hole is proportional to the pressure drop across it. We investigate the effect of iridotomy size on the pressure value in the PC and the wall shear stress on the cornea, two quantities that are of clinical interest. We also consider the condition of partial pupillary block, which occurs when part of the pupil is blocked for the outflow and another part is open. The results suggest that large values of the pressure are reached only when the pupil is almost completely blocked and demonstrate that an iridotomy of about 50 μm in diameter is sufficient to avoid excessive pressure in the PC.

In chapter 3 we propose a theoretical model of the flow induced in the AC by rotations of the eye bulb. This is a clinically relevant flow, as it has been proven to be the most intense among other flow mechanisms in the AC and thus it contributes significantly both to the generation of stresses on ocular tissues and to mixing processes in the AC. Various authors studied this problem through numerical simulations (Abouali et al., 2012; Repetto et al., 2015). We take advantage of the fact that the AC is a shallow domain and assume harmonic eye rotations, which allows us to approach the problem analytically. In this respect our approach is complementary to the existing numerical works. We predict that the flow filed is highly three dimensional and we highlight features that had not been observed by previous authors. We also find the existence of a steady streaming flow, which we describe in great detail, and we show that it is one of the key players in transport processes in the AC.

Part II. Fluid transport across the retinal pigment epithelium

The retinal pigment epithelium (RPE) is the outermost cell layer of the retina that separates the photoreceptors from Bruch's membrane and the choroidal blood supply. It has several important physiological functions, among which is removal of excess fluid and CO_2 from the sub-retinal space into the choroid. Fluid transport across the RPE is regulated by the epithelial pumping, failure of which leads to fluid accumulation in the sub-retinal space and is closely associated with several pathological conditions, such as age-related macular degeneration, macular edema and retinal detachment. Failure to remove CO_2 results in acidosis, which inhibits retinal function. Identifying and quantifying the mechanisms that are responsible for this transport can suggest strategies to prevent or treat fluid and CO_2 accumulation in the sub-retinal space. In chapter 4 we give an overview of the possible mechanisms for water transport across the RPE, with a particular focus on standing gradient osmotic flow and electroosmosis.

In chapter 5 we propose a mathematical model that contemplates these mechanisms. Osmosis is governed by spatial variations in ion concentrations, which we obtain solving the ion transport problem in the tissue, governed by Poisson-Nernst-Plank equations for three ions: Na^+ (sodium), K^+ (potassium) and Cl^- (chloride). These ions cross cell membranes through ion channels by passive and active transport mechanisms. Electroosmosis can occur in the gap between adjacent cells as a result of interaction between the electric field and the charged fluid in the electrical double layer (EDL). To model such a flow we resolve the EDL to find spatial charge density and the electric field is obtained from the solution of the ion transport problem. The resulting system is nonlinear and fluid and ion transport are fully coupled. Taking advantage of the fact that the cleft gap is long and thin, we perform asymptotic expansions and reduce the whole system to a set of ordinary differential equations (ODEs) and algebraic equations.

The model suggests that the distribution of ion concentrations in the gap between two adjacent cells drives a local osmotic flow, and this flow largely dominates over electroosmosis. Moreover, the

predicted flow magnitude is close to the measured values of the flow across the RPE, indicating that osmosis is the main mechanism of fluid transport.

Recent studies suggest that transport of CO_2 (carbon dioxide) and fluid are coupled in the RPE (Adijanto et al., 2009). In order to understand the mechanisms of this coupling, in chapter 6, we extend the model to account for the presence of CO_2. Due to the existence of chemical reactions in the cell and extracellular space, we add the four following species to the model: CO_2, HCO_3^- (bicarbonate), H^+ (proton) and H_2CO_3 (carbonic acid) and the corresponding channels that transport them across cell membranes. As in three-ion model, a significant reduction of the system is performed using asymptotic expansions.

With the increased number of species in the model, the problem of parametrisation of the fluxes of ions across the cell membranes gets more complex. To capture the variations of the model output induced by changing the parameters and investigate their relative importance, we perform global sensitivity analysis, using extended Fourier amplitude sensitivity test (eFAST).

We find that, in agreement with the three-ion model, the flow across the RPE is driven by osmotic gradient in the cleft. In addition to this, the model reproduces in a better way experimentally observed ion and water fluxes. Moreover, the model provides possible explanations of the mechanisms behind the functioning of drugs used to treat fluid accumulation in the sub-retinal space, such as inhibitors of ion channels or CA and indicates how other interventions may inadvertently impact the retina.

Table of Contents

PREFACE

According to the World Health Organisation (WHO), 36 million people in the world are blind and 217 million have moderate or severe visual impairment. The leading causes of visual impairment include uncorrected refractive errors, cataract, age-related macular degeneration, glaucoma, diabetic retinopathy, corneal opacity and trachoma. Their relative impact on the population, however, is varying across the countries. For example, cataract is a dominant cause of blindness in countries with low and middle income, whereas in countries with high income it is cured by a common surgical procedure. However, in high-income countries, other eye disorders remain sight threatening, mainly diabetic retinopathy, glaucoma and age-related macular degeneration (Bourne et al., 2017). Moreover, according to data in Pascolini and Mariotti (2012) relative to the year 2010, at least 37% of the blinding causes, excluding cataract, are associated with fluid motion in the eye. Thus, studying fluid flows in the eye from mechanical point of view is relevant to understand, prevent and/or treat such pathological conditions.

The eye consists of three different layers (Kolb, 2012). The external layer is formed by the sclera (the white of the eye) and cornea (the transparent thin tissue at the front of the eye), see figure 0.1. The intemediate layer is divided into two parts: anterior, that consists of the iris (coloured part of the eye) and the ciliary body, and posterior, that comprises the choroid (the region that contains the majority of blood vessels in the eye). Finally, the inner layer, or the

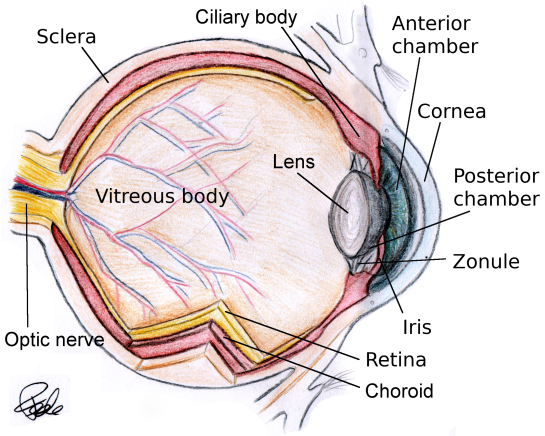

Figure 0.1: Sketch of the cross-section of the eye. Drawing by Prof. Federica Grillo.

sensory part of the eye, includes the retina, a light-sensitive tissue that borders with the choroid and lines the back two-thirds of the eyeball.

The bulk of the eye is divided into three sections: (i) anterior chamber (AC), located between cornea and iris, (ii) posterior chamber (PC), which lies between the iris, zonule fibers and the lens and (iii) the vitreous chamber, that is between the lens and the retina (Kaufman et al., 2011). The AC and PC are filled with aqueous humor, which is a transparent fluid with properties similar to those of water. The vitreous chamber is filled with vitreous humor (or vitreous body), a transparent fluid that has a gel-like structure and can be mechanically characterised as a visco-elastic fluid.

Fluids in the eye have many important physiologycal functions, such as maintaining the intraocular pressure and keeping the shape of the eye globe, supplying avascular tissues with oxygen and nutrients, removing waste products and providing adhesion forces between the retina and the retinal pigment epithelium. Failure to perform these functions may lead to a number of eye pathologies. Mathematical models, particularly those based on mechanics, have proven to be extremely useful tools, both for understanding eye physiology and also for studying its pathophysiology (Siggers and Ethier, 2012). They can also potentially help diagnosis of pathological states, improve medical and surgical treatments and the design of prosthetic devices.

In this thesis we address two areas of fluid mechanics in the eye, which are discussed in two separate parts. Each part consists of an introductory chapter and two chapters describing various research projects. In the first part we study the flow of aqueous humor in the anterior segment of the eye under physiological and certain pathological conditions. In the second part, we discuss the problem related to fluid and ion transport across the retinal pigment epithelium. The thesis is concluded with a discussion of the main findings and their relevance along with possible future directions and extensions of the work.

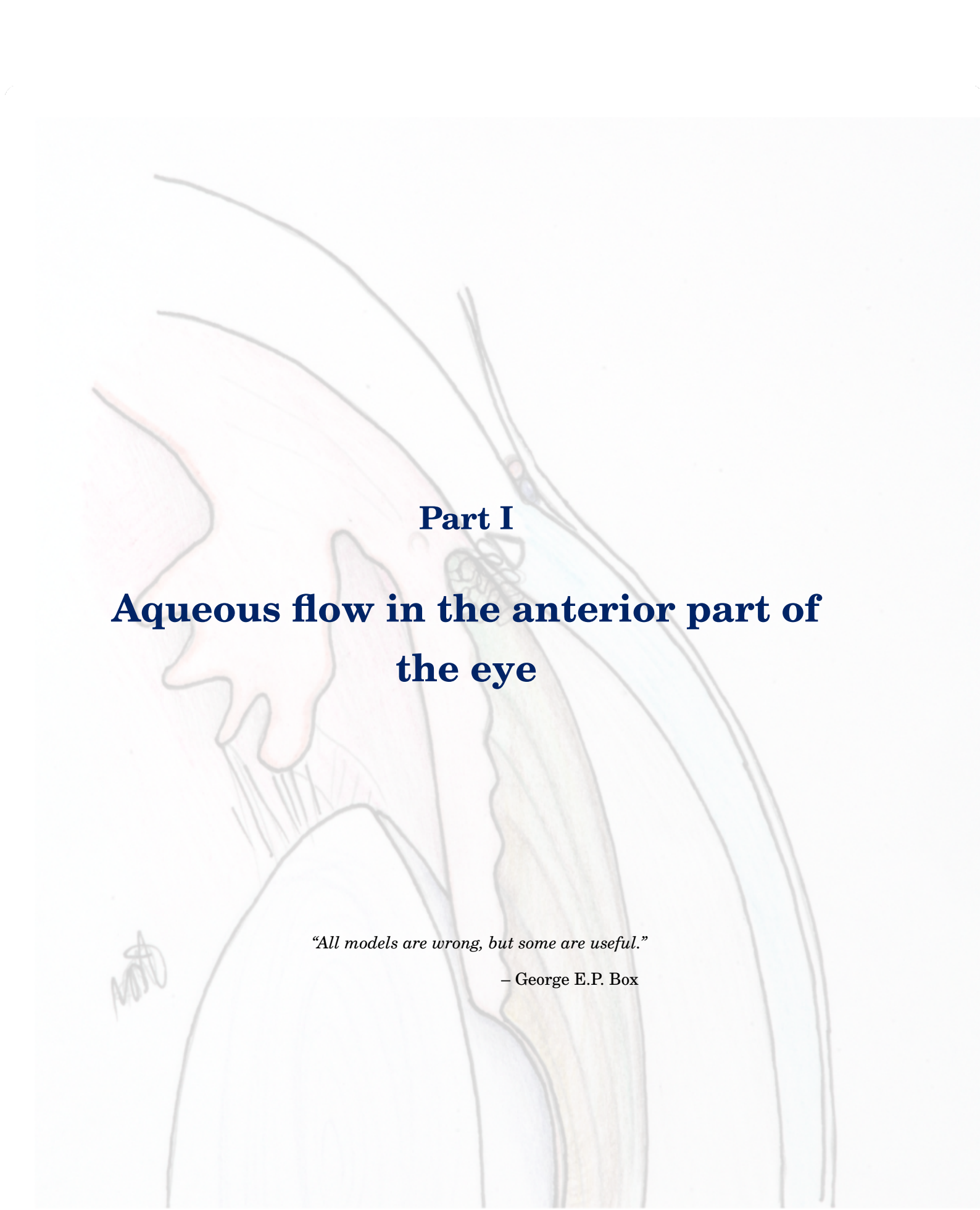

Part I

Aqueous flow in the anterior part of the eye

"All models are wrong, but some are useful."

– George E.P. Box

CHAPTER 1

OVERVIEW OF MATHEMATICAL MODELS OF AQUEOUS HUMOUR DYNAMICS

This review chapter is partly based on the book chapter by Dvoriashyna et al., to which we refer the reader for a detailed description of mathematical models of aqueous flow.

1.1 The aqueous humour

The aqueous humour (AH) is the fluid contained in the posterior (PC) and anterior (AC) chambers of the eye (see figure 0.1 and figure 1.1). These two chambers are connected to each other through the pupil and AH can thus flow from one to the other. AH is an aqueous solution containing a mixture of electrolytes, organic solutes, growth factors and other proteins (Fautsch and Johnson, 2006). From the rheological point of view AH has properties similar to those of water and behaves as a Newtonian fluid.

AH is continuously produced by the ciliary processes, at a rate of approximately 3 μl/min ($\approx 5 \times 10^{-11}$ m^3/s) (Brubaker, 1989, 1991), it flows along the PC, passes through the pupil into the AC and eventually exits the eye via the conventional and uveoscleral pathways. In the former pathway, which in humans accounts for the majority of the drainage (Alm and Nilsson, 2009), AH percolates through the trabecular meshwork, enters Schlemm's canal and is finally drained into the venous system through small, roughly evenly spaced, channels. In the uveoscleral (or unconventional) outflow pathway, AH passes from the AC into the ciliary muscle and then into the supraciliary and suprachoroidal spaces, and finally exits the eye through the sclera.

One of the main functions of AH flow is to regulate the mean intraocular pressure (IOP), i.e. the fluid pressure inside the eye, which is the result of a balance between aqueous production and resistance to aqueous outflow. Physiological values of the IOP range between 12 and 22 mmHg

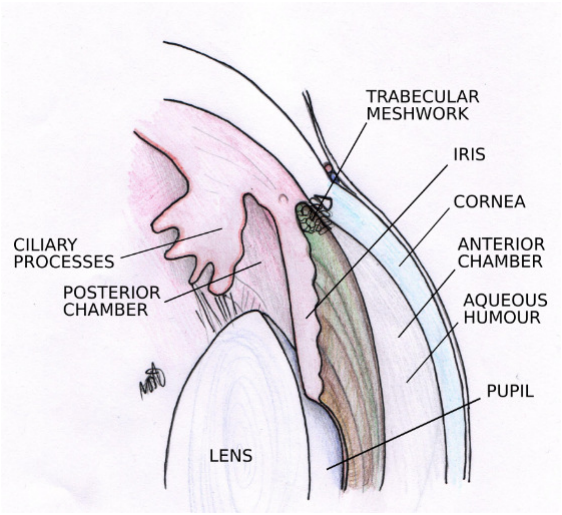

Figure 1.1: Sketch of the anterior segment of the eye. Drawing by Prof. Federica Grillo.

(1660–2933 Pa) and it is known that an elevated IOP is correlated with the occurrence of open angle glaucoma (Weinreb and Khaw, 2004; Kwon et al., 2009), one on the most common causes of blindness worldwide (Klaver et al., 1998; Rudnicka et al., 2006).

AH also has the role of delivering nutrients to ocular avascular tissues, such as the lens and the cornea (Gabelt and Kaufman, 2003).

Various mathematical models have been proposed for studying aqueous flow, which significantly contributed to our understanding of the underlying physical phenomena. In this section we briefly review the state of the art of the research regarding aqueous flow modelling. We will proceed following the AH path, from its production to its drainage out the eye.

1.2 Aqueous humour production

AH is produced by the ciliary body and, in particular, at the ciliary processes, which are a series of wrinkles that have the role of increasing the surface area available for fluid production (Delamere, 2005). The ciliary processes are linen by a double layer of epithelial cells, which are responsible for AH production.

There are three mechanisms involved in the process of aqueous production, which are briefly described below.

Mechanical pressure. A standing pressure drop exists between blood in the capillaries and AH in the PC. This pressure difference tends to pump fluid into the PC.

Oncotic pressure. Tight junctions connect the cells in the ciliary epithelium and act as a sieve for large molecules. Since large molecules cannot flow across the double layer of cells into

the PC an oncotic pressure difference is established across the ciliary epithelium, which drives water flux from the PC back to the stroma.

Osmotic pressure. Ions are actively transported across the ciliary epithelium and the typical picture is that 'water follows the ions', i.e. water motion occurs in the main direction of ion transport. The osmotic pressure difference established across the ciliary epithelium is such to drive water flux from the stroma into the PC.

The most common approach to model the process of aqueous production is to treat the whole epithelium as a semipermeable membrane (Lyubimov et al., 2007; Kiel et al., 2011; Szopos et al., 2016). The volumetric flux per unit surface through the ciliary epithelium F (positive if the flux is from the stroma to the PC) can be written as follows, accounting for the mechanisms described above,

$$F = L_p \left(\Delta p - \sigma_p \Delta \Pi_p - \sigma_s \Delta \Pi_s \right), \tag{1.1}$$

where L_p is the membrane hydrodynamic conductivity (measured in the international system in $\mathrm{m}^2\mathrm{s/kg}$), p denotes the mechanical pressure, Π_p the oncotic pressure and Π_s the osmotic one. The operator Δ denotes the difference between the value of the quantity it is applied to in the stroma and in the aqueous. Finally, σ_p and σ_s are the reflection coefficients for proteins and low-molecular components, respectively. Estimates of the values of the various parameters that appear in equation (1.1) are provided in Lyubimov et al. (2007) and Szopos et al. (2016).

Kiel et al. (2011) improved the above simple model by also accounting for the role of ciliary blood flow on aqueous production, making use of a lumped parameter model, showing that there is an interplay between ciliary blood flow and aqueous humour production.

Avtar et al. (2008), proposed a model of aqueous production by the ciliary epithelium based on the standing gradient osmotic flow hypothesis originally proposed by Diamond and Bossert (1967), which exploits the role of the cleft gap between adjacent cells. This is a mechanism known as 'local osmosis' that will be dealt with in great detail in chapters 5 and 6 in the context of water transport across the retinal pigment epithelium.

1.3 Flow in the posterior chamber

AH produced at the ciliary processes flows along the PC towards the pupil, the flow being driven by a pressure gradient. The PC is a thin region, the thickness of which progressively decreases towards the pupil, reaching a depth of some microns in correspondence of the iris-lens channel. Since the AC is much thicker than the PC most of the resistance to AH flow from the ciliary processes to the trabecular meshwork, and therefore most of the pressure drop, occurs in the PC and, in particular, in the iris-lens channel.

The first analytical model of aqueous flow in the PC was proposed by Friedland (1978) and was based on the assumption that the PC has a constant depth. A similar model was also developed by

Silver and Quigley (2004), who, however, just considered the flow through the iris-lens channel, which they modelled as a gap of constant height. In chapter 2 we will present a more refined model of the flow in the PC, that accounts for a realistic geometry of the domain. We will also consider the flow that can be generated in the PC by changes of the geometry, due for instance to pupil expansions or contractions, which have not been studied by previous authors.

1.4 Flow in the anterior chamber

We keep following the AH during its flow and, after passing through the iris/lens channel we enter the AC. AH motion in the AC can be driven by various mechanisms and has been the object of quite a lot of attention from modellers. The main mechanisms responsible for AH motion in the AC are: (i) aqueous secretion and drainage; (ii) temperature difference across the thickness of the AC, that drive flow through buoyancy effects; (iii) eye rotations; (iv) change of the shape of the AC as a result of iris contraction, dilation or lens accommodation. As for the latter mechanism, to our knowledge, there are no mathematical models in the literature that address it. Thus, in the following of this section we review the characteristics and mathematical models of the former three flows.

1.4.1 Pressure driven flow

The flux entering the AC through the pupil is driven towards the trabecular meshwork by a pressure gradient. Pressure losses along this path are extremely small. Numerical simulations by Repetto et al. (2015) show that, in normal conditions, the pressure drop across the AC is as small as 7×10^{-7} mmHg. The corresponding velocity in the AC is also very small, of the order of 10^{-6} m/s.

A numerical model that combines aqueous flow with iris deformation due to a pressure difference between the PC and AC has been proposed by Heys et al. (2001). Later, Villamarin et al. (2012) proposed a three-dimensional numerical model based on a real reconstructed human eye geometry. They coupled the pressure driven flow and the flow induced by temperature differences across the AC (discussed in the next section). Moreover, they considered flow in the AC, PC, trabecular meshwork (which they modelled as a porous medium) and Schlemm's canal.

The fact that the pressure drop due to the pressure driven flow in the AC is so small compared to the pressure jump across the iris/lens channel suggests that, for most purposes, the flow in the AC can be studied independently of that in the PC.

1.4.2 Thermally driven flow

The anterior region of the AC is typically at a lower temperature than the posterior region, close to the iris. This establishes a thermally driven flow produced by buoyancy effects (the fluid in

the anterior part of the chamber has a larger density). The existence of such a flow was observed clinically already more than a century ago by Türk (1906).

This flow was studied analytically by Canning et al. (2002) and Fitt and Gonzalez (2006), under the assumption that the AC can be modelled as a thin domain, which allowed them to use lubrication theory. The authors showed that the flow consists in a single convection cell, rising (opposing gravity) in the back of the AC and falling in the front (along the cornea). Moreover, lateral fluid movement, in the nasal-temporal direction, is very weak (absent in the thin domain limit). The authors found that the maximum fluid velocity is approximately 2×10^{-4} $(T - T_0)$ m/s/K, where $T_1 - T_0$ is the temperature difference across the AC. This means that, when $T_1 - T_0$ is equal to a few degrees (which is what happens in normal conditions), the velocity generated by thermal effects is much larger than that produced by aqueous production/drainage.

Heys and Barocas (2002), Fitt and Gonzalez (2006) and Repetto et al. (2015) confirmed the above analytical results with fully numerical simulations.

Aqueous motion in the AC induced by thermal effects is important since it is one of the primary mechanisms inducing fluid mixing, at least during daytime. As mentioned above, one of the key roles of AH is to deliver nutrients to ocular avascular tissues. The existence of relatively effective mixing processes in the AC avoids the generation of local regions of nutrient depletion in the AH, which in turn would decrease the efficiency of transport to the target tissues.

1.4.3 Fluid flow induced by eye rotations

Movements of the eye induce motion of AH in the AC. The motion of a rigid body can be decomposed into a translation and rotation about an axis. In the case of pure translation, of the AC, there is no fluid motion relative to the domain, and the acceleration is balanced by a pressure gradient (Fitt and Gonzalez, 2006). Thus, we focus in the following on the motion induced by eye rotations.

Saccades are rapid rotations of the eyes causing an abrupt change the direction of sight (Purves et al., 2001). The range of amplitude of such movements is very wide, from small eye rotations when a person is reading, to large ones when gazing around a room. Rapid eye movements (REMs) that occur involuntarily during sleep are also a type of saccade. AH motion in the AC secondary to single and periodic saccades and periodic REM, have been studied with numerical models by several authors, and we will review such works in this section.

Abouali et al. (2012) first studied with numerical simulations the flow induced in the AC by single and periodic saccades. They showed that eye rotations generate fluid velocities in the AC larger than any other mechanisms. The authors computed the wall shear stress on the cornea produced by this flow and showed that it invariably peaks at the centre of the cornea and reaches values of the order of 0.1 Pa. For the periodic motion, the authors observed that a steady component of the flow is generated (steady streaming), owing to the nonlinearity of the governing

equations. The occurrence this steady flow component is important for mixing processes (Riley, 2001).

Modarreszadeh et al. (2014) used a similar approach to study the flow due to REMs, mainly focusing on the possible contribution to mixing, and also observed the generation of steady streaming. When a person is asleep and the eyelids are closed, no thermally driven flow occurs in the AC and this means that the mixing discussed in previous section cannot take place. It has thus been hypothesised by Maurice (1998) that REMs are responsible for AH mixing during sleep. The results of Modarreszadeh et al. (2014) confirm this hypothesis and show that during night REM is the main mixing mechanism in the AC.

An analytical model of the flow due to eye rotations is presented in chapter 3.

1.5 Aqueous drainage

The AH exits the AC through two outflow routes, which are called the conventional and uveoscleral routes. In what follows, we will describe each one of them.

1.5.1 The conventional route

In the conventional route AH flows from the AC through the trabecular meshwork and the juxtacanalicular tissue in the angle of the eye, into the Schlemm's canal. It then leaves Schlemm's canal through collector channels that drain into the venous system. The flow in the conventional pathway is driven by a pressure drop between the AC and the episcleral veins, which is needed to overcome the resistance to flow of the tissues in the pathway, and it is known to decrease with advancing age due to increased resistance of the pathway (Toris et al., 1999; Tamm, 2009).

This pathway has gained major interest in recent years also from modellers, as it is linked with the development of primary open-angle glaucoma. In this disease, pathological changes in the drainage tissues gradually increase resistance to the flow of aqueous probably over a period of many years. This forces the IOP to rise in order to maintain the overall flow of AH, leading also to a greater flow through the uveoscleral pathway (Johnson and Johnson, 2001). In turn, an elevated IOP is thought to lead to damage of the optic nerve head and death of retinal ganglion cells, eventually resulting in vision loss. The location of the increase in resistance to outflow during glaucoma is not precisely known, but studies have confirmed it is in either the extracellular matrix of the juxtacanalicular meshwork, the basement membrane of Schlemm's canal or the endothelial cells in the inner wall of Schlemm's canal (Johnson, 2006).

One study that shows what parts of Schlemm's canal are the main contributors to resistance is that by Johnson and Kamm (1983). In their work the juxtacanalicular meshwork and the endothelial lining of the inner wall of Schlemm's canal are considered jointly as the inner wall, with the primary intent to study the possible collapse of the canal. Schlemm's canal is modelled as a compliant channel with porous walls that is held open by the trabecular meshwork. The

trabecular meshwork is modelled as a series of linear springs that allow deformation of the inner wall of Schlemm's canal in proportion to the local pressure drop across it. Results obtained by Johnson and Kamm (1983) show that the flow rate Q increases as the pressure drop $\mathscr{P}$ between the AC and the collector channel increases. For small pressure drops Q is a linear function of $\mathscr{P}$, indicating that the resistance to flow is approximately constant, which, in turn, means that the majority of the resistance comes from traversing the inner wall of Schlemm's canal. When the pressure drop is large the resistance to flow in the canal increases, since the canal collapses and becomes narrower.

More recent studies have extended this model by including a better geometrical representation of Schlemm's canal (Avtar and Srivastava, 2007), and adding a poroelastic model of the trabecular meshwork, the porosity of which changes under strain as Schlemm's canal collapses.

Ethier et al. (1986) analysed transmission electron micrographs of the juxtacanalicular tissue to estimate its Darcy permeability, and they found that the resistance of the juxtacanalicular tissue alone is too small by a factor of 10–100 to explain the pressure drop across the tissue. They proposed that the excess resistance is generated by the existence of an extracellular matrix gel between the tissues.

Johnson et al. (1992) suggested that, in addition to the extracelluar matrix, the fact that the high-resistance juxtacanalicular tissue abuts the inner wall of Schlemm's canal means the AH has to converge through the juxtacanalicular tissue towards each of the holes in the inner wall. This leads to the so-called 'funnelling hypothesis', in which the total resistance of the combined tissues is greater than the sum of the resistances of the tissues separately, because the flow is not parallel in the juxtacanalicular tissue due to the requirement that the flow converges onto the pores in the inner wall. Johnson et al. (1992) used a mathematical model to study this problem. In the limit of small pore radius they were able to obtain an analytical solution for the effective resistance of the combined tissue.

Merchant and Heys (2008) showed that allowing for spatially heterogeneous permeability of the juxtacanalicular tissue leads to an increased tissue resistance, and furthermore that adding a model of the pores in the endothelial cells of the inner wall of Schlemm's canal significantly increases the resistance of the combined tissue.

1.5.2 The uveoscleral route

The uveoscleral route was discovered in humans by Bill and Phillips (1971). Unlike the posterior surface, the anterior surface of the iris is not covered by epithelial tissue, and this allows AH to flow through the iris root and into the clefts between the ciliary muscle bundles, from where it can pass through the sclera and out of the eye. A comprehensive review is provided by Alm and Nilsson (2009). The percentage of uveoscleral flow as a fraction of the total outflow varies widely in different species, constituting up to 60% in primates and as low as 3% in the cat and rabbit. In humans, reported flows vary widely between about 12% and 54% of the total outflow, and the

absolute flow generally decreases with advancing age, due to additional connective tissue that appears in the ciliary muscle, reducing its permeability and decreasing the uveoscleral flow (Alm and Nilsson, 2009). On the other hand, despite being pressure-driven, the flow has only a weak dependence on IOP, which is because the main source of resistance is within the ciliary muscle, and when the IOP increases it increases on both sides of this muscle, meaning the pressure gradient across the muscle itself stays relatively unchanged (Alm and Nilsson, 2009).

To our knowledge, no mathematical models of the flow in the uveoscleral route exist.

1.6 Contents of this part of the thesis

Part I of the present thesis is concerned with problems related to AH flow.

In chapter 2 we study the fluid mechanics in the anterior segment of the eye in the presence of an iridotomy. This is a surgically produced hole through the iris, that creates an additional path for the AH to pass from the PC to the AC. Iridotomy has the role of reducing a pathologically high pressure in the PC that can induce an angle closure glaucoma, a very serious, sight threatening condition. The aim of the work is to use mathematical modelling to investigate the ideal size and location of an iridotomy. To this end we first propose a more refined model of the flow in the PC than those presented in § 1.3 and then modify it, to account for the presence of the iridotomy.

In chapter 3 we propose a model of the flow induced in the AC by rotations of the eye bulb. The model is semi-analytical and, in this respect, complements the numerical approaches mentioned in § 1.4.3. The model allows us to highlight features of the flow not described by previous authors. We also confirm the existence of a steady streaming flow, and show that it is one of the key players in transport processes in the AC.

CHAPTER 2

AQUEOUS HUMOUR FLOW IN THE POSTERIOR CHAMBER OF THE EYE IN THE PRESENCE OF PUPILLARY BLOCK AND IRIDOTOMY

This chapter is based on the publication by Dvoriashyna et al. (2017)

2.1 Introduction

As discussed in the previous chapter, aqueous humour (AH) flows from the posterior (PC) to the anterior (AC) chamber through the narrow iris–lens channel. When iris and lens come into contact, a pathological condition named pupillary block may occur, which can be total or partial, according to whether the entire length of the pupil is blocked or only part (Liebmann and Ritch, 2002). This means that the iris–lens channel has a greater resistance to flow, potentially leading to a significant increase in the aqueous pressure in the PC, which can in turn result in the iris being pushed forward, so that the angle between the cornea and the iris, where the trabecular meshwork is located, closes and aqueous drainage out of the AC is impeded (Tarongoy et al., 2009). This is called angle-closure glaucoma and it occurs in about 0.5% of whites and blacks and about 1.5% of Chinese and Indian individuals over the age of 40 (Friedman, 2007). Even though angle-closure glaucoma is less prevalent than open-angle glaucoma it may be responsible for as much blindness worldwide (Quigley and Broman, 2006).

Angle-closure glaucoma requires immediate surgical treatment, typically by creating an iridotomy, that is a hole through the iris that connects the PC and the AC, thus alleviating the large pressure difference between them (Wright et al., 2016). Iridotomies are also normally created during implantation of iris-fixated and sulcus implanted phakic intraocular lenses in order to avoid the risk of IOP increase (Dick et al., 2009).

Iridotomy has been demonstrated to be a relatively safe procedure, but it has potential

complications for the cornea that are discussed in detail by Wang et al. (2014). In particular, various authors have described the development of corneal decompensation following iridotomy (e.g. Lim et al., 2006; Ang et al., 2007), which is a result of the failure of the corneal endothelium functioning and might eventually lead to the need of a corneal transplantation. Various mechanisms have been hypothesised for endothelial damage (see Wang et al., 2014), and among these is the shear stress on the corneal endothelium due to aqueous humour hydrodynamics (Yamamoto et al., 2006). In particular, Kaji et al. (2005) used in vitro experiments to investigate the hypothesis that the jet of aqueous humour entering the AC from the iridotomy could produce large stresses on the corneal endothelium and found that the number of detached cells increased with the shear stress exerted by the fluid. This assumption is supported by Marraffa et al. (1995), who found the loss of endothelial cells to be approximately inversely proportional to the distance of the iridotomy from the corneal endothelium and the scleral spur. Moreover, Lim et al. (2005) suggested that iridotomy could be correlated with cataract formation, even though this hypothesis is not universally accepted (Bobrow, 2008). Hydrodynamic stresses generated on the lens could contribute to cataract formation in the presence of an iridotomy.

In spite of iridotomy being of standard use in surgical practice, very little is known concerning the changes it induces in the flow in the PC. In particular, the optimal size and location of the iridotomy is still an open issue. Understanding the characteristics of flow in the PC and risk factors associated with laser iridotomy may allow physicians to counsel and treat patients in a safer and more efficient way. In the biomechanical literature there are very few works that address these issues. Fleck (1990) proposed a basic mathematical model of aqueous flow through an iridotomy in the case pupillary block, using the Hagen–Poiseuille formula to calculate the pressure drop across the iridotomy tunnel. His work suggests that in theory a 15 μm diameter iridotomy should be large enough to prevent angle closure glaucoma, but that in his clinical experience larger diameters in the range 150–200 μm are needed. Silver and Quigley (2004) used a similar approach to consider an iridotomy in their iris–lens channel model, and found that a diameter of 50 μm would make the pressure difference between posterior and anterior chamber fall below 1 mmHg. Yamamoto et al. (2006) measured the jet velocity through an iridotomy experimentally in rabbit eyes, and Yamamoto et al. (2010) studied this flow numerically.

The aim of the present work is to improve our mechanical understanding of the flow in the PC and its modifications due to pupillary block and iridotomy. We develop a mathematical model based on lubrication theory for the flow in the PC. This allows us to avoid the numerical difficulties that would arise as a consequence of the strong spatial variability of the size of the domain. We consider two mechanisms that drive aqueous flow: aqueous production in the ciliary body and iris motion due to pupil constriction/dilation (miosis/mydriasis); and show that the latter mechanism, which was not considered in previous works, can cause a significantly more intense flow. We also discuss the effect of a partial pupillary block on the flow. We then study how the flow in the PC is modified by the presence of an iridotomy, which we model as a point sink for

the flow in the PC. The flux through this sink is set proportional to the pressure and, to avoid the singularity in the pressure that occurs in correspondence of a point sink, we introduce a suitably regularised pressure to find the solution. We propose a mathematical theory, which allows us to solve the problem semi-analytically.

2.2 Methods

2.2.1 Geometry of the posterior chamber

We study the flow in the PC of the eye, considering both the motion produced by aqueous production at the ciliary processes and that induced by variations in the pupil diameter. Visualising the PC is very challenging owing to its small size and to the fact that high resolution optical imaging techniques, such as OCT, cannot penetrate behind the iris. In this study, in order to measure the geometrical characteristics of the PC, we employed a high-frequency ultrasound scan, with a 50 MHz transducer (VuMax 35/50 Sonomed). Examinations were performed under topical anaesthesia (oxybuprocaine hydrochlororide 0.4%) on a healthy human subject, applying an eye cup containing physiological saline. Serial transverse and radial scans were performed. This allowed us to obtain a clear view of the posterior surface of the iris and of the anterior surface of the lens.

We used the cross-sectional image of the PC shown in figure 2.1(a). This has a resolution of 20–30 μm (axial–lateral), which is sufficient to measure the geometrical characteristics away from the pupil, but not the thickness of the iris–lens channel (ILC), the narrow part of the PC nearest to the pupil, which we estimate from the image to have length of approximately 1.14 mm. In the absence of clinical data, and following Silver and Quigley (2004), we assume that the minimum depth H_p of the ILC, which occurs at the pupil, is between 3 and 7 μm. We call the rest of the PC outside of the ILC the *bulk posterior chamber* (bPC).

We note that even for a single patient, the shape of the PC can change quite substantially with environmental conditions, but that, aside from in the very narrow ILC, the details of the geometry in the bPC do not make a significant difference to the flow. Therefore owing to the impossibility of considering all possible PC geometries, we considered one image as a representative, as we believe this provides us with a realistic geometry that is sufficient for the purposes of this work.

To describe the shape of our domain and in the mathematical formulation that follows in § 2.2.2, we work in a system of spherical coordinates (r,θ,ϕ), see figure 2.1(b), with the axis $\theta = 0,\pi$ orthogonal to the equatorial (coronal) plane of the eye (i.e. in the antero–posterior direction) and passing through the centre of the pupil. We model the PC as an axisymmetric region with respect to this axis (i.e. independent of ϕ). We approximate the shape of the anterior surface of the crystalline lens as part of a spherical surface of radius R, the centre of which is the origin $r = 0$ of the coordinate system (which is not the centre of the eye), and we denote the thickness of the posterior chamber in the radial direction as $h(\theta)$, so that the posterior surface of the iris is

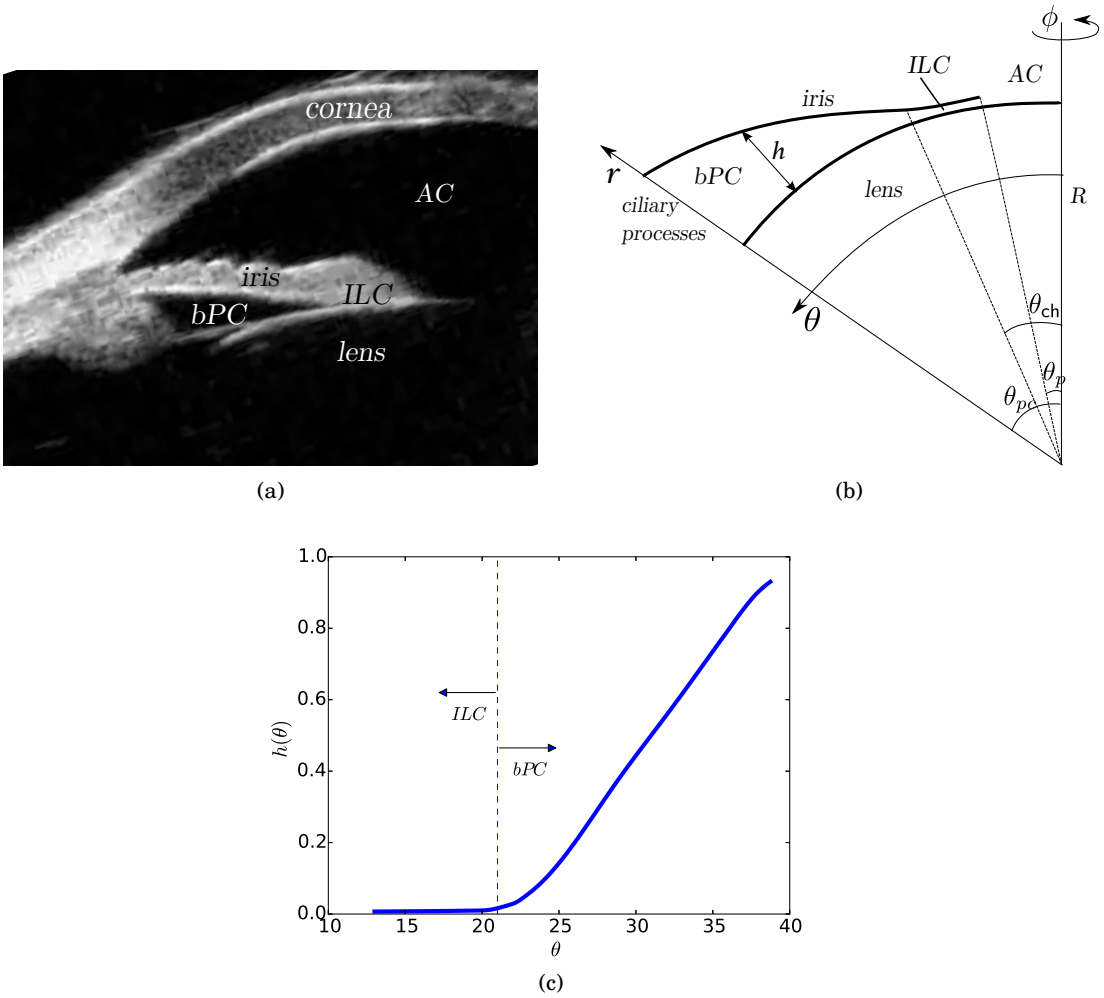

Figure 2.1: (a) Ultrasound scan of the anterior segment of the eye. (b) Sketch of the notations and coordinate system. (c) Plot of the resulting function $h(\theta)$ (in mm) that we use to model the height of the PC. ILC: iris–lens channel; bPC: bulk posterior chamber; AC: anterior chamber.

given by $r = R + h(\theta)$. We use the image to estimate three particular angles as follows: θ_p is the value of θ at the pupil (the inner boundary of the ILC); θ_{ch} is at the outer boundary of the ILC, which we take to be the last point at which the PC can be distinguished in the image (rightmost end of the bPC in figure 2.1(a)); and $\theta = \theta_{pc}$ is the location of the outer boundary of the posterior chamber (left end of the bPC in figure 2.1(a)). To construct a height function $h(\theta)$ for the PC, we used measurements from the image in the range $\theta_{ch} \le \theta \le \theta_{pc}$ together with $h(\theta) = H_p$ at $\theta = \theta_p$ and used a monotonic cubic interpolation to obtain values of h at intermediate values of θ, the result of which is shown in figure 2.1(c). The PC therefore lies in the region $R \le r \le R + h(\theta)$, $\theta_p \le \theta \le \theta_{pc}$, $0 \le \phi < 2\pi$.

We estimated the radius of curvature of the lens as $R \approx 8.19$ mm, which is in the range of typical values given by Katz and Kruger (2009), and we measured the maximum height of the PC

(which is obtained at the outside edge of the PC) as 0.94 mm. The bPC approximately spans the range $21^\circ \leq \theta \leq 39^\circ$, which corresponds to a length of about 2.57 mm. The characteristic dimensions of the PC (length, depth, volume *etc.*) corresponding to the resulting height function $h(\theta)$ are in line with published data (Dorairaj et al., 2009), and the relevant geometrical characteristics of the domain are reported in table 2.1.

2.2.2 Model of aqueous flow

2.2.2.1 Flow in the posterior chamber

We model the aqueous flow as being driven by aqueous production and iris motion, and treat the fluid as Newtonian and incompressible with density ρ, dynamic viscosity μ, velocity $\mathbf{u} = (u_r, u_\theta, u_\phi)$ and pressure p. Fluid flow is governed by the Navier–Stokes and continuity equations, and we neglect gravity, since buoyant effects are negligible in the PC (although they are known to play an important role in the AC of the eye; see Canning et al., 2002; Heys and Barocas, 2002; Fitt and Gonzalez, 2006). We assume the pressure in the AC is uniform and equal to the reference value zero, and thus p is the departure from the hydrostatic pressure distribution and is also relative to the AC pressure. This assumption is justified by the observation that the width of the AC is significantly greater than that of the PC, meaning that pressure drops within it are negligible (Repetto et al., 2015).

Let us now estimate the magnitude of various terms in the Navier–Stokes equations. We evaluate the aspect ratio of each region of the domain as $\epsilon_i = H_i/L_i$, with $i = \text{bPC, ILC}$, and where H_i and L_i are the average depth and length of region i. From our measurements we estimated the following values: $\epsilon_{\text{bPC}} \approx 0.17$ and $\epsilon_{ILC} \approx 0.01$. We base the scale for the velocity U on the volumetric flux F through the PC according to the following expression $U_i = F/A_i$, $i = \text{bPC, ILC}$, where A_i is the average cross section area of region i. The volumetric flux F has to be estimated separately for the flow generated by aqueous production/drainage and by iris motion. In the case of production/drainage, $F \approx 3$ μl/s (Brubaker, 1991), giving $U_{\text{bPC}} \approx 4.6$ μm/s, $U_{\text{ILC}} \approx 221$ μm/s, which corresponds to the following Reynolds numbers: $Re_{\text{bPC}} = U_{\text{bPC}} L_{\text{bPC}} \rho/\mu \approx 0.014$; $Re_{ILC} = U_{\text{ILC}} L_{\text{ILC}} \rho/\mu \approx 0.34$.

The case of iris motion during miosis is trickier. Milton and Longtin (1990) report that pupil constriction typically lasts less than one second, whereas pupil dilation takes a couple of seconds. Dorairaj et al. (2009) performed challenging experiments in which they estimated the PC volume from ultrasound images before and after pupil dilation, showing that, as the pupil dilates, some eyes have an increase in PC volume while others have a decrease. They report that, in both the case of pupil dilation and that of pupil contraction, changes in the PC volume ΔV during iris motion are small and so here we assume ΔV to be a small percentage of the PC volume V. Since we are interested in the effect of the jet of aqueous through the iridotomy on the cornea, and the pupil diameter changes faster during pupil contraction than during dilation, we investigate the worst case scenario by focusing on contraction (miosis) in the case in which the

Parameter	**Value**	**Source**
Radius of the lens, R	8.19 mm	measured from the image
Minimum height of the iris-lens channel, H_p	7 μm	Silver and Quigley (2004)
Flux produced by ciliary body, Q	3 μl/min	Brubaker (1991)
Volume of the posterior chamber, V	32.4 μl	measured from the image
Thickness of the iris, S	0.457 mm	Pavlin et al. (1992)
Dynamic viscosity of aqueous humour, μ	0.71 mPa·s	Scott (1988)
Density of aqueous humour, ρ	1000 kg/m^3	

Table 2.1: Geometrical values and fluid properties

			Steady iris		Moving iris	
Region	ϵ	ϵ^2	Re	$\epsilon^2 Re$	Re	$\epsilon^2 Re$
bPC	0.17	$2.9\cdot10^{-2}$	0.014	$4\cdot10^{-4}$	0.51	$1.5\cdot10^{-2}$
ILC	0.01	10^{-4}	0.34	$3.4\cdot10^{-5}$	12	$1.2\cdot10^{-3}$

Table 2.2: Dimensionless parameters in two different regions

PC volume decreases (so that a jet is forced out of the PC towards the cornea). With $\Delta V = 0.05V$ and $T = 1$ s, we obtain a flux of 106 μl/min, which is significantly larger than the flux due to production/drainage, and the corresponding Reynolds numbers are $Re_{\mathrm{bPC}} \approx 0.51$ and $Re_{ILC} \approx 12$.

The parameter values are reported in table 2.2, and, with these estimates, ϵ_i^2 and $\epsilon_i^2 Re_i$ are small ($i = \mathrm{bPC},\ \mathrm{ILC}$), meaning that lubrication theory is valid in the bPC and in the ILC. According to this approach, in region i we scale the space in the radial direction with H_i and in azimuthal and zenithal directions with L_i for $i = \mathrm{bPC},\ \mathrm{ILC}$. Moreover, inspection of the continuity equation suggests scaling u_θ and u_ϕ with U_i and u_r with $\epsilon_i U_i$. With these choices, and neglecting terms of order ϵ_i^2 and $\epsilon_i^2 Re_i$, the dimensional Navier–Stokes and continuity equations simplify to

$$\nabla_h p = \mu \frac{1}{r^2}\frac{\partial}{\partial r}\Big(r^2 \frac{\partial \mathbf{u}_h}{\partial r}\Big), \tag{2.1}$$

$$\nabla_h \cdot \mathbf{u}_h + \frac{1}{r^2}\frac{\partial (r^2 u_r)}{\partial r} = 0, \tag{2.2}$$

where p is independent of r, and 'h' is a subscript indicating that only the (θ,ϕ)-components are considered. We have neglected the time-derivatives in (2.1) and (2.2), meaning that we solve the problem in a fixed domain and account for the iris motion by imposing the axisymmetric velocity field $\mathbf{v} = (v_r, v_\theta, 0)$ at $r = R + h(\theta)$. The choice of the velocity field $\mathbf{v}$ is discussed in § 2.2.2.3.

The solution of (2.1), subject to no-slip boundary conditions, is

$$\mathbf{u}_h = \frac{1}{2\mu}\nabla_h p\Big(r^2 + R(R+h) - r(2R+h)\Big) + \mathbf{v}_h \frac{R+h}{h}\Big(1 - \frac{R}{r}\Big), \tag{2.3}$$

where $\mathbf{v}_h$ is set to zero in the case with no miosis. Integrating the continuity equation (2.2) with respect to r and using the no-slip conditions $u_r = 0$ at $r = R$ and $u_r = v_r$ at $r = R + h$, we obtain

the governing equation for the pressure

$$\frac{1}{12\mu}\,\mathbf{A}(p) = v_r + \frac{h}{2(R+h)}\nabla_h \cdot \Big((R+h)\mathbf{v}_h\Big) - \frac{1}{2}\nabla_h h \cdot \mathbf{v}_h \tag{2.4}$$

where the differential operator $\mathbf{A}$ is defined as

$$\mathbf{A} = \frac{1}{\sin\theta(R+h)^2}\left(\frac{\partial}{\partial\theta}\left(\sin\theta h^3\frac{\partial}{\partial\theta}\right) + \frac{h^3}{\sin\theta}\frac{\partial^2}{\partial\phi^2}\right), \tag{2.5}$$

and in the above expressions v_r denotes the radial component of $\mathbf{v}$ and the operator ∇_h is computed with fixed $r = R + h$. The problem is therefore governed by equation (2.4) together with boundary conditions at the ciliary processes ($\theta = \theta_{pc}$) and at the pupil ($\theta = \theta_p$). At $\theta = \theta_{pc}$ we impose the aqueous production flux Q, which leads to the following condition:

$$\frac{Q}{\pi\sin\theta} = \frac{\partial p}{\partial\theta}\frac{h^3}{6\mu} - (R+h)hv_\theta \qquad \text{at } \theta = \theta_{pc}. \tag{2.6}$$

At $\theta = \theta_p$ we impose a constant pressure, equal to the one in the AC, which we set to be 0:

$$p = 0 \qquad \text{at } \theta = \theta_p. \tag{2.7}$$

We will also consider the case of pupillary block. Specifically, we study the case in which the pupil is entirely blocked in certain regions but allows fluid flow in others. This modifies the condition at the pupil as follows:

$$\begin{cases} p = 0 & \text{at } \theta = \theta_p,\ 0 \le \phi < \phi_b, \\ \dfrac{\partial p}{\partial\theta}\dfrac{h^3}{6\mu} - (R+h)hv_\theta = 0 & \text{at } \theta = \theta_p,\ \phi_b \le \phi < 2\pi. \end{cases} \tag{2.8}$$

where ϕ_b denotes the azimuthal angle at the boundary between the open and blocked regions, and the condition in the blocked region $\phi_b \le \phi < 2\pi$ is no flux through the ILC. Pupillary block is clinically relevant since it induces a persistent increase of pressure in the PC that pushes the iris forward and occludes the angle between the cornea and the iris, blocking drainage of aqueous from the AC. As the time scale for the pressure buildup is much longer than the one of the pressure variations induced by miosis, such variations are neglected in this framework, even though the equations stated above are for the general case.

2.2.2.2 Flow in the posterior chamber with iridotomy

In this section we consider the effect of creating an iridotomy on the flow and pressure in the PC. Away from the location of the hole we can use the method developed in § 2.2.2.1 to reformulate the problem as a second-order differential equation for p in (θ,ϕ)-space (2.4), but in this case we require additional boundary conditions at the iridotomy as well as the boundary conditions (2.6)–(2.7) (or (2.8) in the case of pupillary block). Iridotomy holes are typically less than 200 μm in diameter (Fleck, 1990), which is small compared to the radius of the PC, meaning the geometry

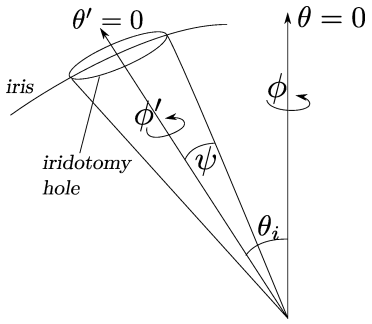

Figure 2.2: Sketch of the coordinate systems $\mathscr{S}$ and $\mathscr{S}'$.

of the resulting domain would be much more difficult to discretise than in the case with no iridotomy. Therefore in this section we formulate a method to reduce the iridotomy to a point sink of zero size in the (θ,ϕ)-surface, at which we imposed a boundary condition relating the volumetric flux into the sink to the pressure. Since such a point sink would give rise to an infinite pressure there we reformulate the problem in terms of a regularised pressure that avoids the singularity.

To obtain the correct regularisation for the pressure we model the iridotomy as an approximately cylindrical hole through the iris, whose central axis is on the radial line $\theta = \theta_i$, $\phi = 0$. For convenience we also refer to a new system of spherical coordinates $\mathscr{S}' = (r,\theta',\phi')$, related to the original coordinates $\mathscr{S} = (r,\theta,\phi)$ by a rotation through the angle θ_i, such that the axis $\theta' = 0$ is the central axis of the iridotomy (figure 2.2). The following relationships link the two coordinate systems $\mathscr{S}$ and $\mathscr{S}'$ (Meskauskas et al., 2011):

$$\cos\theta' = \sin\theta\cos\phi\sin\theta_i + \cos\theta\cos\theta_i, \tag{2.9}$$

$$\tan\phi' = \frac{\sin\theta\sin\phi}{\sin\theta\cos\phi\cos\theta_i - \cos\theta\sin\theta_i}. \tag{2.10}$$

For simplicity we define the boundary of the iridotomy hole to be the surface $\theta' = \psi$, where ψ is a constant, meaning the radius of the hole is approximately $R\psi$. The volumetric flux entering the hole is then given by

$$Q_i = \int_{Surface\{\theta'=\psi, R<r<R+h\}} \mathbf{u}\cdot(-\mathbf{n}_{\theta'})\,dA, \tag{2.11}$$

where $\mathbf{u}$ is the fluid velocity in the posterior chamber and $\mathbf{n}_{\theta'}$ is the unit vector in the direction of increasing θ'. We obtain

$$Q_i = \int_R^{R+h(\theta)} \int_0^{2\pi} \mathbf{u}\cdot(-\mathbf{n}_{\theta'})\, r\sin\psi\, d\phi'\, dr = \int_0^{2\pi} \frac{1}{12\mu}\frac{\partial p}{\partial\theta'}h^3\sin\psi - \frac{1}{2}\mathbf{v}\cdot\mathbf{n}_{\theta'}h(R+h)\sin\psi\, d\phi', \tag{2.12}$$

where $\mathbf{v}$ is the iris velocity and we have used solution (2.3). Assuming that $\mathbf{v}$ and h are approximately uniform over the area of the hole (owing to its small size), the second term in the integrand

can be neglected (since $\mathbf{v}\cdot\mathbf{n}_{\theta'}$ averages to zero around the hole circumference), and the first term simplified to give

$$Q_i \approx \frac{1}{12\mu} h_i^3 \sin\psi \int_0^{2\pi} \frac{\partial p}{\partial \theta'}\, d\phi', \tag{2.13}$$

where $h = h_i$ is the height of the posterior chamber at the hole.

We note that the singular pressure field

$$\hat{p} = \frac{6\mu Q_i}{\pi h_i^3} \log\left(\frac{\tan(\theta'/2)}{\tan(\psi/2)}\right), \tag{2.14}$$

representing a uniform volumetric flux Q_i towards a sink located at the centre of the iridotomy, is the ϕ'-independent solution of (2.13) such that $\hat{p} = 0$ at the boundary of the hole $\theta' = \psi$. Thus, assuming the flow into the iridotomy is uniformly distributed in ϕ', we can introduce the regularised pressure

$$p_{reg} = p - \hat{p}. \tag{2.15}$$

To close the problem we also need a relationship between Q_i and the pressure drop across the hole, and to do this we use the formula developed by Dagan et al. (1982), which is an approximation of Sampson's classic formula (Sampson, 1891) for the volumetric flux of a Newtonian incompressible fluid though a hole in a plate at zero Reynolds number for the case of a plate of finite thickness:

$$\Delta P = \left(\frac{8l}{\pi a} + 3\right)\frac{\mu Q}{a^3}, \tag{2.16}$$

where a is the hole radius and l is the plate thickness, ΔP is the pressure drop across the hole and Q is the volumetric flux through the hole. We note that Silver and Quigley (2004) used Poiseuille's formula to estimate the resistance of the flow through an iridotomy. The formula proposed by Dagan et al. (1982) tends to Poiseuille's one in the limit of long holes and to Sampson's formula in the limit of holes of zero length, and represents a better approximation than either of these for holes of intermediate length. Assuming the anterior chamber is at a uniform zero pressure, the pressure drop across the iridotomy is given by the value of p_{reg} at the hole (which we denote as $p_{\mathrm{reg}}|_{\mathrm{hole}}$), since $\hat{p}$ is zero there, and thus we have

$$\left(\frac{8S}{\pi a_i} + 3\right)\frac{\mu Q_i}{a_i^3} = p_{\mathrm{reg}}|_{\mathrm{hole}}, \tag{2.17}$$

where S is the thickness of the iris.

Therefore, the flow and pressure are governed by (2.4), subject to the boundary conditions (2.6) and (2.7) or (2.8) and the condition at the hole (2.17). We can rewrite (2.4)–(2.8) in terms of the regularised pressure using (2.14)–(2.15) and substitute (2.17) to eliminate the unknown Q_i, leading to the problem

$$\frac{1}{12\mu}\nabla_h\cdot(h^3\nabla_h p_{reg}) = v_r + \frac{h}{2(R+h)}\nabla_h\cdot\Big((R+h)\mathbf{v}_h\Big) - \frac{1}{2}\nabla_h h\cdot\mathbf{v}_h - \frac{a_i^3 p_{\mathrm{reg}}|_{\mathrm{hole}}}{2\mu\pi h_i^3 (R+h)^2\sin\theta'(8S/(\pi a_i)+3)}\frac{dh^3}{d\theta}\frac{\partial\theta'}{\partial\theta}, \tag{2.18}$$

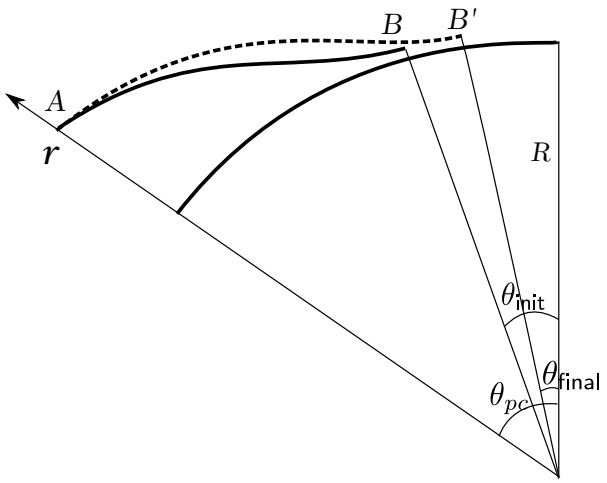

Figure 2.3: Sketch of the iris before (solid line) and after (dashed line) pupil contraction.

where the last term accounts for the flux though the hole, subject to the boundary conditions

$$\frac{\partial p_{reg}}{\partial \theta} = \frac{6\mu Q}{\pi \sin\theta h^3} + \frac{6\mu(R+h)v_\theta}{h^2} - \frac{6a_i^3 p_{reg}|_{hole}}{\pi h_i^3(8S/(\pi a_i)+3)\sin\theta'}\frac{\partial\theta'}{\partial\theta} \quad \text{at } \theta=\theta_{pc}, \tag{2.19}$$

$$\begin{cases} p_{\mathrm{reg}} = -\dfrac{6a_i^3 p_{reg}|_{hole}}{\pi h_i^3(8S/(\pi a_i)+3)}\ln\dfrac{\tan(\theta'/2)}{\tan(\psi/2)} & \text{in open regions} \\ \dfrac{\partial p_{reg}}{\partial\theta} = \dfrac{6\mu(R+h)v_\theta}{h^2} - \dfrac{6a_i^3 p_{reg}|_{hole}}{\pi h_i^3(8S/(\pi a_i)+3)\sin\theta'}\dfrac{\partial\theta'}{\partial\theta} & \text{in blocked regions} \end{cases} \quad \text{at } \theta=\theta_p. \tag{2.20}$$

2.2.2.3 Velocity of the iris.

The governing equations developed in § 2.2.2.1 are quasi-steady, and so the velocity field at a given time is fully determined by the iris velocity at that time $\mathbf{v}(\theta)$, which we assume to be axisymmetric. In order to prescribe $\mathbf{v}(\theta)$ we preliminary need to specify the duration T of miosis, the zenithal angle $\Delta\theta$ through which the ILC moves and the volume decrease ΔV. Following Milton and Longtin (1990) we assume $T = 1$ s throughout the chapter. Since ΔV is small (Dorairaj et al., 2009) we restrict attention to volume changes of up to 10% of the PC volume. Moreover, we assume $\Delta\theta = 0.2\theta_p$, which corresponds to a change of pupil diameter from approximately 3.68 to 2.95 mm and is consistent with values reported in Dorairaj et al. (2009) for the pupil dilation.

During miosis we assume the tip of the iris at the pupil (the point θ_p) moves through a zenithal angle $\Delta\theta = \theta_{init} - \theta_{final}$ over a time T and that the ciliary body (point A in figure 2.3) remains fixed and the whole of the ILC (the region near point B) moves in the θ-direction only. Note that this implies that H_p does not change during miosis, which is probably not realistic, since if the PC pressure builds up too much it will force the iris to move anteriorly, increasing H_p. Huang and Barocas (2004) developed an axisymmetric model of the flow of aqueous humour in

the posterior and anterior chambers with the iris modelled as an elastic solid with additional active elastic terms. They found the steady state position of the iris for both a normal eye and an eye with primary angle-closure glaucoma, and were thus able to investigate the force required to induce pupillary block. They did not report the gap at the iris–lens channel, and as they commented in the paper, it would be useful to extend this study to consider the dynamical behaviour during miosis. For the present work, owing to the uncertainties about the mechanical properties of the iris and the high sensitivity of pressure on the ILC height, we believe that it would be difficult to obtain reliable values of the transient pressure in the PC during miosis, and so we limit this study to prescribed iris motion.

We choose the zenithal velocity distribution $v_\theta(\theta)$ to be the simplest possible function that satisfies the assumption that θ_{pc} stays fixed and that at θ_p the iris moves at the average velocity $R\Delta\theta/T$, leading to the linear function

$$v_\theta(\theta) = -\frac{R\Delta\theta}{T}\frac{(\theta_{pc}-\theta)}{(\theta_{pc}-\theta_{\mathbf{i}nit})}, \tag{2.21}$$

(note the minus sign indicates contraction). The assumptions on the iris velocity imply the radial velocity $v_r(\theta)$ takes the value zero both at the ciliary body ($\theta = \theta_{pc}$) and within the ILC ($\theta_p \le \theta \le \theta_{ch}$). We set

$$v_r = \begin{cases} 0 & \text{for } \theta_p \le \theta \le \theta_{ch}, \\ -\dfrac{A}{T}(1-x^2)x^2 & \text{for } \theta_{ch} < \theta \le \theta_{pc}, \text{ where } x = (\theta-\theta_{ch})/(\theta_{pc}-\theta_{ch}), \end{cases} \tag{2.22}$$

which is also a continuously differentiable function with a single minimum. We choose the constant A so that the instantaneous rate of volume change is $-\Delta V/T$. The function v_r is negative in the case in which the PC volume decreases, which is the case considered in this chapter. We also note that the functional form of the iris velocity $\mathbf{v}$ given here is only valid instantaneously and not through the whole duration of miosis.

2.2.3 Solution

In the case of an eye with no pupillary block (axisymmetric boundary conditions), the system (2.4)–(2.7) becomes an ODE in θ for the pressure, which can be solved using a finite difference method. For the case of partial pupillary block, the boundary condition (2.8) is not axisymmetric, and we need to solve a two-dimensional problem. Equations (2.4), (2.6) and (2.8) are solved using a second-order central finite difference scheme. We introduce the grid $\omega = \{(\theta_l, \phi_m) |\ \phi_m = m\cdot d_\phi,\ \theta_l = \theta_{l-1} + s_{l-1},\ \theta_0 = \theta_p,\ m = 0\ldots N_\phi - 1,\ l = 1\ldots N_\theta - 1\}$, where $d_\phi = 2\pi/N_\phi$, and the length of the step s_l in the θ-direction is constructed to make the distances between neighbouring points in the θ- and ϕ-directions approximately equal: we set $s_0 = d_\phi \sin(\theta_p)$, $s_l = d_\phi \sin(s_{l-1} + \theta_{l-1})$ for $l = 1,\ldots N_\theta - 3$ and $s_{N_\theta-2} = \theta_{pc} - \theta_{N_\theta-2}$. Note that in this discretisation we choose only the number of points in ϕ, N_ϕ, and then N_θ is determined by the requirements on the step size s_l.

After discretising the equations (2.4), (2.6) and (2.8) with respect to the grid ω, a linear system consisting of $N_\theta \cdot N_\phi$ equations is obtained, which we solve with the built-in sparse solver in SciPy, Python.

In the presence of an iridotomy, we discretise the equations as described above. However, in this case, owing to the presence of the hole, we need to use finer grid, in order to preserve the fluxes, and this makes it impractical to use a sparse solver. For this reason, we solved the system by using the method of reduction introduced in Samarskiy and Nikolaev (1978) (pp. 154-157, in Russian), although we adapted the method to account for the terms in Equations (2.18)–(2.20) that are associated with the point sink, as terms of this sort were not present in the equations considered by Samarskiy and Nikolaev. The method requires the number of points in the discretisation of ϕ to be an exact power of 2. We combine equations for neighbouring values in the discretisation of ϕ to eliminate alternate variables and thus reduce the number of equations to be solved by a factor of 2 (only every other value of ϕ appears). We combine the resulting equations again, which again removes every other value of ϕ and reduces the size of the system by an additional factor of 2. We repeat this until there are only two values of ϕ left (which are 0 and π). At this point the number of equations in the system is small enough to solve it quickly on a computer. Having solved for p_{reg} on $\phi = 0$ and $\phi = \pi$, it is straightforward to reverse the algebraic manipulations already performed to find p_{reg} for the intermediate values of ϕ, and we can then use (2.17) to find the flux through the hole Q_i and (2.14)–(2.15) to find the actual pressure p.

2.2.4 A simple model to estimate the wall shear stress on the cornea

As discussed in the Introduction, the jet through the iridotomy might produce a significant wall shear stress (WSS) on the corneal endothelium opposite the iridotomy hole, which could be the cause of corneal damage that is sometimes observed in post-iridotomy patients (Wang et al., 2014). To check whether this is plausible, we use the idealised axisymmetric model shown in figure 2.4 to estimate the WSS. It consists of two circular parallel rigid plates at a distance l, representing the anterior iris with a circular hole that has radius a_i representing the iridotomy (bottom) and the corneal endothelium (top). We impose a normal inflow velocity v_{jet} through the hole, which is an average velocity through the iridotomy predicted by our model. The outlet is located at a distance $10l$ form the symmetry axis, which is far enough to not influence the flow around the hole. We impose zero pressure at the outlet, and no-slip boundary conditions at the surfaces of the plates.

We use COMSOL Multiphysics® to find the flow numerically and hence compute the maximum WSS on the wall representing the cornea (WSS_{max}). Admittedly, this model is very rough and less refined than the others presented in this chapter. Since we adopt a fully numerical approach we could clearly account for a more detailed description of the geometry. This, however, would necessarily add more parameters and would unnecessarily complicate the interpretation of the

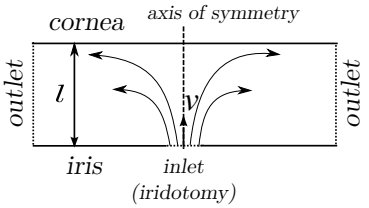

Figure 2.4: Sketch of the simplified geometry used to estimate the WSS on the cornea generated by the jet of aqueous through the iridotomy.

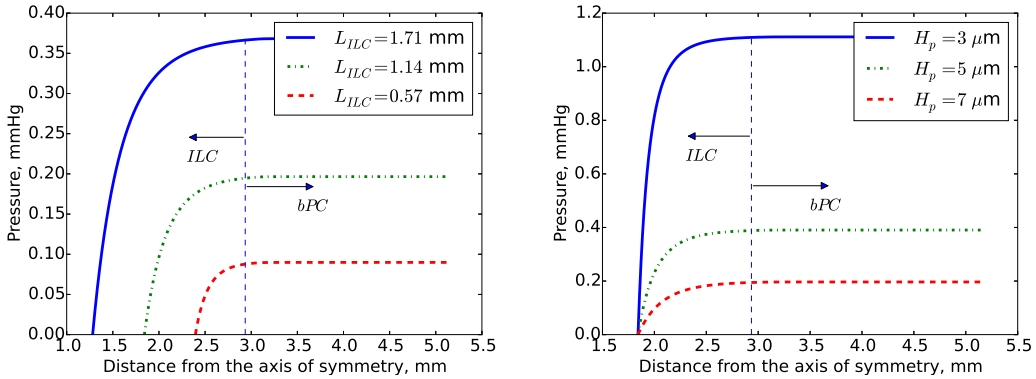

Figure 2.5: Pressure distribution along the PC with fixed iris due to the production-drainage flow (a) for different length of the iris–lens channel L_{ILC} and fixed height at the pupil $H_p = 7$ μm and (b) for different height at the pupil H_p and fixed $L_{ILC} = 1.14$ mm. Ranges of variation of L_{ILC} and H_p are similar to those adopted in Silver and Quigley (2004).

results and would be beyond the scope of the present work, for which we just need an estimate of the order of magnitude of the WSS on the cornea.

2.3 Results

2.3.1 Flow in the PC

2.3.1.1 Flow due to the production and drainage of aqueous humour.

First we consider the case without pupillary block and find the flow induced by production and drainage. Iris motion will be considered in § 2.3.1.2.

Figure 2.5 shows the pressure profile in the PC along the zenithal direction, with part (a) of the figure showing the effect of ILC length and part (b) showing the effect of ILC height at the pupil H_p. Lubrication theory predicts that, for a domain of uniform height, the resistance to

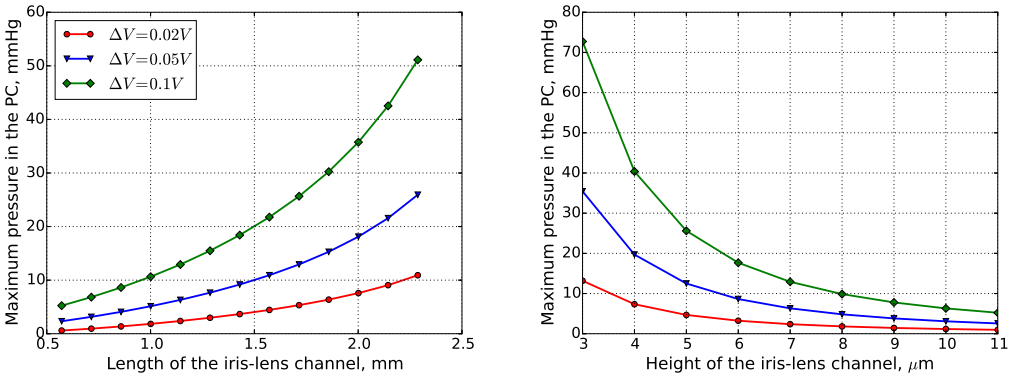

Figure 2.6: Miosis. Maximum pressure in the PC (a) as a function of ILC length and (b) as a function of ILC height for different percentage P of volume change in the PC. The legend is common to both panels and ΔV denotes the change in the PC volume during miosis. In each case we use the miosis duration $T = 1$ s and angular change of the pupil $\Delta\theta = 0.2\theta_p$, corresponding to a pupil diameter change 0.73 mm.

flow, and thus the pressure drop across the domain, is proportional to the inverse third power of the domain height multiplied by the length of the domain. Due to our choice of the height function to model the ILC, which is not uniform, the pressure drop grows faster than linearly with L_{ILC} (figure 2.5(a)), while the pressure drop grows less than the inverse third power of H_p (figure 2.5(b)). As assumed by Silver and Quigley (2004), the pressure is almost constant in the bPC where the domain height is much greater, meaning the resistance there is comparatively negligible. In all cases considered here the pressure drop across the ILC is very small compared to the intraocular pressure, which is about 15 mmHg in normal subjects (Cunningham and Barry, 1986).

2.3.1.2 Flow during miosis.

Figure 2.6 shows the maximum pressure in the PC for different values of ΔV as a function of (a) L_{ILC} and (b) H_p. The pressures predicted by the model are very large, especially if the ILC is long and has small height. As discussed in § 2.2.2.3, our model uses an assumption that H_p is fixed during iris motion, which implies that the pressure values are likely to be overestimated. Nevertheless, our results clearly suggest that miosis generates significantly higher flow velocities and pressure than aqueous production and drainage, even if the PC volume change is very small. We anticipate that similarly large flows would be generated during lens accommodation, although we neglect this in the present work.

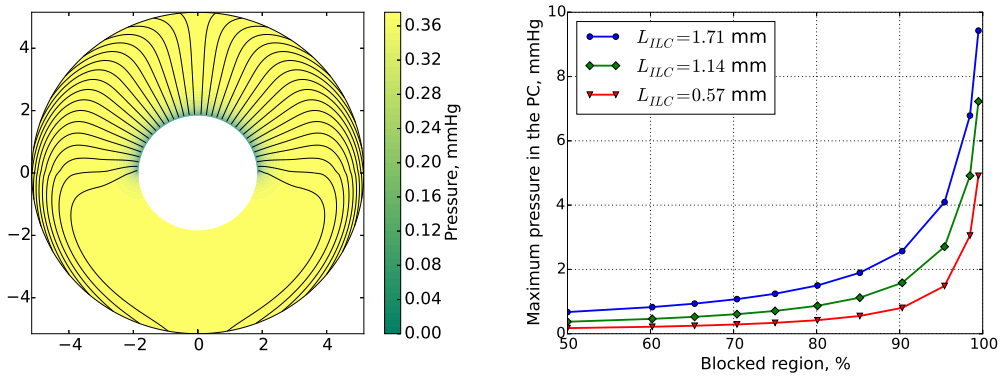

(a) (b)

Figure 2.7: (a) Pressure distribution (shading) and streamlines of the r-average velocity in the posterior chamber in the case of partial pupillary block with the lower half of the pupil blocked. In this plot and in figures 2.8 and 2.10(a) the radial distance is given by $R\sin\theta$ for $\theta_p \le \theta \le \theta_{pc}$. (b) Maximum pressure in the PC as a function of the percentage of blocked region of the pupil for different length of iris–lens channel L_{ILC}.

2.3.1.3 Partial pupillary block

We model partial pupillary block by imposing zero flux around part of the pupil, using equation (2.8), and in this section we assume the flow is driven by the production/drainage of aqueous humour. Figure 2.7(a) shows an example of the resulting flow and pressure distribution with the lower half of the pupil blocked ($\pi < \phi < 2\pi$). As more of the pupil becomes blocked, the pressure increases without bound as shown in figure 2.7(b), but pressures significantly higher than in physiological conditions (of the order of several mmHg) are attained only when the block is almost total.

2.3.2 Flow in the PC with iridotomy

2.3.2.1 Flow due to the production and drainage of aqueous humour.

Figure 2.8 shows the pressure and streamlines of the depth-averaged velocity (averaged over the thickness of the PC) in the presence of an iridotomy with diameter (a) 60 μm and (b) 120 μm. In both cases the streamlines are very different from the radial streamlines that would be observed in the absence of an iridotomy, and for the larger diameter even fluid that starts on the opposite side from the iridotomy hole ends up draining into the iridotomy.

Figure 2.9(a) shows the flux through the iridotomy as the percentage of the total flux as a function of iridotomy diameter. The iridotomy diameter has a strong impact on the flow, and for diameters used in typical surgical practice, which are between about 50 and 150 μm (Fleck, 1990), most of the aqueous flows through the iridotomy hole, with almost all of it going through the

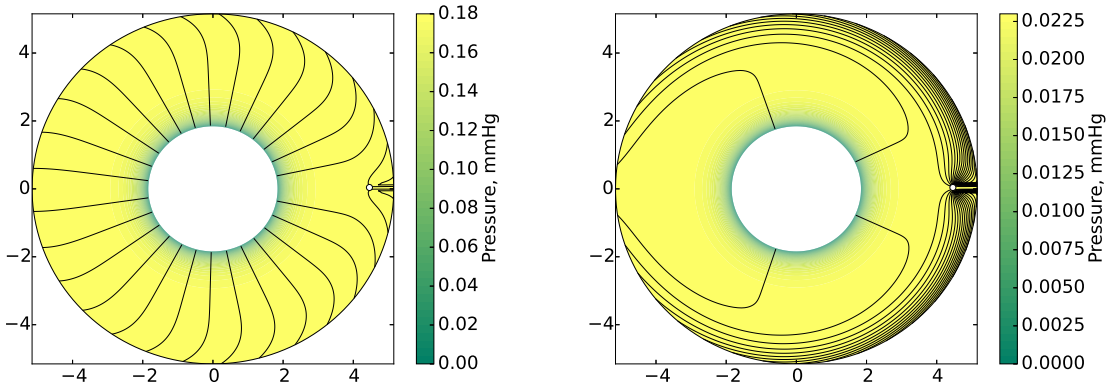

(a) (b)

Figure 2.8: Pressure distribution (shading) and streamlines of the r-averaged velocity in the PC projected on the plane in the presence of an iridotomy of diameter (a) 60 μm and (b) 120 μm. Miosis is not considered in this figure ($\mathbf{v} = \mathbf{0}$) and the iridotomy is located 2/3 of the way through the bPC towards the ciliary body.

iridotomy for diameters larger than 150 μm. The percentage of aqueous that passes through the iridotomy also depends on the iris–lens channel length L_{ILC}; greater channel lengths increase the resistance to flow through the pupil, thus increasing the total flow through the iridotomy, see figure 2.9(a). In contrast, the location of the iridotomy only changes the total flow by 2% from an iridotomy placed in the middle of the bPC to one placed peripherally (results are not shown), which is because the pressure is approximately uniform across the bPC, see figure 2.5. Henceforth we fix the iridotomy location in our model at 2/3 of the way from the innermost point of the bPC (corresponding to the value $\theta = \theta_{ch}$) to the ciliary body ($\theta = \theta_{pc}$).

Figure 2.9(b) shows the average jet velocity through the iridotomy (calculated as flux divided by cross-sectional area) as a function of the iridotomy diameter. Interestingly, a peak velocity is obtained for an intermediate value of the diameter: for small diameters the hole has too much resistance to allow much flow and for large diameters the total flow is almost constant (most of the aqueous goes through the iridotomy), but it is spread over a larger area so the average velocity is lower.

Since iridotomy is performed to treat pupillary block with the aim of reducing the pressure drop from the posterior to the anterior chambers, we now consider the extreme case in which no fluid exits from the pupil, to find the minimum iridotomy diameter that will maintain the pressure in the PC within safe levels, i.e. close to physiological conditions. Figure 2.10(a) shows the flow streamlines and pressure distribution, with no fluid exiting through the pupil. The maximum pressure in the PC is shown in figure 2.10(b) as a function of the iridotomy diameter, indicating that if the iridotomy diameter is larger than about 50 μm the pressure drop is less than 1 mmHg, which is comparable with the physiological pressure differences shown in figure 2.5.

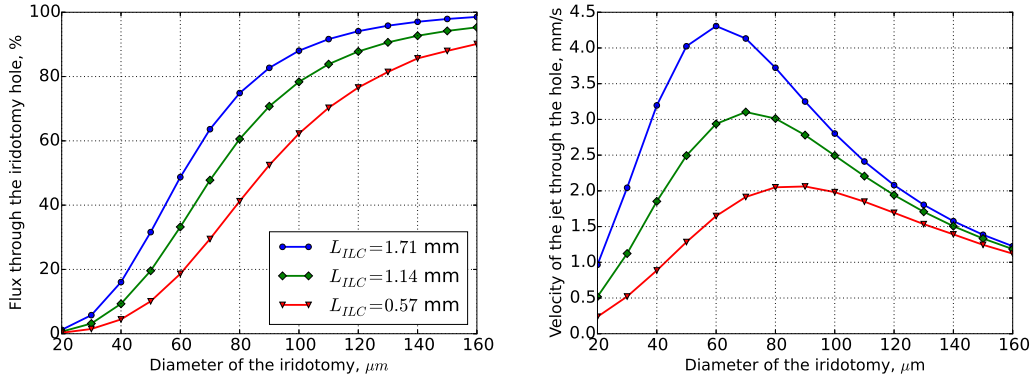

(a) (b)

Figure 2.9: (a) Total volumetric flux through iridotomy as a percentage of total flux produced by ciliary body plotted against iridotomy diameter. (b) Average velocity of the jet through the iridotomy. Cases with different iris–lens channel length L_{ILC} are shown. The legend is common to both panels.

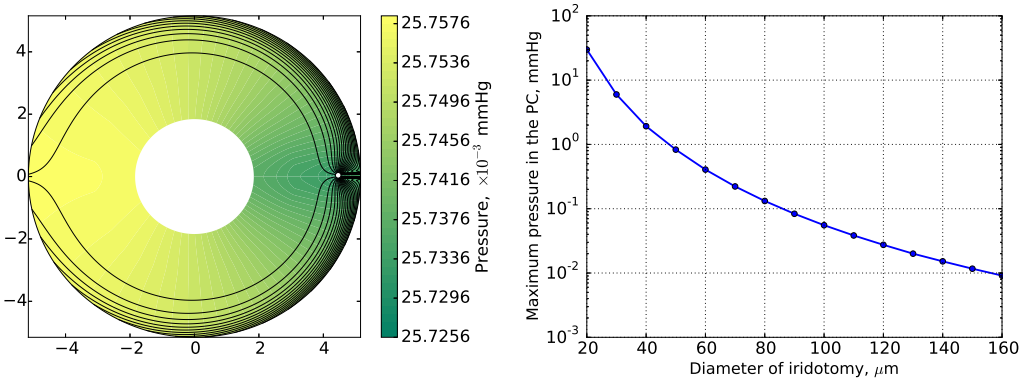

(a) (b)

Figure 2.10: (a) Pressure distribution (shading) and streamlines of the r-averaged velocity in the PC projected on the plane in the presence of pupillary block with an iridotomy of diameter 120 μm. (b) Maximum pressure in the PC with pupillary block as a function of the iridotomy diameter.

2.3.2.2 Flow during miosis.

As in the case with no iridotomy, see § 2.3.1.2, we predict the flow during miosis to be significantly more intense than that due to aqueous production alone, even for small changes in the PC volume. We find that, although the total volumetric flux through the iridotomy is much larger than when miosis is not occurring, the proportion of the flow that goes through the iridotomy as a fraction

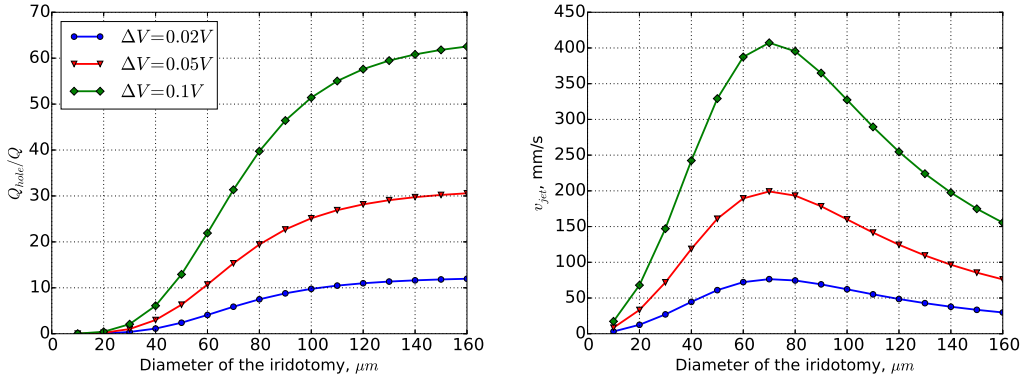

(a) (b)

Figure 2.11: Miosis. (a) Volumetric flux (as a multiple of that produced by the ciliary body) passing through the iridotomy at the start of miosis. (b) Average velocity of the flow through the iridotomy. The legend is common to both panels and ΔV denotes the decrease in PC volume during miosis. In each case we use the miosis duration $T = 1$ s and angular change of the pupil size $\Delta\theta = 0.2\theta_p$, corresponding to a pupil diameter change of 0.74 mm.

of the total flow out of the PC remains approximately the same. We note that in the limit of $\Delta T \to 0$ the total flow induced by miosis is proportional to ΔV. The volumetric flux is shown as a function of iridotomy diameter in figure 2.11(a) for different values of the volume change of the PC, and figure 2.11(b) shows the corresponding average velocity in the jet through the iridotomy. As in the case of the flow due to production/drainage alone, the velocity through the iridotomy is maximised at an iridotomy diameter of around 70 μm; however, in this case the velocity magnitudes are much larger. As discussed in § 2.3.1.2, our model might overestimate the velocity since we assume H_p remains constant, but nevertheless the results suggest that significant velocities could be generated.

2.3.2.3 Wall shear stress on the cornea in front of the iridotomy

Figure 2.12(a) shows the maximum WSS on the cornea as a function of iridotomy diameter for different values of the PC volume change during miosis ΔV. The figure suggests that the WSS peaks for a slightly larger iridotomy diameter than that corresponding to the peak of the average jet velocity. The iridotomy for which the WSS is maximised are similar to those used in surgical practice. Figure 2.12(b) shows WSS_{max} as a function of the iris–cornea separation distance for a fixed iridotomy diameter. The WSS predicted by these results are consistent with the predictions by Yamamoto et al. (2010). Furthermore, the WSS_{max} grows rapidly as the distance between the cornea and the iris reduces, suggesting that if the iridotomy is located close to the boundary of bPC it is more likely to cause corneal damage. We note however that in such a case our assumption that the plates are parallel and have large radii might not be realistic, as the outer

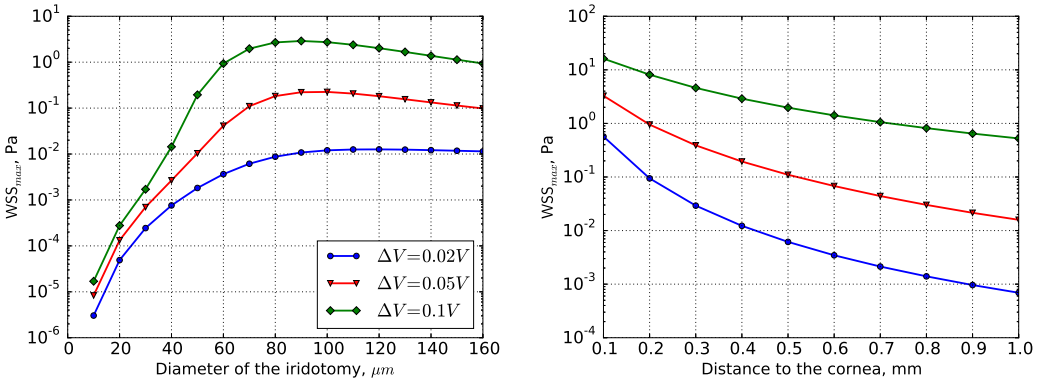

Figure 2.12: (a) Maximum WSS on the cornea (with the plate separation $l = 0.5$ mm fixed). (b) Maximum WSS on cornea (iridotomy diameter 70 μm fixed). The legend is common to both panels and ΔV denotes the decrease in PC volume during miosis. In each case we use the miosis duration $T = 1$ s and angular change of the pupil size $\Delta\theta = 0.2\theta_p$, corresponding to a pupil diameter change of 0.74 mm.

boundary of bPC is close to where the cornea meets the iris. Nevertheless, we anticipate that the order of magnitude estimate will remain valid.

2.4 Discussion and conclusions

Studying aqueous humour motion in the posterior chamber (PC) of the eye is of clinical and mechanical interest. In particular the pressure drop from posterior to anterior chamber depends on the aqueous flow; it is relevant for angle-closure glaucoma because if it is too large the iris is pushed forward and can block the iridocorneal angle, which is where aqueous drainage from the anterior chamber occurs. Moreover, knowledge of aqueous flow characteristics is important to estimate shear forces on ocular tissues. In this chapter we developed a mathematical model of aqueous flow in the PC and investigated its modification in the presence of partial pupillary block and iridotomy.

We first presented a model of the flow induced by aqueous production and miosis (pupil contraction) in the PC. The model is based on lubrication theory, an approximation technique valid for long and thin domains and aimed at simplifying the governing equations. A similar approach was used by Friedland (1978) for the flow in PC, which was assumed to have a constant thickness, and Silver and Quigley (2004), in their model of the flow in the iris–lens channel (ILC). Our model is an extension of these works, as the PC thickness has a realistic profile and the effect of miosis is accounted for.

In the case of the flow induced by aqueous production only (i.e. without considering iris

motion), the pressure drop from the posterior to the anterior chamber Δp is very small (much smaller than the IOP). We note, that our estimates of the pressure in the PC are significantly affected by the geometry of the ILC. Since there are no measurements of ILC height available we made assumptions on the geometry, and investigated the effect of the tunable parameters on the results. However, even by varying the ILC thickness and length within a relatively large range we found that the pressure jump between the two chambers remains below 1 mmHg, suggesting that $\Delta p < 1$ mmHg in physiological conditions. This result agrees with the numerical work of Huang and Barocas (2004), which was based on a fluid–structure interaction model of the iris. In that paper they also find that a pressure difference of a few mmHg is required to induce significant forward bowing of the iris and thus narrow the iridocorneal angle.

In the case of miosis the velocities generated depend on the change in the volume of the PC, which Dorairaj et al. (2009) suggest is small and significantly variable among subjects. We found that even for a PC volume change as small as 5% the aqueous flow generated is much more intense than in the case of the flow due to production/drainage only, with correspondingly higher pressures produced in the PC. However, we note that such high values of the pressure last for a short time and are thus less likely to have clinical significance. In this case of miosis, we were forced to make assumptions concerning the iris motion, owing to the lack of experimental data, which affect the results from the quantitative point of view; in particular, we assumed that the minimum height of the ILC remains unchanged during pupil contraction. This implies that we neglect the possible expansion of the ILC due to PC pressure build up, as also discussed by Huang and Barocas (2004). To overcome this assumption, a more comprehensive model of this phenomenon is needed, coupling transient iris mechanics with aqueous flow, which is however, beyond the scope of the present work.

We also used the model to consider the condition of partial pupillary block, when the iris touches the lens part of the way around the pupil, blocking the iris–lens channel there. Our results show the pressure drop only rises to large values (some mmHg) if the blockage affects a significant region of the pupil.

Laser peripheral iridotomy as well as cataract extraction have proved their effectiveness in treating angle-closure glaucoma since it prevents the closure of the angle. The possible side effects of the treatment are mainly related to the size of the iridotomy, and they include structural zonular damage, corneal endothelium damage, pigment dispersion, double vision, intraocular haemorrhages (Hu et al., 2017). The second part of this work is therefore focused on studying the modification of aqueous flow and pressure in the presence of iridotomy with the aim of understanding the role of the size of the hole. First, the iridotomy hole needs to be sufficiently large to keep the pressure close to physiological conditions, so as to avoid the iris bowing anteriorly and blocking the trabecular meshwork. Second, it has been hypothesised that changes in the aqueous flow secondary to iridotomy might be partly responsible for the corneal decompensation that affects some post-iridotomy patients. Specifically, Yamamoto et al. (2006) hypothesised that

increased progressive endothelial cell detachment might result from increased wall shear stress (WSS) on the cornea opposite the iridotomy. This hypothesis is corroborated by the observation that corneal decompensation sometimes occurs several years after iridotomy, suggesting the mechanisms involved act over a long period of time rather than being related to damage sustained during the surgical procedure. The observation that iridotomy can cause cataract can also be related to the possible occurrence of large values of the WSS on the lens opposite to the iridotomy when fluid flow is directed from the anterior to the posterior chamber.

The model allowed us to find the proportion of aqueous flux that passes through the iridotomy as well as the average jet velocity. To our knowledge, the only previous models are due to Fleck (1990); Silver and Quigley (2004); Yamamoto et al. (2010). Our model improves on these since we solve for the flow in the PC and also account for the effect of iris motion. The model predicts that, for realistic values of the iridotomy diameter, the majority of the flow goes through the iridotomy rather than through the pupil, owing to the narrowness of the ILC. Moreover, the location of the iridotomy hardly affects the flow through it, as long as the hole is well away from the narrow ILC.

In the presence of total pupillary block, which is usually treated by iridotomy and represents the worst case scenario, the model predicts that a minimum hole diameter of around 50 μm is needed to ensure a pressure in the PC close to physiological conditions. In practice typical diameters of 100–150 μm are found to be sufficient (Fleck, 1990), agreeing with our results.

Our model also suggests that especially large jet velocities through the iridotomy can be generated during miosis. Both during miosis and when miosis is not occurring the highest average velocity in the jet is achieved for a hole of around 70 μm and the highest WSS on the cornea is achieved for a hole of around 100 μm, which is similar to those used in the clinic. The maximum WSS drops rapidly for smaller values of the diameter, which, however, soon become clinically unacceptable as they do not sufficiently decrease the pressure. On the other hand the WSS decreases relatively slowly as the iridotomy diameter is increased. If the PC volume decreases by 5% our model predicts a WSS of around 0.1 Pa, which agrees with the model of Yamamoto et al. (2010), even though we find a higher jet velocity, due to their use of a larger iridotomy diameter (560 μm). For greater volume changes or if the iridotomy is closer to the corneal endothelium, the predicted WSS is still higher. In particular, this means that if the iridotomy is located next to iridocorneal angle or the anterior chamber of a patient is shallow, the risk of corneal damage will be more severe. We note that if the PC volume becomes larger during miosis, the direction of flow through the iridotomy will reverse and the jet of aqueous will impact on the crystalline lens. In this case our results on the mechanical stresses on the corneal endothelial surface can also be applied to the mechanical stresses on the lens.

The level of WSS at which corneal endothelial damage would be sustained is unknown. However, Kaji et al. (2005) plated porcine corneal endothelial cells on glass slides for 3 hours, and found significant detachment if the WSS was greater than around 0.1 Pa. In vivo it is likely that the cells would be more strongly attached, thus necessitating higher values of the WSS. This

is also confirmed by the numerical simulations of Abouali et al. (2012) and Repetto et al. (2015), which suggest the maximum WSS generated on the cornea during typical everyday eye rotations is of the order 0.1 Pa. The fact that corneal endothelial cells do not detach in physiological conditions suggests that much larger values of the WSS would be required to detach them. Our model predicts that the WSS in the presence of an iridotomy during miosis can attain values that are an order of magnitude larger, and hence we cannot rule out the possibility that this mechanism could play a role in detaching endothelial cells in post-iridotomy patients. To answer this question would require more clinical data.

CHAPTER 3

FLOW IN THE ANTERIOR CHAMBER INDUCED BY EYE ROTATIONS

This chapter is based on the publication by Dvoriashyna et al. (2019)

3.1 Introduction

Forcing oscillations at a single frequency of a fluid are known to lead to a primary flow that oscillates with the same frequency as the driver, and secondary flows that are typically smaller and occur due to nonlinear interactions, oscillating at integer multiples of the driving frequency. The steady streaming component is the contribution to the flow that has frequency zero. In a biological context the component oscillating at the driving frequency typically has primary influence on the stresses generated, since it is the largest, while the steady streaming component is of interest for mass transport.

In the present work we study the oscillatory and steady streaming flow in the anterior chamber of the eye (AC) generated during eye rotations. Repetto et al. (2015) showed that, among the mechanisms that drive aqueous flow in the AC (excluding miosis, see §1.4 in chapter 1), rotations of the eye produce the most intense flow in the AC, and thus contribute to the majority of the wall shear stress on the cornea. Moreover, Abouali et al. (2012) showed that periodic rotations of the eye can produce a steady streaming flow that is intense enough to contribute to mixing at least as much as the thermally driven flow. When the eyes are closed during sleep, almost no thermal flow occurs in the AC, meaning that most of the mixing happens due to the rapid eye movements (REM).

As discussed in §1.4, analytical approaches based on lubrication theory have been extensively used to study the flow induced by aqueous secretion and the buoyancy driven flow in the AC. On the other hand, all previous investigations of the flow induced by eye rotations are based on

fully numerical solutions of the Navier–Stokes equations. Although numerical simulations allow one to consider complex and very realistic geometries, they require large computational efforts, especially for time dependent simulations, and make it difficult to obtain a clear picture of the dependency of the results on the controlling parameters. In this work we propose an analytical approach to study aqueous humour flow in the eye, which takes advantage of the small thickness of the AC, and use our results to investigate the parameter space more thoroughly than was previously possible.

Movements of the eye are routine and take a variety of different forms. Some rotations are close to periodic oscillations, and approximating them as a pure frequency oscillation has been a popular simplification in the literature, both in experimental works (Repetto et al., 2005; Bonfiglio et al., 2013, 2015) and theoretical works (David et al., 1998; Repetto et al., 2010; Abouali et al., 2012; Modarreszadeh et al., 2014). In this work we also make use of this assumption.

As long as the shape of the AC does not change during an eye movement, the motion can be decomposed into a translational motion and an instantaneous rotational motion about an axis. In the case of pure translational motion, there would be no fluid motion relative to the domain, and the acceleration is balanced by a pressure gradient within the fluid. In this chapter we simplify the problem to the case of rotational motion, and, furthermore, we assume the axis of rotations remains fixed. Thus, in principle, our work can be generalised to any motion of the eye, by adding a pressure gradient onto our solutions.

We model the AC as a thin domain sitting on the surface of a sphere that either has a constant height (in which case we can solve the problem analytically) or a more realistic shape (in which case we reduce the problem to a set of ODEs). We investigate both the primary oscillatory flow and the steady streaming, showing that both have a three-dimensional structure, the full details of which have not been highlighted by previous authors.

This chapter is organised as follows: in § 3.2 the problem is formulated mathematically and simplified, and in § 3.3 the solution procedure is described. In § 3.4 we present the results, both in the constant height domain (§ 3.4.1), and for the more realistic geometry (§ 3.4.2). In § 3.5 we discuss the physiological and clinical relevance of the results.

3.2 Formulation of the problem

In this study we develop a model to find the motion of the aqueous humour during rotations of the eyeball. As discussed in the Introduction, the AC is relatively narrow in the anterior–posterior direction, and is delimited anteriorly by the cornea and posteriorly by the iris and lens, see figure 0.1 and the parameters given in table 3.1. In this model, we describe the iris and lens as a single continuous surface, thus neglecting the passage of the aqueous through the iris–lens channel, and hence also the turnover of the aqueous due to secretion and drainage. We justify this by comparing the flows found in the present model with those that would be expected due to

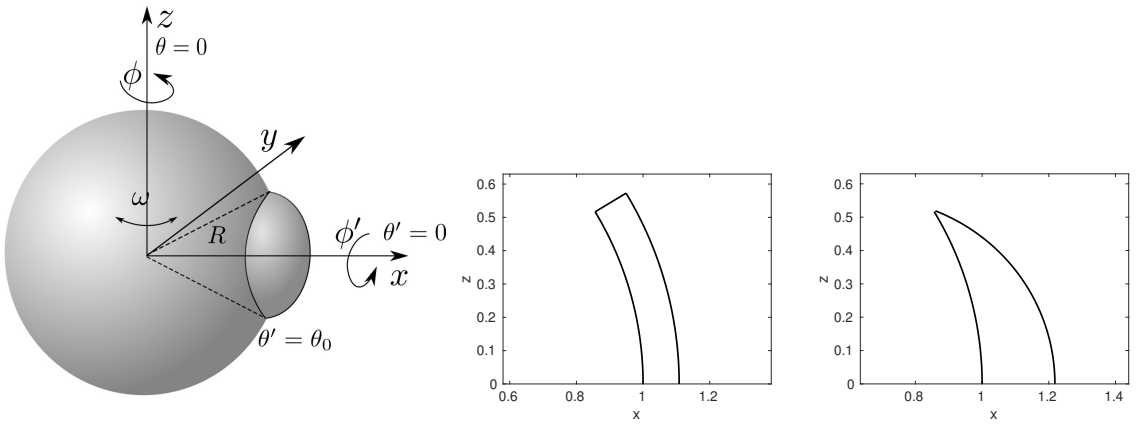

Figure 3.1: (a) Sketch of the eye, showing the eyeball (large sphere) and the domain representing the AC attached to the sphere on the right. Sketch of the coordinate systems $\mathscr{C}$ and $\mathscr{C}'$. (b) and (c) cross-sections of the domains considered; (b) idealised constant-height domain; (c) more realistic representation of the AC geometry.

Maximum height, $h_{\max}$	2.62 mm (ISO-11979-3 Helmholtz (1909))
Average height, $\bar{h}$	1.3 mm
Diameter of the posterior boundary of the AC	≈ 6.2 mm
Radius of the eyeball, R	≈ 12 mm
Zenithal boundary of the AC, θ_0	31.1°
Aqueous humor kinematic viscosity, ν	$0.75 \cdot 10^{-6}$ m^2/s (Beswick and McCulloch, 1956)
Aqueous humor density, ρ	1000 kg/m^3

Table 3.1: Geometrical characteristics of the domain and fluid properties.

aqueous turnover (e.g. Repetto et al., 2015), and noting that the flows found in the present model are much larger.

3.2.1 Geometry of the domain

To describe the eye rotations and the shape of the domain, it is convenient to introduce a set of Cartesian coordinates and two sets of spherical polar coordinates, which will be used interchangeably through the chapter, and which are all illustrated in figure 3.1(a). The z-axis of the Cartesian coordinates is the axis of rotation and the x-axis points through the centre of the pupil. The set $\mathscr{C} = (r^*, \theta, \phi)$ of spherical polar coordinates is convenient for describing the rotations, and has origin at the centre of the eye, $\theta = 0$ along the axis of rotation and the centre of the pupil along the line $\theta = \pi/2$, $\phi = 0$. Finally the set $\mathscr{C}' = (r^*, \theta', \phi')$ of spherical polar coordinates is convenient for describing the geometry of the AC, and is obtained by rotating $\mathscr{C}$ through $\pi/2$ about the y-axis using right-handed rule of rotations. Thus it has the same origin, with the line $\theta' = 0$ through the centre of the pupil and the axis of rotation of the domain along $\theta' = \pi/2$,

$\phi' = 0, \pi$. The transformation from $\mathscr{C}$ to $\mathscr{C}'$ can be performed using the following formulae (e.g. Meskauskas et al., 2011):

$$\begin{aligned} \cos\theta &= -\sin\theta'\cos\phi', & \cos\theta' &= \sin\theta\cos\phi, \\ \tan\phi &= \tan\theta'\sin\phi', & \tan\phi' &= -\tan\theta\sin\phi. \end{aligned} \tag{3.1}$$

To a good approximation, the AC is axisymmetric about the anterior–posterior axis ($\theta' = 0$), and thus its geometry is independent of ϕ'. We also assume for simplicity that its posterior surface (the iris and the lens) is a region of a spherical surface of radius R centred on the centre of the eye, see figure 3.1(a). In particular we neglect the thickness of the inner boundary of the iris at the iris–lens channel, which is about 0.4 mm in reality. In addition, the assumption that the centre of the posterior spherical surface and the centre of the eye coincide is not necessary (in reality the radius of curvature of the lens is around 1 cm and that of the eye is 1.2 cm), but this allows us to find an analytical solution in the case of constant height. We denote the thickness of the AC as $h(\theta')$. We consider two cases: first, the case of uniform h, in which we set h equal to the maximum height $h = h_{\max}$, see figure 3.1(b), which allows us to find a completely analytical solution for the fluid flow. Second, we consider we consider a more realistic shape in which the domain is defined as $R \le r^* \le R + h(\theta')$ for $0 \le \theta' \le \theta_0$, where $h(\theta')$ is a smooth monotonic decreasing function with $h(0) = h_{\max}$. In order to avoid numerical difficulties, we do not allow h to reach zero at the outer boundary, and we arbitrarily set $h(\theta_0)$ to the small value $h_{\min} = h_{\max}/50$. We adopted the following expression for h:

$$h = h_{max}\cos\theta' + \frac{h_{min} - h_{max}\cos\theta_0}{1-\cos\theta_0}(1-\cos\theta'), \tag{3.2}$$

which is illustrated in figure 3.1(c). We typically use the parameter values given in table 3.1, except where otherwise stated, in which case the aspect ratio of the anterior chamber is $\epsilon = \overline{h}/R \approx 0.11$, where $\overline{h}$ is the average height of the AC (volume of the AC divided by posterior surface area), defined below.

3.2.2 Eye rotations

In this work we consider harmonic rotational oscillations of the domain, with amplitude β and angular frequency ω_f. Since we wish to apply our results to the flow in the AC during eye rotations, we adopt values representative of real eye movements and, in particular, of saccadic eye rotations and rapid eye movements (REM) during sleep.

Saccadic rotations are performed to redirect the sight from one target to another, and they tend to be fast and of short duration. Becker (1989) proposed empirical relationships relating saccadic amplitude A, duration D, maximum angular velocity and acceleration time. We relate β and ω_f using the fact that for saccadic rotations $D = D_0 + dA$, which is approximately valid in the range $5^\circ \lessapprox A \lessapprox 50^\circ$, with D measured in seconds and A in degrees, $d \approx 0.0025$ deg/s and $0.02 \lessapprox D_0 \lessapprox 0.03$ (Becker, 1989). To be able to model the eye rotations as saccadic movements, we assume that

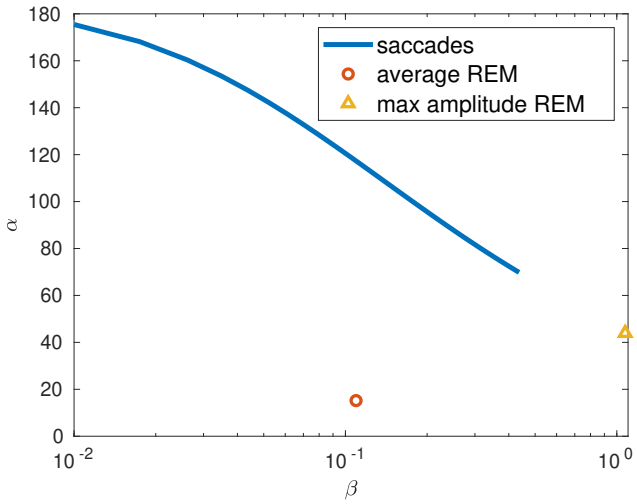

Figure 3.2: Relationship between the Womersley number α and the amplitude of rotations β for saccadic eye rotations (curve), average REM (circle) and maximum amplitude REM (triangle) (Modarreszadeh et al., 2014).

a period of rotation consists of two successive saccadic movements, each with amplitude A and duration D, and thus model the saccade as a harmonic rotation with amplitude $\beta = A/2$ and angular frequency $\omega_f = 2\pi/(2D) = \pi/(D_0 + 2d\beta)$. Note that this approach to model periodic saccades differs from the one in Abouali et al. (2012), where authors considered four saccadic movements per period instead of two. We nondimensionalise this relationship by converting β to radians and also working in terms of the Womersley number $\alpha = \sqrt{\rho\omega_f R^2/\mu}$, where ρ is the fluid density and μ its shear viscosity (see table 3.1). This leads to the relationship shown by the curve in figure 3.2.

REM is a normal feature of a particular phase of sleep, and consists of repeated side-to-side rotations that can have a wide range of amplitudes (Takahashi and Atsumi, 1997). For our model we adopt the same parameters as Modarreszadeh et al. (2014) and consider two cases: (i) 'average REM' with $\beta = 6.27$ deg and $\omega_f = 58.73$ deg/s, corresponding to the average of the experimental data by Takahashi and Atsumi (1997), and (ii) 'maximum amplitude REM' with $\beta = 61.5$ deg and $\omega_f = 491.98$ deg/s, which is the highest amplitude reported in the measurements, and these points are also reported in figure 3.2.

3.2.3 Derivation of the governing equations

In the following we work in a reference frame that rotates with the domain, and use superscript stars to denote dimensional variables that will be made dimensionless. Neglecting gravity, the

continuity and Navier–Stokes equations become (e.g. Batchelor, 1967)

$$\nabla^* \cdot \mathbf{u}^* = 0, \tag{3.3a}$$

$$\rho\left(\frac{D\mathbf{u}^*}{Dt^*} + \dot{\omega}^* \times \mathbf{x}^* + 2\omega^* \times \mathbf{u}^* + \left(\omega^* \cdot \mathbf{x}^*\right)\omega^* - \omega^{*2}\mathbf{x}^*\right) = -\nabla^* p^* + \mu\nabla^2 \mathbf{u}^*, \tag{3.3b}$$

where $\mathbf{u}^*$ is fluid velocity relative to the reference frame, p^* is the departure of the pressure from the hydrostatic profile (thus we omit the gravitational acceleration), ω^* is the prescribed angular velocity of the domain (and $\omega^* = |\omega^*|$), $\mathbf{x}^*$ is the position vector, ∇^* is spatial gradient and $D\mathbf{u}^*/Dt^*$ denotes a dimensional material derivative. Recalling the utilised coordinate system $\mathscr{C} = (r^*, \theta, \phi)$, we consider sinusoidal rotations with prescribed angular displacement $\beta \sin \omega_f t^*$ about the axis $\theta = 0$ ($z = 0$), giving the angular velocity $\omega^* = \omega^*(\cos\theta, -\sin\theta, 0)$ with magnitude $\omega^* = \beta\omega_f \cos\omega_f t^*$.

A characteristic depth of the anterior chamber may be obtained by calculating the volume of the anterior chamber divided by inner surface area, which, assuming $h \ll R$, is approximately $\overline{h} = \int_0^{\theta_0} h(\theta')\sin(\theta')\,d\theta'/(1-\cos(\theta_0))$. Dividing by the length of the chamber gives the aspect ratio of the anterior chamber $\epsilon = \overline{h}/(2R\theta_0)$.

We introduce the following scales for nondimensionalisation:

$$\begin{gathered} r^* = R + \overline{h}r, \quad t^* = \frac{t}{\omega_f}, \quad u_\phi^* = U u_\phi, \quad u_\theta^* = U u_\theta, \quad u_r^* = \epsilon U u_r, \\ p^* = P_0 p, \quad \omega^* = \beta\omega_f \omega. \end{gathered} \tag{3.4}$$

We choose $U = \overline{h}\beta\omega_f$ as the velocity scale and $P_0 = R^2\omega_f^2\beta\rho$ as the pressure scale (chosen so that the pressure gradient in the ϕ direction balances the angular acceleration term), and let $\epsilon = \overline{h}/R$ be the approximate aspect ratio of the domain.

With the above scales the dimensionless continuity and Navier–Stokes equations (3.3) read

$$\frac{\partial u_r}{\partial r} + \frac{1}{\sin\theta}\frac{\partial}{\partial\theta}(u_\theta \sin\theta) + \frac{1}{\sin\theta}\frac{\partial u_\phi}{\partial\phi} + \epsilon\left(r\frac{\partial u_r}{\partial r} + 2u_r\right) = 0, \tag{3.5a}$$

$$\begin{aligned} &\epsilon^3\frac{\partial u_r}{\partial t} + \epsilon^4\beta\mathbf{u}\cdot\nabla u_r - \epsilon^3\beta\frac{u_\phi^2 + u_\theta^2}{1+\epsilon r} - 2\beta\epsilon^2\omega u_\phi \sin\theta - \epsilon\beta\omega^2(1+\epsilon r)\sin^2\theta = \\ &\quad = -\frac{\partial p}{\partial r} + \frac{\epsilon}{\alpha^2}\left(\nabla^2 u_r - \epsilon^2\frac{2u_r}{(1+\epsilon r)^2} - \frac{2\epsilon}{(1+\epsilon r)^2\sin\theta}\left(\frac{\partial(u_\theta\sin\theta)}{\partial\theta} + \epsilon\frac{\partial u_\phi}{\partial\phi}\right)\right), \end{aligned} \tag{3.5b}$$

$$\begin{aligned} &\epsilon\frac{\partial u_\theta}{\partial t} + \epsilon^2\beta\mathbf{u}\cdot\nabla u_\theta + \epsilon^3\beta\frac{u_r u_\theta}{1+\epsilon r} - \epsilon^2\beta\frac{u_\phi^2\cot\theta}{1+\epsilon r} - 2\epsilon\beta\omega\cos\theta u_\phi - \beta\omega^2(1+\epsilon r)\cos\theta\sin\theta = \\ &\quad = -\frac{1}{1+\epsilon r}\frac{\partial p}{\partial\theta} + \frac{1}{\epsilon\alpha^2}\left(\nabla^2 u_\theta + \frac{2\epsilon^3}{(1+\epsilon r)^2}\frac{\partial u_r}{\partial\theta} - \frac{\epsilon^2}{r^2\sin^2\theta}\left(u_\theta + 2\cos\theta\frac{\partial u_\phi}{\partial\phi}\right)\right) \end{aligned} \tag{3.5c}$$

Type	A	β	ω_f, 1/s	α	$\epsilon\beta$	$1/\alpha^2$	$1/\epsilon\alpha^2$
Small saccades	5°	0.04	96.7	136.2	0.0048	$5.4\cdot10^{-5}$	$4.8\cdot10^{-4}$
Large saccades	50°	0.43	21.7	64.5	0.049	$2.4\cdot10^{-4}$	$2.1\cdot10^{-3}$
Average REM	12.54°	0.11	1.03	14	0.012	$5.1\cdot10^{-3}$	$4.6\cdot10^{-2}$
Maximum amplitude REM	123°	1.07	8.58	40.6	0.12	$6.1\cdot10^{-4}$	$5.4\cdot10^{-3}$

Table 3.2: Typical values of the dimensionless parameters, with $\epsilon \approx 0.11$ in all cases.

$$\begin{aligned}\epsilon\frac{\partial u_\phi}{\partial t}+\epsilon^2\beta\mathbf{u}\cdot\nabla u_\phi+\epsilon^3\beta\frac{u_\phi u_r}{r}+\epsilon^2\beta\frac{u_\theta u_\phi\cot\theta}{r}+(1+\epsilon r)\dot\omega\sin\theta+\\ +2\epsilon\beta\omega(u_\theta\cos\theta+\epsilon u_r\sin\theta)=-\frac{1}{(1+\epsilon r)\sin\theta}\frac{\partial p}{\partial\phi}+\\ +\frac{1}{\epsilon\alpha^2}\left(\nabla^2u_\phi+\frac{2\epsilon^2}{(1+\epsilon r)^2\sin\theta}\left(\frac{\partial u_r}{\partial\phi}+\cot\theta\frac{\partial u_\phi}{\partial\phi}\right)-\epsilon^3\frac{u_\phi}{(1+\epsilon r)^2\sin^2\theta}\right)\end{aligned}\tag{3.5d}$$

with $\omega=\cos t$ and $\dot\omega=-\sin t$, and

$$\begin{aligned}\nabla^2 f=\frac{\partial^2 f}{\partial r^2}+\frac{2\epsilon}{1+\epsilon r}\frac{\partial f}{\partial r}+\frac{\epsilon^2}{(1+\epsilon r)^2\sin\theta}\frac{\partial}{\partial\theta}\left(\sin\theta\frac{\partial f}{\partial\theta}\right)+\frac{\epsilon^2}{\sin^2\theta(1+\epsilon r)^2}\frac{\partial^2 f}{\partial\phi^2}=\\ =\frac{\partial^2 f}{\partial r^2}+2\epsilon\frac{\partial f}{\partial r}+\mathcal{O}(\epsilon^2),\end{aligned}\tag{3.6}$$

for any function f.

Using the geometrical values from table 3.1, we estimate

$$\epsilon\approx 0.11,\quad \epsilon^2\approx 0.012,\tag{3.7}$$

and in table 3.2 we report the remaining dimensionless parameters appearing in the governing equations (3.5) in four cases (taken from the data in figure 3.2): small and large saccadic rotations (amplitude 5° and 50°, respectively), average REM and maximum amplitude REM.

In the remainder of this work we drop from equations (3.5) any terms of orders ϵ^2, $\epsilon\beta$, $1/\alpha^2$, which can be seen to be small from table 3.2, as well as smaller terms. This leaves terms of order 1, β, ϵ and $1/(\epsilon\alpha^2)$. Despite the fact that $1/(\epsilon\alpha^2)$ is typically smaller than both ϵ^2 and $\epsilon\beta$ we choose to keep terms with this coefficient, as they are not negligible within the boundary layer. The same approach was used by Blondeaux and Vittori (1994) for a different problem, who showed that it leads to the same results as formal boundary layer analysis. Note also, that for maximum amplitude REM, terms of order $\epsilon\beta$ are comparable to those of order ϵ, implying that the model might not be very accurate in this case.

With the above simplifications we obtain the following system:

$$\frac{\partial p}{\partial r}=0,\tag{3.8a}$$

$$\epsilon\frac{\partial u_\theta}{\partial t}-\beta\omega^2\cos\theta\sin\theta=-(1-\epsilon r)\frac{\partial p}{\partial\theta}+\frac{1}{\epsilon\alpha^2}\frac{\partial^2 u_\theta}{\partial r^2},\tag{3.8b}$$

$$\epsilon\frac{\partial u_\phi}{\partial t}+(1+\epsilon r)\dot\omega\sin\theta=-\frac{1-\epsilon r}{\sin\theta}\frac{\partial p}{\partial\phi}+\frac{1}{\epsilon\alpha^2}\frac{\partial^2 u_\phi}{\partial r^2},\tag{3.8c}$$

coupled to the continuity equation (3.5a), which remains in full. Equations (3.8) should be solved subject to no-penetration and no-slip boundary conditions at $r = 0$ and $r = h(\theta,\phi)/\bar{h}$ and zero flux at $\theta' = \theta_0$. We note that the latter does not imply no-slip condition at the boundary $\theta' = \theta_0$ and is a consequence of the application of lubrication theory. Therefore, the solution close to $\theta' = \theta_0$ is not accurate. We also require the solution to be regular at $\theta' = 0$.

3.3 Solution

3.3.1 Decomposition of the solution

As is usual in lubrication theory, equation (3.8a) shows that the pressure does not depend on the r-coordinate. The motion is forced by the term proportional to ω^2 in equation (3.8b) and that proportional to $\dot{\omega}$ in equation (3.8c). Recalling that $\omega = \cos t = e^{\mathrm{i}t}/2 + \text{c.c.}$, where c.c. denotes the complex conjugate, we note that three frequencies are effectively forced: 0, 1 and 2, corresponding to the terms proportional to $e^{0\mathrm{i}t}$, $e^{\mathrm{i}t}$ and $e^{2\mathrm{i}t}$. In other words, harmonic oscillations of the domain with dimensionless frequency 1, force a steady streaming component, a flow with the same frequency as the forcing and also flow at twice that frequency. Thus, we seek a solution for the velocity and the pressure in the form

$$\mathbf{u}(\mathbf{x},t) = \mathbf{u}^{(0)}(\mathbf{x}) + \mathbf{u}^{(1)}(\mathbf{x})e^{\ it} + \mathbf{u}^{(2)}(\mathbf{x})e^{2\mathrm{i}t} + \text{c.c.}, \tag{3.9}$$

$$p(\mathbf{x},t) = p^{(0)}(\mathbf{x}) + p^{(1)}(\mathbf{x})e^{\mathrm{i}t} + p^{(2)}(\mathbf{x})e^{2\mathrm{i}t} + \text{c.c.} \tag{3.10}$$

Substituting into equations (3.8a)–(3.8c) we obtain the following set of equations for $k = 0,1,2$, respectively:

$$\frac{\partial p^{(k)}}{\partial r} = 0, \tag{3.11a}$$

$$\mathrm{i}k\epsilon u_\theta^{(k)} - \frac{1}{\epsilon\alpha^2}\frac{\partial^2 u_\theta^{(k)}}{\partial r^2} = -(1-\epsilon r)\frac{\partial p^{(k)}}{\partial \theta} + \Theta^{(k)}, \tag{3.11b}$$

$$\mathrm{i}k\epsilon u_\phi^{(k)} - \frac{1}{\epsilon\alpha^2}\frac{\partial^2 u_\phi^{(k)}}{\partial r^2} = -\frac{1-\epsilon r}{\sin\theta}\frac{\partial p^{(k)}}{\partial \phi} + \Phi^{(k)}, \tag{3.11c}$$

where $\Theta^{(0)} = \Theta^{(2)} = (\beta/8)\sin(2\theta)$, $\Phi^{(1)} = -(\mathrm{i}/2)(1+\epsilon r)\sin\theta$ and $\Theta^{(1)} = \Phi^{(0)} = \Phi^{(2)} = 0$. Equations (3.11) are coupled with the continuity equation for each harmonic.

3.3.2 Derivation of the equation for the pressure

Following the standard approach in lubrication theory, we solve equations (3.11b) and (3.11c) to find the r-dependence of $u_\theta^{(k)}$ and $u_\phi^{(k)}$, respectively, which, when combined with the no-slip boundary conditions gives

$$\mathbf{u}_{\mathrm{h}}^{(k)} = A_k(r,h)\nabla_{\mathrm{h}} p^{(k)} + B_k(r,h)\mathbf{v}_k, \tag{3.12}$$

for $k = 0,1,2$, where $\mathbf{v}_0 = \mathbf{v}_2 = \sin 2\theta \mathbf{e}_\theta$, $\mathbf{v}_1 = \sin\theta \mathbf{e}_\phi$. The unit vectors $\mathbf{e}_\theta$ and $\mathbf{e}_\phi$ point in the directions of increasing θ and ϕ, respectively and a subscript h on a vector indicates that the projection of the vector on the θ and ϕ directions is taken. The functions A_k and B_k are different for every harmonic and are reported below

$$A_0(r,h) = \frac{\epsilon a^2}{2}\left(r(r-h) - \frac{\epsilon r}{3}(r^2-h^2)\right), \tag{3.13a}$$

$$B_0(r,h) = \frac{\beta\epsilon a^2}{16}\left(rh - r^2\right), \tag{3.13b}$$

$$A_1(r,h) = \frac{i}{\epsilon}\left(\frac{\sin ar(\epsilon h + \cos ah - 1)}{\sin ah} - \cos ar - (\epsilon r - 1)\right), \tag{3.13c}$$

$$B_1(r,h) = \frac{1}{2\epsilon}\left(\frac{\sin ar(\epsilon h - \cos ah + 1)}{\sin ah} + \cos ar - (\epsilon r + 1)\right), \tag{3.13d}$$

$$A_2(r,h) = \frac{i}{2\epsilon}\left(\frac{\sin br(\epsilon h + \cos bh - 1)}{\sin bh} - \cos br - (\epsilon r - 1)\right), \tag{3.13e}$$

$$B_2(r,h) = \frac{i\beta}{16\epsilon}\left(\sin br\frac{1-\cos bh}{\sin bh} + \cos br - 1\right), \tag{3.13f}$$

where $a = \sqrt{-i}\,\epsilon\alpha = \pm(1-i)\epsilon\alpha/\sqrt{2}$ and $b = \sqrt{-2i}\,\epsilon\alpha = \pm(1-i)\epsilon\alpha$.

It is convenient from now on to work in the coordinate system $\mathscr{C}'$ defined in § 3.2.1, so that we can make use of the fact that the domain is axisymmetric with respect to $\theta' = 0$ (see figure 3.1a). In this coordinate system (3.12) takes the form

$$\mathbf{u}_{\mathrm{h}}^{(k)} = A_k(r,h)\nabla'_{\mathrm{h}} p^{(k)} + B_k(r,h)\mathbf{v}'_k, \tag{3.14}$$

where $\mathbf{v}'_0 = \mathbf{v}'_2 = -\sin 2\theta' \cos^2\phi' \mathbf{e}_{\theta'} + \sin 2\phi' \sin\theta' \mathbf{e}_{\phi'}$, $\mathbf{v}'_1 = \sin\phi' \mathbf{e}_{\theta'} + \cos\theta' \cos\phi' \mathbf{e}_{\phi'}$ and ∇' are vectors $\mathbf{v}_k$, $k = 0,1,2$ and ∇ expressed in $\mathscr{C}'$ coordinate system. Substituting (3.14) into the continuity equation (3.5a) and integrating it over r, we obtain a partial differential equation for $p^{(k)}$ for $k = 0,1,2$:

$$\mathscr{A}(\gamma_k)p^{(k)} + \mathscr{B}_k(\delta_k) = 0, \tag{3.15}$$

where

$$\gamma_k(h) = \int_0^h (1+\epsilon r)A_k(r,h)\,\mathrm{d}r, \quad \delta_k(h) = \int_0^h (1+\epsilon r)B_k(r,h)\,\mathrm{d}r, \tag{3.16}$$

that, calculated for each harmonic, give the following expressions

$$\gamma_0(h) = \frac{\beta\epsilon a^2 h^3}{180\beta}\left(4\epsilon^2 h^2 - 15\right), \tag{3.17a}$$

$$\delta_0(h) = \frac{\beta\epsilon a^2}{96}\left(\frac{\epsilon h^4}{2} + h^3\right), \tag{3.17b}$$

$$\gamma_1(h) = -i\left(\frac{\epsilon h^3}{3} - \frac{h}{\epsilon} - \frac{\epsilon h}{a^2} + \frac{2 - 2\cos ah + \epsilon^2 h^2 \cos ah}{\epsilon a \sin ah}\right), \tag{3.17c}$$

$$\delta_1(h) = -\frac{1}{2}\left(\frac{\epsilon h^3}{3} + h^2 + \frac{h}{\epsilon} - \frac{h\epsilon}{a^2} + \frac{\epsilon(\epsilon h^2 + 2h)\cos ah - 2\epsilon h + 2(\cos ah - 1)}{\epsilon a \sin ah}\right), \tag{3.17d}$$

$$\gamma_2(h) = -\frac{i}{2}\left(\frac{\epsilon h^3}{3} - \frac{h}{\epsilon} - \frac{\epsilon h}{b^2} + \frac{2-2\cos bh + \epsilon^2 h^2 \cos bh}{\epsilon b \sin bh}\right), \tag{3.17e}$$

$$\delta_2(h) = -\frac{i\beta}{16\epsilon}\left(\frac{(2+\epsilon h)(\cos bh - 1)}{b\sin bh} + h + \frac{\epsilon h^2}{2}\right). \tag{3.17f}$$

In (3.15), $\mathscr{A}(\gamma_k)$ is a linear differential operator given by

$$\mathscr{A}(\gamma_k) = \frac{1}{\sin\theta'}\left(\frac{\partial}{\partial\theta'}\left(\sin\theta'\gamma_k\frac{\partial}{\partial\theta'}\right) + \frac{\gamma_k}{\sin\theta'}\frac{\partial^2}{\partial\phi'^2}\right), \tag{3.18}$$

with

$$\mathscr{B}_0(\delta_0) = 2\left(3\sin^2\theta'\cos^2\phi' - 1\right)\delta_0(h) - 2\cos^2\phi'\sin\theta'\cos\theta'\frac{d\delta_0(h)}{d\theta'}, \tag{3.19a}$$

$$\mathscr{B}_1(\delta_1) = \sin\phi'\frac{\partial\delta_1}{\partial\theta'}, \tag{3.19b}$$

$$\mathscr{B}_2(\delta_2) = \mathscr{B}_0(\delta_2). \tag{3.19c}$$

The r-integrated velocity, or flux per unit length, reads

$$\mathbf{q}_{\mathrm{h}}^{(k)} = \int_0^h (1+\epsilon r)\mathbf{u}_{\mathrm{h}}^{(k)}\,\mathrm{d}r = \gamma_k\nabla'_{\mathrm{h}}p^{(k)} + \delta_k\mathbf{v}'_k, \tag{3.20}$$

where ∇'_{h} is computed on the spherical surface $r = 1$.

The no-flux condition at the boundary $\theta' = \theta_0$ can then be written as

$$\mathbf{q}_{\mathrm{h}}^{(k)}\cdot\mathbf{e}_{\theta'} = 0 \quad\Rightarrow\quad \gamma_k\frac{\partial p^{(k)}}{\partial\theta'} + \delta_k\mathbf{v}'_k\cdot\mathbf{e}_{\theta'} = 0, \tag{3.21}$$

and we also require the solution $p^{(k)}$ to be regular (in this case, continuous and with continuous derivative) at $\theta' = 0$. Note that each $p^{(k)}$ is uniquely defined up to the addition of an arbitrary constant. Thus, in what follows, without loss of generality, we assume that $p^{(k)} = 0$ at $\theta' = 0$.

In the following subsections, we simplify the problem for each harmonic $k = 0, 1, 2$ by separating the θ'- and ϕ'-dependence, and we derive an analytical solution for each in the case of constant h.

3.3.3 Separation of variables and solution for the case of constant h

3.3.3.1 Dominant frequency component ($k = 1$)

For the case $k = 1$ we note the ϕ'-dependence in (3.15) and (3.21) and seek a solution of the form

$$p^{(1)}(\theta', \phi') = g(\theta')\sin\phi'. \tag{3.22}$$

This leads to

$$\frac{1}{\sin\theta'}\frac{d}{d\theta'}\left(\sin\theta'\gamma_1\frac{dg}{d\theta'}\right) - \frac{\gamma_1}{\sin^2\theta'}g + \frac{d\delta_1}{d\theta'} = 0, \tag{3.23a}$$

with boundary condition

$$\frac{dg}{d\theta'} = -\frac{\delta_1}{\gamma_1} \quad \text{at } \theta' = \theta_0. \tag{3.23b}$$

and the regularity condition at $\theta' = 0$.

In the general case (3.23) must be solved numerically. We use a second order finite difference method to solve the system (3.23), imposing $g = 0$ at $\theta = 0$ to satisfy regularity condition.

In the special case of constant h, γ_1 and δ_1 are both constant, and we obtain

$$p^{(1)} = -\frac{\delta_1}{\gamma_1}\frac{\sin^2\theta_0}{1-\cos\theta_0}\frac{1-\cos\theta'}{\sin\theta'}\sin\phi', \tag{3.24a}$$

$$u_r^{(1)} = 0, \tag{3.24b}$$

$$u_\theta^{(1)} = \left(B_1(r) - A_1(r)\frac{\delta_1}{\gamma_1}\frac{\sin^2\theta_0}{1-\cos\theta_0}\frac{1-\cos\theta'}{\sin^2\theta'}\right)\sin\phi', \tag{3.24c}$$

$$u_\phi^{(1)} = \left(B_1(r)\cos\theta' - A_1(r)\frac{\delta_1}{\gamma_1}\frac{\sin^2\theta_0}{1-\cos\theta_0}\frac{1-\cos\theta'}{\sin^2\theta'}\right)\cos\phi', \tag{3.24d}$$

where we have set the arbitrary constant of integration to zero in the expression for $p^{(1)}$, $\mathbf{u}_h^{(1)}$ was obtained from (3.14) and $u_r^{(1)}$ was found from the continuity equation (3.5a).

3.3.3.2 Steady streaming ($k = 0$) and double frequency ($k = 2$) components

For the cases $k = 0$ and $k = 2$ the procedure is similar, and we derive the solutions together in this section. Noting the ϕ'-dependence in (3.15) and (3.21), we seek a solution of the form

$$p^{(k)}(\theta', \phi') = f_0^{(k)}(\theta') + f_1^{(k)}(\theta')\cos 2\phi', \tag{3.25}$$

which leads to

$$\frac{1}{\sin\theta'}\frac{d}{d\theta'}\left(\gamma_k \sin\theta' \frac{df_0^{(k)}}{d\theta'}\right) - \sin\theta'\cos\theta'\frac{d\delta_k}{d\theta'} + (3\sin^2\theta' - 2)\delta_k = 0, \tag{3.26a}$$

$$\frac{1}{\sin\theta'}\frac{d}{d\theta'}\left(\gamma_k \sin\theta' \frac{df_1^{(k)}}{d\theta'}\right) - \frac{4\gamma_k f_1^{(k)}}{\sin^2\theta'} - \sin\theta'\cos\theta'\frac{d\delta_k}{d\theta'} + 3\sin^2\theta'\delta_k = 0. \tag{3.26b}$$

with boundary conditions

$$\frac{df_{0,1}^{(k)}}{d\theta'} = \frac{\delta_k}{2\gamma_k}\sin 2\theta' \quad \text{at } \theta' = \theta_0. \tag{3.26c}$$

As for the harmonic $k = 1$, in the general case (3.26) must be solved numerically and, to this end, we use a second order finite difference method. The regularity condition now imposes $\mathrm{d}f_0/\mathrm{d}\theta' = 0$ and $f_1 = 0$ at $\theta' = 0$.

In the case of constant h we obtain the following analytical solution

$$p^{(k)} = -\frac{\delta_k}{2\gamma_k}\left(1-2\cos^2\phi'\sin^2\theta'\right), \tag{3.27a}$$

$$u_r^{(k)} = -\left(\frac{\delta_k\hat{\gamma}_k(r)}{\gamma_k} - \hat{\delta}_k(r)\right)\frac{\left(1+3\cos 2\theta'\right)\cos^2\phi' - 2\cos 2\phi'}{(1+\epsilon r)^2}, \tag{3.27b}$$

$$u_\theta^{(k)} = \left(A_k(r)\frac{\delta_k}{\gamma_k} - B_k(r)\right)\sin 2\theta'\cos^2\phi', \tag{3.27c}$$

$$u_\phi^{(k)} = -\left(A_k(r)\frac{\delta_k}{\gamma_k} - B_k(r)\right)\sin 2\phi'\sin\theta', \tag{3.27d}$$

where we have set the arbitrary constant to zero in the expression for $p^{(k)}$, $\mathbf{u}_h^{(k)}$ was obtained from (3.14), $u_r^{(k)}$ was found from the continuity equation, and $\hat{\gamma}_k(r) = \int_0^r (1+\epsilon s)A_k(s)\,\mathrm{d}s$ and $\hat{\delta}_k = \int_0^r (1+\epsilon s)B_k(s)\,\mathrm{d}s$. It is straightforward to check that the r-integrated velocity $\mathbf{q}_h^{(k)}$ is zero for $k = 0, 2$.

3.4 Results

3.4.1 Constant-height domain

We start with the special case of constant h. In figure 3.3 we show the flow component with frequency 1 ($k = 1$), which we expect to be much larger than the other two components ($k = 0, 2$). On the different rows we show the flow and pressure via snapshots at four different times through the first half period (those during the second half period are the reflections of these). The first row ($t = 0$) corresponds to the time when the angular velocity is maximum and the domain is moving in the direction of the positive y-axis, and the subsequent rows correspond to subsequent times spaced 1/8th period apart.

In the first column of plots in figure 3.3, we show the velocity on the horizontal midplane $z = 0$ and $y > 0$ (the other half is an antisymmetric reflection). In each case the fluid close to the inner wall moves in the same direction as the rotation and that near the outer wall moves in the opposite direction (with the exception of $t = \pi/2$ when the domain is not moving, figure 3.3g). Note that the fact that the velocity does not go to zero at the boundary $\theta' = \theta_0$ (as can be seen in the first and second column) is because, due to the simplification of the lubrication theory, we can only impose zero flux there rather than a full no-slip condition. Close to $\theta' = \theta_0$ the assumptions of lubrication theory do not hold, and the radial velocity component would be comparable to the other components.

In the second column of figure 3.3, we show the r-integrated velocity field obtained from equation (3.20) and the pressure distribution on the surface $r = 1$, both projected onto a plane of constant x. At $t = 0$ the angular acceleration is zero, and thus the pressure is almost constant on the surface $r = 0$, figure 3.3(b), but the pressure gradient is much larger at the other three times, especially at $t = \pi/2$ when the angular acceleration peaks, figure 3.3(h). Each plot shows

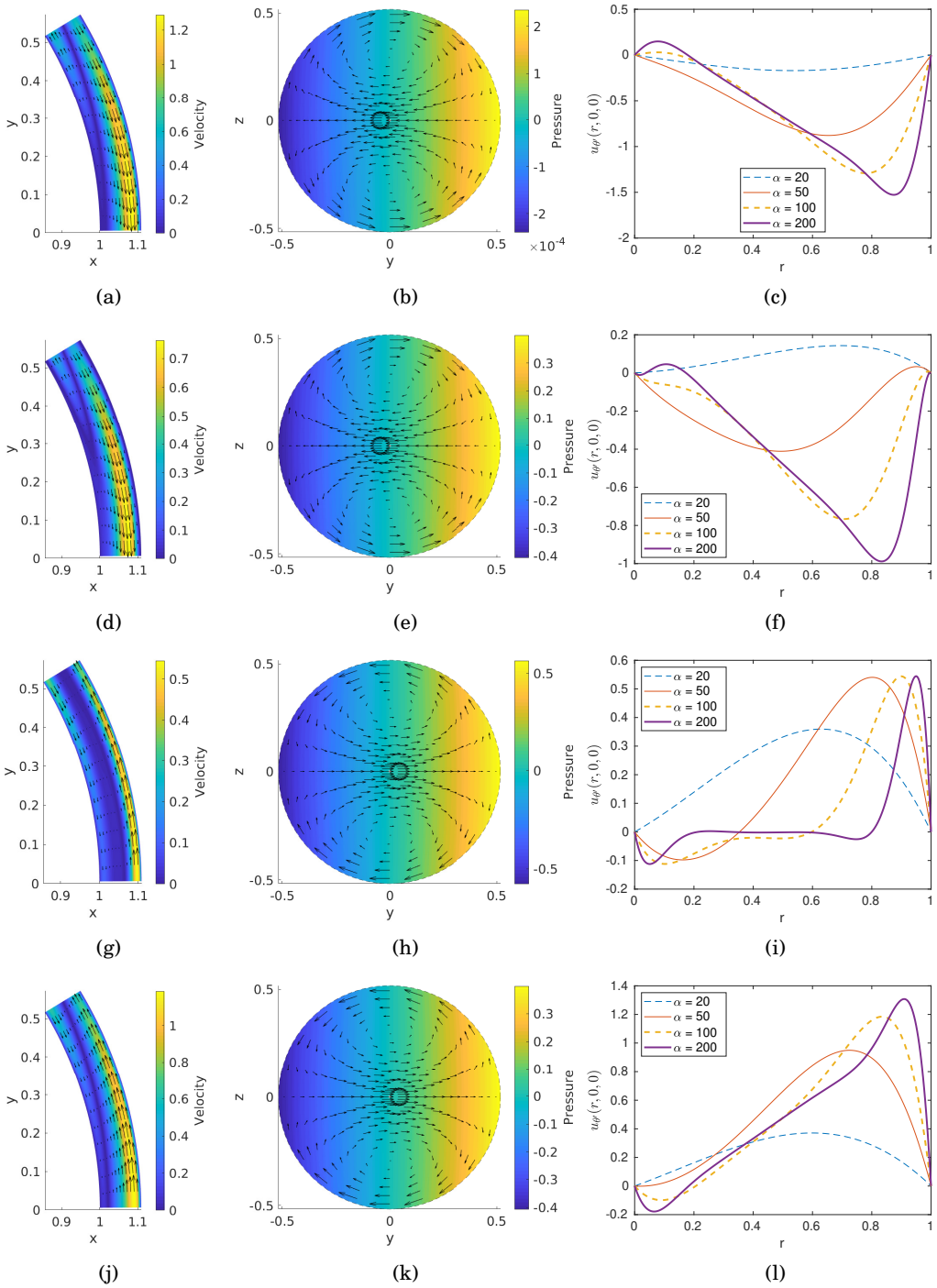

Figure 3.3: The flow of the dominant harmonic component ($k = 1$) in the special case h constant. The four rows show four equally spaced times: $t = 0$, $\pi/4$, $\pi/2$ and $3/4\pi$. First column: arrows indicate fluid velocity relative to the domain $\mathbf{u}^{(1)}$ and shading indicates its dimensionless magnitude on half of the midplane $z = 0$. Second column: dimensionless pressure $p^{(1)}$ at $r = 0$ (shading) and r-integrated velocity $\mathbf{q}_{\mathrm{h}}^{(1)}$ (arrows), projected onto a plane of constant x. Third column: profiles of $u_{\theta'}$ along the axis $\theta' = 0$. For all plots $\beta = 6.5°$ and $\epsilon = 0.11$, and in the first two columns $\alpha = 100$. The velocity vectors in the first two columns are normalised so that their maximum length is the same in all plots.

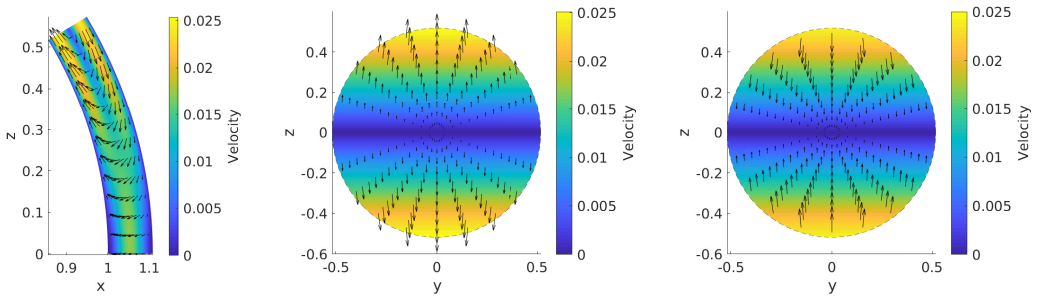

Figure 3.4: The steady streaming flow in the special case of a domain of constant height, shown (a) on half of the midplane $y = 0$ ($\phi' = \pi$) (the other half is a symmetric reflection) (b) on the plane $r = 0.2$ and (c) $r = 0.8$. The arrows indicate the relative velocity $\mathbf{u}^{(0)}$ and colours indicate its magnitude. The parameter values are $\alpha = 100$, $\beta = 6.5°$, $\epsilon = 0.11$.

two circulations that are reflections of one another, which indicates that the instantaneous flow has a highly three-dimensional structure.

The third column of figure 3.3 shows the relative velocity component $u_{\theta'}$ along the line $\theta' = 0$, which is a region of the positive x-axis with $x = 1 + \epsilon r$. Each line corresponds to a different value of the Womersley number α. Inspection of the plots shows that, as the Womersley number increases, a progressively thinner oscillatory Stokes boundary layer forms at both walls, as expected.

In figure 3.4(a) we show the steady streaming flow on the vertical plane $y = 0$. We only plot the upper half of the domain since the flow is symmetric in the x-axis, as can be seen by inspecting equations (3.27b) and (3.27c). In the outer part of the domain fluid particles move towards the midplane $z = 0$ and in the inner part of the domain they move away from $z = 0$. This is consistent with what is found in a periodically rotating sphere (Repetto et al., 2008; Colombini, 2014), where a circulation with the same sense of rotation is found, and also with the numerical findings of Abouali et al. (2012), relative to the flow in the AC. Since the model does not capture the behaviour of the oscillatory flow close to the boundary of the domain (at $\theta' = \theta_0$), we cannot rule out the possibility that boundary effects could produce a steady streaming in the core of the domain. The flow on the planes $r = 0.2$ and $r = 0.8$ are shown in figures 3.4(b,c). The velocity profile is almost vertical in both cases and there is very little transversal flow. Moreover, we recall that in the case of the constant thickness domain the r-integrated velocity $\mathbf{q}_{\mathrm{h}}$ is equal to zero.

In figure 3.5 we show the maximum dimensional value over time and space attained by the velocity for each of the harmonics as a function of the Womersley number α. As expected the magnitude of the dominant harmonic $k = 1$ velocity is much larger than the others. Moreover, the steady streaming velocity has a significantly larger magnitude than the harmonic $k = 2$ for large values of α.

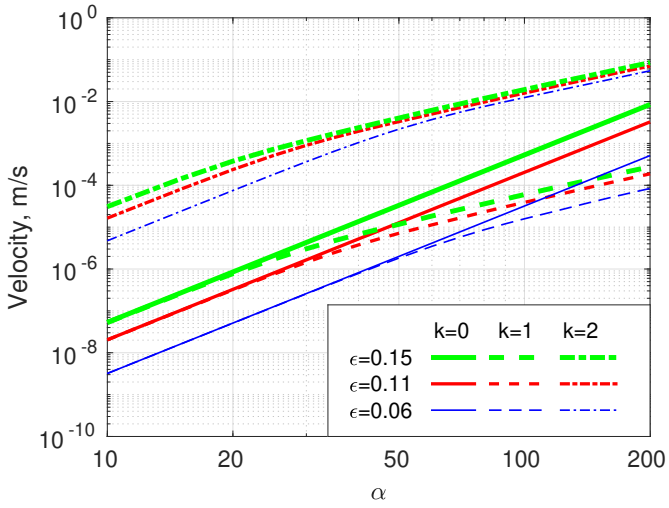

Figure 3.5: Velocity magnitudes over a range of frequencies in the special case of a constant height domain. Maximum value (over both time and space) attained by the magnitude of the velocity as a function of the Womersley number α. The different line styles denote the different harmonics: $k = 0$ (solid); $k = 1$ (dot-dashed); and $k = 2$ (dashed); and the thickness and color show the values of ϵ: $\epsilon \approx 0.15$ (thick green); $\epsilon \approx 0.11$ (medium red); and $\epsilon \approx 0.06$ (thin blue). The amplitude is fixed at $\beta = 6.5°$ in each case.

3.4.2 More realistic eye geometry

In this section we report the results obtained using the more realistic shape of the anterior chamber (AC) of the eye, shown in figure 3.1(c). Figure 3.6 is the analogy of figure 3.3 for this case, and mostly shows qualitatively similar findings. However, in the case of the more realistic domain shape, the velocity decreases near the periphery of the domain (θ' near to θ_0), since the domain is thinner there. It is interesting to note that the circulations in the r-integrated velocity fields that were observed in the case of the constant height domain are still present in this case, suggesting that the flow induced by eye rotations is highly three-dimensional.

In figure 3.7 we plot the maximum dimensional value over space and time of the wall shear stress on the cornea as a function of the eye rotation amplitude in the case of both saccades and REM. We compared the results for three different values of maximum thickness of the AC, within the physiological range (e.g. Jivrajka et al., 2008). The maximum wall shear stress increases with the height of the domain, and for a given domain, peaks for saccade amplitudes around 0.15 rad or 8.6°.

Figure 3.8 shows the steady streaming, which indicates similar behaviour to the constant-height case, figure 3.4, but in this case a closed circulation is visible in figure 3.8(a), which forms since the domain gets thin close to the periphery $\theta' = \theta_0$. Furthermore, the r-integrated velocity is non-zero (figure 3.8b), unlike in the constant-height case, meaning that the streaming flow is

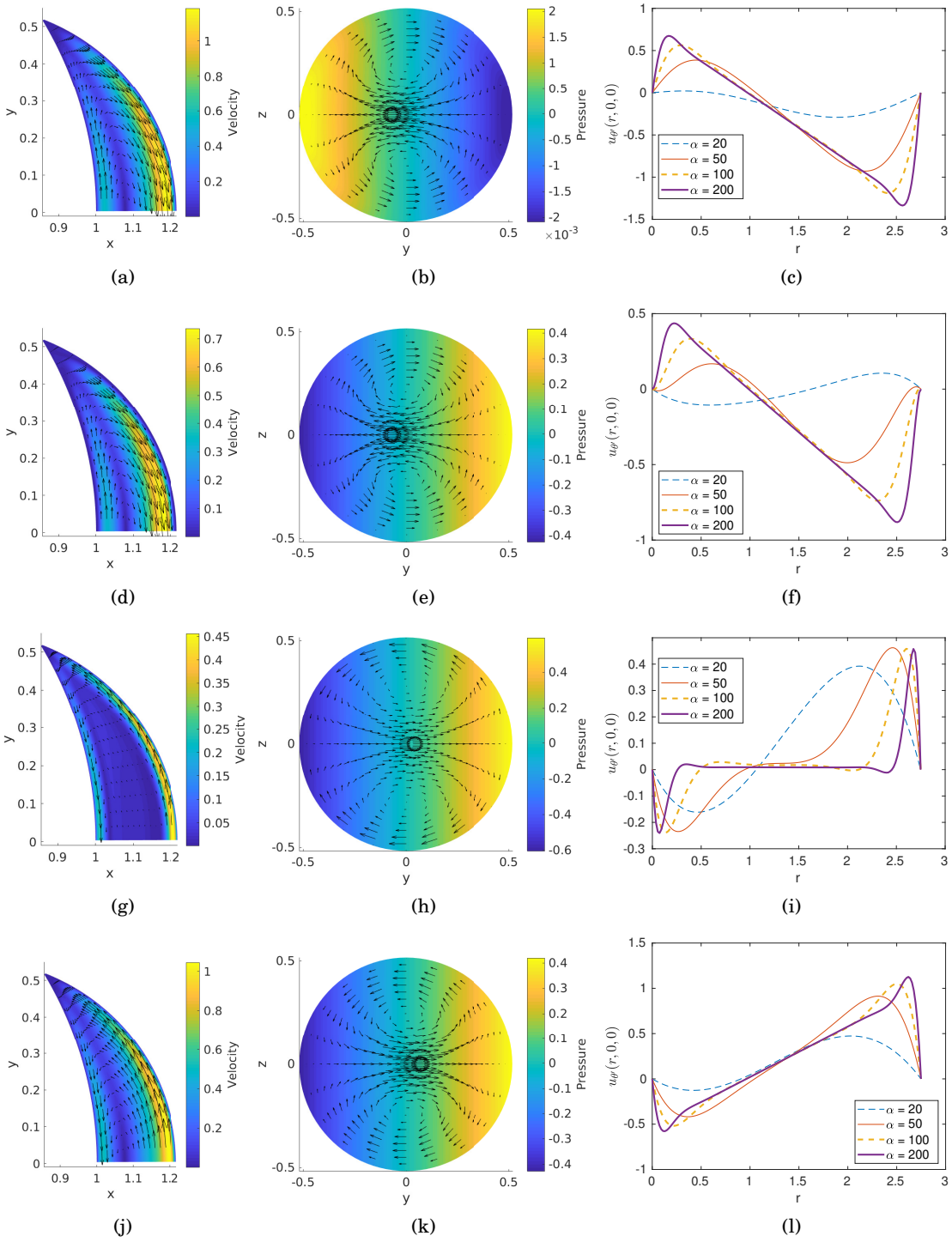

Figure 3.6: As for figure 3.3, but for the case of the more realistic eye shape described in the introduction of § 3.2.1.

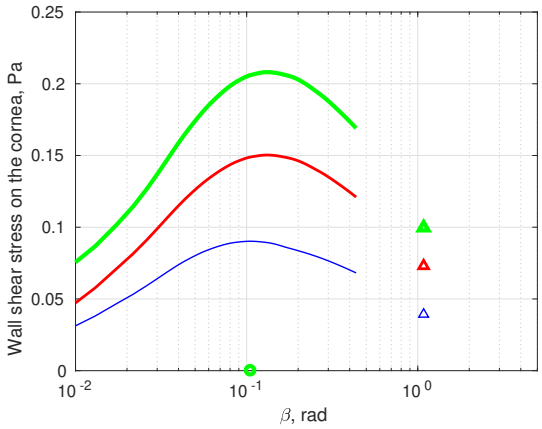

Figure 3.7: Maximum dimensional value over space and time of the wall shear stress on the cornea as a function of the angular amplitude of the saccadic eye rotation β in the case of the more realistic eye shape. For each value of β the curve for saccades in figure 3.2 was used to find the corresponding value of α. The lines with different thickness and color correspond to different values of $h_{\max}$: medium red: $h_{\max} = 2.62$ mm ($\epsilon \approx 0.11$); thin blue: $h_{\max} = 1.5$ mm ($\epsilon \approx 0.06$); thick green: $h_{\max} = 3.5$ mm ($\epsilon \approx 0.15$). The symbols refer to REM: triangles represent maximum amplitude REM and circles average REM, with their thickness and color corresponding to maximum height of the domain considered. The three symbols for average REM cannot be distinguished as they are approximately on top of one another.

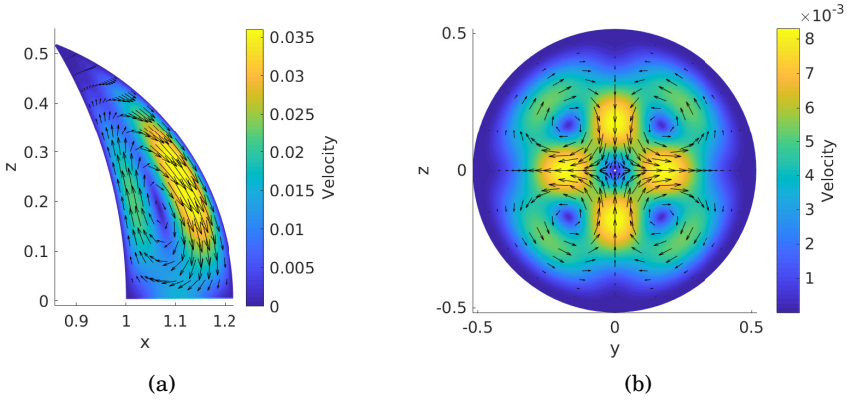

Figure 3.8: The steady streaming flow for the more realistic domain shape: (a) Relative velocity $\mathbf{u}^{(0)}$ on the vertical cross section $y = 0$; (b) The r-integrated velocity, projected onto the (y,z)-plane. In both figures, colours indicate velocity magnitude and arrows show magnitude and direction. The parameters are $\alpha = 100$, $\beta = 6.5°$, $\epsilon = 0.11$.

fully three-dimensional and there is a formation of four symmetrically arranged circulations. The flow on four equally distributed surfaces along the thickness of the domain is shown in figure 3.9. Close to the inner boundary of the AC, the flow has similar characteristics as in the case of

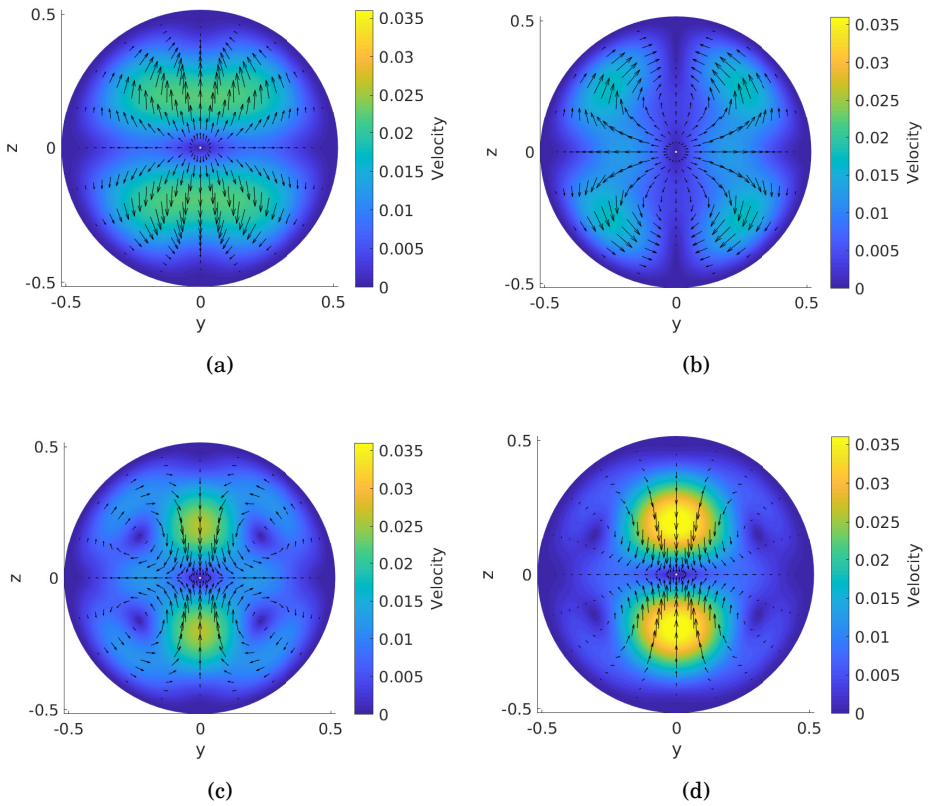

Figure 3.9: Steady streaming flow $\mathbf{u}^{(0)}$ for the case of realistic shape at the planes: (a) $r = 0.2h/\bar{h}$ (b) $r = 0.4h/\bar{h}$ (c) $r = 0.6h/\bar{h}$ (d) $r = 0.8h/\bar{h}$. In all figures, colours indicate velocity magnitude and arrows show magnitude and direction. The parameters are $\alpha = 100$, $\beta = 6.5°$, $\epsilon = 0.11$.

constant thickness. The steady streaming has a complicated structure, which is highly variable in the radial direction, and the flow reversal observed on the plane $y = 0$ in figure 3.8(a) does not occur everywhere in the domain. The magnitude of the transversal flow is smaller than that on the midplane shown in figure 3.8(a), but it is likely to have physiological importance, as they lead to transverse mixing in the AC.

Figure 3.10 shows the dependence of the maximum dimensional steady streaming velocity on the saccade amplitude, with the colours corresponding to different thicknesses of the domain. Maximum steady streaming velocity increases with the saccade amplitude. The steady streaming velocity of maximum amplitude REM is also similar, whereas that of average REM is much lower. Increasing the thickness of the AC leads to higher steady streaming velocities in each case.

The results of the model are based on various assumptions, which have been discussed in §3.2. In particular, we neglected the terms of order $\epsilon\beta$, compared with terms of order ϵ, but also discussed cases in which the amplitude of oscillations β is quite large, such as large saccades and maximum amplitude REM, which is formally out of the range of validity of our asymptotic

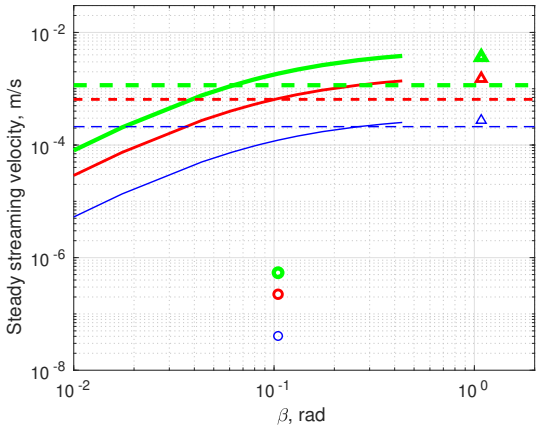

Figure 3.10: Maximum over space and time of the magnitude of the steady streaming flow as a function of the angular amplitude of the eye rotation. The solid curves and symbols are as in figure 3.7. The thermal flow due to body heating is also shown (as horizontal dashed lines since they do not correspond to a particular value of β), calculated based on Canning et al. (2002) (see Discussion for the details), colored and having width representing thickness of the domain (as in figure 3.7).

approach. In order to verify the accuracy of our results, we have run a series of three-dimensional unsteady simulations using the commercial software COMSOL Multiphysics®. In particular, we focused on the oscillatory component of the flow and did not consider the steady streaming. We compared our theoretical results with the numerics in terms of the $u_{\theta'}$ velocity component along the line $\theta' = 0$ and computed the corresponding time averaged normalised L_2 error between our model and the numerical predictions. We performed several numerical simulations varying both ϵ and β. We find that the error is of order ϵ and weakly depends on β for values of β up to 1. These results are reassuring concerning the validity of the theory for values of β of order 1, such as large saccades or REM.

3.5 Discussion

We have studied the flow in a thin domain performing harmonic rotations about a fixed axis, in order to investigate the flow in the anterior chamber of the eye (AC) induced by eye rotations. As mentioned in the Introduction, this is relevant to the study of nutrient and drug delivery to the tissues of the eye, and allows us to estimate the shear stresses on the cornea, which could lead to the detachment of endothelial cells.

We worked in a reference frame moving with the domain, and assumed that the aspect ratio of the AC is small, the Womersley number α is large and the angular amplitude $\beta < 1$ rad, which allowed us to reduce the governing equations to a linear system forced by the angular and the

	Saccade 6°	Saccade 30°	average REM	max amplitude REM
This work	0.094	0.1	$0.2{\cdot}10^{-3}$	0.074
Previous works	0.12	0.147	$0.248{\cdot}10^{-3}$	0.06

Table 3.3: Comparison of the maximum WSS (in Pa) on the cornea calculated with the present model with the results from numerical works of Abouali et al. (2012) (saccades) and Modarreszadeh et al. (2014) (REM).

centrifugal accelerations. We considered both the case of a domain with constant thickness, for which we found a fully analytical solution, and a more realistic approximation of the AC geometry. The flow has three components: the largest oscillates with the forcing frequency, and the others are a steady streaming component and a component that has twice the fundamental frequency.

In both the cases of a constant height chamber and the more realistic shape, we find that the dominant frequency component of the flow has a complex three-dimensional structure, which has not been observed in previous numerical simulations of the flow in the AC (Abouali et al., 2012; Modarreszadeh et al., 2014). This is because in our analysis we work in a frame moving with the domain, making some of the details of the flow easier to observe, since they are not disguised by the velocities of the chamber itself. The dominant frequency component of the flow is associated with much higher velocities than the other components, and therefore contributes the majority of the wall shear stress (WSS) on the cornea. The WSS is larger for higher Womersley numbers as boundary layers develop, and it is also larger for thicker chambers. We found that WSS is maximised in the centre of the cornea (see also Abouali et al., 2012), and reaches a maximum value of around 0.15 Pa for $\beta \approx 8.6°$ and $\alpha = 124$. A direct comparison of our results with those of Abouali et al. (2012) is not possible, since we model the saccades differently: in that work, four saccades per period were used, whereas in our model we use two. We therefore adapted our model to use the same saccadic motion, and present the results in table 3.3, which show good agreement between our model and the work of both Abouali et al. (2012) and Modarreszadeh et al. (2014). The WSS values predicted by both our model and the models of Abouali et al. (2012) and also Repetto et al. (2015) are of a similar order of magnitude to those found to cause detachment (~ 0.1 Pa) by Kaji et al. (2005), who studied the corneal endothelial cells *in vitro*. This suggests that higher values of WSS would be required *in vivo* for the corneal cells to detach. Note that the values of the WSS due to eye rotations are much larger than those produced by the boyancy driven flow due to temperature differences in the AC, which is about 0.0016 Pa (e.g Repetto et al., 2015).

The steady streaming flow is forced by the centrifugal acceleration, and its velocity is much smaller than that of the flow oscillating with the forcing frequency, but nevertheless can have a key role in mixing processes, as it is time independent. The steady streaming flow has a complicated three-dimensional structure, which was not fully highlighted in the numerical simulations of Abouali et al. (2012) and Modarreszadeh et al. (2014), and has a non zero r-integrated velocity

for realistic shape of the domain. We note that Modarreszadeh et al. (2014) also observed smaller vortices close to the pupil boundary and next to the trabecular meshwork, which we cannot capture with our model due to our geometrical simplifications and use of lubrication theory.

In order to estimate the effective importance of the steady streaming flow on mixing in the AC, we compute the Péclet number, which measures the strength of advection over diffusion, and is given by $Pe = LU/D$, where D is the diffusion coefficient, L is the radius of the AC and U is characteristic velocity. With $D = 10^{-9}$ m^2/s (Lide, 1996), $L = 6.2$ mm and a typical value of the velocity of $5 \cdot 10^{-4}$ m/s (see figure 3.10) we obtain $Pe \approx \mathcal{O}(10^3)$. The r-integrated steady streaming is much smaller, and the corresponding Péclet number is of order 10^2. In both cases it is clear that advection largely dominates over diffusion, and confirms that eye rotations have a key role in governing transport processes in the AC. An effect that could be potentially relevant for transport processes in the AC, and that has been neglected in the present work, is shear augmented diffusion via a "Taylor dispersion" mechanism. We leave the consideration of such an effect for the possible future work.

Besides eye rotations, the other mechanism that is known to produce a flow that significantly contributes to fluid mixing is the temperature gradient across the AC, since it also leads to the generation of a steady flow. To compare the steady streaming flow during saccades with the thermal flow we make use of the results of Canning et al. (2002), who developed an idealised model in which the geometry of the AC was approximated as a spherical cap to derive an analytical expression for the thermal flow. This showed that the flow is directed along the vertical planes. The maximum magnitude of the fluid velocity was found to be

$$u_{T,max} = \frac{\Delta T \rho g \alpha_T h_{max}^2 \sqrt{3}}{216 \nu}, \tag{3.28}$$

where ΔT is the temperature difference between the cornea and the iris, $\alpha_T = 3 \cdot 10^{-4}$ K^{-1} is the coefficient of thermal expansion, g is gravitational acceleration, ρ and ν are fluid density and kinematic viscosity, respectively and $h_{\max}$ is the maximum thickness of the anterior chamber (see table 3.1). With $\Delta T = 3$ K, we estimate $u_{T,max} = 6.47 \cdot 10^{-4}$ m/s. Tweedy et al. (2017) used a similar method and, using their code with the same geometry as used here, they found a maximum velocity of $6.84 \cdot 10^{-4}$ m/s, while Repetto et al. (2015) used a numerical method for a slightly different geometry and found a maximum velocity of $5.92 \cdot 10^{-4}$ m/s for $\Delta T = 3$ K, which are both close to the value derived analytically from (3.28). We therefore assume that (3.28) provides a sufficiently accurate estimate for our purposes. We compare the thermal flow and the steady streaming flow induced by eye rotations in figure 3.10, which show that the steady flow induced by eye rotations has the same order of magnitude for large saccades and REM. Thus the two flows both effectively contribute to mixing in the AC.

During the night, thermally driven flow becomes insignificant, and, aside from shape changes of the AC, the mechanisms driving flow are the REM and aqueous secretion. The maximum magnitude of the latter is $\approx 5.89 \cdot 10^{-5}$ m/s (Repetto et al., 2015) at the pupil and its average

velocity is $\approx 8 \cdot 10^{-6}$ m/s, which are both significantly smaller than the steady streaming flow found in the work. This provides confirming evidence for the hypothesis of Maurice (1998), which is that REM could promote mixing in the otherwise almost stagnant aqueous humour in order to maintain the nutrient supply to the cornea.

This work neglects any interactions between the flow induced by eye rotations and the other flow mechanisms in the AC. For small fluid velocities, due to linearity, the total flow may be approximated as the sum of the flow due to saccades, that due to secretion and drainage of the aqueous and the thermally driven flow. However, any flow due to shape deformations in the AC would be fully interactive with the other flows and would thus require a separate study.

To summarise, we find good agreement with previous numerical solutions and highlight characterestics of the flow that were not previously described. We show that the flow induced by eye rotations is a significant part of the aqueous humour dynamics and an important player in mixing processes. Finally, we remark that the model developed here could be useful for other applications involving oscillating thin domains.

Part II

Fluid transport across the retinal pigment epithelium

"Make a model as simple as possible, but not simpler."

CHAPTER 4

OVERVIEW AND RELEVANCE OF WATER TRANSPORT MECHANISMS IN THE RETINAL PIGMENT EPITHELIUM

4.1 Introduction

The retina is a light-sensitive tissue approximately 0.5 mm thick, which is located in the posterior part of the eye between the vitreous chamber and the choroid (Kolb, 2011). It consists of several cell layers which are classified as (from the inner to the outer) ganglion cell layer, inner plexiform layer, inner nuclear layer, outer plexiform layer, outer nuclear layer, photoreceptors and pigment epithelium (RPE). The RPE separates the photoreceptors from Bruch's membrane and the choroidal blood supply (Sharma and Ehinger, 2003), see figure 4.1. The RPE is a monolayer of cuboidal epithelial cells, arranged as hexagonal tiles approximately 14 μm in diameter in the central retina. The epithelial cells are bound together by junctional complexes with tight junctions, that separate the extracellular regions into apical and basolateral (Sharma and Ehinger, 2003). The basal side of the RPE faces Bruch's membrane, which is elastic and approximately 2 μm thick. The apical membrane borders the subretinal space, the extracellular space surrounding the photoreceptor cells (La Cour, 2003). This membrane forms long microvilli (5-7 μm long), that interdigitate the rod outer segments. The main functions of the RPE include creating a barrier between the choroid and retina, phagocytosing shed photoreceptor outer segments and transporting water, ions and metabolites between the retina and the choroid (Sharma and Ehinger, 2003). In particular, a fundamental role of the RPE is the removal of excess fluid and CO_2 (carbon dioxide) from the subretinal space (La Cour, 2003).

The RPE transports ions, the largest concentrations of which are Na^+(sodium), K^+(potassium), Cl^- (chloride) and HCO_3^- (bicarbonate). The transepithelial transport of these ions has been studied *in vitro* in various species and the mechanisms for this transport have been quantitatively

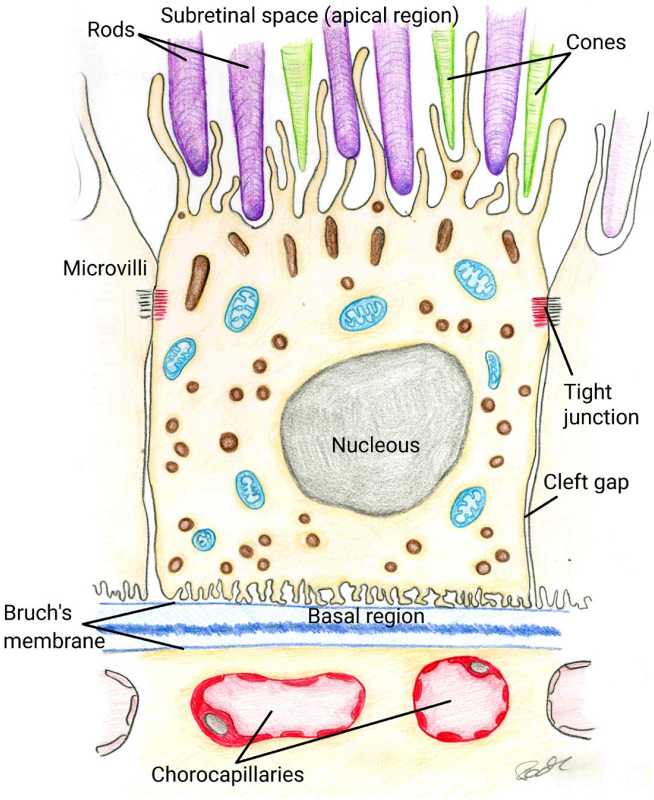

Figure 4.1: Sketch of the RPE cell layer. Drawing by Prof. Federica Grillo.

identified (e.g. Gallemore et al., 1998; Dornonville de la Cour, 1993; Reichhart and Strauß, 2014). The route and mechanisms for the transepithelial water transport, on the other hand, are less well understood (Spring, 2010). The rate of transport has been estimated to range from 1.4 to 11 μl/cm^2/h and is hypothesised to follow a transcellular route, directed from the apical to basolateral side, based on the fact that the RPE is a tight epithelium (Strauss, 2011).

Under normal physiological conditions, fluid has to be pumped out of the subretinal space. This process regulates the normal retinal adhesion, helps recovery from retinal detachment, and acts as one of the pathways for fluid outflow from the eye (Gallemore et al., 1998). Failure of the fluid pump leads to accumulation of fluid in the subretinal space, which is closely associated with the formation and development of numerous pathological conditions, such as age-related macular degeneration, diabetic macular oedema and retinal detachment (Marmor, 1990). Hence, quantifying and classifying the mechanisms that drive fluid flow across the RPE is relevant to develop a predictive understanding of how fluid accumulation may be ameliorated, motivating the present work.

4.2 Mechanisms of fluid flow across a semipermeable membrane

The most common representation of the flow F across biological membranes that separate two compartments (like epithelium) is described by (1.1) in Chapter 1, which we recall here for convenience

$$F = L_p \left(\Delta p - \sigma_p \Delta \Pi_p - \sigma_s \Delta \Pi_s \right), \tag{4.1}$$

where L_p is the membrane hydrodynamic conductivity, p denotes the mechanical pressure, Π_p the oncotic pressure and Π_s the osmotic one. The operator Δ denotes the difference between the value of the quantity it is applied to in different compartments. Finally, σ_p and σ_s are the reflection coefficients for proteins and low-molecular components, respectively.

An oncotic pressure difference can arise if the cell layer is impermeable to large proteins than can, therefore, be present at different concentrations on the two sides of the layer.

The osmotic flux described in equation (4.1), on the other hand, is due to active ion transport across the cell layer. Many well documented examples are present in the literature, see for instance Weinstein and Stephenson (1979) for transport the Necturus gallbladder, Krahn and Weinstein (1996) in the proximal tubules. The typical picture is that 'water follows the ions', i.e. water motion occurs in the main direction of ion transport. We note that this is not a 'passive flow' in the sense that it requires energy expenditure for the 'active' ion transport.

In the context of epithelial transport, the model described by equation (4.1) represents a cell layer as a membrane with zero thickness and considers the difference in quantities between the two sides of it (the apical and basal side). While for the epithelia that have an evidence of the establishment of difference in osmolarity, oncotic pressure difference and/or mechanical pressure difference, the model (4.1) might be a good choice (e.g. ciliary processes, Lyubimov et al., 2007), this is not the case for the RPE, for reasons that are detailed in the following.

To determine the relative contributions of the above mechanisms to fluid absorption in the RPE Negi and Marmor (1986) injected balanced saline solution into the subretinal space in vivo (in rabbit). Under physiological conditions, the solution was absorbed at a rate of 12 μl/cm^2/hr. Modifying the solution to a non-ionic isotonic solution this rate was reduced down to 3 μl/cm^2/hr and for the solution with a metabolic inhibitor, down to 4 μl/cm^2/hr with, suggesting that about 70% of the absorption depends upon active ion transport, the osmotic component in (4.1), and the other two factors might contribute only by 30%.

Let us now consider the three mechanisms accounted for in (4.1), separately, starting from the mechanical pressure difference. Mechanical pressure difference between the IOP and choroid is established due to outflow of fluid from the vitreous chamber into the retina. This pressure difference, however, has been experimentally estimated to be about 1-4 mmHg (in cynomolgus monkey and cat, Emi et al., 1989; Van Alphen and Robinette, 1961), which is a relatively small

value compared to the possible osmotic effects. In fact, a difference of osmolarity 1 mOsm across the epithelia would cause an osmotic pressure of about 19 mmHg, which is significantly higher than the estimated mechanical pressure drop. Therefore, mechanical pressure gives a very small contribution to transepithelial water transport.

To our knowledge no data on the oncotic composition of the fluid in the subretinal and choroidal spaces are available, but, as mentioned above, oncotic pressure difference accounts only for a small fraction of the total water flux.

Finally, there is evidence that RPE transports ions and fluid isotonically, i.e. without significant difference in ion concentrations from the apical to basal sides (as shown in the frog Hughes et al., 1984; Edelman et al., 1994; Hamann, 2002). This means the difference in osmolarity between the apical and basal regions cannot be the main driver of transepithelial water flux, and, consequently, there should be other mechanisms not accounted for in (4.1) that maintain fluid transport and occur at the cellular level. In what follows we will describe two of the possible mechanisms.

4.3 Standing gradient osmotic flow

A possible refinement of the model described by equation (4.1) consists in accounting for 'local osmotic flow'. Such flow occurs when there is a localised buildup of osmolarity in a certain region, maintained by active mechanisms, which drives fluid towards that region.

Many works in the field of water transport across epithelial and endothelial layers have shown that, in particular, the cleft gap between adjacent cells can play a significant role. The underlying physical mechanism was first very clearly explained by Diamond and Bossert (1967), who proposed a mathematical model of what is known as standing gradient osmotic flow (or local osmosis). The idea behind this mechanism is explained in figure 4.2, where cells are schematised as grey rectangles separated by a gap (the cleft gap). On one side we have a tight junction and on the other the cleft opens into the basal region. Ions are actively pumped into the cleft owing to the presence of Na/K-ATPase on cell membranes that governs active ion transport across the epithelia. This creates an excess ion concentration in the cleft, which drives water flux from the cell into the cleft. Ions in turn are transported along the cleft to the choroid by advection and electrodiffusion. This effectively couples fluid and ion transport. The model by Diamond and Bossert (1967) considered the coupling of osmolarity of a generic solute that is supported by active pumping in the cleft with the transport of solvent. The authors took advantage of the slender shape of the cleft to reduce the governing system of PDEs to a set of ODEs and solved them numerically.

This work has been extended by Weinstein and Stephenson (1979), who accounted for the transport of three ions: Na^+, K^+ and Cl^- in the Necturus gallbladder and considered the presence of ion channels and transporters in cell membranes. The authors also considered the coupling

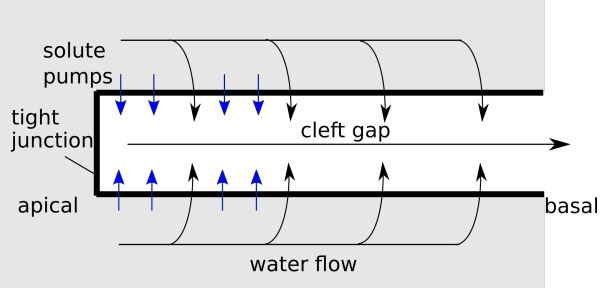

Figure 4.2: Diagram of the standing gradient system. Blue arrows indicate ion fluxes and black arrows water motion.

between the cell and the cleft and solved a one-dimensional problem for these two compartments numerically. Since then, many authors have used modelling to investigate the role of local osmosis as a possible transport mechanism for various epithelia (see e.g. Weinstein and Stephenson, 1981; Krahn and Weinstein, 1996; Avtar et al., 2008).

The validity of the theory of standing gradient osmotic flow, however, has been criticised by Shachar-Hill and Hill (2002) and Hill (2008), mainly because the models use 'questionable' geometrical parameters and membrane hydrodynamic permeabilities, which are governed by the presence of aquaporins (AQPs). In particular, it has been shown that knockout of AQPs in different epithelia in mice results in a decrease of osmotic permeability, for example by a factor of between $0.11-0.22$ for the murine proximal tubule, with about a 50% decrease in water transport Hill et al. (2004). This observation suggests that local osmosis may not be the only mechanism responsible for active fluid transport and other mechanisms have to be considered.

4.4 Electroosmosis

Another possible mechanism, which has been extensively studied recently in other cell layers, particularly in the corneal endothelium, is electroosmosis (Sanchez et al., 2016; Fischbarg, 2003; Sanchez et al., 2002). Electroosmosis occurs due to the interaction of an electric field with non-zero net charge located in the thin layer next to the cell wall, the Debye layer, which results in a Coulomb body force acting on the fluid (Probstein, 2005).

To understand this better, let us consider an electrolyte solution, containing positive and negative ions (e.g. NaCl dissolved in water) in a thin channel with charged walls (e.g. cell membrane). The negatively charged wall attracts positively charged ions in the solution, which leads to the formation of a thin layer with non-zero net charge density called electric double layer (EDL) or Debye layer (see figure 4.3). The thickness of the EDL is determined by a balance between the intensity of thermal (Brownian) fluctuations and the strength of the electrostatic attraction to the wall and is called the Debye length (typically 1-100 nm). As a result, the EDL is a capacitor itself, which has a small voltage jump ζ across it, the zeta potential (typically 0.01 -

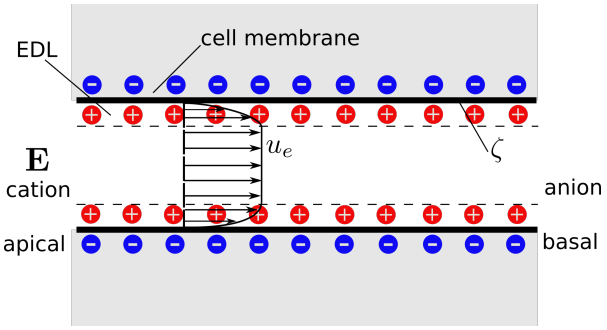

Figure 4.3: Sketch of uniform electroosmotic flow with Helmholtz-Smoluchowski velocity.

0.1 V), defined as the potential of the surface minus the potential just outside the EDL (Squires and Bazant, 2004).

In the presence of an external electric field $\mathbf{E}$, with magnitude E, the fluid in this charged Debye layer acquires a momentum, which is then transmitted to adjacent fluid layers through the effect of viscosity. If the fluid phase is mobile (such as in a narrow capillary or a gap between two cells), it would cause the fluid to flow. Thus phenomenon is called electroosmosis (Ghosal, 2004).

In the limit of thin Debye layer, one may use the velocity in the Debye layer as a boundary condition for the flow in the bulk of the domain (the slip velocity). The classical example is the uniform flow (plug flow) with Helmholtz-Smoluchowski slip velocity. This is a solution of the simplified problem in a channel with uniformly charged walls and the same pressure at the inlet and outlet. In this case, when an electric field of magnitude E is applied along the channel, the flow that is generated is uniform throughout the cross-section of the channel except for a very thin EDL near the wall where the flow velocity rapidly decreases from its free stream value to zero at the boundary (because of no-slip condition there, see figure 4.3). The velocity at the outer boundary of the Debye layer can be seen as a slip velocity (Helmholtz-Smoluchowski slip velocity) for the flow in the bulk and it takes the expression

$$u_e = -\frac{\epsilon E \zeta}{\mu}, \tag{4.2}$$

where u_e is stream-wise fluid velocity, ϵ is dielectric constant of the solution and μ is fluid viscosity (Probstein, 2005).

In the context of RPE, the transepithelial electrical potential (TEP) has been measured to be around 5-15 mV (apical positive Reichhart and Strauß, 2014), which indicates the possibility that the electric field, interacting with spatial charge density in the EDLs, drives an electroosmotic flow. To evaluate the prospect of electroosmotic contributions to water transport in the RPE, and epithelia more generally, a model of ion transport is required that can encompass both osmolarities and the possible generation of electric fields. Moreover, one needs to refine Debye layers to quantify the distribution of spatial charges there.

4.5 Content of this part of the thesis

In Part II of this thesis we propose an integrated mathematical model based on electrodiffusion that captures both ion and fluid transport in the RPE, together with their coupling. In Chapter 5 we develop the first generation model, which considers the presence of three different species: Na^+, K^+ and Cl^-. We quantify transport of these species across the epithelial layer. The model is applied to study the relative importance of osmosis and electroosmosis for water flow across the RPE. In Chapter 6 we refine the model to account for HCO_3^-, CO_2, H_2CO_3 and H^+, their transport and chemical reactions. Such refinement gives better representation of the physiology of the system and allows us to couple water and CO_2 transport.

CHAPTER 5

MATHEMATICAL MODEL OF FLUID TRANSPORT ACROSS THE RETINAL PIGMENT EPITHELIUM

This chapter is based on the publication by Dvoriashyna et al. (2018)

5.1 Introduction

In this chapter we propose a mathematical model to study fluid transport across the RPE. We consider osmosis and electroosmosis as possible mechanisms and study their relative importance. The model considers the presence of three different species: Na^+, K^+ and Cl^-. Transport and concentration of such species governs osmotic flow. Electroosmosis is driven by interaction of the electric field with the nonzero spatial charge stored in Debye layers. In § 5.2 we present the mathematical formulation of the model. Based on separation of spatial scales, we use asymptotic expansions to reduce the model. The choice of model parameters is described in the § 5.3, the results of the model are reported in § 5.4 and the discussion and conclusions of the work are presented in § 5.5.

5.2 Methods

5.2.1 Model setup

We model the RPE cell layer as a two-dimensional row of rectangles with length L and width H as in figure 5.1, separated by a distance $2h$, which constitutes the cleft gap. As schematically shown in figure 4.1, the apical membrane of the cells is highly folded, having a surface area approximately 30 times larger than the basolateral one in amphibians (Miller et al., 1978) and 10 times in mammals (Adijanto et al., 2009). We neglect this folding in the geometrical domain,

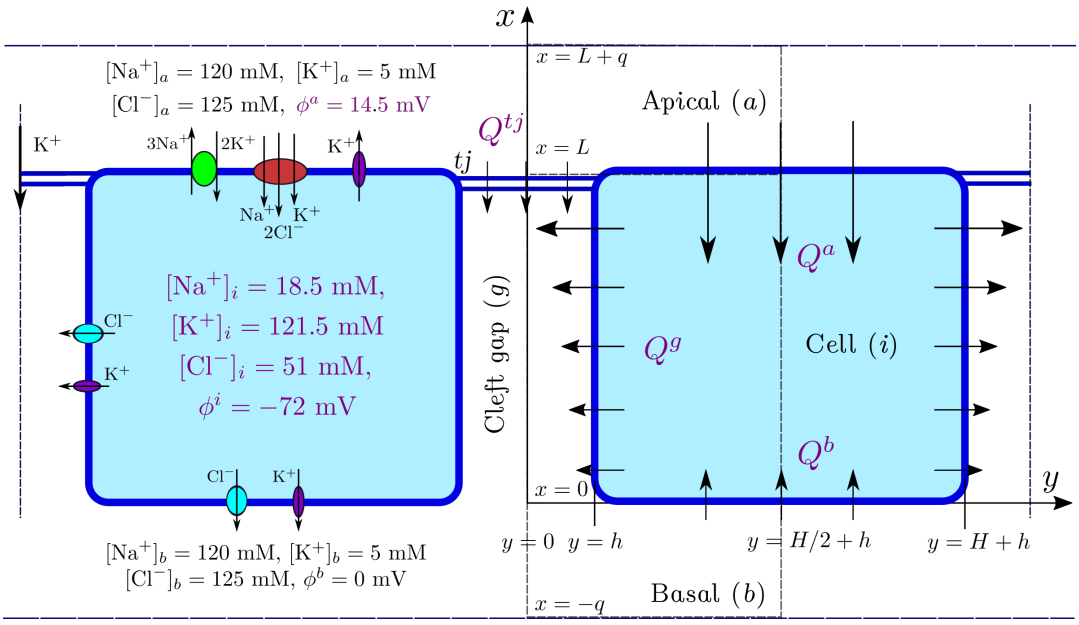

Figure 5.1: Sketch of the idealised geometry of the RPE. Cells have height L, width H and the thickness of the cleft gap is $2h$. Left panel: transepithelial transport of ions considered in the model and ion concentrations. The apical membrane has Na^+/K^+-ATPases (depicted in green), K^+ channels (purple) and $Na^+/K^+/2Cl^-$ co-transporters (red). Cl^- (light blue) and K^+ (purple) channels are present in the basolateral membrane. The tight junction is permeable to K^+. The values of concentration and electrical potential in the cell and extracellular space are shown. The values computed from the model are $[Na^+]_i$, $[K^+]_i$, $[Cl^-]_i$, ϕ^i, ϕ^a (reported in purple) and other values are prescribed (in black). Right panel: the coordinate system used in the model and water fluxes directions. The dashed box represents the 'reference' frame. The arrows represent schematically the directions and magnitude of the fluid flow across the membranes. Q^s ($s \in \{a, b, g, tj\}$) denotes the flux through the membrane s. tj denotes the tight junction. The sketch is not to scale.

but consider its effect on the transport properties of the membrane via geometrical adjustments to permeability coefficients for water and ions.

In our model we consider four different regions: apical (or subretinal space) (a), intracellular space (i), the basal (or Bruch's membrane) (b) and the cleft gap between two cells (or paracellular space) (g) (see figure 5.1). Every extracellular region is separated from the cell by a membrane that we name according to the respective region (a, b, g). The apical region is separated from the cleft gap by a tight junction (tj), while the basal one is directly connected to the cleft gap.

We consider that RPE cells are located in a physiological solution of Na Cl and K Cl, which dissociate into Na^+, $K^+$and Cl^- ions. We neglect the presence of HCO_3^- and H^+, because Na^+, K^+ and Cl^- represent the major ion fluxes across the RPE (Miller and Edelman, 1990). The presence of these additional species will be accounted for in the extension of the model, presented in chapter 6. Thus, Cl^- is the only anion accounted for in the extracellular space. The cell however, has an anion gap due to the presence of large non-diffusible molecules, the concentration of which

a, b, g, i	values of s labelling apical, basal, cleft gap and intracellular regions respectively
n_k^s	concentration of ion k in region s (mM) such that $n_0^s = [Na^+]^s$, $n_1^s = [K^+]^s$ and $n_2^s = [Cl^-]^s$
X	concentration of non-diffusible anions in the cell (mM)
z_k	valence and charge ('+' or '-') of ion k
z_X	average valence of non-diffusible anions in the cell
ϕ^s	electrical potential in region s (V)
ρ^s	volume charge density in region s (C/m^3)
σ_0	surface charge density of the cell membrane (C/m^2)
$\mathbf{j}_k^s$	flux of ion k per unit area in region s (mol/m^2/s)
I_k^{sm}	electric current of ion k per unit area from region s to region m (A/m^2)
Q^s	water flux per unit area through the membrane s (m^2/s)
$\mathscr{P}$	flux through the membrane due to Na^+-K^+ATPase (mol/m^2/s)
$\mathscr{M}$	flux through the membrane due to NKCC co-transporter (mol/m^2/s)
$\mathscr{J}_k^{sm}$	diffusive flux of ion k from region s to region m (mol/m^2/s)
$\mathbf{u} = (u, v)$	fluid velocity field in the cleft gap (m/s)
p	fluid pressure in the cleft gap (Pa).

Table 5.1: A list of parameters and variables used in the model, together with their units.

we denote with X and the corresponding fixed negative charge with $X^i := z_X X$, where z_X is the mean valence of these molecules. We account for active and passive ion transport across the cell membranes. In particular, on the apical membrane we consider the presence of Na^+-K^+ATPases (active transport), the channels which co-transport Na^+, K^+ and two Cl^-(the NKCC channel) and K^+ channels (see figure 5.1). The basolateral membrane is assumed to have K^+ and Cl^- channels (Wimmers et al., 2007; Reichhart and Strauß, 2014). The tight junction is considered to be potassium selective (Peng et al., 2010). As possible mechanisms that drive water flow across the RPE we consider transcellular osmosis and electroosmosis along the cleft gap.

Throughout this part of the thesis we adopt the notation presented in table 5.1. Unless stated otherwise, we use superscripts to label regions and subscripts to label ions.

The modelling procedure is split into several steps. Although fluid and ion transport are fully coupled, we present the corresponding models individually and simplify them using asymptotic expansions. First we construct the model for ion transport, accounting for the spatial variability of the electrical field and species concentrations. Due to the possibility of electroosmosis, we also need to resolve the Debye layer at the cell membrane in the cleft gap and, in particular, predict its surface charge. We therefore develop a solution in the double layer, which is relevant for the fluid flow in the cleft. Then, we model the fluid flow in the cleft. Ion and fluid transport are fully coupled because of the appearance of an advective term in ion fluxes and also because osmotic water fluxes are based on jumps of ion concentration across the membranes.

Parameter	Value	Source
Geometry		
Length of the cell, L	10 μm	Marmor (1998)
Height of the cell, H	10 μm	Marmor (1998)
Width of the cleft, $2h$	20 nm	
Debye length, λ_D	1.8 nm	
Aspect ratio of the cleft, $\delta = h/L$	0.001	
Aspect ratio of the EDL, $\lambda = \lambda_D/L$	$1.8{\cdot}10^{-4}$	
Thermodynamics		
Ideal gas constant, R	8.314 J/K/mol	
Temperature, T	310 K	
Faraday constant, F	96485 C/mol	
Electric permittivity of fluid, ϵ	$73 \cdot 8.854 \cdot 10^{-12}$ F/m	Gavish and Promislow (2016)
Ion transport		
Diffusion coefficient (K^+ in water), D	$1.7{\cdot}10^{-9}$ m^2/s	Miller et al. (1978)
Electric capacitance of the cell membrane, C_m	10^{-2} F/m^2	Matthews (2009)
Area factor of apical membrane folding, A_f	10	Adijanto et al. (2009)
Average valence of fixed negative charge inside the cell, z_X	1.5	
Maximum flux through the Na/K pump, P	10^{-6} mol/m^2/s	McLaughlin and Mathias (1985)
Na/K/Cl co-transporter coefficient, M	$3{\cdot}10^{-6}$ mol/m^2/s	

Permeability of membrane s to ion k, P_k^s m/s

s	a	b	tj
Na^+	0	0	0
K^+	$5 \cdot 10^{-7}$	$1.5 \cdot 10^{-7}$	10^{-6}
Cl^-	0	$0.8 \cdot 10^{-8}$	0

Concentration of ion k in region s, n_k^s, mM

k	Na^+	K^+	Cl^-
a	120	5	125
b	120	5	125

Fluid dynamics		
Volume flow through the RPE, V	4-10 μl/hour/cm^2	Hughes et al. (1984), Shi et al. (2008)
Hydrodynamic permeability of the membrane, k_m	$1.28 \cdot 10^{-12}$ m/s/Pa	Mathias and Wang (2005)
Permeability of the tight junction, k_{tj}	$1.28 \cdot 10^{-10}$ m/s/Pa	
Dynamic viscosity, μ	$0.75 \cdot 10^{-3}$ Pa/s	water at 35°C

Table 5.2: Model reference parameters; please refer to the text for further details on their motivation.

5.2.2 Ion transport

Since we are interested in studying water transport across the RPE we do not need to consider transient variations of the ion concentrations and the electrical potential, induced for instance by

response to variations in light conditions, and look instead for steady-state solutions. The ion transport model in region s consists of the conservation of fluxes for each ion k (Nernst-Plank equations) and the Poisson equation for the electrical potential (Probstein, 2005)

$$\nabla \cdot \mathbf{j}_k^s = 0, \quad \mathbf{j}_k^s = -D_k \left(\nabla n_k^s + \frac{z_k F}{RT} n_k^s \nabla \phi^s \right) + \mathbf{u} n_k^s, \; k \in \{0,1,2\}, \tag{5.1a}$$

$$\nabla^2 \phi^s = -\frac{\rho^s}{\epsilon}, \quad \rho^s = F\left(\sum z_k n_k^s - X^s\right), \quad s \in \{a,b,i,g\}, \tag{5.1b}$$

where $X^i = X z_X > 0$ is a fixed negative charge in the cell and is assumed constant, and X^s is zero in all other regions ($s \neq i$). For simplicity, we assume that the diffusion coefficient D_k of all considered ions is the same, and is denoted as D below. All other variables and parameters are defined in table 5.1 and 5.2. It can be verified *a posteriori* that the Péclet number of the flow is typically small ($Pe \approx 0.04$) and thus it might be tempting to drop advection from ion transport (the term $\mathbf{u} n_k^s$ in (5.1a)). However, the Péclet number might be a slightly misleading estimate of the importance of advection over diffusion when the concentration drop is small with respect to the concentration itself, which is the case in this model, in particular for Na^+. Advective terms are found to play non-negligible role and are thus retained in the model.

5.2.2.1 The bulk

We assume that the solution in the bulk of each region is electroneutral, which implies

$$\sum_{k=0,1,2} z_k n_k^s = X^s, \; s \in \{a,b,i,g\}. \tag{5.2}$$

This does not need to hold within a few Debye lengths of the cell membranes, which have a lengthscale of nanometres (Weiss, 1996a,b). The use of (5.2) is justified by the observation that cellular systems will relax to electroneutrality in the bulk on a timescale of nanoseconds (Weiss, 1996a,b) and we neglect such fast dynamics.

Equation (5.1b) cannot be used together with the electroneutrality assumption (Probstein, 2005) as they are not independent. Instead, following the approach of Mori *et al.* (Mori and Peskin, 2009; Mori et al., 2007), given electroneutrality in the bulk of each region, we can weight the equations (5.1a) for ion k by z_k, sum them over the species and use (5.2) to obtain the following equation for the electrical potential

$$\nabla \cdot \left(\left[\sum_{k=0}^{2} n_k^s \right] \nabla \phi^s \right) = 0. \tag{5.3}$$

We finally eliminate chloride concentration n_2^s as a variable using (5.2). Therefore, in the bulk of every region we have three unknowns, n_0^s, n_1^s and ϕ^s, and the corresponding two second-order conservation equations (5.1a) (for $k = 0, 1$) and (5.3) for the electrical potential.

All the membranes and the tight junction are subject to membrane-type conditions. At the membrane between the generic regions s and m, we impose the conservation of ion fluxes for

each species k, which is implemented by imposing that the ion current I_k^{sm} on the s side of the membrane equals the flux of charge due to the movement of species k passing from s to m,

$$Fz_k\mathbf{n}^{sm}\cdot\mathbf{j}_k^s = I_k^{sm}, \tag{5.4}$$

where $\mathbf{n}^{sm}$ is the unit normal pointing from region s to region m. The current I_k^{sm} is prescribed to account for all passive and active flows of ion k due to channels and pumps on the corresponding membrane and it is a nonlinear function of concentrations and potential on both sides of the membrane. The choice of constitutive relations for these currents is described in § 5.2.2.2. Note that the above membrane conditions 'jump' across the Debye layers and involve only the values of the variables in the bulk.

Noting that Cl^- concentrations are no longer independent variables due to their elimination via electroneutrality (5.2), it is convenient to implement a summation over the species, giving a condition in the terms of the potential; in particular rather than the chloride boundary condition we use

$$\sum_k Fz_k\mathbf{n}^{sm}\cdot\mathbf{j}_k^s = \sum_k I_k^{sm}. \tag{5.5}$$

To close the system, we have Dirichlet and symmetry conditions at the outer boundaries of the domain

$$n_k^a(x=L+q) = N_k^a, \quad n_k^b(x=-q) = N_k^b,\ k\in\{0,1\}, \tag{5.6a}$$

$$\phi^b(x=-q) = 0, \tag{5.6b}$$

$$\partial\phi^s/\partial y = \partial n_k^s/\partial y = 0 \text{ at } y=0,\ y=h+H/2, \tag{5.6c}$$

where q is the thickness of the apical and the basal regions (see Figure 5.1) and N_k^a, N_k^b, $k\in\{0,1,2\}$ are the imposed ion concentrations at the top of the apical and the bottom of the basal regions, respectively. *In vivo* conditions are well described assuming that there is no electrical current across the RPE, which means that we can model the system as an open-circuit. Moreover, we wish to predict the value of TEP for comparing the model results with *in-vitro* experimental measurements. Also in the experiments, TEP is normally determined using open circuit conditions (Li et al., 2004). This can be achieved by imposing a Neumann condition of zero electrical current, which we set at the top of apical region, so that

$$\frac{\partial\phi^a}{\partial x} = 0, \qquad \text{at } x = L+q. \tag{5.6d}$$

At the boundary between the basal region and the cleft gap we impose continuity of variables and fluxes.

To summarise, in every region $s=a,b,i,g$ there are three equations, (5.1a) for $Na^+$and K^+ ($k=0,1$) and (5.3) for the electrical potential. Noting the geometry of figure 5.1 we have at every side of the membrane and at the tight junction membrane conditions (5.4) for $k=0,1$ and (5.5),

making 24 conditions in total. We also have 5 Dirichlet (5.6a)–(5.6b), one Neumann (5.6d) and 18 symmetry conditions (5.6c) at the outer boundaries of the domain and 6 conditions at the boundary between the basal region and the cleft gap. Therefore in total we have 54 conditions. However, the lower boundary of the apical region $x = L$ consists of the boundary with the tight junction for $0 \le y < h$ and with the cell for $h \le y \le H/2 + h$, and we can describe the conditions on the corresponding regions as a single y-dependent boundary condition at $x = L$. This merging allows us to reduce the number of effective boundary conditions to 51. The same argument is valid at the basal region for the boundary $x = 0$, reducing the number of boundary conditions to 48. In this way, we have a second order problem in four rectangles, having a single condition at each side of the rectangle, leading to a well defined system of 12 nonlinear coupled second order PDEs for 12 unknowns in the regions with four boundaries, and also 48 boundary conditions. The chloride concentration n_2^s is found from the electroneutrality condition (5.2).

5.2.2.2 Ion fluxes through cell membranes

In this section we describe the choice of constitutive relations for the currents across the cell membranes. We consider the components for the ion transport across the RPE as shown in figure 5.1 and discussed in § 5.2.1. Ion fluxes through the membranes take into account both active and passive currents. We model the diffusive fluxes through the k ion channel across the membrane from region s to region m with the Goldman-Hodgkin-Katz (GHK) flux equation (Keener and Sneyd, 2009)

$$\mathscr{J}_k^{sm} = z_k P_k^s \frac{F}{RT} V^{sm} \frac{n_k^s - n_k^m \exp\left(-\frac{z_k F V^{sm}}{RT}\right)}{1 - \exp\left(-\frac{z_k F V^{sm}}{RT}\right)}, \tag{5.7}$$

where $V^{sm} = \phi^s - \phi^m$ is the potential across membrane s; for the meaning and values of all constants please refer to table 5.2.

To model the Na^+/K^+-ATPase and $Na^+/K^+/2Cl^-$co-transporter fluxes through the apical membrane we use relations as in the work of Strieter et al. (1990). The flux from Na^+/K^+-ATPase is given by

$$\mathscr{P} = P \left(\frac{n_0^i}{K_{Na} + n_0^i}\right)^3 \left(\frac{n_1^a}{K_K + n_1^a}\right)^2, \tag{5.8}$$

where $K_{Na} = 0.2(1 + n_1^i/8.33)$ mM and $K_K = 0.1(1 + n_0^a/18.5)$ mM are apparent $Na^+$and K^+ dissociation constants (see Strieter et al., 1990) and P is the maximum flux through the pumps.

The model for NKCC co-transporter flux can be linked to free energy as described in Strieter et al. (1990). This approach has an advantage with respect to kinetic models, as the only parameter to estimate is the co-transporter coefficient M. The flux through NKCC channels has the following expression

$$\mathscr{M} = M \log \frac{n_0^i n_1^i (n_2^i)^2}{n_0^a n_1^a (n_2^a)^2}. \tag{5.9}$$

The fluxes through the membranes for every ion can therefore be rewritten as follows

$$J_0^{ia} = 3\mathscr{P} + \mathscr{M}, \qquad J_0^{ib} = 0, \tag{5.10a, b}$$

$$J_1^{ia} = \mathscr{J}_1^{ia} - 2\mathscr{P} + \mathscr{M}, \qquad J_1^{ib} = \mathscr{J}_1^{ib}, \tag{5.10c, d}$$

$$J_2^{ia} = 2\mathscr{M}, \qquad J_2^{ib} = \mathscr{J}_2^{ib}, \tag{5.10e, f}$$

where b denotes both basal and lateral membranes. The tight junction is modelled as a membrane which is permeable only to K^+ and the fluxes are modelled using the GHK model

$$J_1^{ag} = \mathscr{J}_1^{ag}. \tag{5.11}$$

Finally, the current of ion k at the membrane between the regions s and m is given by the expression $I_k^{sm} = z_k F J_k^{sm}$.

5.2.2.3 Model reduction

To simplify the system we take advantage of the fact that the cleft gap has a very small aspect ratio $\delta = h/L \approx 0.001$. This allows us to make some assumptions that are all verified *a posteriori* with a direct numerical solution in Comsol Multiphysics® 5.3a.

The first simplification of the system (5.1a), (5.3)–(5.6c) is to neglect all the spatial variations in the apical and basal regions. This is not obviously true in the vicinity of the tight junction in the apical region and the boundary with the cleft gap in the basal one. However, the numerical simulations in Comsol Multiphysics show that the relative deviations of concentrations and the potential in the apical and basal regions from the imposed values at $x = -q$ and $x = L + q$ are of the order of 1-2%. We, therefore, consider all the model variables in the apical and basal region to be uniform and equal to the values at the boundaries (5.6a), (5.6b) and impose the zero current condition at the apical membrane, so that it reads

$$\mathscr{P} + \mathscr{J}_1^{ia} + 2\delta \mathscr{J}_1^{ga} = 0. \tag{5.12}$$

Since water transport across the RPE is isotonic (Hamann, 2002) we assume that there is no concentration jump across the epithelium, and thus osmotic flux can occur only due to local osmosis through the cleft gap, implying that the lateral fluxes of water and ions have the same order of magnitude as the fluxes through the cell. This in turn means that the flux per unit area emerging from the cleft is $1/\delta$ times larger than the one supported by the cell. This implies that the spatial variability in the cell is negligible compared to the cleft (diffusion being strong enough to suppress ionic concentration gradients) and suggests that all intracellular variables can be considered as uniform and can be found by solving a spatially averaged problem. In fact, *a posteriori* estimates show that the potential and concentration changes in the cell have an order of magnitude of less than 1% of the corresponding average values. Following the above reasoning,

the flux balance (5.1a) for $Na^+$and K^+ and the equation for electrical potential (5.3) in the cell are simplified to a set of algebraic equations for the averaged quantities (see A.1 for the derivation)

$$3\mathscr{P} + \mathscr{M} = 0, \tag{5.13a}$$

$$\mathscr{J}_1^{ia} - 2\mathscr{P} + \mathscr{M} + \mathscr{J}_1^{ib} + \frac{2}{H}\int_0^L \mathscr{J}_1^{ig} dx = 0, \tag{5.13b}$$

$$\mathscr{P} + \mathscr{J}_1^{ia} + \mathscr{J}_1^{ib} - \mathscr{J}_2^{ib} + \frac{2}{H}\int_0^L \left(\mathscr{J}_1^{ig} - \mathscr{J}_2^{ig}\right) dx = 0. \tag{5.13c}$$

For the meaning of all other symbols and variables refer to Table 5.1 and 5.2. In summary, the flux balance equation (5.1a) for $Na^+$and K^+ and the equation for electrical potential (5.3) in the cell are simplified to a set of algebraic equations for the averaged quantities.

Taking advantage of the fact that the cleft is long and thin, the equations there can also be simplified by using an asymptotic expansion in terms of δ, which leads to a set of three coupled ODEs (derived in A.2)

$$D\left(\frac{d^2 n_0^g}{dx^2} + \frac{d}{dx}\left(\frac{F}{RT} n_0^g \frac{d\phi^g}{dx}\right)\right) - \left(q\frac{dn_0^g}{dx} - Q^g n_0^g\right) = 0, \tag{5.14a}$$

$$D\left(\frac{d^2 n_1^g}{dx^2} + \frac{d}{dx}\left(\frac{F}{RT} n_1^g \frac{d\phi^g}{dx}\right)\right) - \left(q\frac{dn_1^g}{dx} - Q^g n_1^g\right) + \mathscr{J}_1^{ig} = 0, \tag{5.14b}$$

$$2\frac{DF}{RT}\frac{d}{dx}\left(\left(n_0^g + n_1^g\right)\frac{d\phi^g}{dx}\right) + \mathscr{J}_1^{ig} - \mathscr{J}_2^{ig} = 0, \tag{5.14c}$$

where $q = \frac{1}{2h}\int_0^{2h} u\,dy$ is the depth-averaged velocity and Q^g is the water flux per unit surface area through the lateral membrane, defined in terms of osmotically driven and pressure driven fluxes, as specified in § 5.2.3. The equations governing the velocity field $\mathbf{u} = (u, v)$ are also described in § 5.2.3.

For boundary conditions at the tight junction ($x = L$) we impose the influx of K^+ with zero-flux for other ions

$$D\left(\frac{dn_0^g}{dx} + \frac{F}{RT} n_0^g \frac{d\phi^g}{dx}\right) - Q^{tj} n_0^g = 0, \tag{5.15a}$$

$$D\left(\frac{dn_1^g}{dx} + \frac{F}{RT} n_1^g \frac{d\phi^g}{dx}\right) - Q^{tj} n_1^g = \mathscr{J}_1^{ag}, \tag{5.15b}$$

$$\frac{2DF}{RT}(n_0^g + n_1^g)\frac{d\phi^g}{dx} = \mathscr{J}_1^{ag} \qquad \text{at } x = L, \tag{5.15c}$$

where Q^{tj} is the water flux per unit surface through the tight junction. At the border with the basal region ($x = 0$) we prescribe Dirichlet conditions, $n_k^g(x = 0) = N_k^b$, $k = 0, 1$ and $\phi^g(x = 0) = 0$. The Cl^- concentration can be found from the electroneutrality condition (5.2). For the definition and meaning of all the symbols please refer to Table 5.2.

We therefore have reduced the nonlinear coupled system (5.1a), (5.3)–(5.6d) to a system of algebraic equations (5.12)–(5.13) for the variables in the cell and TEP, coupled with three ODEs

(5.14) for Na^+, K^+ concentrations and the potential in the cleft gap. In the above set of equations the concentration of fixed negative charge X^i is unknown and is a surrogate for the unknown cell volume; to determine it we need to impose an additional equation, which comes from water balance and will be discussed in Section 5.2.4). This model of ion transport is the basis to model osmotic flow. However, more information is needed to model electroosmosis, as we need to resolve the Debye layers in the cleft gap.

5.2.2.4 The electrical double layer

In the electrical double layer (EDL), electroneutrality is not valid and the full system (5.1) in the gap ($s = g$) has to be solved. The boundary conditions (5.4) for the bulk variables are unchanged. However, we need an additional condition at the membrane for the electrical potential. This condition imposes that the component of the electrical field normal to the membrane equals the surface charge density over the dielectric permittivity

$$\frac{\partial \phi^{EDL}}{\partial y} = \frac{C_m(\phi^g - \phi^i) - \sigma_0}{\epsilon} \quad \text{at } y = h,\ x \in [0, L]. \tag{5.16}$$

In the above expression $C_m(\phi^g - \phi^i)$ is the Debye layer stored charge associated with capacitance and σ_0 is the wall charge. The former is related to the electrical potential difference between the bulk of the cell and cleft via the membrane capacitance per unit area, C_m, while the latter is the fixed charge due to the presence of charged membrane proteins.

At the boundary of the EDL and the bulk of the cleft we match the solution with the corresponding values in the bulk.

The model can be simplified due to the small aspect ratio between the electrical double layer and the cleft gap length, $\lambda = \lambda_D/L \approx 1.8 \cdot 10^{-4}$, using an asymptotic expansion in terms of λ; the analytical solution for the leading-order problem, in terms of the ion concentrations n_k^{EDL}, $k = 0, 1, 2$ and the potential ϕ^{EDL} in the EDL is derived in A.3. We note that at the leading order advection is subdominant in the EDL and is thus neglected. This solution allows us to estimate the value of the slip velocity for the electroosmotic flux in the cleft, as discussed in § A.3.

5.2.3 Water flow in the cleft gap

We finally investigate water flow in the cleft gap driven by electroosmosis, osmotic and mechanical pressure differences. The solution is constructed by using a boundary-layer theory, with the inner region corresponding to the EDL (similar to the works of Squires and Bazant (2004) and Yariv (2009)) and the outer one, the bulk of the cleft gap. The analysis requires separation of scales between the thickness of the cleft gap and the EDL, i.e. $\lambda/\delta \ll 1$. This ratio is 0.18, which, given that the quantities in the EDL decay exponentially (as in (A.28)), is sufficiently accurate for our objectives. Moreover, the error of this approximation is $(\lambda/\delta)^2 \approx 0.03$. Matching between the solutions in the two regions provides us with an expression for the slip velocity to be used later as a boundary condition in the outer problem.

In the inner region (the EDL), the presence of non-zero net charge density is accounted for in the context of fluid mechanics as a body force in the inertialess fluid momentum balance. Therefore the problem is governed by the following system

$$-\nabla p + \mu\nabla^2\mathbf{u} + \epsilon\left(\nabla^2\Phi\right)\nabla\Phi = 0, \tag{5.17a}$$

$$\nabla\cdot\mathbf{u} = 0, \tag{5.17b}$$

where $\mathbf{u} = (u, v)$ is fluid velocity, p is pressure and Φ is the potential in the cleft gap, obtained as a composite solution by matching the potential in the EDL and in the bulk.

The problem in the outer region (the bulk of the cleft gap, away from the cell membrane) is governed by the standard Stokes equations, i.e. (5.17a), (5.17b) without the body force term. The matching procedure is reported in A.4 and results in the following expression for the slip velocity at the boundary between the EDL and the bulk of the cleft:

$$u_{slip} = -\kappa\epsilon\frac{C_m(\phi^g - \phi^i) - \sigma_0}{\mu\sqrt{C(x)}}\frac{\partial\phi^g}{\partial x} - \kappa^2\epsilon C'(x)\frac{(C_m(\phi^g - \phi^i) - \sigma_0)^2}{8\mu C^2(x)}, \tag{5.18}$$

where $C(x) = \sum_{k=0}^{2} n_k^g$ and $\kappa = \sqrt{RT/\epsilon F^2}$. The first term of the above expression is analogous to the standard Helmholtz–Smoluchovsky slip velocity (Probstein, 2005) for variable electric field and zeta potential; the second term appears due to the fact that the concentrations in the bulk of the cleft are non-uniform.

We use this velocity as the slip boundary condition at the lateral walls to solve the problem for water flow in the bulk. We assume that hydrostatic pressure difference across the cell layer and across cell membranes (but not tight junctions) is negligible (Hamann, 2002). Thus, without loss of generality, we can set p equal to zero in the cell, apical and basal regions, and hence p measures the pressure relative to its value in these regions. We consider the presence of osmotic and pressure-driven fluxes through the tight junction Q^{tj} and lateral membranes Q^g, which are given by the following expressions

$$Q^g(x) = k_m\left[RT\left(\sum_{k=0}^{2}(n_k^i - n_k^g(x)) + X\right) + p(x)\right], \tag{5.19}$$

$$Q^{tj} = k_{tj}\left[RT\sum_{k=0}^{2}(n_k^a - n_k^g(L)) + p(L)\right], \tag{5.20}$$

where k_m and k_{tj} are the hydrodynamic permeabilities of the cell membrane and the tight junction respectively. Note that all reflection coefficients in this and following similar expressions are taken to be unity as is reported to be typical in the context of ion transport for animal cell homoeostasis (Weiss, 1996a). Equation (5.17) is, therefore, reduced using lubrication theory, to give the water velocity in the bulk as

$$u = \frac{1}{2\mu}\frac{\partial p}{\partial x}(y^2 - h^2) + u_{slip}, \quad -h \le y \le h, \quad 0 \le x \le L \tag{5.21}$$

(the trans-cleft coordinate y is illustrated in figure 5.1). The equation for the pressure is obtained by integrating the continuity equation, to give

$$-\frac{h^3}{3\mu}\frac{d^2p}{dx^2}+h\frac{du_{slip}}{dx}=-Q^g, \tag{5.22a}$$

subject to boundary conditions

$$p=0 \quad \text{at } x=0, \tag{5.22b}$$

$$-\frac{h^3}{3\mu}\frac{dp}{dx}+hu_{slip}=Q^{tj} \quad \text{at } x=L. \tag{5.22c}$$

Equation (5.22a) balances the gradient of fluid flux along the cleft with osmotic transport driven by pressure differences across the lateral walls. Finally, the y-component of the velocity v can be obtained from (5.17b). The derivation of the above expressions is reported in A.4.

5.2.4 Coupling between ion and fluid flow

We now have a model for ion and fluid transport. To couple the two we write the flux-balance equation in the cell as

$$\int_0^H Q^a\,dy+\int_0^H Q^b\,dy+2\int_0^L Q^g\,dx=0, \tag{5.23}$$

where the fluid fluxes Q^a, Q^b are defined as

$$Q^a=A_f k_m RT\left(\textstyle\sum_{k=0}^2(n_k^i-n_k^a)+X\right), \quad Q^b=k_m RT\left(\textstyle\sum_{k=0}^2(n_k^i-n_k^b)+X\right). \tag{5.24}$$

This balance is required for the volume of the cell to remain constant. It provides the additional equation needed to determine the concentration of large negatively charged molecules in the cell X, and in turn gives a feedback to ion concentrations and the potential through the electroneutrality condition (5.2). Moreover, the lateral flux Q^g in (5.23) depends on the mechanical pressure $p(x)$ that is governed by fluid flow in the cleft. This equation therefore provides an additional coupling between the fluid flow and ion transport.

5.2.5 Solution of the fully coupled problem

We proceed to summarise how ion and fluid dynamics are coupled in our model and how the solution, including the water balance constraint, is obtained. The system of equations in dimensional

form is the following

Ion transport in the cell

(5.25a) $$3\mathscr{P} + \mathscr{M} = 0,$$

(5.25b) $$\mathscr{J}_1^{ia} - 2\mathscr{P} + \mathscr{M} + \mathscr{J}_1^{ib} + \frac{2}{H}\int_0^L \mathscr{J}_1^{ig} dx = 0,$$

(5.25c) $$\mathscr{P} + \mathscr{J}_1^{ia} + \mathscr{J}_1^{ib} - \mathscr{J}_2^{ib} + \frac{2}{H}\int_0^L \left(\mathscr{J}_1^{ig} - \mathscr{J}_2^{ig}\right) dx = 0;$$

Open circuit condition

(5.25d) $$\mathscr{P} + \mathscr{J}_1^{ia} + 2\delta\mathscr{J}_1^{ga} = 0,$$

Ion transport in the cleft

(5.25e) $$D\left(\frac{d^2 n_0^g}{dx^2} + \frac{d}{dx}\left(\frac{F}{RT} n_0^g \frac{d\phi^g}{dx}\right)\right) - \left(\left[-\frac{h^2}{3\mu}\frac{dp}{dx} + u_{slip}\right]\frac{dn_0^g}{dx} - Q^g n_0^g\right) = 0,$$

(5.25f) $$D\left(\frac{d^2 n_1^g}{dx^2} + \frac{d}{dx}\left(\frac{F}{RT} n_1^g \frac{d\phi^g}{dx}\right)\right) - \left(\left[-\frac{h^2}{3\mu}\frac{dp}{dx} + u_{slip}\right]\frac{dn_1^g}{dx} - Q^g n_1^g\right) + \mathscr{J}_1^{ig} = 0,$$

(5.25g) $$2\frac{DF}{RT}\frac{d}{dx}\left(\left(n_0^g + n_1^g\right)\frac{d\phi^g}{dx}\right) + \mathscr{J}_1^{ig} - \mathscr{J}_2^{ig} = 0;$$

Fluid transport in the cleft

(5.25h) $$-\frac{h^3}{3\mu}\frac{d^2 p}{dx^2} + h\frac{du_{slip}}{dx} = -Q^g,$$

(5.25i) $$u_{slip} = -\kappa\epsilon\frac{C_m(\phi^g - \phi^i) - \sigma_0}{\mu\sqrt{C(x)}}\frac{\partial\phi^g}{\partial x} - \kappa^2\epsilon C'(x)\frac{(C_m(\phi^g - \phi^i) - \sigma_0)^2}{8\mu C^2(x)};$$

Water balance

(5.25j) $$Q^a + Q^b + \frac{2}{H}\int_0^L Q^g \, dx = 0,$$

where $C(x) = n_0^g + n_1^g + n_2^g$ and in the last equation we used spatially uniformity of the variables. Equations (5.25a)–(5.25d) and (5.25d) are algebraic equations. All constitutive equations for fluxes of water and ions are reported in table 5.3. The ODEs in the cleft (5.25e)– (5.25g), are accompanied by the corresponding boundary conditions

(5.26a-d) $$n_0^g = N_0^b, \qquad n_1^g = N_1^b, \qquad \phi^g = 0, \qquad p = 0 \qquad \text{at } x = 0;$$

(5.26e, f) $$D\left(\frac{dn_0^g}{dx} + \frac{F}{RT} n_0^g \frac{d\phi^g}{dx}\right) - Q^{tj} n_0^g = 0, \qquad D\left(\frac{dn_1^g}{dx} + \frac{F}{RT} n_1^g \frac{d\phi^g}{dx}\right) - Q^{tj} n_1^g = \mathscr{J}_1^{ag},$$

(5.26g, h) $$\frac{2DF}{RT}(n_0^g + n_1^g)\frac{d\phi^g}{dx} = \mathscr{J}_1^{ag}, \qquad -\frac{h^3}{3\mu}\frac{dp}{dx} + hu_{slip} = Q^{tj} \qquad \text{at } x = L.$$

The first step of the model is to solve the problem for ion transport in the cell with open circuit numerically (5.25a)–(5.25d), imposing an initial value of X, to obtain values for TEP, ϕ^i, n_0^i and n_1^i. These quantities appear in boundary conditions for the problem in the cleft and, therefore, also in equations (5.25e)–(5.25g). Resolving the double layer is essential to obtain the expression

Flux	Expression
Ion k from region s to region m	$\mathscr{J}_k^{sm} = z_k P_k^s \frac{F}{RT} V^{sm} \frac{n_k^s - n_k^m \exp\left(-\frac{z_k F V^{sm}}{RT}\right)}{1-\exp\left(-\frac{z_k F V^{sm}}{RT}\right)}$
Na^+/K^+pump	$\mathscr{P} = P\left(\frac{n_0^i}{K_{Na}+n_0^i}\right)^3\left(\frac{n_1^a}{K_K+n_1^a}\right)^2$
$Na^+/K^+/Cl^-$ co-transporter	$\mathscr{M} = M \log \frac{n_0^i n_1^i (n_2^i)^2}{n_0^a n_1^a (n_2^a)^2}$
Water flux through cell membrane s	$Q^s = k_m^s \left[RT\left(\sum_{k=0}^2 (n_k^i - n_k^s) + X\right) - (p^i - p^s)\right]$
Water flux through tight junction	$Q^{tj} = k_{tj}\left[RT\sum_{k=0}^2 (n_k^a - n_k^g(L)) + p(L)\right]$

Table 5.3: Constitutive relations for water and ions adapted throughout the model. For the meaning of the symbols please refer to table 5.2. Here in the expressions for water fluxes, $k_m^s = k_m$ for $s = b, g$, $k_m^a = A_f k_m$ and $p^a = p^b = p^i = 0$.

for the slip velocity (5.25i), which appears in the problem for the fluid in the cleft (5.25h). The slip velocity depends on the bulk concentrations and the potential in the cleft gap. The problem for ion transport in the cleft (5.25e)–(5.25g) is thus coupled with fluid transport (5.25h) via advection, osmotic water fluxes and the slip velocity. They are solved numerically together to obtain the concentration profiles $n_k^g(x)$, $k = 0, 1$, the potential $\phi^g(x)$ in the bulk of the cleft, fluid velocity $\mathbf{u}(x, y)$ and pressure $p(x)$.

The last step of the solution is to enforce water flux balance in the cell, which is given by equation (5.25j). This condition is satisfied by recalculating the value of X and setting up an iterative procedure with respect to X, until water balance is enforced with the required precision. This is implemented by the following steps:

1. For a given value of X, denoted X_{prior}, we solve the spatially-averaged problem for ion transport (5.25a)–(5.25d) for the unknowns TEP, ϕ^i, n_0^i and n_1^i in the cell.

2. We solve the problem for fluid and ion transport in the bulk of the cleft (5.25e)–(5.25g), (5.25h) to find the distributions of potential ϕ^g, concentrations n_0^g and n_1^g, fluid pressure p and velocity $\mathbf{u}$, using the expression for the slip velocity (5.25i).

3. We find the fluxes Q^s, $s \in \{a, b, g, tj\}$ and use (5.25j) to solve for the iteration update of X, that is X_{update}.

4. We go to step 1 with the updated value of X, now resetting $X_{prior} = X_{update}$, for the next iteration until the condition (5.25j) is satisfied with X_{prior} for a desired tolerance.

This solution procedure was implemented in Matlab to obtain all the results reported in §5.4. We have also verified the stability of the solution by keeping time derivatives in the governing equations and integrating them in time.

5.3 Choice of the parameter values

The choice of parameters is very challenging due to the lack of clinical measurements on human RPE. Some data on ion fluxes and membrane permeabilities have been reported for other species, such as frog and cow, but to our knowledge, no such measurements are available for humans. We thus were forced to make assumptions on some of the parameter values. As a general rule, we tried to use data from the literature whenever possible and attempted to reproduce with the model concentrations of the various species and TEP close to measured values. Since the model is a simplification of the real system and not all ingredients are considered, the values of some parameters we use might need adjustment in more refined models. The list of reference parameters used in the model is reported in table 5.2 and their choice is discussed below.

5.3.1 Geometry

We consider the RPE as a monolayer of rectangular cells with thickness H and length L. The typical RPE length varies from 10 to 60 μm (Marmor, 1998), with the lower value at the macula. The diameter of the RPE cells is ≈ 14 μm (Sharma and Ehinger, 2003). In our model we consider $L = H = 10$ μm. The reference width of the cleft gap h is fixed to be 20 nm. The apical membrane of the RPE cell has long microvilli (Sharma and Ehinger, 2003), and the folding factor A_f was estimated by Adijanto et al. (2009) in human cells to have the value of 10, based on CO_2 transport. We therefore set $A_f = 10$.

5.3.2 Ion transport

We consider the RPE to be in a bath of 120 mM NaCl and 5 mM KCl solution, giving a total osmolarity of 250 mM. Therefore, ion concentrations in the apical and basal regions are $N_0^s =$ 120 mM, $N_1^s = 5$ mM and $N_2^s = 125$ mM, $s \in \{a, b\}$. In our model we neglect the presence of HCO_3^- and all the active and passive transport associated with it, such as the Na^+-HCO_3^- co-transporter and HCO_3^--Cl^- exchanger in the basolateral one. Since we do not consider passive transport of Na^+ across membranes and of Cl^- across the apical membrane, the corresponding permeabilities are set to be zero, $P_0^a = P_0^b = P_2^a = 0$.

K^+ channels in the apical membrane were studied by Kusaka et al. (2001) in the rat RPE, who found the ratio between conductance and cell capacitance to be $g_1^a/C_m \approx 0.14$ nS/pF, from which we can compute, using the value of C_m reported in table 5.2, $g_1^a \approx 1.4$ S/m^2. Using linear expression for the current, one would write $I_1^{ai} = g_1^a\left(\phi^a - \phi^i + RT/F \ln(n_1^a/n_1^i)\right)$. However, we use the GHK model for the current (5.7) and estimate the order of magnitude of membrane permeability P_1^a, we match the two expressions for the following values of potential and concentrations: $n_1^i = 120$ mM, $\phi^i = -75$ mV and $\phi^a = 15$ mV, and obtain $2.5 \cdot 10^{-8}$ m/s. To account for apical membrane folding this value has to be multiplied by 10. In the following we use $P_1^a \approx 5 \cdot 10^{-7}$ m/s. In our framework,

increasing this permeability does not cause significant change of ion concentrations in the cell, but results in a depolarization of the apical membrane, thus decreasing TEP.

The basolateral membrane permeability to Cl^-, P_2^b, is controlled by the presence of Cl^- channels Reichhart and Strauß (2014). The conductance of this membrane was estimated in the frog RPE by La Cour (1992) to be ≈ 5.9 S/m^2. The value refers to the whole epithelium rather than the membrane itself, and thus the presence of lateral membranes is incorporated into this value, which leads to an estimate of the permeability $\approx 2.7 \cdot 10^{-8}$ m/s via similar calculation as for P_1^a with $n_2^i = 50$ mM. Increasing P_2^b results in depolarisation of basolateral membrane, elevation of n_0^i, decrease of n_1^i and n_2^i and the increase of water flux. To ensure the TEP is within the range of observed values (Reichhart and Strauß, 2014) we have fixed $P_2^b = 0.8 \cdot 10^{-8}$ m/s. For same reasons, the basolateral permeability to K^+, P_1^b, was fixed to be $P_1^b = 1.5 \cdot 10^{-7}$ m/s. Increasing permeability P_1^b results in polarisation of the basolateral membrane and decrease of TEP.

We consider tight junctions to be permeable to K^+, based on the observations of Peng et al. (2010). The value of this permeability P^{tj} is unknown, we therefore investigate the effect of variation of this parameter in the §5.4 (see figures 5.3, 5.5(a)) and take the reference value for the permeability to be $P^{tj} = 10^{-6}$ m/s.

The order of magnitude for the amplitude of the Na^+-K^+ pump, P, has been chosen based on the work of McLaughlin and Mathias (1985), where they estimated the current from Na^+-K^+ATPase to be 10 μA/cm^2. We fix the maximum value of the pump to correspond to this current, $P \approx 10^{-6}$ mol/m^2/s. Increasing the pump rate results in the elevation of TEP and the increase of water flux across the RPE.

In equation (5.9), the co-transporter coefficient, M, is assumed to be triple that of the pump, $M = P \cdot 3 \approx 3 \cdot 10^{-6}$ mol/m^2/s to obtain a Cl^- concentration in cell in the range of observed values in frog and bovine RPE (Fujii et al., 1992; Bialek and Miller, 1994). Increasing M results in depolarisation of the basolateral membrane.

The average valence of negatively charged large molecules in the cell, z_X, differs among cells and species. Lew et al. (1979) calculated it to be 1.85 with parameters from amphibian skin and urinary bladder. In this work we fix $z_X = 1.5$.

Finally, for the solution in the EDL we need to fix the surface charge due to proteins, σ_0. We fix it to correspond to a zeta potential of -10 mV, which is in the range of standard values for the cell membrane (Rubashkin et al., 2006).

5.3.3 Fluid dynamics

We consider intracellular and extracellular fluid to have the properties of water. The electric permittivity ϵ is used for 250 mM NaCl solution at 35°C (Gavish and Promislow, 2016). Water is transported across the cell membrane through a lipid bilayer, which has low permeability, and water channels, aquaporins AQP1 (and other AQPs Stamer et al., 2003; Juuti-Uusitalo et al., 2013), that elevate the hydrodynamic permeability. In fact, for some epithelia, the water

velocity scale across the membrane can be elevated from 10^{-4} cm/s to 10^{-2} cm/s by aquaporins (Hill, 2008). In our model we consider the reference value for membrane permeability to be $k_m = 1.28 \cdot 10^{-12}$ m/s/Pa (Mathias and Wang, 2005) and study the dependence of fluxes on its variation in figure 5.6.

The hydrodynamic permeability of the tight junction is chosen to be 100 times that of the reference value for the membrane permeability, k_m, so that $k_{tj} = 1.28 \cdot 10^{-10}$ m/s/Pa. The variation of this parameter is also shown in figure 5.6.

5.4 Results

Throughout this section we use, as baseline, the parameter values reported in table 5.2, unless otherwise specified. As discussed in §5.2, the concentration of all species in the cell are assumed to be spatially uniform. The values predicted by the ion transport model (5.13) are shown in figure 5.1 (left panel) in purple. The values of the concentrations in the apical and the basal regions N_k^s, $k = 0,1,2,\ s \in \{a,b\}$ are prescribed and are reported in the figure in black. The concentrations predicted for Na^+, $K^+$and $Cl^-$are $n_0^i = 18.5$ mM, $n_1^i = 121.5$ mM and $n_2^i = 51$ mM, respectively. All calculated values are close to those observed in the RPE (Adijanto et al., 2009; Reichhart and Strauß, 2014; Strauss, 2011). The existing measurements of Cl^- concentration provide values varying in a relatively wide range, from 62 mM in the bovine RPE (Bialek and Miller, 1994) to approximately 20 mM in the toad and chick RPE (Fujii et al., 1992; Gallemore and Steinberg, 1989). We note that the Cl^- values reported are high compared to the other mammalian cell types.

In figure 5.1 we also report the predicted values of the potential in all regions. The potential is, without loss of generality, imposed in the basal region (reported in black) and computed in the interior of the cell and the apical region. The transepithelial potential $TEP = \phi^a - \phi^b$ is positive and equal to ≈ 14.6 mV, which is within the range of values observed in different species, from 2.2 mV to 15 mV (Reichhart and Strauß, 2014; Frambach et al., 1989; Quinn and Miller, 1992).

The fluxes of K^+ and Cl^- are about $2.96 \cdot 10^{-6}$ mol/m^2/s. There is no net Na^+ transport, since we do not consider the Na^+- HCO_3^- co-transporter in the basolateral membrane (Hamann, 2002). The value of Cl^- flux predicted by our model is larger than the one measured by La Cour (1992) in the frog RPE, which was $\approx 2 \cdot 10^{-6}$ mol/m^2/s, but has the same order of magnitude.

Ion fluxes occur from the cell both to the basal region and the cleft gap. The flux through the lateral wall has to be balanced by a flux along the cleft, which is supported by ion concentration and electrical potential gradients. In figure 5.2(a) we plot the departure of the concentration of all species from their basal values along the cleft. K^+ and Cl^- concentrations increase towards the tight junction. The Na^+ concentration, on the other hand, decreases and, since lateral membranes are impermeable to it, its behaviour is governed by electroneutrality. The variation of concentration has the same order of magnitude for all species. The potential along the cleft gap is

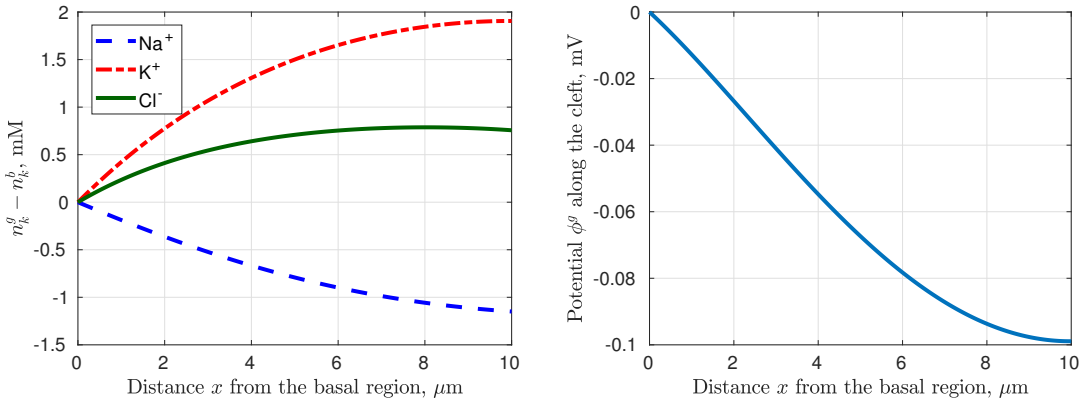

(a) (b)

Figure 5.2: (a) Deviation of the ion concentrations along the cleft from those in the basal region. The x - axis goes along the symmetry midline ($y = 0$) of the cleft from the basal region to the tight junction, as shown in Figure 5.1. (b) The electrical potential along the cleft. $P^{tj} = 10^{-6}$ m/s, $\delta = 10^{-3}$. All other parameters are given in table 5.2.

shown in figure 5.2(b). The figure shows that the potential decreases from zero at the basal region to a negative value at the tight junction, despite the fact that the apical potential is positive. This implies that the potential drop across the tight junction has a larger magnitude than the TEP.

The value of tight-junction permeability to K^+, P^{tj}, appearing in the equation (5.11), is unknown in the RPE, and in other epithelia it could vary over several orders of magnitude, depending whether the epithelium is leaky or tight (Anderson and Van Itallie, 2009). The drop of ion concentrations and of the potential in the cleft is shown in figure 5.3. We vary P^{tj} from $1.5 \cdot 10^{-8}$ to $1.5 \cdot 10^{-4}$ m/s. Within this range (4 orders of magnitude) the concentrations and the potential remain almost constant, implying our lack of knowledge about the permeability of the tight junction does not significantly affect the model results.

The concentration variation of all species in the cleft, along with the fact that the concentrations in the cell are not spatially variable, implies that an osmotic flux is generated across the cell lateral membrane. Such a water flux is directed from the cell to the cleft, since the osmolarity in the cleft is larger than in the cell. Moreover, the existence of an electrical field along the cleft generates an electroosmotic flow. Since electroosmotic flow follows the potential gradient, it is directed from the basal to the apical region and therefore competes with the osmotic flux.

The velocity field in the cleft is shown in figure 5.4(a). The effect of the slip velocity can be seen through the circulation next to the walls, close to the boundaries of the cleft with the basal region. The slip velocity is directed from the basal to the apical region, which is a consequence of the negative sign of the potential gradient along the cleft. However, water flow is mostly due to the lateral osmotic fluxes. The inflow from the tight junction is barely visible in the plot because its magnitude is much smaller than the one from the lateral walls.

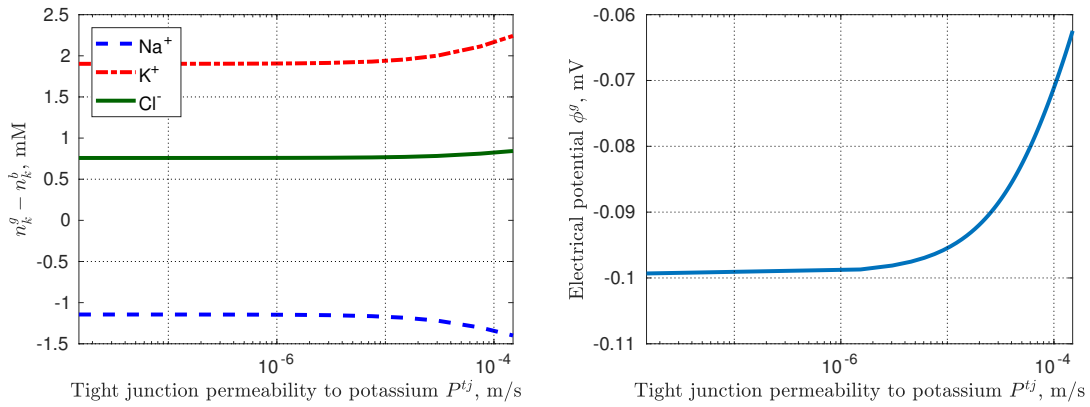

(a) (b)

Figure 5.3: Differences in ion concentrations (a) and the potential (b) between model predictions in the cleft at the boundary with the tight junction and at the basal region, as a function of tight junction permeability to K^+, P^{tj}. All other parameters are given in table 5.2.

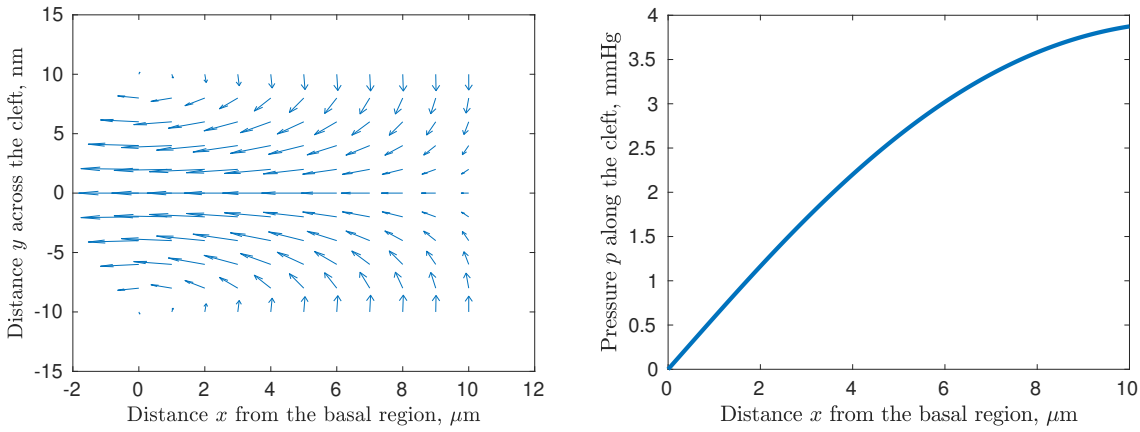

(a) (b)

Figure 5.4: (a) The velocity vectors in the cleft. The x-axis spans from basal to apical region, the y-axis spans across the cleft. The cleft thickness is magnified for clearer visualisation. The maximum velocity magnitude is 5.2 μm/s. (b) Fluid pressure along the cleft. Parameters are reported in table 5.2 with $P^{tj} = 10^{-6}$ m/s, $\delta = 10^{-3}$, $k_{tj} = 1.28 \cdot 10^{-10}$ m/s/Pa.

Figure 5.4(b) shows the pressure along the cleft gap relative to the pressure in the cell, which we assume to be constant and equal to zero. The maximum value is close to the tight junction and is about 4 mmHg. We note that in reality the cleft gap is compliant and such pressure values might induce an increase of its thickness. Introducing this effect to the model would add extra complexity and additional unknown parameters (see Weinstein and Stephenson, 1979), without qualitatively changing the results. For instance, for a cleft gap 5 times thicker, $h = 50$ nm, the maximum pressure value drops to 0.025 mmHg, but the water flux reduces only by a factor of 1.5.

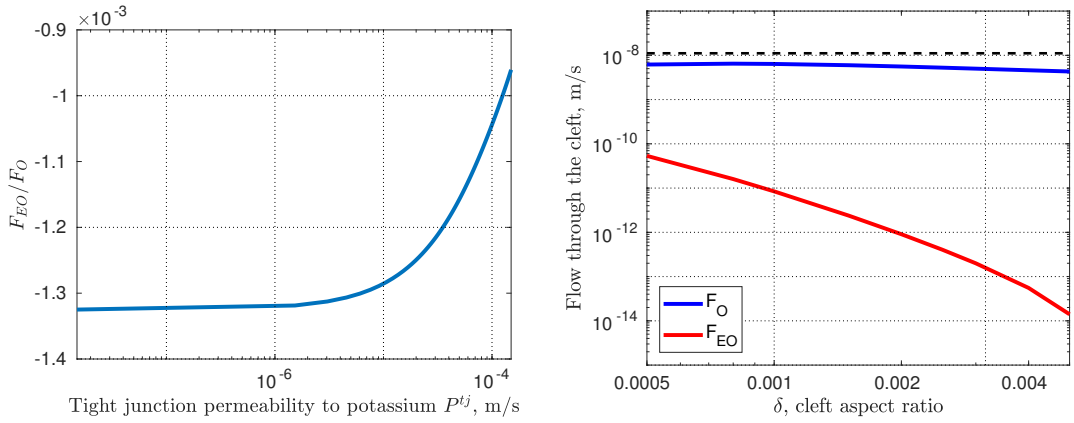

Figure 5.5: (a) Ratio between predicted electroosmotic and osmotic fluxes across the RPE as a function of tight junction permeability P^{tj} with $\delta = 10^{-3}$. (b) Osmotic flux F_O and electroosmotic flux F_{EO} magnitudes as a function of aspect ratio of the cleft $\delta = h/L$ with $P^{tj} = 10^{-6}$ m/s. The black dashed line corresponds to the measured value of transepithelial water transport 4 μl/h/cm^2 $\approx 1.1 \cdot 10^{-8}$ m/s (Shi et al., 2008). In both figures $k_{tj} = 1.28 \cdot 10^{-10}$ m/s/Pa. All other parameters are given in table 5.2.

Therefore, similarly to what has been implemented in various other works on epithelial transport (e.g. Mathias, 1985), we do not account for the compliance in the present model.

The contribution of the electroosmotic flux in the cleft F_{EO} to the total flow is computed via $F_{EO} = F_{TOT} - F_O$, where F_{TOT} is the transepithelial flux per unit surface and F_O is the flux, driven only by osmosis, obtained by solving (5.22), with zero slip velocity $u_{slip} = 0$ (thus 'switching off' electroosmosis). The model predicts, that $F_{EO} \approx 0.9 \cdot 10^{-11}$ m/s and $F_O \approx 0.7 \cdot 10^{-8}$ m/s, indicating that osmosis dominates electroosmosis. The overall flux is therefore directed towards the basal region. In figure 5.1 we show the direction of water fluxes predicted by the model. The length of the arrows schematically indicates the magnitude of the corresponding flux. We note that there is an osmotic flux also from the basal region to the cell, but it is smaller than that from the apical region, owing to the fact that the apical membrane is highly folded. For baseline values for the parameters, the water flux per unit surface through the RPE is equal to $0.7 \cdot 10^{-8}$ m/s.

The ratio between osmotic and electroosmotic fluxes as a function of the tight-junction permeability to K^+ is shown in figure 5.5(a). The flux ratio is negative since the electroosmotic flow has an opposite direction to the osmotic flow. Moreover, this ratio keeps the same order of magnitude over a wide range of values of P^{tj}, which indicates that electroosmotic flux is subdominant. Figure 5.5(b) shows the effect of the cleft aspect ratio (h/L) on the osmotic and electroosmotic contributions to the total flow. Increasing the cleft aspect ratio results in smaller potential and concentration gradients and both fluxes decrease. Electroosmosis becomes more

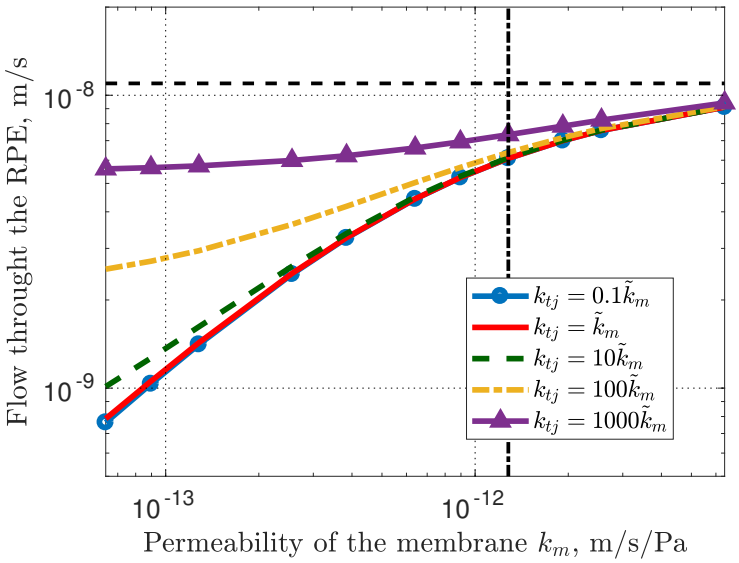

Figure 5.6: Flux per unit surface through the RPE as a function of the membrane hydrodynamic permeability k_m for different values of tight junction hydrodynamic permeability k_{tj}. $\tilde{k}_m$ is the typical value for hydrodynamic permeability of the cell membrane, $\tilde{k}_m = 1.28 \cdot 10^{-12}$ m/s/Pa (Mathias and Wang, 2005). The baseline value for the membrane permeability is represented by the vertical black punctured line. The horizontal black dashed line corresponds to the measured value of transepithelial water transport $1.1 \cdot 10^{-8}$ m/s. $\delta = 10^{-3}$, $P^{tj} = 10^{-6}$ m/s. All other parameters are given in table 5.2.

relevant as the aspect ratio tends to zero.

In figure 5.6 we investigate the effect of the hydrodynamic permeability of the lateral membrane k_m and of the tight junction k_{tj} on the flow (see equation (5.22a)). The five curves correspond to different values of k_{tj} for which, to our knowledge, there are no measurements. We thus consider it to be a multiple of the typical membrane permeability, which we denote as $\tilde{k}_m$. Figure 5.6 shows that the hydrodynamic permeability of the cell membrane k_m has a significant influence on the magnitude of the flow in the cleft, since it governs the osmotic fluxes. On the other hand, due to the small cleft aspect ratio δ, the permeability of the tight junction, k_{tj}, has a smaller effect on water flux. k_{tj} should be of order k_m/δ for the osmotic fluxes through the tight junction and lateral walls to have the same magnitude. In fact, it can be seen from the plot that for large values of k_{tj} the flux is weakly affected by changes in k_m.

So far we assumed that the osmolarity in the apical and basal regions is the same. This assumption, however, might be too restrictive in physiological systems. Figure 5.7 shows the response of water flux across the RPE to a perturbation of apical NaCl concentration from its baseline value (given in table 5.2), while keeping the basal NaCl composition fixed. This response is linear with a slope of $2.11 \cdot 10^{-12}$ m/s/Pa, that may be physiologycally interpreted as an osmotic permeability of the RPE. We note that the line does not pass through the origin since for baseline

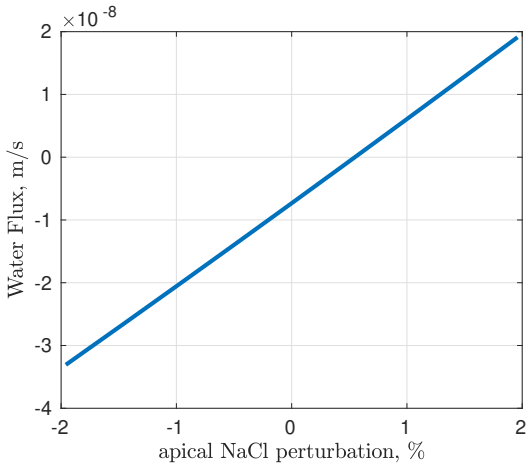

(a)

Figure 5.7: Water flow across the RPE as a function of apical NaCl perturbation. $k_m = 1.28 \cdot 10^{-12}$, $P^{tj} = 10^{-6}$ m/s, $\delta = 10^{-3}$ and all other parameters are given in table 5.2.

NaCl concentration there is non-zero water flux due to the presence of ion concentration gradients in the cleft.

5.5 Discussion

A significant proportion of ocular pathology is due to fluid accumulation in the subretinal space. It occurs in diabetic maculopathy and some forms of age-related macular degeneration, the two being among the most common causes of visual impairment or blindness. One of the reasons of fluid accumulation in the subretinal space is failure of fluid pumping by the retinal pigment epithelium (RPE). Failure of such a pumping is also associated with increased risk of retinal detachment (Gallemore et al., 1998). Understanding the mechanisms of fluid transport across the RPE is important to obtain an insight about preventing and/or treating the pump failure and it is the primary aim of the present work.

The mechanisms that drive fluid across various types of epithelia have been thoroughly investigated (Fischbarg, 2003). In addition, many authors studied water transport across the corneal endothelium, in particular focusing on the role of electroosmosis (Fischbarg and Diecke, 2005; Fischbarg et al., 2006; Sanchez et al., 2016). However, the details of RPE water transport are poorly understood, despite their clinical relevance, though the close integration with ion transport suggests there are favourable prospects for furthering a mechanistic description for water transport in the RPE.

In this chapter we propose a mathematical model that incorporates this coupling between cellular ion and fluid transport within a coherent framework that resolves ion concentrations and the electric potential within the cleft gap. The model accounts for the presence of three ions

(Na^+, K^+ and Cl^-), which, according to experimental measurements, are dominant in terms of concentrations and magnitude of ion fluxes across the RPE (Miller and Edelman, 1990). Although it neglects some potentially important elements, such as bicarbonate, protons, carbon dioxide and lactate, the three-ion model is anticipated to be sufficient, as a first approximation, to describe the essential features of RPE water and ion transport, as well as illustrating that physically consistent, spatially resolved models for water and ion transport can be developed, which is a further aim of this work. In the next chapter we add more components to the model.

The model of ion transport consists of conservation equations for ion fluxes and the Poisson equation for the electrical potential together with prescribed boundary and membrane conditions. We consider the apical membrane to be flat, disregarding the presence of microvilli in the geometry, but accounting for them in terms of membrane transport properties. In the bulk of the cell and extracellular space we assume electroneutrality. The small aspect ratio of the cleft ($\delta = h/L \approx 0.001$), allows us to significantly simplify the system. As a result, we obtain distributions of concentrations and the potential in the bulk of both the cell and the cleft gap. We also resolve the Debye layers, at the cell membranes, to obtain the spatial profile of potential and charge density in the cleft, which are necessary to describe electroosmotic flow.

To model the flow in the cleft gap between adjacent cells we account for the effects of osmotic fluxes through the lateral walls and the tight junction and electroosmosis along the cleft gap. The ion transport model provides the necessary information to describe these mechanisms. Taking advantage of the cleft geometry, we use thin-film approximation to model fluid flow and note that water and ion transport are coupled through the effect of advection. An additional coupling arises from the overall water balance which controls cell volume.

For the chosen set of parameters (given in table 5.2), the model reproduces ion concentrations in the cell and membrane potentials close to those observed in the RPE experimentally. The model resolves the heterogeneous profiles in the cleft gap in concert with a coupling of the ion and fluid transport within a coherent framework. Unlike most works on epithelial transport (e.g. Weinstein and Sontag, 2009; Strieter et al., 1990; Lew et al., 1979), the present model treats the system as fully spatial until and unless there is evidence to neglect spatial variability, and it is found that some spatial effects need to be retained. In particular, the predicted spatial variability of ion concentrations and electrical potential along the cleft gap has important consequences and cannot be predicted by standard compartmental models of epithelial transport.

The importance of spatial variability was already highlighted by Weinstein and Stephenson (1979), who developed a mathematical model for general epithelia, with particular attention to Necturus gallbladder. Despite the similarities, our model holds several substantial differences with the work of Weinstein and Stephenson (1979). First, the authors aimed at investigating the transport in leaky epithelia, whereas the RPE is tight. Second, as a result of distinct cell types in two models, different ion channel composition and, therefore, constitutive laws were adapted. Moreover, our model investigates the possibility of electroosmosis along the cleft, and

therefore the electrical double layers close to the cell membranes are accounted for, which was not implemented in Weinstein and Stephenson (1979). However, the authors also considered the effect of compliance of the cell membranes, that we neglect even if we account for the changes in cell volume, advocating that this additional effect would not change the qualitative and quantitative in terms of water flux conclusions of the present work.

The results show that the transepithelial flow has a direction from the apical to the basal region and its magnitude is about $0.7 \cdot 10^{-8}$ m/s, which is close to the measured value of the flow through the human RPE of 1.1–2.8 $\cdot 10^{-8}$ m/s (Shi et al., 2008). If we account for a hexagonal arrangement of the cells, and assuming that L is the side of cell, then the calculated flux value should be multiplied by a factor of $\approx 2/\sqrt{3}$. Although we are in the regime of isotonic transepithelial fluid transport, there is an osmotic flow through the RPE driven by the spatial variability of ion concentrations in the cleft (figure 5.1). The transport from the cell to the cleft gap is hypertonic, reaching isotonicity at the boundary with the basal region and is known as local osmosis (Diamond and Bossert, 1967; Hill, 1975). We must emphasise, however, that the model prescribes the same concentrations in the apical and basal regions, which is a restrictive assumption according to the physiological definition of isotonic transport. Weinstein and Stephenson (1979) proposed that the transepithelial difference in osmolarity can be 1-2% for epithelium to transport isotonically. In our framework, a 2% change of bathing NaCl solution in the apical or basal side will result in additional water flux of about $2.5 \cdot 10^{-8}$ m/s, which is comparable with the value we find for local osmosis and no transepithelial osmotic gradients. This confirms that the contribution of the interspace gradients is important and has to be considered in such models. Moreover, the model predicts that transepithelial water flux depends linearly on NaCl concentration in the apical (or basal) region. The slope of this linear dependency may be physiologically interpreted as an osmotic permeability of the whole epithelial layer, which we estimate to be approximately $2.11 \cdot 10^{-12}$ m/s/Pa. Furthermore, it has been observed that fluid transport is enhanced by transepithelial Cl^- flux (e.g. Bialek and Miller, 1994). Our model is consistent with this finding, as increasing basolateral Cl^- conductance results in higher concentration gradients in the cleft, driving more fluid across the RPE.

To estimate the electroosmotic flux one might be tempted to perform a simple order-of-magnitude calculation, using the Helmholtz-Smoluchovsky streamwise slip velocity expression (Probstein, 2005), $u_{slip} = -\frac{\epsilon\zeta E}{\mu}$, where ϵ, ζ, μ are electric permittivity of the fluid, wall zeta potential and fluid viscosity, respectively, and E is the streamwise electric field. The natural estimate for the electric field would be based on the transepithelial potential $TEP \approx 5$ mV, thus, $E = -TEP/L \approx -500$ V/m (where L is the length of the cell) with the field directed from the subretinal space to the choroid. In reality, it is likely that the majority of the potential drop occurs across the tight junction rather then the whole epithelial layer, entailing that the electric field above is overestimated. It is, however, not obvious how to estimate the value of the potential drop along the cleft, thus we use TEP for this order-of-magnitude argument. Using the values of ϵ

and μ from table 5.2 and the standard value for the zeta potential for the cell walls $\zeta = -10$ mV (Rubashkin et al., 2006), we estimate $u_{slip} \approx 4.3$ μm/s, directed towards the choroid and the electroosmotic flux per unit surface $\approx 8.6 \cdot 10^{-9}$ m/s, which is comparable to the measured transepithelial flow. This intuitive calculation, however, is misleading and in disagreement with the model outcomes, since for physiological values of the parameters the electric field is predicted to be directed from the basal region to the tight junction, forcing electroosmotic flow towards the subretinal space, in the opposite direction to the water flux across the RPE. The magnitude of electroosmosis in the cleft is also much smaller and it is thus predicted to be subdominant, stressing the importance of the integrated mathematical model for the epithelial transport.

Due to the small aspect ratio in the cleft, the impact of the slip velocity on the total flow is insignificant comparing to osmotic fluxes through the lateral walls. In fact, the osmotic flux is about three orders of magnitude larger than the electroosmotic one, and this difference is robust with respect to changes of parameter values. We advocate that above conclusions would apply to other tight epithelia, in particular that electroosmosis is subdominant, though the direction of electroosmotic flow might change depending on the characteristics of the epithelium. Clearly, in the case of non-isotonic transport osmosis will be even more dominant. The present model neglects the possible electroosmotic flow in the tight junctions, noting that such mechanisms have been proposed only for leaky epithelia, whilst the predominance of Claudin-3 and Claudin-19 in human RPE suggest tight epithelia, without relatively low permeability tight junctions (Rizzolo et al., 2011). We also have neglected the possible effect of Bruch's membrane, which would result in an additional resistance to the flow.

For physiological values of the membrane permeability ($\approx 10^{-12}$ m/s/Pa (Mathias and Wang, 2005)), the majority of the flow occurs due to the osmotic fluxes through the lateral membrane, via the paracellular route. If, however, the lateral hydrodynamic permeability is low, which can occur due to a lack (or knockdown) of aquaporins, the permeability of the tight junction has to be much larger than the membrane permeability in order to support the necessary amount of flow, which will then have a paracellular route. Nevertheless, for low or moderate tight junction hydrodynamic permeability, the transepithelial water flux is approximately proportional to the lateral membrane permeability, which means that this model framework cannot immediately be deployed to explain the effect of aquaporin knockdown that occurs in some leaky epithelia (Hill et al., 2004).

To summarise, our model predicts that the spatial gradient of ion concentrations and potential in the cleft is capable of driving physiological amounts of fluid through the RPE without additional mechanisms. We must emphasise, however, that since the model neglects pH balance and the presence of HCO_3^- and CO_2, some of the conclusions might change when adding these components, which will be discussed in the next chapter. Moreover, due to the absence of certain species, the present model cannot predict ion fluxes measured experimentally, that again motivates the model extension. Nonetheless, we anticipate that the presence of spatial heterogeneity in the cleft, and

its influence on driving flow across the lateral membranes, will be retained, as will the prediction that electroosmosis is subdominant and the prediction that the water transport may not be as sensitive to membrane permeability as one might initially anticipate.

CHAPTER 6

FLUID, ION AND CO_2 TRANSPORT ACROSS THE RETINAL PIGMENT EPITHELIUM

6.1 Introduction

In the previous chapter we developed a model that couples fluid and ion transport across the retinal pigment epithelium (RPE). We considered the presence of three ions: Na^+, K^+ and Cl^-. The model allowed us to understand the relative importance of the mechanisms responsible for fluid transport across the RPE.

In the present chapter we refine the model introduced in chapter 5 by accounting for further potentially important ingredients that had been neglected. We anticipate that this will provide a more accurate quantitative estimate of transepithelial water and ion fluxes. In particular we now consider the presence of the following additional species: bicarbonate (HCO_3^-), carbon dioxide (CO_2), carbonic acid (H_2CO_3) and protons (H^+).

We added HCO_3^- since its concentration is comparable to that of the other three ions. Moreover, in the RPE, HCO_3^- and Na^+ transport are coupled through NBC-type channels that co-transport Na^+ and HCO_3^- and are located in the apical and basolateral membrane (Reichhart and Strauß, 2014; Adijanto et al., 2009). Therefore, adding HCO_3^- is essential to describe physiological ion fluxes in detail and it allows us to model the possible occurrence of Na^+ flux across the RPE, which was imposed to be zero in the model presented in chapter 5. HCO_3^- is also transported across the RPE (Adijanto et al., 2009) and it interacts with the ions considered in the previous chapter. Hughes et al. (1984) suggested that HCO_3^- transport across the RPE is linked to water flux (an increase of the former should correspond to an increase of the latter).

Retinal photoreceptors consume a relatively large amount of oxygen, with a consequent significant production of carbon dioxide (CO_2) in the subretinal space (SRS). One of the key roles

of the RPE is to remove the CO_2 produced by the photoreceptors. Failure to perform this activity would result in acidosis (Sillman et al., 1972; Takahashi et al., 1993). CO_2 is removed from the SRS partly being transported across the RPE to the choroid, where it is up taken by blood flow, and partly because it is converted into H_2CO_3. This, in turn, dissociates into HCO_3^- and H^+. Thus, a further reason for the development of the model proposed in this chapter is to be able to describe CO_2 transport and reaction in the RPE.

The reaction between CO_2 and H_2CO_3 is catalysed by an enzyme, carbonic anhydrase (CA). It has been shown with *in-vivo* animal studies that CA inhibition (for example with acetazolamide treatment) results in an increase of transepithelial water flux towards the choroid (Wolfensberger et al., 2000; Kita and Marmor, 1992). In addition, some patients with macular oedema respond to acetazolamide treatment that also inhibits CA (Cox et al., 1988; Fishman et al., 1989). The mechanisms behind the functioning of such treatments are elusive and a physically based mathematical model might help shed some light into this problem.

Adijanto et al. (2009) conducted in-vitro experiments on the human fetal RPE suggesting that increase of apical and basal CO_2 enhances water transport. This is another point suitable for investigation with mathematical modelling.

In this chapter we address the above questions by developing a mathematical model that considers the aforementioned ingredients into a framework that couples water and solutes transport and chemical interactions.

The chapter is organised as follows. We first describe and simplify the mathematical model in § 6.2 . Since the model is relatively complicated and it involves a large number of parameters, many of which are difficult to estimate, we use a global sensitivity analysis to investigate which parameters affect the model outcomes the most and in what direction. The method adopted is described in § 6.3 and the choice of model parameters is addressed in § 6.4. The results of the model are presented in § 6.5, which is followed by a discussion in § 6.6.

6.2 The model

6.2.1 Model setup

We preserve the geometry and coordinate system from the previous chapter and account for the same four regions: apical (a), basal (b), cell (i) and cleft (g). Following the same reasoning as in the previous chapter we assume that the solution in the apical and basal regions is homogeneous for all species. Therefore, we formulate a mathematical model for water and ion transport in the cell and the cleft gap and impose boundary conditions directly on the apical membrane, tight junction and basal membrane. In the cell and the cleft gap we consider the presence of seven species: Na^+, K^+, Cl^-, HCO_3^-, CO_2, H_2CO_3 and H^+.

Investigating the coupling of CO_2 with water and ion transport is one of the objectives of the present work. Unlike the species considered in previous chapter, CO_2 and HCO_3^- are subject to

chemical rearrangement via the following reaction

$$\mathrm{HCO_3}^- + \mathrm{H}^+ \underset{k_{-1}}{\overset{k_1}{\rightleftharpoons}} \mathrm{H_2CO_3} \underset{k_h}{\overset{k_d}{\rightleftharpoons}} \mathrm{CO_2} + \mathrm{H_2O}. \tag{6.1}$$

These reactions consists of two parts. The first is dissociation of H_2CO_3 into the ions HCO_3^- and H^+ and it happens almost instantaneously. The second part is normally slow, but can be catalysed up to six orders of magnitude by carbonic anhydrase (CA) (Krahn and Weinstein, 1996). CA is present in the RPE, in the form of CA II in the cell (Korte and Smith, 1993) and in the extracellular membranes in the form of membrane bound CA IV or XIV (Wolfensberger et al., 1994; Nagelhus et al., 2005). The rates of this reaction are reported in table 6.2.

The second step of reaction (6.1) involves production and consumption of water. The resulting change in the amount of water, however, is insignificant compared to the total water concentration, which is ≈ 55 M. Therefore, we neglect this change and keep the amount of water fixed.

The cell has an anion gap due to the presence of large non-diffusible molecules. These molecules can be categorised into two effective groups: those that react with H^+ (with charge -1) and those that do not. The first group includes cytosolic buffer, denoted with B, which tends to react with H^+. This reaction can be modelled in a simple way as:

$$\mathrm{B}^- + \mathrm{H}^+ \underset{k_{-3}}{\overset{k_3}{\rightleftharpoons}} \mathrm{HB}, \tag{6.2}$$

where HB is a protonated buffer, a product of the reaction (6.2), and it is not charged. The total buffer concentration is fixed and conserved, and we denote it with $C_B := B + HB$, where B and HB denote concentrations of B and HB respectively. We note that this representation of cytosolic buffering is highly simplified, as reactions happening in the cell are much more complex and involve many different species.

The second group of non-diffusible molecules that do not react with H^+ is analogous to the anion gap in the previous chapter. We denote their concentration with X and the corresponding fixed negative charge with $\tilde{X} := z_X X$, where z_X is the mean valence of these molecules. Therefore, the total concentration of fixed negative charge in the cell is $\tilde{X} + B$ and the total concentration of non-diffusible molecules is $X + C_B$.

The pumps, co-transporters and ion channels are adopted based on Reichhart and Strauß (2014) and Adijanto et al. (2009), see Figure 6.1. As in the previous chapter, the apical membrane is assumed to have Na^+/K^+ATPase that pumps three Na^+ out of the cell and two K^+ in (denoted in the following with subscript ATP), the NKCC co-transporter that transports Na^+, K^+ and two Cl^-($NKCC$) and K^+ channels. In addition, we consider the presence of the electrogenic channel NBC1 that co-transports two HCO_3^- and one Na^+(NBC_a) and the Na^+/H^+exchanger (NHE) (Lin and Miller, 1991; Lin et al., 1992). Following Adijanto et al. (2009), we also account for the possible presence of electroneutral Na^+-HCO_3^- co-transporter (NBC_e). As before, the basolateral membrane has K^+ and Cl^- channels. This is complemented by the HCO_3^-/Cl^- exchanger AE2 (AE) and a channel that co-transports Na^+ and HCO_3^-. The existence and stochiometry of the latter

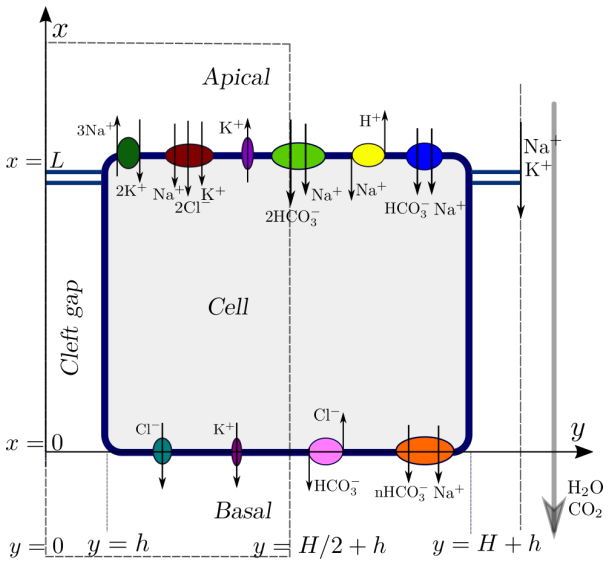

Figure 6.1: Diagram of ion channels in the RPE. Sketch of the considered domain and coordinate system.

channel in the basolateral membrane remains an open question in RPE physiology. Adijanto et al. (2009) suggested that this channel has stochiometry 1:2 (Na^+:HCO_3^-) or 1:3, while some other authors considered only the presence of a Na^+ channel alone (Dyka et al., 2005). We thus assume that there is a combination of NBC channels with stochiometry 1:2 (NBC_{b12}) and 1:3 (NBC_{b13}) in the basolateral membrane. The tight junction is considered to be impermeable to anions (Peng et al., 2010; Adijanto et al., 2009). We note that in the previous chapter we considered that the tight junctions are permeable only to K^+, following Peng et al. (2010). However, Adijanto et al. (2009) suggests that there is a paracellular Na^+ transport, thus we consider here that the tight junction is permeable to both Na^+ and K^+. Additionally, every membrane is permeable to CO_2 and H_2CO_3, since they are not polarised and can pass the lipid bilayer. Water is being transported across the membranes by aquaporins and we assume that each membrane has a certain hydraulic conductivity.

Throughout this chapter we adopt the notation presented in table 6.1 and the values reported in table 6.2 as baseline. Unless stated otherwise, we use superscripts to label regions, using the same notation as in the previous chapter, and subscripts to label species, which we number in the following way:

Na^+	K^+	Cl^-	HCO_3^-	H^+	CO_2	H_2CO_3
0	1	2	3	4	5	6

The modelling procedure is similar to that adopted in the previous chapter. We first present a spatially resolved model of solute transport with reactions. Then we perform model simplification in the cell and cleft based on asymptotic expansions in terms of the aspect ratio of the cleft,

a, b, g, i	values of s labelling apical, basal, cleft gap and intracellular regions respectively
n_k^s	concentration of species k in region s (mM) such that n_0^s =[Na^+]^s, n_1^s =[K^+]^s, n_2^s =[Cl^-]^s, n_3^s =[HCO_3^-]^s, n_4^s =[H^+]^s, n_5^s =[CO_2]^s and n_6^s =[H_2CO_3]^s
X	concentration of non-diffusible anions in the cell (mM)
B and HB	concentration of cytosolic buffer and protonated buffer (mM)
z_k	valence and charge of species k
ϕ^s	electrical potential in region s (V)
ρ^s	space charge density in region s (C/m^3)
$\mathbf{j}_k^s$	flux of species k per unit area in region s (mol/m^2/s)
I_k^{sm}	electric current of ion k per unit area from region s to region m (A/m^2)
Q^{sm}	water flux per unit area from region s to region m (m^2/s)
$\mathscr{J}_{channel}$	flux through the membrane due the corresponding channel or pump (mol/m^2/s)
$\mathscr{J}_k^{sm}$	(electro)diffusive flux of species k from region s to region m (mol/m^2/s)
$\mathbf{u}$	fluid velocity in the cleft gap (m/s)
p	fluid pressure in the cleft gap (Pa).

Table 6.1: A list of variables used in the model, together with their units. Superscripts s and m denote generic regions from the set $\{a, b, i, g\}$.

$\delta = h/L$ and exploiting the fact that different time scales characterise reaction and diffusion processes. We then model fluid transport in the cleft. We do not consider electroosmosis, as it has been demonstrated to be subdominant, and focus on water transport driven by osmosis. Finally, we impose water balance in the cell.

6.2.2 Model of solute transport

The electrodiffusion model in the generic region s consists of the conservation of electrodiffusive fluxes for each species k and the electroneutrality condition (Probstein, 2005)

$$\frac{\partial n_k^s}{\partial t} = -\nabla \cdot \mathbf{j}_k^s + f_k^s, \qquad \mathbf{j}_k^s = -D_k \left(\nabla n_k^s + \frac{z_k F}{RT} n_k^s \nabla \phi^s \right) + \mathbf{u} n_k^s, \qquad k \in \{0, 1, ..., 6\}, \tag{6.3a}$$

$$\sum_{k=0}^{4} z_k n_k^s = X^s, \qquad s \in \{i, g\}, \tag{6.3b}$$

where $X^i = z_X X + B$ and $X^g = 0$. In the cell we have an additional equation for the negatively charged cytosolic buffer (which we assume cannot diffuse)

$$\frac{\partial B}{\partial t} = f_B^i. \tag{6.3c}$$

The concentration of HB can be found from the relation $HB = C_B - B$. Note that the diffusion coefficients are different among the species, and are reported in table 6.2. f_k^s are the reaction terms, modelled with the mass action law (Keener and Sneyd, 2009) as follows

$$\begin{aligned} &f_3^s = k_{-1} n_6^s - k_1 n_3^s n_4^s, \qquad f_B^i = k_{-3} HB - k_3 n_4^i B, \qquad f_4^s = f_3^s + f_B^s, \\ &f_5^s = -k_h n_5^s + k_d n_6^s, \qquad f_6^s = -f_5^s - f_3^s, \end{aligned} \tag{6.4}$$

and all other f_k^s are zeros.

Parameter	Value	Source
Geometry		
Length of the cell, L	10 μm	Marmor (1998)
Height of the cell, H	10 μm	Marmor (1998)
Width of the cleft, $2h$	20 nm	
Thermodynamics		
Ideal gas constant, R	8.314 J/K/mol	
Temperature, T	310 K	
Faraday constant, F	96485 C/mol	
Membrane transport		
Factor of apical membrane folding, A_a	10	Adijanto et al. (2009)
Average valence of fixed negative charge in the cell, z_X	1.5 eq/mol	
Total concentration of intracellular buffer, C_B	60 mM	fitting
Representative diffusion coefficient, D	1.7 m^2/s	
Representative species concentration, N	100 mM	

Pump, co-transporter and antiporter amplitudes, mol/s/m^2

P_{ATP}	P_{NKCC}	P_{NBC_a}	P_{NBC_e}	P_{NHE}	P_{AE}	$P_{NBC_{b12}}$	$P_{NBC_{b13}}$
$1.77\cdot10^{-6}$	$1.78\cdot10^{-6}$	$5.62\cdot10^{-7}$	10^{-7}	$3.16\cdot10^{-7}$	$5.62\cdot10^{-7}$	$5.62\cdot10^{-7}$	10^{-7}

valence z_k, diffusion coefficient D_k, permeability of membrane s, P_k^s of species k

molecule	Na^+	K^+	Cl^-	HCO_3^-	H^+	CO_2	H_2CO_3
k	0	1	2	3	4	5	6
z_k	+1	+1	-1	-1	+1	0	0
$D_k\cdot10^{-9}$m^2/s	1.7	1.7	1.7	1.23	9.69	1.5	1.5
P_k^a m/s	0	$2.23\cdot10^{-7}$	0	0	0	0.015	$1.28\cdot10^{-4}$
P_k^b m/s	0	$3.16\cdot10^{-8}$	$1.25\cdot10^{-8}$	0	0	0.0015	$1.28\cdot10^{-5}$
P_k^{tj} m/s	10^{-5}	10^{-5}	0	0	0	0.015	$1.28\cdot10^{-4}$
Concentrations, mM					pH		
n_k^s, $s=a,b$	143.7	5	122.5	26.2	7.45	1.7	0.005

Reaction rates		
Hydration of CO_2 (catalysed), k_h	$1.45\cdot10^3$ 1/s	Weinstein (2005b)
Dehydration of CO_2 (catalysed), k_d	$4.96\cdot10^5$ 1/s	
Equilibrium constant of H_2CO_3 dissociation, $K_d=k_1/k_{-1}$	5.3 1/mM	Adijanto et al. (2009)
Equilibrium constant of buffering reaction, $K_b=k_{-3}/k_3$	$1.7\cdot10^{-4}$ mM	fitting

Fluid dynamics		
Volume flow through the RPE, V	4-10 μl/hour/cm^2	Hughes et al. (1984), Shi et al. (2008)
Hydrodynamic permeability of the membrane, k_m	$1.28\cdot10^{-12}$ m/s/Pa	Mathias and Wang (2005)
Hydrodynamic permeability of the tight junction, k^{tj}	$1.28\cdot10^{-10}$ m/s/Pa	
Dynamic viscosity, μ	$0.75\cdot10^{-3}$ Pa/s	water at 35°C

Table 6.2: Model reference parameters; please refer to § 6.4 for further details on their motivation.

6.2.2.1 Boundary conditions

At the membrane between the generic regions s and m, we impose the conservation of ion fluxes for each ion species k ($k \in \{0,1,2,3,4\}$), which is implemented by imposing that the ion current

I_k^{sm} on the s side of the membrane is equal to the flux of charge due to the movement of species k passing from s to m,

$$Fz_k \mathbf{n}^{sm} \cdot \mathbf{j}_k^s = I_k^{sm}, \tag{6.5}$$

where $\mathbf{n}^{sm}$ is the unit normal pointing from region s to region m. The flux I_k^{sm} is prescribed to account for all passive and active flows of ion k due to channels and pumps on the corresponding membrane and it is a nonlinear function of concentrations and potential on both sides of the membrane. The choice of constitutive relations for these currents is described in § 6.2.2.2.

For uncharged species, we also impose fluxes across each membrane and write

$$\mathbf{n}^{sm} \cdot \mathbf{j}_k^s = \mathcal{J}_k^{sm}, \qquad k \in \{5,6\}, \tag{6.6}$$

where constitutive choices for $\mathbf{j}_k^s$ are again given is § 6.2.2.2.

We prescribe all the concentrations and potential in the basal region. At the bottom of the cleft gap, $x = 0$, we assume continuity of the value taken by all variables, so that

$$n_k^g(x=0,y) = n_k^b \qquad \phi^g(x=0,y) = \phi^b, \qquad k \in \{0,...,6\}. \tag{6.7a}$$

We also have symmetry conditions, at $y = 0$ and $y = H/2 + h$

$$\partial\phi^s/\partial y = \partial n_k^s/\partial y = 0 \text{ at } y = 0,\ y = h + H/2, \qquad k \in \{0,...,6\}, \qquad s \in \{i,g\}. \tag{6.7b}$$

Finally, we impose zero current at the apical membrane to simulate open circuit condition and to be able to compute the potential in the apical region (ϕ^a)

$$\sum_0^4 z_k \mathbf{j}_k^a \cdot \mathbf{n} = 0, \qquad \text{at } x = L. \tag{6.7c}$$

Therefore, we have a system of 7 PDEs in the cleft (6.3a) and 8 in the cell, with the addition of (6.3c), coupled with the electroneutrality condition (6.3b) and open circuit condition (6.7c) for 8 unknowns in the cleft, 9 in the cell and ϕ^a subject to the boundary conditions (6.5), (6.6) and (6.7).

6.2.2.2 Ion fluxes through cell membranes

In this section we describe the choice of constitutive relations for the fluxes of species across the membranes. Na^+/K^+ATPase and NKCC co-transporter are chosen to be the same as in chapter 5,

$$\mathcal{J}_{ATP} = P_{ATP} \left(\frac{n_0^i}{K_{Na} + n_0^i} \right)^3 \left(\frac{n_1^a}{K_K + n_1^a} \right)^2, \tag{6.8a}$$

$$\mathcal{J}_{NKCC} = P_{NKCC} \log \frac{n_0^i n_1^i (n_2^i)^2}{n_0^a n_1^a (n_2^a)^2}, \tag{6.8b}$$

where with $P_{channel}$ we denote the amplitude of the flux through the corresponding channel or pump.

All other fluxes are modelled based on linear non-equilibrium thermodynamics (similar to Krahn and Weinstein, 1996). This approach minimises the number of unknown parameters, since only the amplitude of the flux has to be fixed. We can then write ion fluxes (from cell to extracellular space) as

$$\mathscr{J}_{NBC_a} = P_{NBC_a}\left(\log\frac{n_0^i\left(n_3^i\right)^2}{n_0^a\left(n_3^a\right)^2} - \frac{F}{RT}(\phi^i-\phi^a)\right), \tag{6.9a}$$

$$\mathscr{J}_{NBC_e} = P_{NBC_e}\left(\log\frac{n_0^i n_3^i}{n_0^a n_3^a}\right), \tag{6.9b}$$

$$\mathscr{J}_{NHE} = P_{NHE}\left(\log\frac{n_0^a n_4^i}{n_0^i n_4^a}\right), \tag{6.9c}$$

$$\mathscr{J}_{AE} = P_{AE}\left(\log\frac{n_2^b n_3^i}{n_2^i n_3^b}\right), \tag{6.9d}$$

$$\mathscr{J}_{NBC_{b12}} = P_{NBC_{b12}}\left(\log\frac{n_0^i\left(n_3^i\right)^2}{n_0^b\left(n_3^b\right)^2} - \frac{F}{RT}(\phi^i-\phi^b)\right), \tag{6.9e}$$

$$\mathscr{J}_{NBC_{b13}} = P_{NBC_{b13}}\left(\log\frac{n_0^i\left(n_3^i\right)^3}{n_0^b\left(n_3^b\right)^3} - 2\frac{F}{RT}(\phi^i-\phi^b)\right). \tag{6.9f}$$

For the meaning and values of all parameters, please refer to tables 6.1 and 6.2. We note that for the Na^+/H^+ exchanger, the 'near-equilibrium' approximation might not hold and a kinetic model could be more appropriate choice (e.g. the one developed for the renal proximal tubule by Weinstein, 1995). However, a kinetic model would involve four extra parameters, the determination of which would require a detailed knowledge of NHE activity in the RPE, that, to our knowledge, is currently unavailable. Therefore, we keep the model reported in (6.9c), noting that it may be an aspect of the study that can be improved should more data become available.

The electrodiffusive fluxes through ion channels are modelled as GHK fluxes, such that the flux from region m to region s (Keener and Sneyd, 2009) is

$$\mathscr{J}_k^{ms} = z_k P_k^s \frac{F}{RT} V^s \frac{n_k^m - n_k^s \exp\left(-\frac{z_k F V^s}{RT}\right)}{1-\exp\left(-\frac{z_k F V^s}{RT}\right)}, \tag{6.10}$$

where $V^s = \phi^m - \phi^s$ is the potential across membrane s.

We assume that CO_2 and H_2CO_3 transported across membranes follow Fick's law, and thus have the following expression

$$\mathscr{J}_k^{ms} = P_k^s\left(n_k^m - n_k^s\right). \tag{6.11}$$

The fluxes through the membranes for every ion can therefore be rewritten as follows

(6.12a,b) $J_0^{ia} = 3\mathscr{J}_{ATP} + \mathscr{J}_{NKCC} + \mathscr{J}_{NBC_a} + \mathscr{J}_{NBC_e} - \mathscr{J}_{NHE}, \qquad J_0^{ib} = \mathscr{J}_{NBC_{b12}} + \mathscr{J}_{NBC_{b13}},$

(6.12c,d) $J_1^{ia} = \mathscr{J}_1^{ia} - 2\mathscr{J}_{ATP} + \mathscr{J}_{NKCC}, \qquad J_1^{ib} = \mathscr{J}_1^{ib},$

(6.12e,f) $J_2^{ia} = 2\mathscr{J}_{NKCC}, \qquad J_2^{ib} = \mathscr{J}_2^{ib} - \mathscr{J}_{AE},$

(6.12g,h) $J_3^{ia} = 2\mathscr{J}_{NBC_a} + \mathscr{J}_{NBC_e}, \qquad J_3^{ib} = 2\mathscr{J}_{NBC_{b12}} + 3\mathscr{J}_{NBC_{b13}} + \mathscr{J}_{AE},$

(6.12i,j) $J_4^{ia} = \mathscr{J}_{NHE}, \qquad J_4^{ib} = 0,$

where b denotes both basal and lateral membranes. The tight junction is modelled as a membrane permeable to K^+, Na^+ and non-charged species (CO_2, H_2CO_3) and the fluxes are modelled using the GHK model and Fick's law respectively

(6.13) $$J_0^{ag} = \mathscr{J}_0^{ag}, \qquad J_1^{ag} = \mathscr{J}_1^{ag}, \qquad J_5^{ag} = \mathscr{J}_5^{ag}, \qquad J_6^{ag} = \mathscr{J}_6^{ag}.$$

For $k = 2,3,4$, $J_k^{ag} = 0$. Finally, the current of ion k at the membrane between the regions s and m is given by the expression $I_k^{sm} = z_k F J_k^{sm}$.

6.2.2.3 Model simplification

We start simplifying our equations by comparing the timescales for reaction and diffusion processes. The time scale for diffusion in the cell is about $L^2/D \approx 0.06$ s, where $D = 1.7 \cdot 10^{-9}$ m^2/s (K^+ in water, Miller et al., 1978) is a representative diffusion coefficient. The time required for the first step of the reaction (6.1) and for the buffer reaction (6.2) is about 10^{-7} s. It thus makes sense to assume that the first step of the reaction (6.1) and the reaction (6.3c) are in equilibrium, leading to the following relations

(6.14a) $$n_6^s = K_d n_3^s n_4^s, \qquad K_d = \frac{k_1}{k_{-1}}, \qquad s \in \{i,g\},$$

(6.14b) $$B = \frac{K_b C_B}{K_b + n_4^i}, \qquad K_b = \frac{k_{-3}}{k_3}.$$

We note that in the cleft the diffusion time scale is much faster due to its small thickness. Nevertheless, the relation (6.14a) still holds as is shown in §B.2.

In the second step of the reaction (6.1), catalysed hydration of CO_2 takes about $\approx 6 \cdot 10^{-4}$ s and dehydration $2 \cdot 10^{-6}$ s. In the absence of carbonic anhydrase these values could increase six orders of magnitude and become comparable to those corresponding to diffusion. As we are interested to study the effect of CA inhibition, we do not assume that this step of the reaction (6.1) is in equilibrium (Krahn and Weinstein, 1996; Weinstein, 2005b).

Considering (6.14a) and summing up the equations (6.3a) for $k = 3,5,6$ we obtain the equation for conservation of total CO_2

(6.15) $$\frac{\partial n_3^s}{\partial t} + \frac{\partial n_5^s}{\partial t} + \frac{\partial n_6^s}{\partial t} = -\left(\nabla \cdot \mathbf{j}_3^s + \nabla \cdot \mathbf{j}_5^s + \nabla \cdot \mathbf{j}_6^s\right), \qquad s \in \{i,g\}.$$

Subtracting from equation (6.3a) for $k = 3$ equation (6.3a) for $k = 4$ and adding (6.3c), we obtain conservation of charge for the reacting species

$$\frac{\partial n_3^s}{\partial t} - \frac{\partial n_4^s}{\partial t} + \frac{\partial B}{\partial t} = -\left(\nabla\cdot\mathbf{j}_3^s - \nabla\cdot\mathbf{j}_4^s\right), \qquad s \in \{i, g\}. \tag{6.16}$$

In the following we will use equations (6.15) and (6.16) along with (6.14a) and (6.14b) instead of equations (6.3a) for $k = 3, 4, 6$ and (6.3c).

As we aim at studying water and CO_2 transport, we do not consider short time variations resulting for instance from the transition from light to dark, but focus on the steady behaviour of the system. Therefore, we drop all time derivatives and consider the system to be in steady state.

Moreover, in §B.1 and B.2 we show that the system is simplified to a set of ODEs in both cell and cleft with an error of approximation of order $\delta = h/L$. The resulting system of equations will be summarised in § 6.2.4.

6.2.3 Fluid flow

The fluid problem is very similar to the one presented in chapter 5, but without the contribution of electroosmosis. It is governed by Stokes equations

$$-\nabla p + \mu\nabla^2\mathbf{u} = 0, \tag{6.17a}$$

$$\nabla\cdot\mathbf{u} = 0, \tag{6.17b}$$

where $\mathbf{u} = (u, v)$ is fluid velocity and p is pressure.

We use the fact the equations have a gauge freedom in the pressure to assign zero pressure in the cell. Following the experimental evidence that the pressure jump across the RPE is negligible, we further assume it has values of zero in the apical and basal regions, treating these regions as zero dimensional compartments. In the cleft we follow the same procedure as in chapter 5. In particular, we apply lubrication theory to simplify the equations (6.17). At the boundaries $y = \pm h$ we assume no-slip conditions for the longitudinal velocity, $u(x, \pm h) = 0$. Moreover, at the cell membrane and tight junction we impose the osmotic and pressure driven fluxes, $v(x, \pm h) = \mp Q^{ig}$ and $u(L, y) = Q^{tj}$, which take the following expressions

$$Q^{tj} = k_{tj}\left(RT\sum_{k=0}^{6}(n_k^a - n_k^g(L)) + p(L) - p_a\right) \tag{6.18}$$

$$Q^{ig} = k_m\left[RT\left(\sum_{k=0}^{6}(n_k^i - n_k^g(x)) + X + C_B\right) + p(x)\right] \tag{6.19}$$

The use of lubrication theory leads to the following dimensionless velocity profile in the cleft,

$$u = \frac{1}{2\mu}\frac{\partial p}{\partial x}\left(y^2 - h^2\right), \tag{6.20}$$

and the pressure in the cleft can be found from the following equation

$$-\frac{h^3}{3\mu}\frac{d^2p}{dx^2} = -Q^{ig}(x). \tag{6.21}$$

$n_k^s(x)$	concentration of solute k in the cell ($s=i$) and cleft ($s=g$)
$B(x)$	concentration of cytosolic cellular buffer
X	concentration of non diffusible negatively charged molecules
$\phi^s(x)$	electrical potential in the cell ($s=i$) and cleft ($s=g$)
ϕ^a	TEP
$p(x)$	fluid pressure in the cleft

Table 6.3: List of the model unknowns.

At the tight junction, $x=L$, we impose flux Q^{tj} and at the boundary between the cleft and the basal region, $x=0$, we impose zero pressure. Thus the boundary conditions read

$$p = 0, \qquad \text{at } x = 0 \tag{6.22a}$$

$$-\frac{h^3}{3\mu}\frac{dp}{dx} = Q^{tj}, \qquad \text{at } x = L. \tag{6.22b}$$

Equations (6.21)–(6.22), (6.20) and (6.17b) describe fluid transport in the cleft.

Finally, we impose water balance in the cell

$$\int_0^L Q^{ia}\, dy + \int_0^L Q^{ib}\, dy + 2\int_0^H Q^{ig}\, dx = 0, \tag{6.23}$$

where the fluid fluxes are given by the following expressions

$$Q^{ia} = A_f k_m RT\left(\textstyle\sum_{k=0}^{6}(n_k^i - n_k^a) + C_B + X\right), \quad Q^{ib} = k_m RT\left(\textstyle\sum_{k=0}^{6}(n_k^i - n_k^b) + C_B + X\right). \tag{6.24}$$

This balance is required for the volume of the cell to remain constant and, similarly to chapter 5, it provides the additional equation needed to determine the concentration of large negatively charged molecules in the cell X, and in turn gives a feedback to ion concentrations and the potential through the electroneutrality condition (6.3b).

6.2.4 Summary and the solution

In this section we present the system of equations to be solved and describe the solution procedure. The considered unknowns are summarised in table 6.3. There are 20 model variables, out of which 18 are functions of x and 2 are spatially independent.

We denote with j_k^s the x-component of the solute flux $\mathbf{j}_k^s$, averaged in y direction

$$j_k^s = -D_k\left(\frac{dn_k^s}{dx} + \frac{z_k F}{RT} n_k^s \frac{d\phi^s}{dx}\right) + \theta^s\left(-\frac{h^2}{3\mu}\frac{dp}{dx}\frac{dn_k^s}{dx} - Q^{ig} n_k^s\right), \tag{6.25}$$

with the advection term being accounted for only in the cleft, so that $\theta^g = 1$ and $\theta^i = 0$. The set of

governing equations in the simplified form reads

Conservation of solute in the cell ($s = i$) and cleft ($s = g$)

$$-\frac{dj_k^s}{dx} + \beta^s J_k^{ig} = 0, \quad k = 0,1,2 \tag{6.26a}$$

$$-\frac{dj_5^s}{dx} + \beta^s J_5^{ig} + \left(k_d n_6^s - k_h n_5^s\right) = 0, \tag{6.26b}$$

Conservation of charge

$$-\frac{dj_3^s}{dx} + \beta^s J_3^{ig} + \frac{dj_4^s}{dx} = 0, \tag{6.26c}$$

Conservation of total CO_2

$$-\frac{dj_6^s}{dx} + \beta^s J_6^{ig} - \frac{dj_5^s}{dx} + \beta^s J_5^{ig} - \frac{dj_3^s}{dx} + \beta^s J_3^{ig} = 0, \tag{6.26d}$$

Conditions for the reactions in equilibrium

$$n_6^s = K_d n_3^s n_4^s, \qquad s \in \{i,g\}, \tag{6.26e}$$

$$B = \frac{K_b C_B}{K_b + n_4^i}; \tag{6.26f}$$

Electroneutrality condition

$$n_0^s + n_1^s - n_2^s - n_3^s + n_4^s - X^s = 0, \qquad s \in \{i,g\}; \tag{6.26g}$$

Fluid transport

$$-\frac{h^3}{3\mu}\frac{d^2p}{dx^2} = -Q^{ig}(x); \tag{6.26h}$$

Water balance in the cell

$$Q^{ia} + Q^{ib} + 2\int_0^H Q^{ig}\, dx = 0, \tag{6.26i}$$

The symbol β^s is a constant that depends on the region considered, $\beta^i = -2$ and $\beta^g = 1/\delta$. This system consists of 7 algebraic equations and 13 ODEs, which are subject to the following boundary conditions

Imposed concentrations, potential and fluid pressure at the exit of the cleft

$$n_k^g = n_k^b,\ k \in \{0,\dots,5\}, \qquad \phi^g = \phi^b, \qquad p = 0, \qquad \text{at } x = 0; \tag{6.27a}$$

Membrane conditions at the basal membrane

$$-j_k^i = J_k^{ib},\ k \in \{0,\dots,4\}, \qquad -j_4^i - j_5^i - j_6^i = J_4^{ib} + J_5^{ib} + J_6^{ib}, \qquad \text{at } x = 0; \tag{6.27b}$$

Membrane conditions at the apical membrane and tight junction

$$j_k^s = J_k^{sa},\ k \in \{0,\dots,4\}, \qquad j_4^s + j_5^s + j_6^s = J_4^{sa} + J_5^{sa} + J_6^{sa}, \qquad s \in \{i,g\}, \qquad \text{at } x = L; \tag{6.27c}$$

Water flux across the tight junction

$$-\frac{h^3}{3\mu}\frac{dp}{dx} = Q^{tj}, \qquad \text{at } x = L, \tag{6.27d}$$

Open circuit condition

$$\mathscr{J}_{ATP} - \mathscr{J}_{NBC_a} + \mathscr{J}_1^{ia} + 2\delta\left(\mathscr{J}_0^{ga} + \mathscr{J}_1^{ia}\right) = 0; \qquad \text{at } x = L. \tag{6.27e}$$

The constitutive relations for transmembrane fluxes are given in equations (6.8)–(6.12).

The solution procedure is very similar to the one presented in chapter 5. In particular, we set up an iteration scheme with respect to the variable X that is repeated until water balance (6.23) is satisfied up to a given tolerance. At every iteration we solve the governing equations in the cell and cleft (6.26) along with the boundary conditions (6.27), using Comsol Multiphysics® 5.3a.

6.3 Sensitivity analysis

As our model involves estimation of many unknown parameters, we perform global sensitivity analysis to determine their relative importance on the model output. To do this we use the eFAST method proposed by Saltelli et al. (1999) and adapted to biological models by Marino et al. (2008). In what follows we briefly describe the method and its setup for our model.

6.3.1 Variance based sensitivity

eFAST is a variance decomposition method, that is valid for non-monotonic and non-linear model behaviours. We consider the generic model $y = f(\mathbf{x})$, where $\mathbf{x} = (x_1, ..., x_n)$ are the model parameters and y is the model output. For a given parameter x_i this method produces two indices: a first order sensitivity index, S_i, and a total sensitivity index, S_{Ti}.

In our application we assume that parameters $\mathbf{x}$ are distributed uniformly on logarithmic scale. However, for simplicity and without loss of generality, in this section we assume that the parameters $\mathbf{x} = (x_1, ..., x_n)$ take values that are distributed uniformly in a unit hypercube $K^n = [0,1]^n$ (even if x_i are not random variables).

The first order sensitivity index is defined as a conditional variance for parameter x_i over the total variance

$$S_i = \frac{V_i}{V} = \frac{\mathrm{v}ar_{x_i}[E_{\mathbf{x}_{\sim i}}(y|x_i)]}{\mathrm{v}ar(y)}, \tag{6.28}$$

where with $\mathbf{x}_{\sim i}$ we denote the set of all parameters but x_i. The expression in square brackets, $E_{\mathbf{x}_{\sim i}}(y|x_i)$, states that the mean of y is taken over all possible values of $\mathbf{x}_{\sim i}$ while keeping x_i fixed. The variance of the resulting quantity is then taken over all possible values of x_i. $V = \mathrm{v}ar(y)$ denotes total variance of the model output.

Due to the identity

$$\mathrm{v}ar_{x_i}[E_{\mathbf{x}_{\sim i}}(y|x_i)] + E_{x_i}[\mathrm{v}ar_{\mathbf{x}_{\sim i}}(y|x_i)] = \mathrm{v}ar(y), \tag{6.29}$$

S_i is a normalised quantity (Saltelli et al., 2010). In the above equation, $\mathrm{v}ar_{x_i}[E_{\mathbf{x}_{\sim i}}(y|x_i)]$ represents the first order effect of parameter x_i. The term $E_{x_i}[\mathrm{v}ar_{\mathbf{x}_{\sim i}}(y|x_i)$ is often called the residual and it represents the effect of all other factors and the interactions between such factors.

S_i only gives partial information about the parameter x_i. It can be interpreted as the expected reduction in variance that would be obtained if parameter x_i could be fixed. In order to capture

the total effect that includes interactions between parameter x_i and all other parameters, we apply identity (6.29) for $\mathbf{x}_{\sim i}$ and introduce the total sensitivity index

$$S_{Ti} = \frac{E_{\mathbf{x}_{\sim i}}[\mathrm{v}ar_{x_i}(y|x_{\sim i})]}{\mathrm{v}ar(y)} = 1 - \frac{\mathrm{v}ar_{\mathbf{x}_{\sim i}}[E_{x_i}(y|x_{\sim i})]]}{\mathrm{v}ar(y)}. \tag{6.30}$$

This index represents total effect of the parameter x_i, which is a sum of first order effects of parameter x_i and the variance induced by interactions of parameter x_i with other parameters. It can also be interpreted as the expected variance that would be left if all factors but x_i could be fixed. In the following we will discuss a method to compute S_i and S_{Ti}.

6.3.2 The eFAST method

Computation of the first order sensitivity index. With the assumption that $\mathbf{x}$ is distributed uniformly, the statistical r^{th} moment is given by

$$\langle y^{(r)} \rangle = \int_{K^n} f^r(x_1, ..., x_n) d\mathbf{x}. \tag{6.31}$$

Cukier et al. (1978) suggested that a multidimensional Fourier transformation of f allows to perform an ANOVA-like decomposition of f, which is useful to compute the main effects of every parameter x_i and interactions between parameters at any order. The authors noted, however, that such a transformation, is computationally expensive problem and, instead proposed an alternative, a one-dimensional Fourier decomposition. To this end a search curve exploring the space K^n is used, defined as

$$x_i(s) = G_i(\sin \omega_i s), \qquad \forall i = 1, 2, ..., n, \tag{6.32}$$

where s is a scalar quantity varying in the range $(-\infty, \infty)$, G_i is a transformation function defined later in this section and $\{\omega_i\}$, $\forall i = 1, ..., n$, is a set of frequencies, associated with each factor.

The exploring curve drives arbitrarily close to any point x_i if and only if the set of frequencies is incommensurate, i.e. none of the frequencies must be a linear combination of the others with integer coefficients, that is $\sum_{i=1}^{n} r_i \omega_i \neq 0 \ \forall r_i \in Z$ (except of $r_i = 0, \forall i$). In this case the search curve is space filling and, by the ergodic theorem (see Saltelli et al. (1999) for details), the r^{th} momentum can be computed as the integral along this curve

$$\langle y^{(r)} \rangle = \bar{y}^{(r)} = \lim_{T \to \infty} \frac{1}{2T} \int_{-T}^{T} f^r(x_1(s), ..., x_n(s)) ds. \tag{6.33}$$

For convenience we will denote $f(x_1(s), ..., x_n(s))$ as $f(s)$.

Practically, the space-filling curve is an idealisation due to the final precision of computers and an approximation of the incommensurate frequencies by rational numbers is required in the implementation. Cukier et al. (1973) showed that for ω_i positive integers, the function $f(s)$ is 2π-periodic and can be integrated within the finite interval $(-\pi, \pi)$, thus transforming (6.33) into

$$\bar{y}^{(r)} = \frac{1}{2\pi} \int_{-\pi}^{\pi} f^r(s) ds. \tag{6.34}$$

The variance V of f is defined as

$$V = \bar{y}^{(2)} - (\bar{y})^2 = \frac{1}{2\pi}\int_{-\pi}^{\pi} f^2(s)ds - \left(\frac{1}{2\pi}\int_{-\pi}^{\pi} f(s)ds\right)^2. \tag{6.35}$$

The function $f(s)$ can be expanded in Fourier series

$$y = f(s) = \sum_{j=-\infty}^{\infty} \{A_j \cos js + B_j \sin js\}, \tag{6.36}$$

where the Fourier coefficients A_j and B_j, $j \in Z$ are defined as

$$A_j = \frac{1}{2\pi}\int_{-\pi}^{\pi} f(s)\cos js \; ds, \tag{6.37}$$

$$B_j = \frac{1}{2\pi}\int_{-\pi}^{\pi} f(s)\sin js \; ds. \tag{6.38}$$

The Fourier spectrum is defined as $\Lambda_j = A_j^2 + B_j^2$, $j \in Z$ and by Parseval's theorem,

$$\sum_{j\in Z} \Lambda_j = \frac{1}{2\pi}\int_{-\pi}^{\pi} f^2(s) \; ds = \bar{y}^{(2)}. \tag{6.39}$$

This allows us to estimate the variance. Noting that $A_{-j} = A_j$, $B_{-j} = -B_j$ and $\Lambda_{-j} = \Lambda_j$, we can write (6.35) as

$$V = \sum_{j\in Z^0} \Lambda_j = 2\sum_{j=1}^{\infty} \Lambda_j, \tag{6.40}$$

where Z^0 is the set of all integer numbers, except zero.

By evaluating the spectrum for the fundamental frequency ω_i, corresponding to parameter x_i and its higher harmonics $p\omega_i$, $p = 2,3,4,...$, we can estimate V_i, the portion of the variance V arising from the uncertainty of factor i as:

$$V_i = 2\sum_{p=1}^{\infty} \Lambda_{p\omega_i}, \tag{6.41}$$

which coincides with the numerator of (6.28). Based on (6.40) and (6.41) we can compute the first order sensitivity index, $S_i = V_i/V$. In principle, its magnitude should not depend on the choice of the set of frequencies used in the computations.

Computation of total-effect indices. Let us now consider the frequencies that do not coincide with of the frequencies assigned to the parameters, i.e. all frequencies but the ones from the set $\{p_1\omega_1, p_2\omega_2, ..., p_n\omega_n\}$ with $p_i = 1,2,...,\infty, \forall i = 1,2,...,n$. Such frequencies contain the residual variance $V - \sum_i V_i$, not accounted for by the first order sensitivity indices as it includes interactions among factors at any order. It would be desirable to determine the impact of these interactions. This task, however, involves computation of $2^n - 1$ indices.

Alternatively, Saltelli et al. (1999) proposed a method to compute total sensitivity index S_{Ti}, which, although does not give a full characterisation of the system, provides a full quantification

of the importance of each x_i. This method consists in assigning a frequency ω_i to the parameter of interest i and a different frequency value $\omega_{\sim i}$ to a set of 'all but i' parameters (a complementary set of i). By evaluating the spectrum of $\omega_{\sim i}$ and higher harmonics $p\omega_{\sim i}$, we can estimate the partial variance $V_{\sim i}$, that comprises the effects of any order not including the factor i. Then, the total variance of parameter i, V_{Ti} can be calculated as $V_{Ti} = V - V_{\sim i}$, and the corresponding total sensitivity index is $S_{Ti} = 1 - S_{\sim i}$. The total sensitivity index can be interpreted as the fraction of the variance that would be left if all but x_i factors could be fixed.

Choice of the search curve. Finally, the search curve G_i has to be chosen to span the parameter space. Based on Saltelli et al. (1999) we use a transformation with a phase shift and resampling, namely

$$x_i = \frac{1}{2} + \frac{1}{\pi}\arcsin(\sin(\omega_i s + \phi_i)), \tag{6.42}$$

where ϕ_i is a random phase shift chosen uniformly in $[0, 2\pi)$. Selecting various $\{\phi_1, ..., \phi_n\}$, generates different curves to span K^n. This procedure is named resampling and we denote by N_r the number of curves used.

The Fourier analysis is performed independently over each of the N_r curves and the variances V_i and $V_{\sim i}$ are obtained by computing arithmetic means over N_r estimates. Saltelli et al. (1999) showed that for the analysis to be reliable, the minimum total number of model runs required per parameter is defined as

$$N_s = (2M\omega_{max} + 1)N_r, \tag{6.43}$$

where ω_{max} is the largest in the set of frequencies and M is an interference factor (usually 4 or higher). This factor considers how many harmonics of frequencies ω_i will be considered in our computations.

6.3.3 Setup of the sensitivity analysis

In the present application, we choose to vary 12 parameters, distributed uniformly of logarithmic scale within fairly wide ranges as reported in table 6.4. We perform separately the sensitivity analysis for two scenarios. In the first one CO_2 has the same concentration in the apical and basal regions, corresponding to 5% CO_2. For this case we set the number of points per searching curve to be $N_s = 400$. We choose the set of frequencies following the algorithm presented in Marino et al. (2008), using five searching curves, so that $N_r = 5$ and we chose the interference factor to be $M = 5$.

In the second case, we impose the apical CO_2 at 7% and the basal one at 5%. We vary 9 parameters as shown in table 6.4 without membrane permeabilities to ions (P_1^a, P_1^b and P_2^b) that are kept constant. In this case we use $N_s = 600$, $N_r = 3$ and $M = 5$.

For the implementation of both cases, we use the Matlab code developed by Marino et al. (2008), which the authors have kindly shared on their website. For both cases we also consider a

Membrane permeability	Range, 10^8 m/s
P_1^b - permeability of basal membrane to K^+	$[1,10]$
P_1^a - permeability of apical membrane to K^+	$[10,50]$
P_2^b - permeability of basal membrane to Cl^-	$[0.5,3.16]$
Amplitudes of ion channels	**Range 10^6 mol/m^2/s**
P_{ATP} - amplitude of the pump	$[1,3.16]$
P_{NKCC} - amplitude of co-transporter	$[0.5,5]$
P_{NBC_a} - amplitude of apical Na^+-HCO_3^- co-transporter	$[0.1,3.16]$
P_{NBC_e} - amplitude of apical Na^+-HCO_3^- electroneutral co-transporter	$[0.01,1]$
$P_{NBC_{b12}}$ - amplitude of basal Na^+-HCO_3^- co-transporter 1:2	$[0.1,3.16]$
$P_{NBC_{b13}}$ - amplitude of basal Na^+-HCO_3^- co-transporter 1:3	$[0.01,1]$
P_{AE} - amplitude of Cl^--HCO_3^- exchanger	$[0.1,3.16]$
P_{NHE} - amplitude of Na^+-H^+ exchanger	$[0.01,10]$
Tight junction permeability	**Range, 10^6 m/s**
P^{tj} - permeability of tight junction to Na^+ and K^+	$[1,100]$

Table 6.4: Parameters for the sensitivity analysis and their ranges.

dummy parameter, that does not appear in the model. The sensitivity index for this parameter should ideally be zero. Therefore, its deviation from zero can be interpreted as an error of the method, e.g. due to interference of frequencies or insufficient number of points N_s. This index is also used as a baseline value to determine the importance of other parameters: those with a sensitivity index less than or equal to that of the dummy parameter should be considered not significantly different from zero (Marino et al., 2008).

In our model it can happen that the system does not admit a physically feasible solution for a chosen set of parameters, e.g. the cell volume is negative or Na^+ concentration is very large (we set a threshold above 100 mM). In this case, the algorithm assigns the values 'NaN' to the solution, which results in a discontinuity of the model output $y = f(s)$. As we need to compute the Fourier coefficients (6.37) and (6.38) for function f, we chose to interpolate the curve in neighborhoods of any points of discontinuity, which makes $f(s)$ defined everywhere in the interval $(-\pi,\pi)$. The results are reported in § 6.5.1.2.

6.4 Selection of parameter values

In this section we describe the choice of the parameters, reported in tables 6.2 and 6.4. All the geometrical, thermodynamic and fluid transport parameters are preserved from the previous chapter, where their choice is addressed in detail in § 5.3. Below we thus focus on the choice of the parameters for ion transport, including the ranges for sensitivity analysis, for the transport of CO_2 and H_2CO_3 and the reactions.

6.4.1 Apical and basal solutions

Following Adijanto et al. (2009), we consider the RPE to be in a bath with the following ion composition (in mM): [Na^+]=147.7, [K^+]=5, [HCO_3^-]=26.2 and [Cl^-]=122.5. We use these values for the prescribed apical and basal ion concentrations n_k^s, $s = a, b$. The Cl^- concentration is computed from the electroneutrality condition and is smaller than in Adijanto et al. (2009) (126.1 mM), owing to the fact that authors have more charged species in the solution.

Our solution is assumed to be perfused with 5% CO_2 (unless stated otherwise), meaning that the partial pressure of oxygen is P_{CO_2} =0.05 atm. From partial pressure we can compute CO_2 concentration, using Henry's law (Henry, 1803), [CO_2]=P_{CO_2}/k_H, where $k_H \approx 29.41$ atm/M is Henry's constant. Thus with 5% CO_2 we obtain $n_5^s \approx 1.7$ mM, $s = a, b$. Throughout § 6.5 we also use different values of CO_2, always computing corresponding concentrations with Henry's law (e.g. 7% CO_2 corresponds to $n_5^s \approx 2.38$ mM and 9% CO_2 corresponds to $n_5^s \approx 3.06$ mM, $s = a, b$).

We assume that both steps of reaction (6.1) are in equilibrium in the apical and basal regions. Therefore, apical and basal H_2CO_3 concentrations can be calculated as $n_6^s = k_h n_5^s / k_d \approx 0.497 \cdot 10^{-2}$ mM, using catalysed values of k_d and k_h from Weinstein (2005a,b), see table 6.2. Following Adijanto et al. (2009), we assumed that pH= 7.45, so that $n_4^s \approx 0.358 \cdot 10^{-4}$ mM, $s = a, b$, for 5% CO_2, which gives us an estimate of dissociation constant for H_2CO_3 (i.e. an equilibrium constant in the first step of the reaction (6.1)): $K_d = k_1/k_{-1} = n_6^s/n_3^s n_4^s \approx 5.3$ 1/mM.

6.4.2 Buffer reaction

The reaction (6.2) is considered to follow the law of mass action. We would like to relate the kinetic description of this reaction to the experimentally measured buffering capacity in the RPE. A buffering solution is able to retain an almost constant pH when a small amount of acid/base is added. A quantitative measure of this resistance to pH changes is called the buffer capacity and is formally defined as

$$\beta = \frac{dn}{dpH}, \tag{6.44}$$

where n is the number of equivalents of added strong base (i.e. the base that ionizes completely or near-completely in solution) per 1 l of the solution. The buffering capacity of the intracellular buffer can be estimated from the physically based equation proposed by Van Slyke (1922)

$$\beta \approx \frac{C_B K_b [H^+]}{(K_b + [H^+])^2} \ln 10, \tag{6.45}$$

where $C_B = B + HB$ is total amount of buffer available and $K_b = k_{-3}/k_3$ is the equilibrium constant for reaction (6.2). Buffer capacity was measured experimentally by in bovine RPE by Kenyon et al. (1994). The authors fitted their data with the following second order polynomial: $\beta(pH) = 1617 - 408pH + 26pH^2$. We fit the equation (6.45) to the above curve, in order to find values for $K_b = 1.7 \cdot 10^{-4}$ mM and $C_B = 60$ mM, using least squares fit, as shown in figure 6.2.

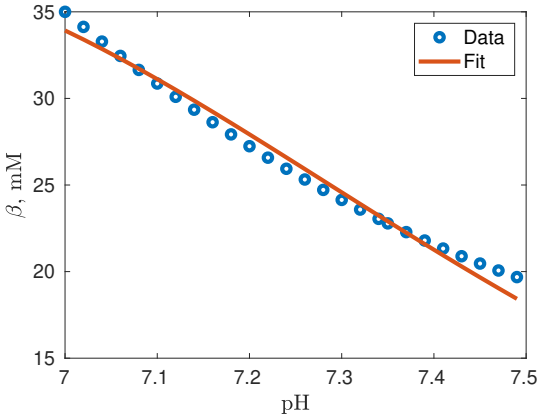

Figure 6.2: Experimental buffering capacity curve from Kenyon et al. (1994) (blue dots) and fitted curve from equation (6.45) (red line).

6.4.3 Ion channels

Diffusion coefficients D_k for Na^+, K^+ and Cl^- are assumed to be the same as in the previous chapter, $D_k = D = 1.7 \cdot 10^{-9}$ m^2/s, $k = 0,1,2$. For HCO_3^-, H^+, CO_2 and H_2CO_3 the diffusion coefficients are adapted from Krahn and Weinstein (1996), $D_3 = 1.23 \cdot 10^{-9}$ m^2/s, $D_4 = 9.69 \cdot 10^{-9}$ m^2/s and $D_5 = D_6 = 1.5 \cdot 10^{-9}$ m^2/s. The average valence of negatively charged molecules in the cell with concentration X, is assumed to be z_X =1.5, as in the previous chapter.

All membranes are permeable to CO_2. Cell membrane permeability to CO_2 varies among cell types, depending on membrane composition. It is, however, known to be much larger than ion permeabilities, as CO_2 can diffuse across the lipid bilayer since it is not charged. Itel et al. (2012) suggested that CO_2 permeability can range from about 10^{-4} m/s to 10^{-2} m/s. In our model we impose $P_5^b = 1.5 \cdot 10^{-3}$ m/s, following the value used in Krahn and Weinstein (1996), for the proximal tubule brush border. The apical permeability is assumed to be 10 times higher due to apical membrane folding, $P_5^a = 1.5 \cdot 10^{-2}$ m/s. Similarly, basolateral permeability to H_2CO_3 is taken to be $P_6^b = 1.28 \cdot 10^{-5}$ m/s (Krahn and Weinstein, 1996) with the apical one being 10 times larger, $P_6^a = 1.28 \cdot 10^{-4}$ m/s. Due to a lack information, the tight junction is assumed to have the same permeability to CO_2 and H_2CO_3 as the apical membrane.

The rest of the parameters are addressed in the sensitivity analysis (see table 6.4). We span the ranges uniformly on logarithmic scale, since most of the parameters are varied over several orders of magnitude. Parameters that are better studied in literature are varied over a smaller range (such as membrane permeabilities and the amplitude of the pump), whereas those for which less information is available are varied through a wider range. The baseline values of the parameters reported in table 6.2 are taken to be the mean of the logarithm of their distribution average of their range. Therefore, in the following when we refer to an 'average' value we mean that we have taken the average of values uniformly distributed on a logarithmic scale. In what

follows, we justify the choice of the ranges reported in table 6.4.

The apical and basolateral membrane permeabilities to K^+ are chosen to be similar to those proposed in the previous chapter (see § 5.3). We span the apical permeability to K^+across the range 1–5·10^{-7} m/s (with the upper bound being equal to the value considered in the previous chapter), and the baseline value is $P_1^a = 2.23 \cdot 10^{-7}$ m/s. Similarly, the basolateral permeability to K^+ is assumed to be within the range 1–10·10^{-8} m/s, with the average value of $P_1^b = 3.16 \cdot 10^{-8}$ m/s.

Basolateral permeability to Cl^- is also kept similar to that in the previous chapter. In particular, for the sensitivity analysis we vary it within the range 0.5–3.2·10^{-8} m/s (the value of 0.8·10^{-8} m/s was used in chapter 5), with the average value of $P_2^b = 1.25 \cdot 10^{-8}$ m/s.

The existence of physically acceptable solutions is very dependent on the amplitude of the pump, P_{ATP}, since it is the main driver of the system. Therefore, in the sensitivity analysis we allow this variable to vary only over small range of $1 - 3.16 \cdot 10^{-6}$ mol/m^2/s (with the lower bound being equal to the value considered in the previous chapter based on McLaughlin and Mathias (1985)), with the average value of $P_{ATP} \approx 1.77 \cdot 10^{-6}$ mol/m^2/s.

The amplitude of NKCC co-transporter, P_{NKCC} is spanned within 0.5–5·10^{-6} mol/m^2/s with an average value of $P_{NKCC} \approx 1.78 \cdot 10^{-6}$ mol/m^2/s (the value 3·10^{-6} mol/m^2/s is used in chapter 5), that is used for the typical solution. We note that La Cour (1992) estimated the Cl^- flux from this channel to be about 0.92·10^{-6} mol/m^2/s, which has similar magnitude as P_{NKCC}.

Much less is known about the magnitude of the other channels. Therefore, we span them across larger ranges for the sensitivity analysis. In particular, amplitudes of the apical and basal 1:2 Na^+-HCO_3^-co-transporters (P_{NBC_a}, $P_{NBC_{b12}}$) and HCO_3^--Cl^-exchanger (P_{AE}) are assumed to be in the range of 0.1–3.16·10^{-6} mol/m^2/s, with the upper bound to be the same as for the pump. The average value is $\approx 5.62 \cdot 10^{-9}$ mol/m^2/s.

The amplitudes of the other two Na^+-HCO_3^-co-transporters (1:1 apical, P_{NBC_e} and 1:3 basolateral, $P_{NBC_{b13}}$) are chosen to have a wider range shifted to the left, 0.01–1·10^{-6} mol/m^2/s, as the existence of these channels is less evident within the literature than that of the previous ones (Adijanto et al., 2009). The corresponding average values are 10^{-7} mol/m^2/s. The Na^+-H^+ exchanger, on the other hand is referred to more extensively in the literature (Lin and Miller, 1991; Lin et al., 1992; Gallemore et al., 1998) and is allowed to span three orders of magnitude, 0.01–10·10^{-6} mol/m^2/s, with the average value of P_{NHE} ≈3.16·10^{-7} mol/m^2/s.

Finally, the tight junction is assumed to be permeable only to cations and uncharged species. The permeability to Na^+ and K^+, P^{tj}, is assumed to be the same. In the previous chapter we showed that the tight junction permeability to K^+ does not affect the solution unless it is greater than 10^{-5} m/s. Moreover, Gallemore et al. (1998) suggested that the passive absorptive flux of Na^+ towards the choroid through the paracellular pathway, might exceed the active secretory Na^+ flux towards the subretinal space through the transcellular route, implying that tight junctions may play a significant role in Na^+transport. We assume here that P^{tj} is within the range (1-100)·10^{-6} m/s, with baseline value of $P^{tj} = 10^{-5}$ m/s.

6.5 Results

6.5.1 The case of no difference in CO_2 concentration between the apical and the basal region

6.5.1.1 Typical solution

In this section we show the model results using, as baseline, the parameter values reported in table 6.2. Moreover, for each considered species, we impose the same concentration in the apical and basal regions, as shown in figure 6.3. In the following of this chapter (§ 6.5.2) we will also consider the case in which CO_2 concentration is higher in the apical region than in the basal.

In the absence of concentration jumps across the RPE the concentration of all species in the cell is constant, as it also happens in the simplified version of the model, presented in chapter 5. In figure 6.3 (left cell) we report in black the values of the ion concentrations that we impose (in the apical and basal region) and in blue the values computed by the model. Moreover, the TEP is also calculated as the potential difference across the RPE. In particular, we impose the value of the potential in the basal region (set equal to zero, without loss of generality) and compute the potential in the apical region. The concentrations predicted for Na^+, K^+ and Cl^- are $n_0^i = 19$ mM, $n_1^i = 129.2$ mM and $n_2^i = 45.8$ mM, respectively. These values are quite close to those reported in figure 5.1 and, as discussed there, to measured values (Adijanto et al., 2009; Reichhart and Strauß, 2014; Strauss, 2011). The TEP is predicted to be equal to 16.8 mV, which is a bit higher than we obtained in chapter 5, but still close to experimental observations (Reichhart and Strauß, 2014; Frambach et al., 1989; Quinn and Miller, 1992). In addition, we find a concentration of HCO_3^-, $n_3 = 17.8$ mM and a pH of 7.28. This is comparable with the observational data in Gallemore et al. (1997), where the authors report 24 mM for HCO_3^- concentration and pH of 7.4. We note that, owing to the large permeability of cell membranes to CO_2 and H_2CO_3, their concentrations in the cell are predicted to be almost exactly the same as the values imposed in the apical and basal regions, i.e. $n_5^i = 1.7$ mM and $n_6^i = 0.49 \cdot 10^{-2}$ mM.

As schematically shown in figure 6.3 (right cell) ion fluxes (K^+, Na^+, $Cl^-$and HCO_3^-) are all directed from the apical to the basal region. For both water and ion fluxes we use the convention that a negative value corresponds to a flux from the subretinal space to the choroid. We note that the model now predicts the existence of a net Na^+ flux, which was zero in the version of the model presented in chapter 5, since now we account for the presence of the Na^+- HCO_3^- co-transporter in the basolateral membrane and Na^+ transport across the tight junction.

Measurements of ion fluxes across the RPE provide very sparse values and different authors even found fluxes in opposite directions. Our model predicts a Na^+flux of $\approx -1.44 \cdot 10^{-6}$ mol/m^2/s, directed towards the choroid, which is in agreement with the experimentally measured flux of $-1.5 \cdot 10^{-6}$ mol/m^2/s in isolated bullfrog RPE-choroid preparation (Hughes et al., 1984). Miller and Edelman (1990) and Miller and Steinberg (1977), however, found that Na^+ flux is directed

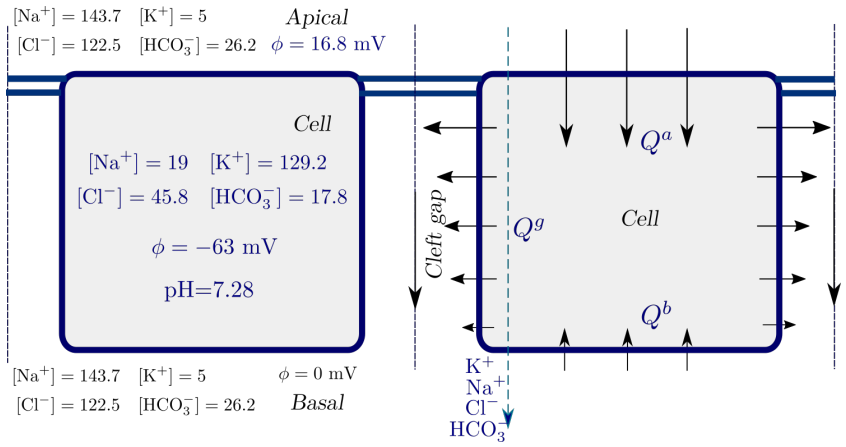

(a)

Figure 6.3: Left cell: typical values for the concentrations and the potential in the cell. The values in black are prescribed and the values in blue are predicted by the model. Right cell: directions and representative magnitudes of water and ion fluxes.

towards the subretinal space.

The K^+ flux predicted by our model is about $\approx -1.69 \cdot 10^{-6}$ mol/m^2/s, which is similar to the one reported in the previous chapter, but greater than observed experimentally, which ranges between $-0.2 \cdot 10^{-7}$ and $-8 \cdot 10^{-7}$ mol/m^2/s (Hughes et al., 1984; Miller and Edelman, 1990). The predicted Cl^- flux is larger than for the previous two species, $\approx -2.34 \cdot 10^{-6}$ mol/m^2/s and is comparable to the measured values ranging between -0.5 and $-2 \cdot 10^{-6}$ mol/m^2/s (La Cour, 1992). Finally, the calculated HCO_3^- flux is $\approx -7.79 \cdot 10^{-7}$ mol/m^2/s, which is smaller than the one estimated by Hughes et al. (1984), $-3.13 \cdot 10^{-6}$ mol/m^2/s. Since CO_2 concentration is almost constant throughout all the considered domains, the CO_2 flux is very small in this case.

Owing to the presence of active ion pumping we find that concentration gradients form in the thin cleft gaps that separate adjacent cells. This is shown in figure 6.4(a), where we report the departure of the concentration of each ion in the cleft from the corresponding values in the basal region. In figure 6.4(b) we show the electrical potential along the cleft gap. Interestingly, the potential gradient is positive, opposite to what we found in the model presented in chapter 5 (see figure 5.2). This is probably due to the fact that the tight junction is now assumed to be permeable to Na^+.

Figure 6.5(a) shows the osmolarity along the cleft (red curve). In the figure we also report the osmolarity in the cell, which is constant (blue curve), and the imposed values of the osmolarity in the apical (yellow circle) and basal (purple circle) regions. The osmolarity in the cleft is higher than in the cell and this induces a local osmotic flux, similarly to what we found in chapter 5. The overall effect is the generation of a net water flux across the RPE, directed from the apical to the basal region. A schematic representation of water fluxes through the cell and the cleft is shown in figure 6.3 (right cell). For this particular set of parameters we find a value of the

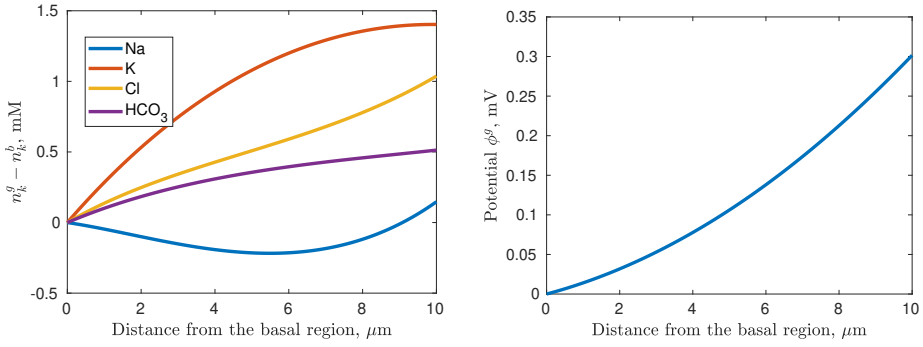

(a) (b)

Figure 6.4: (a) Deviation of the ion concentrations along the cleft from those in the basal region. The x-axis goes along the symmetry mid line ($y = 0$) of the cleft, from the basal region to the tight junction, as shown in figure 6.1. (b) The electrical potential along the cleft.

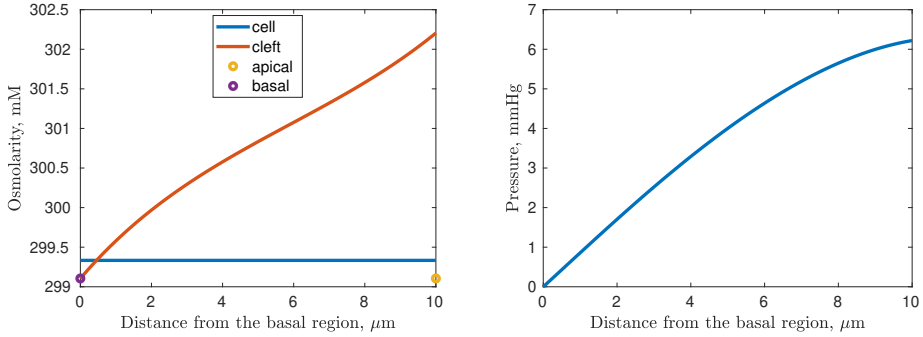

(a) (b)

Figure 6.5: (a) Osmolarity distribution in the cell and the cleft. (b) Fluid pressure along the cleft.

flux per unit surface averaged over apical membrane and tight junctions, through the RPE to be equal to $Q \approx -9.36 \cdot 10^{-9}$ m/s, comparable with the measured values of $-[1.1, 2.8] \cdot 10^{-8}$ m/s (Shi et al., 2008).

Fluid pressure along the cleft gap is shown in figure 6.5(b). We note that the maximum pressure in the cleft is relatively large (≈ 7 mmHg). As commented in chapter 5, such a large pressure might not occur in reality since cell membranes are compliant and will be pushed apart by a pressure build up in the cleft. We note, however, that a small change in the cleft thickness would modify significantly the pressure, which depends on the depth of the domain to the third power, without notable modification of the flow, as it can be anticipated on the basis of the results shown in figure 5.5(b).

6.5.1.2 Sensitivity analysis

The model discussed in this chapter has a number of parameters, many of which are extremely difficult to quantify. For this reason we perform a global sensitivity analysis, applying the method described in § 6.3, and we describe in this section the results obtained. We modify the 12 parameters reported in table 6.4, which all characterise ion transport across the cell membranes and the tight junction. In the table we also report, for each quantity, the range of variation adopted for the sensitivity analysis, which we keep quite large.

We investigate the sensitivity of water flux, TEP and ion fluxes to model parameters. The main outputs of the global sensitivity analysis are the first order and the total sensitivity indexes. We recall here the meaning of these parameters. We estimate the sensitivity based on the expected variance of the output upon changes of the parameters. The first order sensitivity index, S_i, describes the 'main effect' for each parameter, as a measure of the expected reduction of variance if that parameter was kept fixed. The total sensitivity index, S_{Ti}, on the other hand, captures first order effect and the interaction of a given parameter x_i with other parameters. It measures the expected variance that would be left if all but a given parameter were fixed.

The results obtained concerning the sensitivity for water flux are reported in figure 6.6, where the histograms represent the values of the first (a) and total (b) sensitivity indexes. The height of each bar is thus a measure of how much the corresponding parameter affects water flux. We note that not all factors are varied by the same percentage. The parameters that have the largest effect on water transport are the tight junction permeability to Na^+ and K^+(P^{tj}), the amplitude of the pump (P_{ATP}), the amplitude of Na^+-H^+ exchanger (P_{NHE}) and, to a smaller extent, the amplitude of basal Na^+-HCO_3^- 1:2 co-transporter ($P_{NBC_{b12}}$). Inspection of figures 6.6(a,b) shows that the two indexes used lead to qualitatively similar results, in the sense that they identify the same parameters as being important for modifying water flux.

For these parameters we show in figure 6.7 scatter plots with the values of water flux, Q, taken in each numerical experiment versus the corresponding value of the parameter. In the plots we also report in black a curve corresponding to a second order polynomial function fitted to the data with the least squares method. This shows how water flux varies with the above parameters (see also the arrows in the bars of figure 6.6). We recall that water flux is towards the choroid when $Q < 0$. The figures show that water flux towards the choroid grows (Q becomes more negative) if P_{ATP}, P_{NHE} and P^{tj}, grow, whereas it decreases for increasing values of $P_{NBC_{b12}}$. The fact that pump (P_{ATP}) has an important role is understandable, from the physical point of view: the pump is the 'active' element in our system and all ion fluxes and standing concentration gradients are a consequence of this pump.

In figure 6.8 we show the sensitivity indexes for TEP. In this case the only parameter that is capable of significantly modifying TEP is the tight junction permeability to Na^+ and K^+(P^{tj}). In particular, if P^{tj} increases TEP decreases. To a significantly lower extent, permeability of the basal membrane to K^+(P_1^b) also has some role on TEP and qualitatively it acts similarly to P^{tj}:

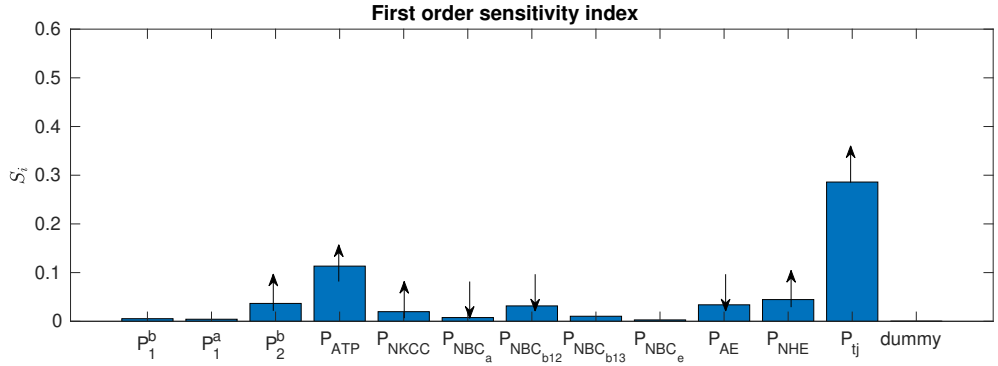

(a)

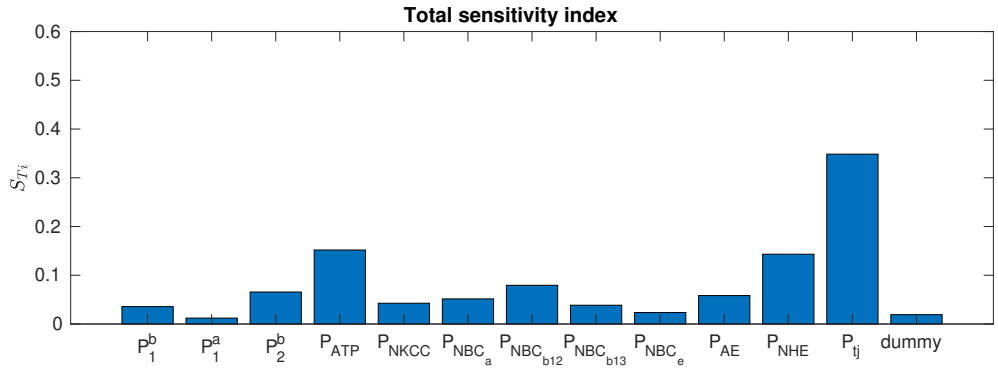

(b)

Figure 6.6: First and total sensitivity indices for water flux. In panel (a) we report within the largest bars arrows that indicate how the magnitude of water flux is modified by that particular parameter. An upward pointing arrow indicates that water flux towards the choroid increases in magnitude if the parameter is increased. The sense of variation is the same in panel (b).

as P_1^b increases TEP decreases.

Finally, in figure 6.9 we report the sensitivity indexes for ion fluxes. In the figure indexes corresponding to different ions are reported with a different colour. Na^+ flux is mostly influenced by P^{tj} and, as expected, it increases with increasing values of the permeability. The amplitude of Na^+-H^+ exchanger (P_{NHE}) also influences Na^+ transport as it facilitates sodium flux across the apical membrane. K^+ flux is strongly affected both by P^{tj} and P_1^b, which is the permeability of the basolateral membrane to it, and the flux grows with both parameters. K^+ flux towards the choroid also grows as the amplitude of the pump is increased. Cl^- flux depends significantly on P_{NHE} and P_{AE}. This flux is generally directed towards the choroid but decreases in magnitude as P_{NHE} increased and can even be reversed for very large values of P_{NHE}. Finally, HCO_3^- flux is significantly affected only by the amplitude of Na^+-H^+ exchanger (P_{NHE}). In summary, the sensitivity analysis for ion fluxes highlights the great importance the Na^+-H^+ exchanger and the tight junction permeability have on the system.

As mentioned in chapter 4 it is believed that ion and water fluxes through epithelia are tightly

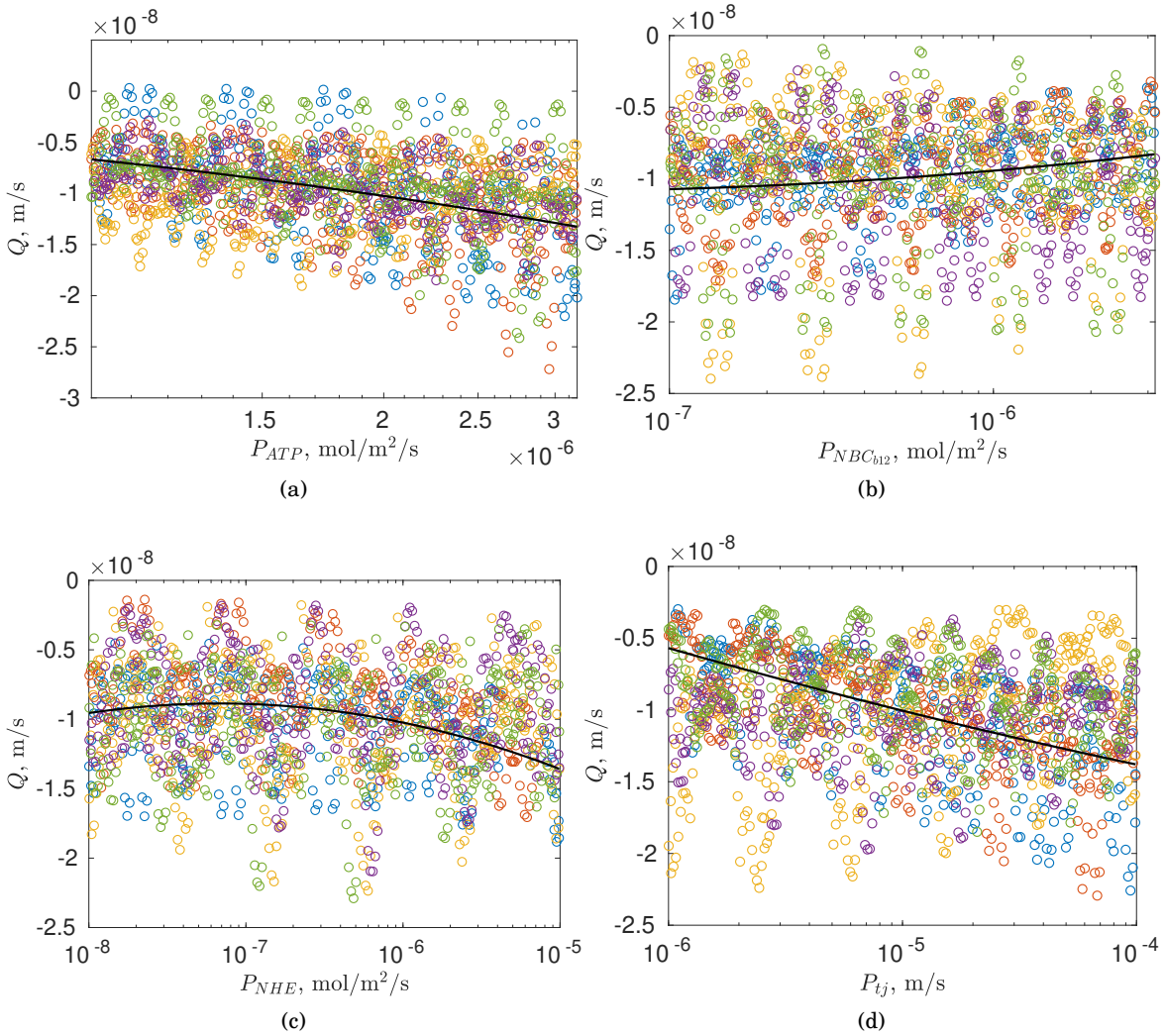

Figure 6.7: Scatter plots for water flux Q vs four parameters with largest sensitivity indices: (a) P_{ATP}, (b) $P_{NBC_{b12}}$, (c) P_{NHE} and (d) P^{tj}. Each point corresponds to a numerical experiment. Different colours correspond to different searching curves from the equation (6.42).

linked to each other and that, roughly speaking, water follows the ions. To verify this statement in figure 6.10 we plot water flux versus each of the ion fluxes. In the figures each point corresponds to a numerical experiment and we identify a general trend in each scatter plot by reporting (in black) a line fitted with the least squares method. The figure shows that a strong link exists between water flux and Na^+ and HCO_3^- fluxes. Cl^- flux is also relatively strongly correlated with water flux. On the other hand a clear correlation is not found for K^+ flux. Generally speaking, the model confirms the link between ion and water fluxes for most, but not all, ions.

We finally investigate the dependency of water flux on CO_2 concentration in the apical and basal regions as shown in figure 6.11. The scatter plot suggest that water flux does not depend on the amount of CO_2. This is in disagreement with Adijanto et al. (2009), where authors performed

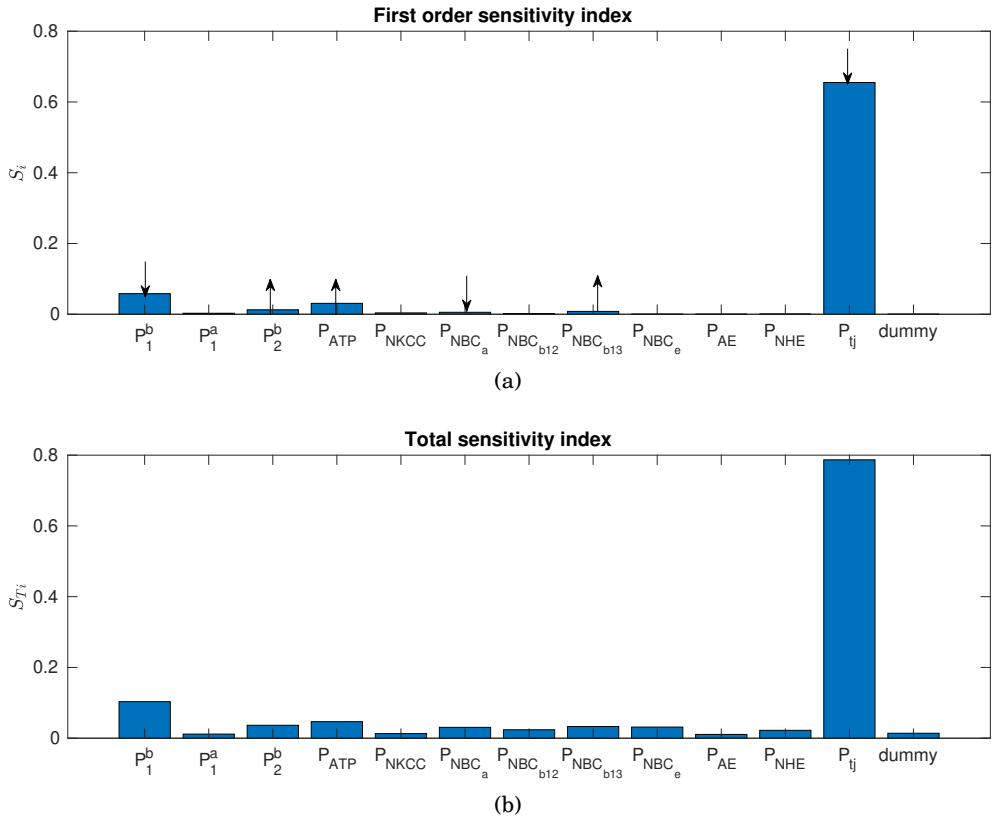

Figure 6.8: First and total sensitivity indices for TEP. In panel (a) we report within the largest bars arrows that indicate how the magnitude of TEP is modified by that particular parameter. An upward pointing arrow indicates that TEP increases in magnitude if the parameter is increased. The sense of variation is the same in panel (b).

experiments in human fetal RPE, and found that increasing the amount of CO_2 in the solution on both sides of the epithelium resulted in the increase in water flux.

6.5.2 The case of an imposed difference in CO_2 concentration between the apical and the basal region

6.5.2.1 Typical solution

We now consider the case in which CO_2 concentration is higher in the apical region than in the basal. This is physically relevant since we know that the retina produces CO_2 and one of the roles of the RPE is to remove it from the subretinal space. It is thus interesting to investigate how the system would respond to CO_2 accumulation in the apical region. To this end we keep CO_2 concentration in the basal region fixed at 5% (as it was done in § 6.5.1) and increase the concentration in the apical region to 7%. This creates a jump in CO_2 concentration across the RPE, which induces spatial variability of all variables in x-direction. As explained in § 6.2.2.3

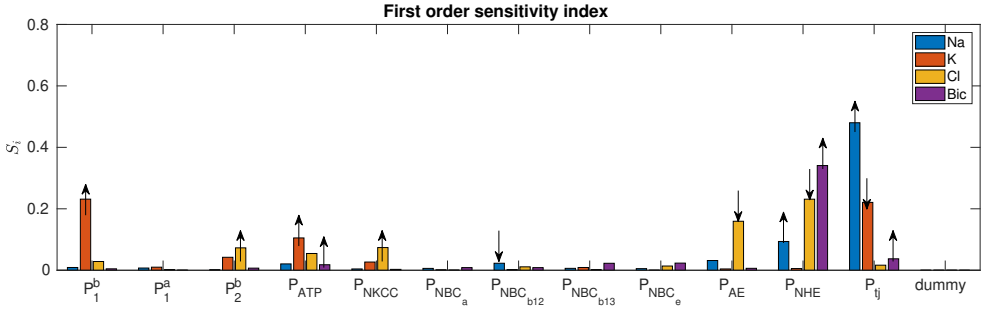

(a)

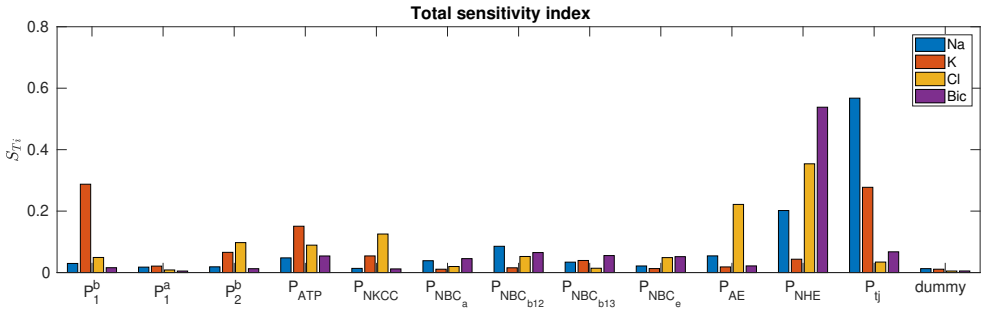

(b)

Figure 6.9: First and total sensitivity indices for ions fluxes. In panel (a) we report within the largest bars arrows that indicate how the magnitude of the ion flux is modified by that particular parameter. An upward pointing arrow indicates that ion flux towards the choroid increases in magnitude if the parameter is increased. The sense of variation is the same in panel (b).

and § B.2 concentration variability in the y-direction is $\approx \delta$ times smaller than in the x direction and is, therefore, neglected.

Departure of ion concentrations from the corresponding average values $\hat{n}_k^i$ along the cell are shown in figure 6.12(a). The average values are approximately the same as reported in figure 6.3. Concentrations of Na^+ and K^+ decrease towards the apical membrane, whereas concentrations of Cl^- and HCO_3^- increase. Moreover, the potential in the cell also has a gradient (not shown in the figures). The potential grows from the basal to the apical region. Ion concentrations in the cleft are shown in figure 6.12(b). The profiles in the cleft are very similar to those found in the case with no CO_2 jump across the RPE, and shown in figure 6.4.

Interestingly, despite the fact that ion concentration gradients are generated in the cell, the net ion fluxes are almost the same as in the case discussed in § 6.5.1. This is because not only the concentrations but also the electrical potential vary along the cell, and they act in opposite directions in the electrodiffusive ion transport. In this scenario transepithelial CO_2 flux equals to $-9.05 \cdot 10^{-5}$ mol/m^2/s, and is directed from apical to basal region.

Figure 6.13(a) shows the deviation of CO_2 profiles in the cell and cleft from the value in the basal region. The profiles are very close to each other, again as a consequence of the large permeability of the membranes to CO_2. The two concentration profiles only differ in a small

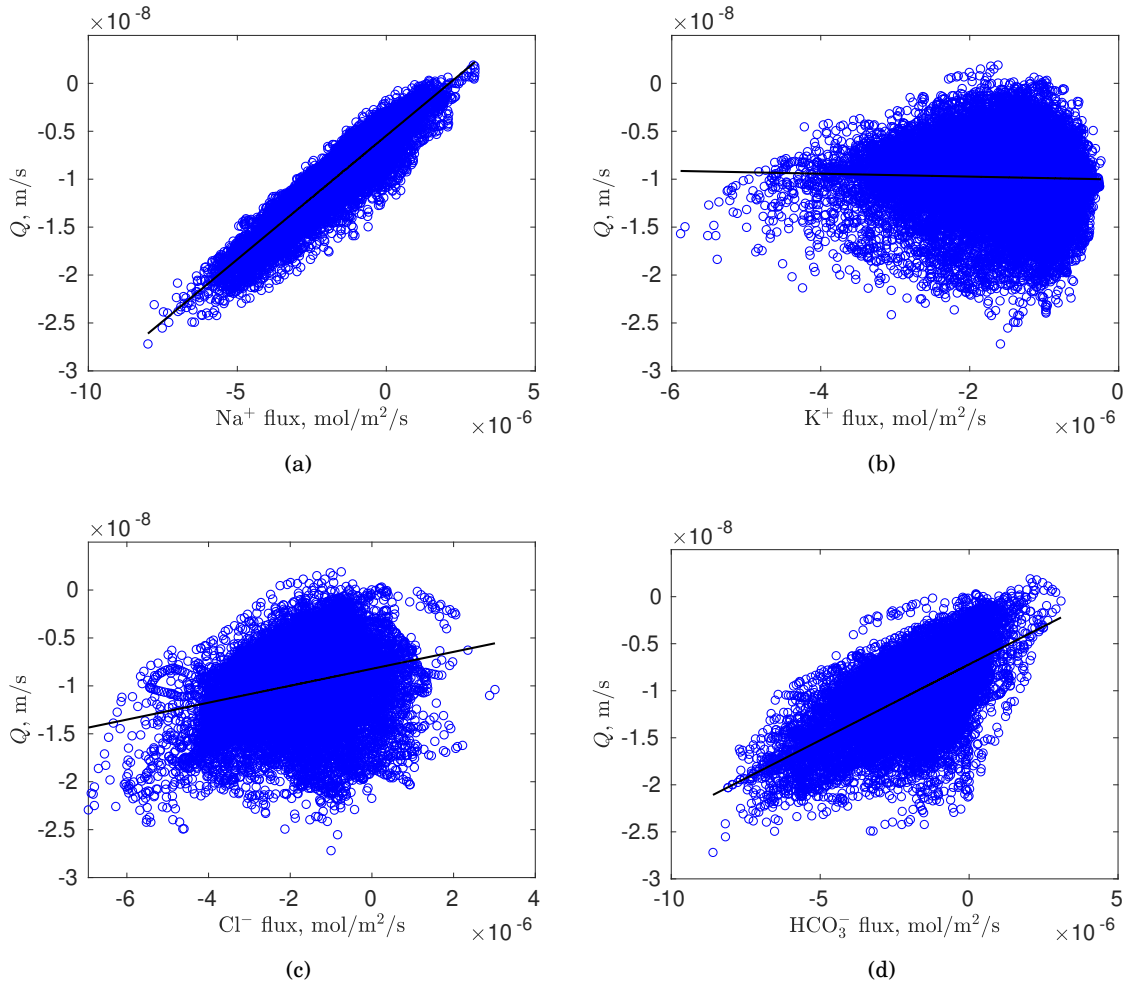

Figure 6.10: Scatter plots for water flux Q vs (a) Na^+, (b) K^+, (c) Cl^- and (d) HCO_3^- flux. Each point corresponds to a numerical experiment.

region at the boundary with basal region, since for the cleft we impose a Dirichlet condition and for the cell we impose a membrane condition and we can have a jump in CO_2 concentration across the basal membrane.

Profiles of pH in the cell and cleft are shown in figure 6.13(b). pH in the cell is lower than in the cleft and both curves decay towards the apical membrane.

The gradients of osmolarity in the cell and the cleft, shown in figure 6.14(a), induce a change in the transepithelial water flux to the value of $-0.43 \cdot 10^{-8}$ m/s. The direction of water fluxes across cell membranes is schematically shown in figure 6.14(b).

In order to test the effect of CA inhibition, we introduce a factor α that multiplies the reaction rates (k_d and k_h) of equation (6.1), and thus allows to reduce them simulating inhibition of this reaction. The response of water flux Q to a progressive decrease of this factor is shown in figure 6.15. The three curves correspond to three different CO_2 concentrations (5, 7 and 9%), imposed

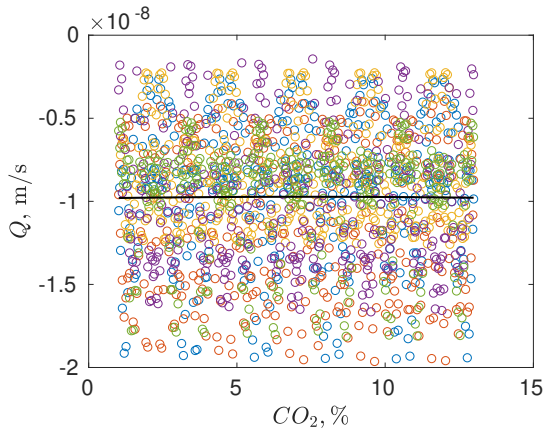

Figure 6.11: Water flux as a function of extracellular CO_2 concentration. Each point corresponds to a numerical experiment and colors correspond to different search curves.

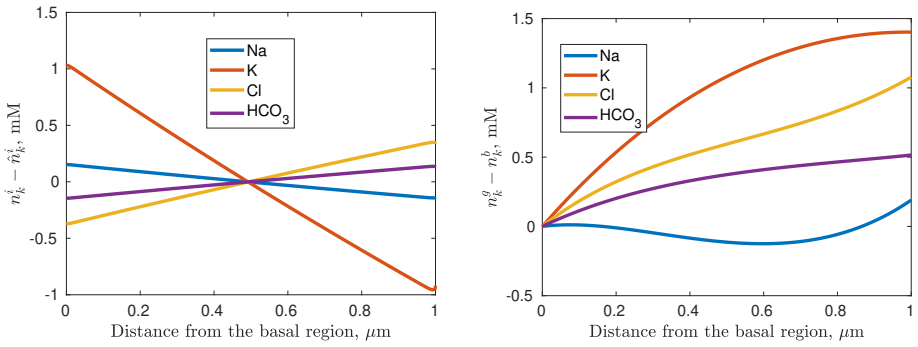

(a) (b)

Figure 6.12: (a) Deviation of ions concentration from the average value in the cell. (b) Deviation of ions concentration in the cleft from their values in the basal region.

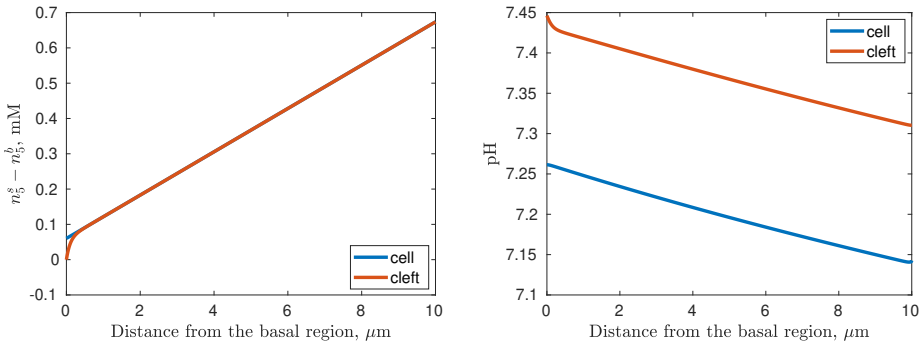

(a) (b)

Figure 6.13: (a) CO_2 concentration in the cell and cleft. (b) pH in the cell and cleft.

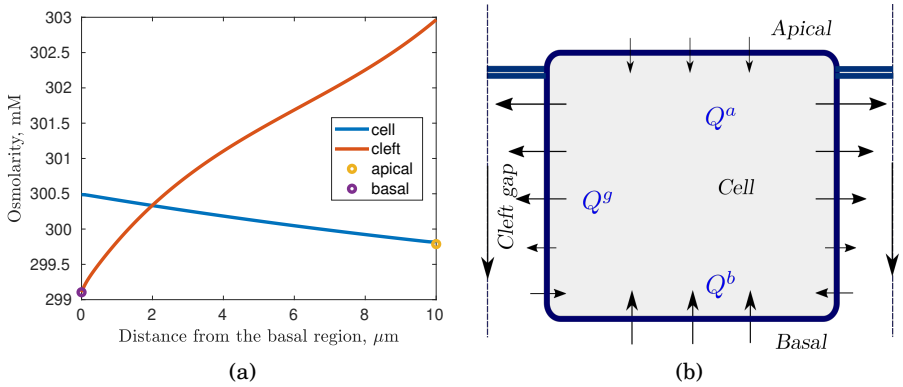

Figure 6.14: (a) Osmolarity distribution in the cell and cleft. (b) Sketch of the direction of water fluxes in the case of CO_2 jump across the RPE.

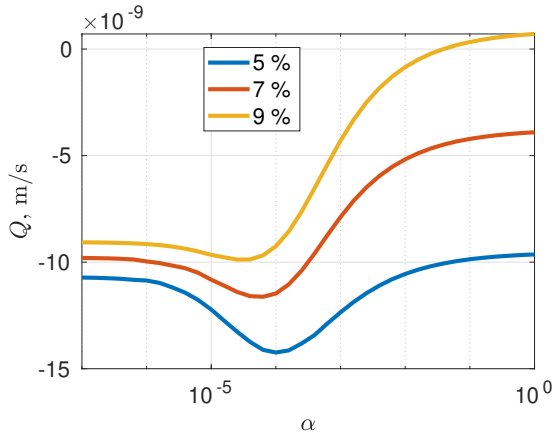

Figure 6.15: Water flux as a function of the CA activity. The values of α on the x-axes are factors that multiply the reaction rates k_d and k_h of the reaction (6.1). The value $\alpha = 1$ corresponds to full catalyser capacity (the reaction rates from table 6.2); as the value of α decreases the catalyser is progressively inhibited. Different curves correspond to different values of apical CO_2 concentration: 5,7 and 9%, while basal CO_2 is kept at 5%.

in the apical region (the basal CO_2 concentration is kept fixed to 5%). The figure shows that inhibition of CA leads to a significant change in water flux towards the choroid. When a CO_2 drop across the RPE is imposed water flux towards the choroid increases significantly by inhibiting the reaction (6.1). When CO_2 concentration is the same in the apical and basal regions the water flux reaches a maximum absolute value for $\alpha \approx 10^{-4}$, which occurs approximately when the time scale for diffusion of CO_2 across the cell and its reaction time are similar.

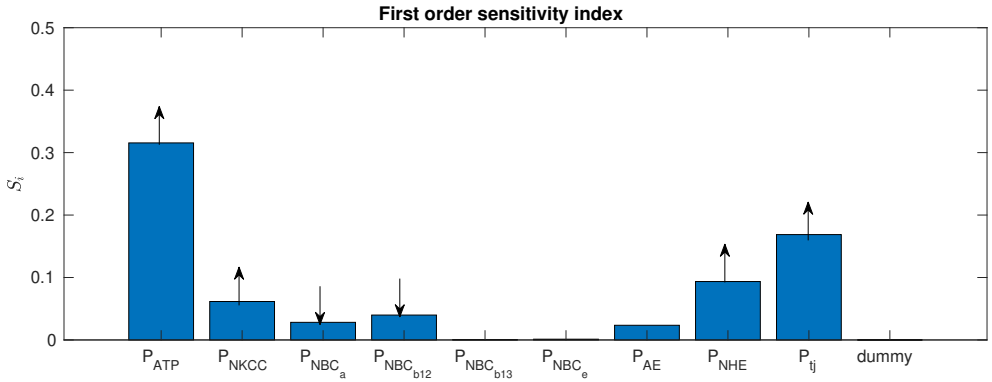

(a)

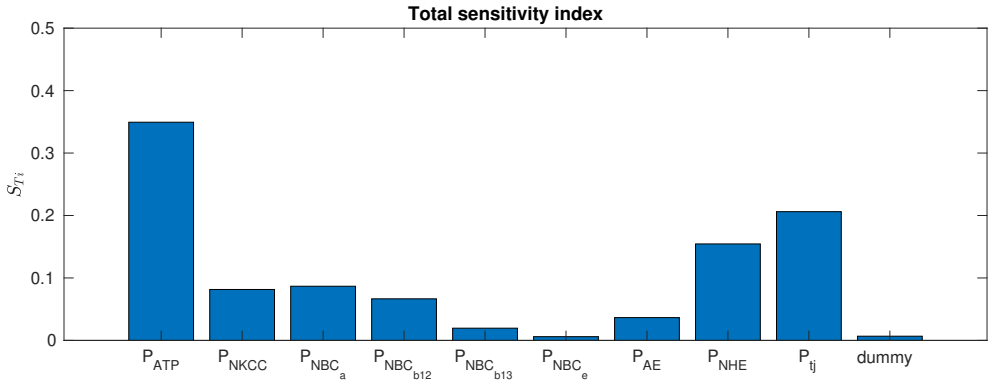

(b)

Figure 6.16: First and total sensitivity indices for water transepithelial water flux in the case of CO_2 jump across the RPE.

6.5.2.2 Sensitivity analysis

In this section we discuss the results of the sensitivity analysis, considering the case in which we have a jump in CO_2 concentration across the RPE. We investigate the sensitivity of the model with respect to the same parameters as in § 6.5.1.2, but now we keep fixed membrane permeabilities to ions to the values we used in § 6.5.2.1, since we showed that they play a relatively minor role (see figures 6.6, 6.8 and 6.9). Thus, in this case we vary 9 model parameters (table 6.2 without membrane permeabilies to ions: P_1^b, P_1^a and P_2^b).

Sensitivity of water flux and TEP to these parameters are shown in figures 6.16 and 6.17(a). These figures show that the results are qualitatively similar to those discussed in the absence of a CO_2 jump across the RPE. In figure 6.17(b) we report the results of the sensitivity analysis for CO_2 flux, which is found to be most sensitive to the amplitude of Na^+-H^+ exchanger (P_{NHE}).

Ion fluxes depend on water flux similarly as we discussed in § 6.5.1.2 (figure 6.9) and we don't show the corresponding plots for the sake of brevity.

The scatter plot in figure 6.18(a) shows the effect of CA inhibition on water flux Q by varying 9 model parameters and α. The average behaviour suggests that Q increases with CA inhibition.

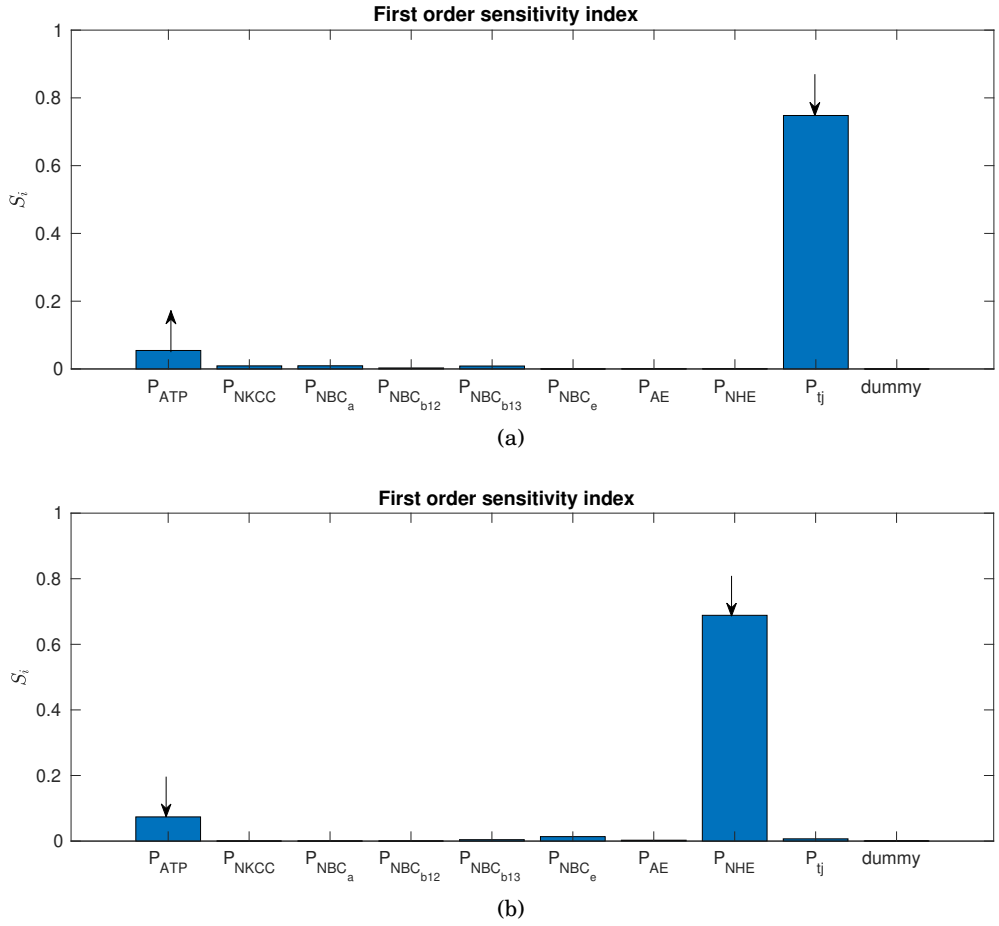

Figure 6.17: First order sensitivity index, S_i, for (a) TEP and (b) CO_2 flux.

Similarly to figure 6.15, we observe that Q has the largest magnitude in the neighborhood of $\alpha \approx 10^{-4}$.

Finally, the scatter plot in figure 6.18(b) shows the effect of CA inhibition on CO_2 flux. We note that variation of this flux from the mean value is less than 2%, suggesting that model parameters do not significantly influence it.

6.6 Discussion

Fluid accumulation in the subretinal space (SRS) remains a relatively poorly understood problem, despite its clinical relevance for the onset and development of various sight-threatening pathological conditions, such as macular oedema, retinal detachment and age related macular degeneration (Gallemore et al., 1998). Understanding fluid transport and the ways to manipulate it to treat these conditions is, therefore, a crucial question in retinal physiology. In particular, inhibition of carbonic anhydrase (an enzyme that catalyses CO_2 hydration) and the basolateral anion exchanger, have been shown to be effective to treat fluid accumulation (Cox et al., 1988;

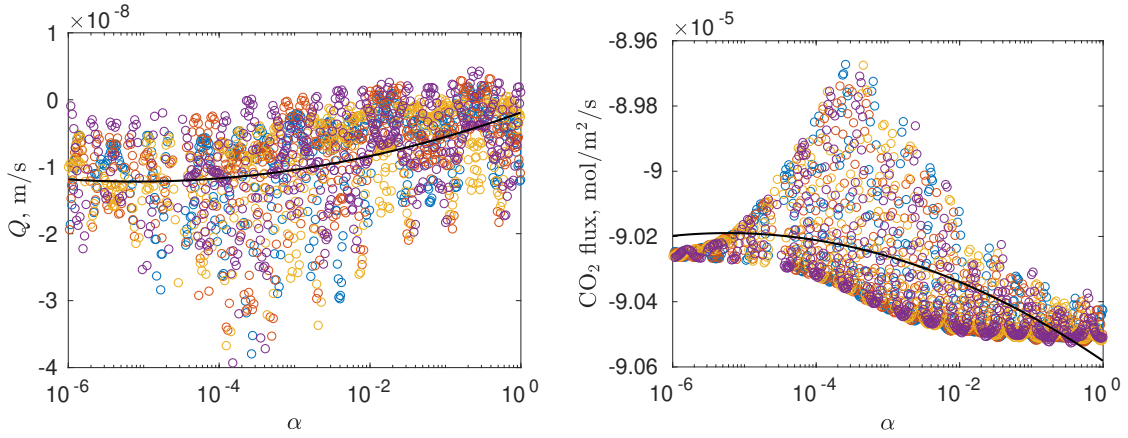

Figure 6.18: Scatter plots for (a) water flux and (b) CO_2 flux as functions of CA inhibition. The values of α on the x-axes are factors that multiply the reaction rates k_d and k_h of the reaction (6.1). The value $\alpha = 1$ corresponds to full catalyser capacity (the reaction rates from table 6.2); as the value of α decreases the catalyser is progressively inhibited. Different colours correspond to different search curves.

Fishman et al., 1989; Iserovich et al., 2011). Nevertheless, the underlying mechanisms remain unclear, motivating the present work.

In chapter 5, we developed a mathematical model aimed at understanding the mechanisms of fluid transport, with a particular focus on the relative importance of osmosis and electroosmosis. The model coupled fluid and ion dynamics in a coherent framework, accounting for the presence and transport of three different species: Na^+, $K^+$and Cl^-. We showed that local osmosis generated by the presence of a concentration gradient in the space between two cells, the cleft gap, driven by active ion pumping, is the dominant mechanism of fluid transport, with electroosmosis being two orders of magnitude smaller. Therefore, this first generation model provided us with qualitative understanding of the relevant flow mechanisms.

To improve this understanding and obtain a better quantitative estimate of water flux, in this chapter we have extended the model from chapter 5 to account for other potentially important species, in particular, HCO_3^-, H^+, CO_2 and H_2CO_3. Considering these species is of relevance since it allows us to predict ion fluxes that better reproduce the physiological behaviour of the RPE, as we account for additional channels that are known to be present in the RPE cell membranes. Moreover, it allows us to investigate the role of CO_2 flux and its possible coupling with water transport. Finally, we account for chemical interactions of the species and study their effect on water transport, with a particular focus CO_2 hydration, as this allows us to investigate the effect of carbonic anhydrase (CA) inhibition.

The model, therefore, considers the presence of seven species in the cell and the cleft, an anion gap in the cell and an intracellular buffer. Ions are transported by active and passive

channels across the membranes and CO_2 and H_2CO_3 can diffuse across them as they are not charged. Fluid transport is assumed to be driven by osmosis, as the results of the previous chapter indicate that electroosmosis is subdominant. Fluid and solute transport are thus coupled through advection, osmotic fluxes and flux balance in the cell. The models in the cell and cleft are significantly simplified via asymptotic approximation to a system ODEs in the choroid–SRS direction, using the fact that the cleft gap is long and thin and that certain reactions are in equilibrium.

The addition of species and of the corresponding ion channels resulted in a large set of parameters, the estimation of which is a crucial point for this model. For this reason we performed a global sensitivity analysis using the extended Fourier amplitude sensitivity test (eFAST) (Saltelli et al., 1999) and determined which parameters affect most the model outputs. The sensitivity analysis also allows us to better understand the behaviour of the system.

We focus on two different conditions. We first consider the same concentration of CO_2 on both sides of the epithelium. This allows us to investigate in a more refined way the coupling between fluid and ion transport across the RPE. We then assume that CO_2 is being excessively produced in the SRS as a result of high photoreceptors metabolic activity (Adijanto et al., 2009). As CO_2 is absorbed into the choroid at a very fast rate, its production in the SRS may result in a transepithelial gradient of CO_2. We model this condition by imposing a higher CO_2 concentration in the SRS with respect to the one in the choroid. For both scenarios (with and without CO_2 jump across the RPE) we present results for a typical case and investigate the sensitivity of the model output to model parameters.

When CO_2 concentration is the same across the epithelium, all variables in the cell can be approximated as constants with the accuracy of order $\delta = h/L \approx 10^{-3}$. This means that the system in the cell can be simplified to a set of algebraic equations by an averaging process analogous to the one adopted in the previous chapter. We find similar concentrations of Na^+, K^+ and Cl^- and TEP to those obtained in chapter 5 and within the physiological range. Moreover, we find that the concentration gradient in the cleft drives a water flux across the RPE of order 10^{-8} m/s, which is compatible with the experimentally measured values of $-(1.1-2.8)\cdot 10^{-8}$ m/s (Hughes et al., 1984; Shi et al., 2008). This essentially confirms the results of the previous chapter, that local osmosis in the cleft gap can produce a water flux that is compatible with experimental observations.

The predicted ion fluxes, however, are different from the ones reported in chapter 5, and have magnitudes comparable to those found experimentally (Hughes et al., 1984; Miller and Edelman, 1990; La Cour, 1992). This is because the extended model considers transepithelial transport of Na^+ and HCO_3^- via membrane Na^+-HCO_3^- co-transporters, which is coupled to the fluxes of other species, and Na^+ transport through the tight junction.

Our results from the sensitivity analysis suggest that the tight junction plays a key role in Na^+ transport, and large tight junction permeabilities are required for Na^+ flux to be directed from the SRS to the choroid. This is in agreement with the hypothesis of Gallemore et al. (1998),

who argued that passive flux through the tight junction towards the choroid might exceed the active flux of Na^+ across the cell towards the SRS and establish net Na^+ transport towards the choroid. Our model also predicts that water flux is roughly proportional to Na^+ flux, with proportionality constant of 0.0026 m^3/mol. We note that coupling between Na^+ and water fluxes are well established in other epithelia (see e.g. Diamond and Bossert, 1967; Matthay et al., 1996; Hamann, 2002), but has not been confirmed in the RPE.

The HCO_3^- flux is closely related to Na^+ transport, due to their coupling through Na^+-HCO_3^- co-transporters in cell membranes. Hughes et al. (1984) performed experiments on isolated bullfrog RPE-choroid preparations and suggested that fluid absorption is strongly dependent on the active absorption of HCO_3^-. The results of our model agree with this finding, as we predict that water flux is roughly proportional to HCO_3^- flux with a proportionality constant of 0.0016 m^3/mol.

The sensitivity analysis suggests that Cl^- transport is directed in most cases towards the choroid. We note that the direction of this flux is obtained form a balance between basal Cl^--HCO_3^- exchanger and basolateral permeability to Cl^-. Our model confirms the hypothesis that fluid transport is enhanced by transepithelial Cl^- flux (e.g. Bialek and Miller, 1994), although, the effect is less evident than that for Na^+ and HCO_3^-. Moreover, our model suggests that inhibition of HCO_3^--Cl^-exchanger facilitates Cl^- and water fluxes to the choroid, which is in agreement with the findings of Iserovich et al. (2011), who tested inhibition of this channel with the aim of developing drugs for treating macular oedema.

Finally, K^+transport is directed towards the choroid, but its magnitude does not strongly correlate with the transepithelial water flux, neither in our model nor in experimental works (Hughes et al., 1984; Adijanto et al., 2009).

The global sensitivity analysis shows that water flux is most sensitive to tight junction permeability to Na^+, as increasing this permeability results in an increase of the transepithelial Na^+ flux, and thus water flux towards the choroid. Moreover, the magnitude of water flux is also highly dependent on the amplitude of Na^+-K^+ATPase, as its activity is the driver of active ion transport and thus, of formation of the concentration gradient in the cleft gap. Water flux is also strongly affected by the amplitude of the Na^+-H^+ exchanger, presumably because it also drives a net Na^+ transport.

The second physiological condition we study considers the presence of a CO_2 gradient across the RPE, which can result from large production of CO_2 by photoreceptors. When CO_2 concentration is the same on both sides of the RPE, the CO_2 flux is extremely small. However, if a jump in CO_2 concentration between apical and basal regions exists, the model predicts a net CO_2 flux, directed towards the choroid, which varies in the range 8.96–9.06$\cdot 10^{-5}$ mol/m^2/s for an apical CO_2 partial pressure equal to 7% and a basal one to 5%.

The gradient of CO_2 induces spatial variability of concentrations of all species and of the potential in cell in the apical to basal direction. The mean values of the resulting variables in

this case are similar to those obtained in the absence of CO_2 gradient. This is also true for ion fluxes and sensitivity to all model variables.

Transepithelial water flux, however, decreases approximately by 50% if apical CO_2 is at 7% and basal is at 5%. This is because the presence of spatial variability of ion concentration in the cell implies a change in osmolarity from the basal to the apical region, such that the osmolarity decreases towards the apical membrane. This, in turn, reduces (or even reverses) osmotic water flux across the apical membrane, resulting in an overall reduction of water flux towards the choroid. In other words the model suggests that CO_2 accumulation in the SRS tends to decrease water transport, which might in turn lead to fluid accumulation. Should this finding be supported by experimental evidence it would imply that acidosis and fluid accumulation might be somehow linked to each other.

Adijanto et al. (2009) studied the dependency of water flux on CO_2 concentration in the apical and basal solution. The authors found that an increase of CO_2 concentration on both sides of the epithelium from 5 to 13% results in doubling water flux, suggesting that water transport is facilitated by CO_2. This conclusion, however, is not obviously consistent with the fact that CA inhibitors (which essentially reduce the degree of coupling between CO_2 and other species) are used to facilitate fluid transport (Wolfensberger et al., 2000; Kita and Marmor, 1992) or to treat macular oedema (Cox et al., 1988; Fishman et al., 1989). Our model suggests that water flux is independent of CO_2 concentration changes on both sides of the membrane, in disagreement with Adijanto et al. (2009), which might imply that some ingredients are missing in our approach. Nevertheless, we find that in the case of CO_2 gradient across the RPE, inhibition of CA smooths the gradients of all species in the cell (except for CO_2), resulting in an increase of water transport towards the choroid, as anticipated by experimental findings. This suggests that our model provides a possible explanation for the physical mechanism behind the functioning of CA inhibitors.

To summarise, the present work has been aimed at improving our understanding of the mechanisms that are responsible for fluid transport across the RPE. This required developing a mathematical model that couples fluid, ion and CO_2 dynamics across the epithelium, as fluid transport is driven by local osmosis in the cleft. The model provides possible explanations of the mechanisms behind the functioning of drugs used to treat fluid accumulation in the SRS, such as inhibitors of ion channels or CA and indicates how other interventions may inadvertently impact the retina. The results of the model, and particularly of the sensitivity analysis, may be used in targeting inhibition of other channels to treat eye pathological states, associated with fluid transport across the RPE. We finally remark that the model is based on ingredients that are common to all absorptive or secretive epithelia and, therefore, can constitute a basic framework for the study of fluid flow across other tissues.

Conclusions and future directions

The eye is an organ of an immense complexity that owing to a combination of many physical and biological processes, grants a subject with vision. Fluids occupy the majority of eye volume and are essential for its proper physiological functioning. Many pathological conditions related to fluids in the eye, such as glaucoma, age related macular degeneration, corneal opacity and diabetic retinopathy, may lead to severe visual impairment or blindness. Therefore, for preventing or treating these conditions, one needs to understand the physiological role of fluids and the effects of their interaction with the surrounding tissues.

In this thesis we make a humble contribution to understanding the role of fluids in the eye from mechanical point of view. Although some of the answers have been obtained, there are still plenty of open questions in the field. In what follows we briefly describe the main conclusions of the work and suggest some possibilities for future developments.

We address two topics in different parts of the eye. The first one is related to the motion of aqueous humour, the fluid located in the anterior segment of the eye. The first problem we address is associated with the motion of aqueous in the posterior chamber (PC), i.e. the region between the natural lens and the cornea. We improve the existing models of such a flow by accounting for a realistic shape of the domain and the effect of miosis (i.e. pupil contraction), and consider two possible scenarios for its modification: partial pupillary block and iridotomy. Partial pupillary block happens when the iris and the lens come into contact in a certain region, impeding the outflow of aqueous from the PC. This might lead to high pressure values in the PC, that can push the iris forward blocking the area where aqueous drains, resulting in angle-closure glaucoma. We find that for reaching high pressure values, the pupillary block must be almost complete, i.e. the blocked region should occupy about 90% of the pupil.

To reduce pressure in the PC iridotomy can be performed. It consists of surgically producing a hole in the iris that serves as an additional outflow from the PC. Despite being a common procedure, the problem of optimal size and location of an iridotomy is poorly understood. The ideal iridotomy should reduce pressure to safe levels, while keeping the risk of producing high wall shear stress (WSS) on the cornea low (which is relevant for its integrity). For the former, we find that an iridotomy with diameter of about 50 μm is sufficient. For the latter, the model predicts that the maximum WSS is achieved for a diameter of about 80-100 μm, producing a value as high as 1-10 Pa. However, to understand whether this value is high enough to cause endothelial cells detachment, experimental measurements are needed.

Our study of the flow in the PC suggests several interesting extensions. To start with, our model does not account for possible fluid-structure interaction between aqueous and iris, which might have a significant effect, especially during miosis, which has not been addressed in detail. This, however, would require a detailed understanding of iris dynamics during pupil contraction and dilation, which, to our knowledge, is not available and could probably be obtained by a suitably designed experiment.

Iridotomy is preformed when the iris is fully dilated. This means that after the iris returns to its normal position, the hole would have a different size and shape than the one produced during the surgery. It would be interesting to estimate this change, and, if it is large, to propose how to modify surgical procedure in order to obtain the desired size of the iridotomy for the iris in regular position. Furthermore, during iris contraction and dilation, an iridotomy might also change its size and shape, which will modify quantitatively our predictions of pressure in the PC. A study from both imaging and solid mechanics perspectives could shed some light on this phenomenon.

The second problem we address in the context of aqueous humour is related to the flow in the anterior chamber (AC) induced by eye rotations. Such a flow is relevant for generation of high stresses on the cornea and for mixing processes in the AC. We develop an analytical model of the flow induced by harmonic oscillation of the eye globe, complementing existing numerical works. This approach allows us to better understand the flow characteristics and perform parameter study. The model predicts that the flow has a complex three-dimensional structure and a steady streaming component is generated. This component is comparable to thermal flow, which is a well established mixing mechanism when the eyelids are open, thus is also important for mixing processes in the AC. Furthermore, the steady streaming flow induces lateral mixing, which is not the case for thermal flow. Finally, during night, when the eyelids are closed and no thermal flow occurs in the AC, rapid eye movements (REM) are shown to be the main mixing mechanism.

Owing to the absence of experimental measurements on the threshold value of WSS that causes endothelial cells detachment we cannot rule out the possibility that eye rotations cause cells detachment. However, common sense suggests that daily physiological activity, such as eye rotations, by design should not harm the cornea. Therefore, the values of the WSS produced by eye rotations could instead be used to indicate safe levels of the WSS for the endothelial cells. Nevertheless, one cannot reach a definite answer without an experimental quantification.

There are several possible extensions of our model, that might also admit semi-analytical approaches. One of the assumptions in our model is that the amplitude of oscillations is small, $\beta \ll 1$. This assumption holds for most of eye rotations; however, in the case of large saccades and maximum amplitude REM, β is of order 1. Thus one of the possible extensions would be to avoid this assumption and modify the solution procedure by retaining terms of order $\epsilon\beta$ (ϵ is the aspect ratio of the domain). This would potentially provide a more accurate solution in aforementioned cases, with possible analytical progress. Furthermore, it would be interesting to understand how

the flow due to eye rotations, particularly its steady streaming component, interacts with the thermal flow. This is relevant for mixing processes and particle transport in the AC.

Another interesting extension would be to study nutrient transport and drug delivery in the AC using our solution for the flow. Particle transport is also relevant, particularly for the formation of Krukenberg's spindle, which happens when there is a patterned accumulation of pigmented iris cells on the inner surface of the cornea. Boushehrian et al. (2016) studied particle transport in the AC using computational approach. A complementary semi-analytical work would be a welcomed extension of our study.

The second topic we address is related to the transport of fluid across the retinal pigment epithelium (RPE), the outermost layer of the retina. The RPE is responsible for transport of fluid from the subretinal space (SRS) to the choroid. This transport is supported by an active pumping, failure of which may lead to fluid accumulation in the SRS, a condition associated with age-related macular degeneration, retinal detachment, diabetic retinopathy and macular edema. In order to treat or prevent fluid accumulation, the mechanisms that drive fluid transport need to be well understood. In our study we aim to quantify and classify such mechanisms with the help of mathematical modelling. In particular, we develop a model that couples fluid and solute transport in the epithelial layer.

The first, simplified, model suggests that local osmosis generated in the cleft gap between two adjacent cells by active pumping of ions is the main mechanism of fluid transport. This finding stresses the importance of coupling ion and fluid transport. Moreover, it suggests that one can regulate the flow by manipulating ion transport with certain drugs that block ion channels on cell membranes.

To get a further insight on the effect of the coupling between solute and water transport, we extend the model to account for more species and their chemical interactions. This model better reproduces physiological conditions of the RPE and, thus, improves estimates of ion and water fluxes. Moreover, we perform sensitivity analysis, that enables us to determine the relative importance of ion channels on water transport. The model accounts for various feedback effects that link active ion transport with water flow; however RPE homeostasis might rely on additional mechanisms, the activation of which can be triggered by the departure from physiological conditions. These effects have not been considered and might be an interesting subject for future studies.

The model predicts that, in order to facilitate transepithelial flow, one needs to inhibit basal Na^+-HCO_3^- (1:2) co-transporter and the Cl^--HCO_3^- exchanger or to increase the tight junction permeability to cations. On the other hand, inhibition of Na^+-H^+ exchanger in the apical membrane decreases the flux towards the choroid, which suggests that Na^+-H^+ inhibitors, such as amiloride, might have a side effect of fluid accumulation in the SRS. The results of the model, and particularly of the sensitivity analysis, may be used in targeting inhibition of other channels to treat eye pathological states, associated with fluid transport across the RPE.

The model admits certain extensions provided that more experimental data is generated for its verification. In particular, a more detailed description of ion channels activity from both theoretical and experimental sides would be a desired improvement. This would involve models of single channel dynamics, a problem on a different scale, which, could be integrated into our model. This is especially of interest for Na^+-H^+ exchanger, as it has large effect on the system and the current use of non-equilibrium thermodynamics approach might not provide an accurate description of its activity. As ever, experimental data is needed to improve models. Furthermore, lactic acid could also have an effect on water transport across the RPE, as it has been shown to be relevant in corneal endothelium (Li et al., 2016). Comprehensive experimental measurements of ion and water fluxes are thus welcomed for further verification of the model.

Our model is just a preliminary step towards the understanding a much more complex and relevant phenomenon: fluid balance in the retina. This is a long term goal, which, like many problems in science should be conquered gradually via small steps, as it involves understanding fluid exchanges between blood vessels, interstitial and intracellular compartments. For making progress in this direction, one needs to integrate relevant experimental measurements with theoretical models at every level of this process.

Finally, the model that we develop might be applied to other absorptive or secretive epithelial layers. The first candidate could be the choroid plexus epithelium (CPE) that contributes to production of cerebrospinal fluid in the brain. Understanding the mechanisms behind this production is relevant for regulating intracranial pressure. Both the RPE and the CPE develop from neural ectoderm, therefore, they share many similarities, in the solute transport mechanisms. Therefore, with certain modifications, our model can be adapted to describe fluid transport across the CPE. Another interesting application of our model would be aqueous production by the ciliary epithelium (CE), which is relevant for regulating intraocular pressure. The CE consists of a double layer of cells, and thus, has a different structure from the RPE. This means that the model has to be modified accordingly to reproduce this particular structure.

To summarise, in the present thesis we have tried to provide answers from mechanical perspective to certain questions related to fluids in the eye. Despite many contributions from different research groups, the field remains open for further questions from both modelling and experimental sides. We sincerely hope that the research will keep moving in that direction and wish luck to those who will try to unravel the mysteries of eyes.

At this point, the author would like to congratulate the reader for reaching the end of this thesis. If this was accomplished without skipping any parts of the work (including the sections about parameter estimates), the author would be delighted to offer the reader a pint, provided that he/she happened to be in the same part of the world.

APPENDIX A

SIMPLIFICATION OF THE MODEL IN CHAPTER 5

A.1 Reduction of the model in the cell to a set of algebraic equations

In this section we simplify the equations (5.1a) for $k = 0, 1$ and (5.3) in the cell to a set of algebraic equations. The aspect ratio in the cleft is $\delta = h/L \approx 0.001$. If we denote schematically the order of magnitude of an ion flux per unit area through the lateral membrane by $\mathscr{F}$, the flux per unit area along the cleft has to be of the order $\mathscr{F}/\delta$. This implies that variations of concentrations and potential in the cell have to be δ times smaller than those in the cleft. We also verify a posteriori that the magnitude of these variations is of order 0.1% of the average values. We thus make use of asymptotic expansions of all variables in the cell and write

$$n_k^i = \hat{n}_k^i + \mathscr{O}(\delta), \qquad \phi^i = \hat{\phi}^i + \mathscr{O}(\delta), \tag{A.1}$$

where $\hat{n}_k^i$ and $\hat{\phi}^i$ do not depend on space. We now integrate equations (5.1a) for $k = 0, 1$ and (5.3) in the main text over the volume of the cell, apply the divergence theorem and implement the membrane conditions (5.4) and (5.5), to obtain the following problem at the leading order

$$3\mathscr{P} + \mathscr{M} = 0, \tag{A.2a}$$

$$\mathscr{J}_1^{ia} - 2\mathscr{P} + \mathscr{M} + \mathscr{J}_1^{ib} + \frac{2}{H}\int_0^L \mathscr{J}_1^{ig} dx = 0, \tag{A.2b}$$

$$\mathscr{P} + \mathscr{J}_1^{ia} + \mathscr{J}_1^{ib} - \mathscr{J}_2^{ib} + \frac{2}{H}\int_0^L \left(\mathscr{J}_1^{ig} - \mathscr{J}_2^{ig}\right) dx = 0, \tag{A.2c}$$

where we have to keep integrals only for the cleft variables, as the values in other regions are uniform. We note that all fluxes ($\mathscr{P}$, $\mathscr{M}$, $\mathscr{J}_1^{ia}$, $\mathscr{J}_1^{ib}$, $\mathscr{J}_1^{ig}$, $\mathscr{J}_2^{ib}$ and $\mathscr{J}_2^{ig}$) are computed using the leading order, spatially constant variables in the cell. In the following we will not distinguish

leading order variables from the exact variables; in other words we will write, for instance, n_k^i rather than $\hat{n}_k^i$. In summary, this reduces the problem in the cell to a system of algebraic equations.

A.2 Reduction of the ion transport model in the cleft to a set of ODEs

In this section we derive the ODEs (5.14a)–(5.14c). We first redefine y via $y \to y-(h+H)$, so that the left wall of the cleft gap is at $y=0$ and the symmetry axes are at $y=h$ and $y=-H/2$. It is convenient from now on to work in terms of dimensionless variables. Let N denote a representative ion concentration, equivalent to 100 mM, corresponding to a physiological solution with molarity 300 mM. With $s \in \{a,b,i,g\}$ we non-dimensionalise all variables as follows

$$x = L\bar{x}, \quad y = h\bar{y}, \quad n_k^s = N\bar{n}_k^s, \quad \phi^s = \frac{RT}{F}\bar{\phi}^s, \quad X = N\bar{X}, \quad u = U\bar{u}, \quad v = \delta U\bar{v}, \tag{A.3}$$

where the choice of fluid velocity scale $U \approx 60$ μm/s is discussed in A.4. In the cleft gap, electrodiffusion is governed by equations (5.1a) for $k=0,1$ and (5.3), which scale as follows

$$\frac{\partial^2 \bar{n}_k^g}{\partial \bar{x}^2} + z_k \frac{\partial}{\partial \bar{x}}\left(\bar{n}_k^g \frac{\partial \bar{\phi}^g}{\partial \bar{x}}\right) + \frac{1}{\delta^2}\left(\frac{\partial^2 \bar{n}_k^g}{\partial \bar{y}^2} + z_k \frac{\partial}{\partial \bar{y}}\left(\bar{n}_k^g \frac{\partial \bar{\phi}^g}{\partial \bar{y}}\right)\right) - Pe\left(\frac{\partial(\bar{u}\bar{n}_k^g)}{\partial \bar{x}} + \frac{\partial(\bar{v}\bar{n}_k^g)}{\partial \bar{y}}\right) = 0, \tag{A.4}$$

$$\frac{\partial}{\partial \bar{x}}\left(\left[\sum_{k=0}^{2} \bar{n}_k^g\right]\frac{\partial \bar{\phi}^g}{\partial \bar{x}}\right) + \frac{1}{\delta^2}\frac{\partial}{\partial \bar{y}}\left(\left[\sum_{k=0}^{2} \bar{n}_k^g\right]\frac{\partial \bar{\phi}^g}{\partial \bar{y}}\right) = 0, \tag{A.5}$$

where Pe is a Péclet number, defined as $Pe = UL/D \approx 0.3$ (with the values taken from table 5.2). Taking advantage of the small ratio δ of the cleft gap, we expand all variables in terms of δ

$$\bar{n}_k^g = \bar{n}_{k,0}^g + \delta^2 \bar{n}_{k,1}^g + \mathcal{O}(\delta^4), \qquad \bar{\phi}^g = \bar{\phi}_0^g + \delta^2 \bar{\phi}_1^g + \mathcal{O}(\delta^4). \tag{A.6}$$

Introducing these expansions into equations (A.4)-(A.5) we obtain the following leading order problem (denoting for simplicity of the notation leading order variables as exact ones, e.g. using $\bar{n}_k^g$, $\bar{\phi}^g$ rather than $\bar{n}_{k,0}^g$ and $\bar{\phi}_0^g$)

$$\frac{\partial}{\partial \bar{y}}\left(\left[\sum_{k=0}^{2} \bar{n}_k^g\right]\frac{\partial \bar{\phi}^g}{\partial \bar{y}}\right) = 0, \tag{A.7}$$

$$\frac{\partial^2 \bar{n}_k^g}{\partial \bar{y}^2} + z_k \frac{\partial}{\partial \bar{y}}\left(\bar{n}_k^g \frac{\partial \bar{\phi}^g}{\partial \bar{y}}\right) = 0, \quad k=0,1. \tag{A.8}$$

Noting the symmetry condition at $\bar{y}=1$, where $\partial/\partial\bar{y}$ operating on any variable yields zero, we have for $k \in \{0,1\}$

$$\frac{\partial \bar{n}_k^g}{\partial \bar{y}} + z_k \bar{n}_k^g \frac{\partial \bar{\phi}^g}{\partial \bar{y}} = 0. \tag{A.9}$$

Hence

$$\bar{n}_k^g = A_k(\bar{x})\exp[-z_k\bar{\phi}^g], \tag{A.10}$$

where A_0 and A_1 arise from the general form of the solution following integration. Noting that the valences for sodium and potassium $z_0 = z_1 = 1$, and using electroneutrality in the gap, $\bar{n}_2^g = \bar{n}_0^g + \bar{n}_1^g$, we have

$$2\frac{\partial}{\partial\bar{y}}\left([A_0(\bar{x}) + A_1(\bar{x})]\exp[-\bar{\phi}^g]\frac{\partial\bar{\phi}^g}{\partial\bar{y}}\right) = 0. \tag{A.11}$$

One integration and the symmetry condition gives

$$\frac{\partial\bar{\phi}^g}{\partial\bar{y}} = 0 \tag{A.12}$$

and hence the leading order bulk potential, and thus the concentrations, have no $\bar{y}$ dependence.

With the 1 superscript denoting the first subleading term and integrating the first-order correction to the concentration balance equation over $\bar{y}$, we have

$$\int_0^2\left\{\frac{\partial^2\bar{n}^g}{\partial\bar{x}^2} + \frac{\partial}{\partial\bar{x}}\left(z_k\bar{n}_k^g\frac{\partial\bar{\phi}^g}{\partial\bar{x}} - Pe(\bar{u}\bar{n}_k^g)\right)\right\}d\bar{y} + \left[\frac{\partial\bar{n}_{k,1}^g}{\partial\bar{y}} + z_k\bar{n}_k^g\frac{\partial\bar{\phi}_1^g}{\partial\bar{y}} + z_k\bar{n}_{k,1}^g\frac{\partial\bar{\phi}^g}{\partial\bar{y}} - Pe(\bar{v}\bar{n}_k^g)\right]_{\bar{y}=0}^{\bar{y}=2} = 0. \tag{A.13}$$

The contribution to the square bracket is determined by the boundary conditions at $\bar{y} = 0$ and $\bar{y} = 2$,

$$\frac{\partial\bar{n}_{k,1}^g}{\partial\bar{y}} + z_k\bar{n}_k^g\frac{\partial\bar{\phi}_1^g}{\partial\bar{y}} + z_k\bar{n}_{k,1}^g\frac{\partial\bar{\phi}^g}{\partial\bar{y}} - Pe\bar{v}\bar{n}_k^g = \pm\hat{P}_k^b z_k(\bar{\phi}^i - \bar{\phi}^g)\frac{\bar{n}_k^i - \bar{n}_k^g\exp[-z_k(\bar{\phi}^i - \bar{\phi}^g)]}{1 - \exp[-z_k(\bar{\phi}^i - \bar{\phi}^g)]}, \tag{A.14}$$

where $\hat{P}_k^b = P_k^b\frac{L}{D\delta}$ and the right hand side sign is '+' for $\bar{y} = 2$ and '-' for $\bar{y} = 0$. As the membrane is impermeable to sodium, $P_0^b = 0$. Non-zero values $\hat{P}_k^b$ have to be of order 1 for the above expression to be valid, and for the values reported in table 5.2 we find $\hat{P}_1^b = 0.88$, $\hat{P}_2^b = 0.05$. We denote the term on the right hand side of the expression (A.14) as $\bar{\mathscr{J}}_k^{ig}$, which represents the dimensionless lateral flux.

Recalling that concentrations and the potential under integral in equation (A.13) are $\bar{y}$ independent, we rewrite the equation (A.13), in the following way

$$\frac{d^2\bar{n}_k^g}{d\bar{x}^2} + \frac{d}{d\bar{x}}\left(z_k\bar{n}_k^g\frac{d\bar{\phi}^g}{d\bar{x}}\right) - Pe\left(\bar{q}\frac{d\bar{n}_k^g}{d\bar{x}} + \frac{\bar{n}_k^g}{2}\int_0^2\frac{\partial\bar{u}}{\partial\bar{x}}d\bar{y}\right) + \bar{\mathscr{J}}_k^{ig}(\bar{n}_k^g, \bar{\phi}^g) = 0, \quad k = 0, 1, \tag{A.15}$$

where $\bar{q} = \frac{1}{2}\int_0^2\bar{u}d\bar{y}$ is dimensionless depth-averaged velocity. Using the continuity equation for the fluid (5.17b) to treat the term with integral, we obtain the following expression

$$\frac{d^2\bar{n}_k^g}{d\bar{x}^2} + \frac{d}{d\bar{x}}\left(z_k\bar{n}_k^g\frac{d\bar{\phi}^g}{d\bar{x}}\right) - Pe\left(\bar{q}\frac{d\bar{n}_k^g}{d\bar{x}} - \bar{Q}^g\bar{n}_k^g\right) + \bar{\mathscr{J}}_k^{ig}(\bar{n}_k^g, \bar{\phi}^g) = 0, \quad k = 0, 1, \tag{A.16}$$

where $\bar{Q}^g$ is the water flux through the lateral membrane.

Using a similar procedure for (A.5) at order δ^2 we obtain the following equation

$$\frac{d}{d\bar{x}}\left(\left[\sum_{k=0}^{2}\bar{n}_k^g\right]\frac{d\bar{\phi}^g}{d\bar{x}}\right)+\bar{\mathscr{J}}_1^{ig}-\bar{\mathscr{J}}_2^{ig}=0. \tag{A.17}$$

The boundary conditions at the tight junction ($\bar{x}=1$) (5.15) are rewritten as follows

$$\frac{d\bar{n}_k^g}{d\bar{x}}+z_k\bar{n}_k^g\frac{d\bar{\phi}^g}{d\bar{x}}-Pe\bar{Q}^{tj}\bar{n}_k^g=\bar{\mathscr{J}}_k^{ag}(\bar{n_k^g},\bar{\phi}^g),\quad k=0,1 \tag{A.18a}$$

$$-2\left(\bar{n}_0^g+\bar{n}_1^g\right)\frac{d\bar{\phi}^g}{d\bar{x}}=\bar{\mathscr{J}}_1^{ag}(A_1,\bar{\phi}^g), \tag{A.18b}$$

with Dirichlet conditions at $\bar{x}=0$

$$\bar{n}_0^g=\bar{N}_0^b,\qquad \bar{n}_1^g=\bar{N}_1^b,\qquad \bar{\phi}^g=0. \tag{A.19}$$

We therefore have 3 coupled ODEs, (A.16) – (A.17), for 3 unknowns $\bar{n}_0^g$, $\bar{n}_1^g$, $\bar{\phi}^g$ with the boundary conditions (A.18a), (A.18b), (A.19).

A.3 Derivation of the solution in the Debye layer

In this section we describe the problem in the electrical double layer (EDL) and derive the solution. As reported in the main text, electroneutrality in the Debye layer breaks down and we have to solve the system (5.1a) and (5.1b).

We work in terms of dimensionless variables, as in A.2, but introducing new spatial scales

$$x=LX,\quad y=\lambda_D Y,$$

where $\lambda_D=\sqrt{\frac{\epsilon RT}{F^2N}}\approx 1.8$ nm is the Debye length. We also define the aspect ratio of the EDL, $\lambda=\lambda_D/L$. As in A.2, we assume that the left wall of the cleft is located at $y=0$.

Using n_k^d, ϕ^d to denote ion concentrations and electrical potential in the Debye layer of the cleft (denoted as n_k^{EDL} and ϕ^{EDL} in the main text), we use a similar expansion as in the bulk of the cleft (A.2) but in terms of the EDL aspect ratio

$$\phi^d=\bar{\phi}_0^d+\lambda^2\bar{\phi}_1^d+\mathscr{O}(\lambda^4),\quad \bar{n}_k^d=\bar{n}_{k,0}^d+\lambda^2\bar{n}_{k,1}^d+\mathscr{O}(\lambda^4),\quad k=0,1,2. \tag{A.20}$$

Rescaling equations (5.1a) and (5.1b) and applying the above expansion at leading order (and again using the same notation for leading-order variables and exact ones), we have

$$\frac{\partial^2\bar{\phi}^d}{\partial Y^2}=-(\bar{n}_0^d+\bar{n}_1^d-\bar{n}_2^d),\quad \frac{\partial^2\bar{n}_k^d}{\partial Y^2}+\frac{\partial}{\partial Y}\left(z_k\bar{n}_k^d\frac{\partial\bar{\phi}^d}{\partial Y}\right)=0,\quad k=0,1,2. \tag{A.21}$$

Integrating the second expression and applying the leading-order boundary condition (5.4) we obtain

$$\frac{\partial\bar{n}_k^d}{\partial Y}+z_k\bar{n}_k^d\frac{\partial\bar{\phi}^d}{\partial Y}=0. \tag{A.22}$$

Integrating the above equation and matching with the solution in the bulk, yields

$$\bar{n}_k^d(X,Y) = \bar{n}_k^g(X,0)\exp\left[-z_k\left(\bar{\phi}^d(X,Y) - \bar{\phi}^g(X,0)\right)\right], \tag{A.23}$$

where $\bar{n}_k^g(X,0)$, $\bar{\phi}^g(X,0)$ are the inner limits of the bulk concentrations and potential. Noting that the outer variables have no Y dependence (at leading order) and using the standard Huckel-Debye approximation (Probstein, 2005) one has

$$\frac{\partial^2}{\partial Y^2}\left(\bar{\phi}^d - \bar{\phi}^g\right) = \left(\sum_{k=0}^{2} \bar{n}_k^g\right)\left(\bar{\phi}^d - \bar{\phi}^g\right). \tag{A.24}$$

Hence, upon matching with the solution in the bulk, we have

$$\bar{\phi}^d(X,Y) - \bar{\phi}^g = K(X)\exp\left[-\left(\sum_{k=0}^{2} \bar{n}_k^g\right)^{1/2} Y\right],$$

where $K(X)$ is given by $\bar{\phi}^d(X,0) - \bar{\phi}^g$. Note that $\bar{\phi}^d(X,0)$ is still undetermined and, to find it, we require the boundary condition for the potential at $Y = 0$

$$\left.\frac{\partial \bar{\phi}^d}{\partial Y}\right|_{Y=0} = \bar{\sigma}, \tag{A.25}$$

where $\bar{\sigma}$ is the non-dimensionalisation of

$$\sigma = C_m(\phi^g - \phi^i) - \sigma_0, \tag{A.26}$$

and it takes into account the surface charge due to the presence of proteins via σ_0 and has a term which is proportional to the jump of the limits of the bulk potentials as they approach the membrane with the membrane capacitance C_m. The scale for the surface charge density is $FNL\lambda$ (for the meaning of the symbols please refer to Table 5.2). The condition at $Y = 0$ is therefore given by

$$\frac{\partial \bar{\phi}^d}{\partial Y} = \chi(\bar{\phi}^g - \bar{\phi}^i) - \bar{\sigma}_0, \tag{A.27}$$

where $\chi = \frac{C_m L}{\epsilon}\lambda \approx 0.02$.

Applying this condition we obtain the inner solution $\bar{\phi}^d$. We note that by construction, the inner solution coincides with the composite solution, which we denote with Φ, and it reads

$$\bar{\Phi}(X,Y) = \bar{\phi}^g - \frac{\chi(\bar{\phi}^g - \bar{\phi}^i) - \bar{\sigma}_0}{\left(\sum_{k=0}^{2} \bar{n}_k^g\right)^{1/2}}\exp\left[-\left(\sum_{k=0}^{2} \bar{n}_k^g\right)^{1/2} Y\right]. \tag{A.28}$$

A.4 Derivation of the expression for the slip velocity

We start with the equations (5.17) for the fluid flow in the EDL.

For convenience, we work in terms of dimensionless variables and introduce the following scales

$$x = LX, \quad y = \lambda_D Y, \quad u = U\bar{u}, \quad v = \delta U\bar{v}, \quad \Phi = \frac{RT}{F}\bar{\Phi}, \quad p = P_0\bar{p}, \tag{A.29}$$

where λ_D is the Debye length, and $U = \frac{\epsilon}{L\mu}\left(\frac{RT}{F}\right)^2 = 60$ μm/s. The scale for the pressure is chosen so that the pressure gradient balances with the dominant viscous term, to obtain $P_0 = L\mu U/\lambda_D^2$. Since the aspect ratio of the Debye layer $\lambda = \lambda_D/L$ is small we use lubrication theory to approximate the Navier Stokes equations. In particular we drop terms of order λ^2 or smaller to obtain the following system of dimensionless equations

$$-\frac{\partial\bar{p}}{\partial X} + \frac{\partial^2\bar{u}}{\partial Y^2} + \frac{\partial^2\bar{\Phi}}{\partial Y^2}\frac{\partial\bar{\Phi}}{\partial X} = 0, \tag{A.30a}$$

$$-\frac{\partial\bar{p}}{\partial Y} + \frac{\partial^2\bar{\Phi}}{\partial Y^2}\frac{\partial\bar{\Phi}}{\partial Y} = 0. \tag{A.30b}$$

Using (A.24) it is convenient to redefine the pressure, so that $p' = \bar{p} - \frac{C(X)}{2}\left(\bar{\Phi} - \bar{\phi}^g\right)^2$, where $C(X) = \sum_{k=0}^{2}\bar{n}_k^g(X)$ and $\bar{\phi}^g$ is the potential in the bulk. With this redefined pressure the above equations take the form

$$-\frac{\partial p'}{\partial X} + \frac{\partial^2\bar{u}}{\partial Y^2} + \frac{\partial^2\bar{\Phi}}{\partial Y^2}\frac{\partial\bar{\phi}^g}{\partial X} - C'(X)\frac{(\bar{\sigma})^2}{2C(X)}\exp[-2\sqrt{C(X)}Y] = 0, \tag{A.31a}$$

$$\frac{\partial p'}{\partial Y} = 0. \tag{A.31b}$$

Note, that now p' does not depend on Y and, therefore, we can integrate equation (A.31a) twice with respect to Y and apply the no slip boundary condition at the wall $Y = 0$ to obtain

$$\bar{u}^{EDL} = \frac{dp'}{dX}\frac{Y^2}{2} + c_1(X)Y + \left(\frac{\bar{\sigma}\left(\exp[-\sqrt{C(X)}Y] - 1\right)}{\sqrt{C(X)}}\right)\frac{\partial\bar{\phi}^g}{\partial X} + \\ + C'(X)\frac{(\bar{\sigma})^2}{8C^2(X)}\left(\exp[-2\sqrt{C(X)}Y] - 1\right), \tag{A.32}$$

and the constant $c_1(X)$ can be determined by matching this solution (inner) with that in the bulk of the cleft gap (outer). In the above expression, we have added a superscript EDL to denote the velocity in this region in order to distinguish it from the solution in the bulk of the cleft.

In the bulk of cleft (outer region) the fluid flow is governed by Stokes equation

$$-\nabla p + \mu\nabla^2\mathbf{u} = 0. \tag{A.33}$$

A similar analysis as for the inner region can be applied also in this case. The scaling will differ from the one above only for the variables $y = h\bar{y}$ and $p = L\mu U/h^2\bar{p}$, and the spatial aspect ratio is $\delta = h/L$.

Rescaling the equations and dropping terms of order δ^2 or smaller we obtain the following equations

$$-\frac{\partial \bar{p}}{\partial \bar{x}} + \frac{\partial^2 \bar{u}}{\partial \bar{y}^2} = 0, \tag{A.34}$$

$$-\frac{\partial \bar{p}}{\partial \bar{y}} = 0. \tag{A.35}$$

Hence, integrating first equation twice with respect to y, we obtain

$$\bar{u}^{bulk} = \frac{\partial \bar{p}}{\partial \bar{x}} \frac{\bar{y}^2}{2} + d_1(\bar{x})\bar{y} + d_2(\bar{x}), \tag{A.36}$$

where we added the superscript $bulk$ to distinguish this velocity from that of the inner region (A.32). Applying the symmetry condition in y – direction we get $d_1(\bar{x}) = 0$. To determine the other constant, we perform matching with the inner region (and recall that in the bulk $\bar{p} = p'$)

$$d_2(\bar{x}) = -\frac{\bar{\sigma}}{\sqrt{C(\bar{x})}} \frac{\partial \bar{\phi}^g}{\partial \bar{x}} - C'(\bar{x}) \frac{(\bar{\sigma})^2}{8C^2(\bar{x})}, \tag{A.37}$$

and $c_1(\bar{x}) = 0$. The slip velocity is thus defined as $u_{slip} = d_2(\bar{x})$.

A.5 Solution of the fluid flow in the cleft

We now work in the bulk of the cleft and shift the $\bar{y}$-axis into the centre of the cleft, so that the cleft spans from $\bar{y} = -1$ to $\bar{y} = 1$ and the symmetry axis is at $\bar{y} = 0$. In the bulk of the cleft the velocity profile is then given by

$$\bar{u} = \frac{1}{2} \frac{\partial \bar{p}}{\partial \bar{x}} \left(\bar{y}^2 - 1\right) + u_{slip}. \tag{A.38}$$

The equation for the pressure is obtained by integrating the continuity equation along the thickness of the cleft with the boundary conditions $\bar{v}(\bar{y} = \pm 1) = \pm \bar{Q}^g(\bar{x})$, where $\bar{Q}^g = Q^g/\delta U = k_m/\delta U \left[RT\left(\sum_{k=0}^{2}(n_k^i - n_k^g(x)) + X\right) + p(x)\right]$ is the dimensionless lateral flux per unit area. The equation for the pressure $\bar{p}$ then becomes

$$-\frac{1}{3}\frac{d^2 \bar{p}}{d\bar{x}^2} + \frac{du_{slip}}{d\bar{x}} = -\bar{Q}^g(\bar{x}), \tag{A.39a}$$

subject to the boundary conditions

$$\bar{p}(0) = 0, \qquad \text{at } \bar{x} = 0, \tag{A.39b}$$

$$-\frac{1}{3}\frac{d\bar{p}}{d\bar{x}}|_{\bar{x}=1} + u_{slip}(1) = \bar{Q}^{tj}, \qquad \text{at } \bar{x} = 1 \tag{A.39c}$$

where $\bar{Q}^{tj} = Q^{tj}/U$ is the dimensionless flux through the tight junction and is given by the expression $Q^{tj} = k_{tj}\left(RT\sum_{k=0}^{1}(n_k^a - n_k^g(L)) + p(L)\right)$.

APPENDIX B

SIMPLIFICATION OF THE MODEL IN CHAPTER 6

B.1 Model simplification in the cell

In this section we will simplify the system (6.3a) for $k = 0,1,2,5$ and (6.15), (6.16), (6.14a) and (6.14b) in the cell to a system of ODEs and algebraic equations. From now on it is convenient to work in terms of dimensionless variables. Given the typical values of species concentrations in physiological systems, we introduce the scale for concentrations N_k for species k. The representative concentrations are chosen as follows: $N_k = N = 100$ mM for $k \in \{0,1,2,3\}$, $N_4 = 10^{-4}$ mM, $N_5 = 1$ mM and $N_6 = 10^{-2}$ mM. We non-dimensionalise all variables as follows

$$x = L\bar{x}, \quad y = L\bar{y}, \quad n_k^i = N_k \bar{n}_k^i, \quad \phi^i = \frac{RT}{F}\bar{\phi}^i, \quad X = N\bar{X}, \quad B = N\bar{B}, \quad \mathbf{u} = U^i\bar{\mathbf{u}}, \quad \mathbf{j} = \frac{DN}{L}\bar{\mathbf{j}}. \tag{B.1}$$

The velocity scale U^i is chosen to correspond to the experimentally measured value of the flow across the RPE, $U^i = 1.5 \cdot 10^{-8}$ m/s (Tsuboi, 1987). With this choice, the Péclet number is $U^i L/D \approx 10^{-4}$, suggesting that the advective flux can be neglected in the cell.

To further simplify the problem in the cell we will reduce the system to a set of ODEs in x-direction, that is from basal to apical. In order for this to be possible we need to prove that all variables in the cell are y-independent. The proof relies on the y-independence of the variables in the cleft, which will be addressed in detail in § B.2.

We will first focus on CO_2, as difference in CO_2 concentrations in the apical and basal regions may potentially lead to a spatial variability in the cell, owing to large membrane permeability to it (see table 6.2). The cleft gap is a long and thin domain, with aspect ratio $\delta = h/L = 10^{-3}$. As the fluxes are required to be equal at the both sides of the membrane, at $\bar{y} = \delta$ we have $\frac{\partial \bar{n}_5^i}{\partial \bar{y}} = \frac{\partial \bar{n}_5^g}{\partial \bar{y}} = \delta \frac{\partial \bar{n}_5^g}{\partial y^*}$, where $y^* = \delta \bar{y}$ is the spatial scale in the cleft. We will show in § B.2 that $\delta \frac{\partial \bar{n}_5^g}{\partial y^*} \sim \mathcal{O}(\delta^2)$. In the middle of the cell, at $\bar{y} = 1/2 + \delta$, we have a symmetry condition, that forces

zero y-derivative. Therefore, the only y variability possible at the leading order is due to the reaction terms.

Let us estimate this variability with respect to y by considering equation (6.15), which imposes total CO_2 conservation, in dimensionless form

$$\bar{\nabla}\cdot\bar{\mathbf{j}}_5^i + \frac{D_6N_6}{D_5N_5}\bar{\nabla}\cdot\bar{\mathbf{j}}_6^i + \frac{D_3N_3}{D_5N_5}\bar{\nabla}\cdot\bar{\mathbf{j}}_3^i = 0. \tag{B.2}$$

We first use equation (6.16) to substitute the last term to obtain

$$\bar{\nabla}\cdot\bar{\mathbf{j}}_5^i + \frac{D_6N_6}{D_5N_5}\bar{\nabla}\cdot\bar{\mathbf{j}}_6^i + \frac{D_4N_4}{D_5N_5}\bar{\nabla}\cdot\bar{\mathbf{j}}_4^i = 0. \tag{B.3}$$

An estimate of the order of magnitude of the coefficients in the above expression (using values reported in table 6.2) shows that $\frac{D_6N_6}{D_5N_5} \approx 10^{-2} \approx \mathcal{O}(\delta)$ and $\frac{D_4N_4}{D_5N_5} \approx 10^{-3} \approx \mathcal{O}(\delta)$. Therefore, these terms can be omitted at the leading order and the equation (B.3) at the leading order reads

$$\bar{\nabla}\cdot\bar{\mathbf{j}}_5^i = 0. \tag{B.4}$$

This equation is subject to boundary conditions, which are zero fluxes at the lateral walls and membrane conditions (6.6) at the apical and basal membranes. The expression $\bar{n}_5^i = a\bar{x} + b$, where a and b are determined from the boundary conditions (6.6) satisfies this problem, justifying the assumption that at leading order CO_2 concentration does not depend on the y coordinate.

From the equation (6.3a) $k = 5$, which we recall here,

$$\bar{\nabla}\cdot\bar{\mathbf{j}}_5^i - \frac{k_hL^2}{D_5}\left(\bar{n}_5^i - \frac{k_dN_6}{k_hN_5}\bar{n}_6^i\right) = 0, \tag{B.5}$$

one may deduce that, at the leading order, n_6^i is also y independent.

From the dimensionless form of the equation (6.16),

$$\bar{\nabla}\cdot\bar{\mathbf{j}}_3^i - \frac{D_4N_4}{D_3N_3}\bar{\nabla}\cdot\bar{\mathbf{j}}_4^i = 0, \tag{B.6}$$

where the coefficient $\frac{D_4N_4}{D_3N_3} \approx 10^{-5}$, one may argue that at the leading order the HCO_3^- flux is conserved, leading to

$$\bar{\nabla}\cdot\bar{\mathbf{j}}_3^i = 0. \tag{B.7}$$

The above equation, along with the conservation of fluxes (6.3a) for ions $k = 0, 1, 2$ can be simplified in a similar way as in § 5.2.2 of chapter 5. Particularly, we will use that the lateral fluxes are of order δ to write

$$\frac{\partial\bar{n}_k^i}{\partial\bar{y}} + z_k\bar{n}_k^i\frac{\partial\bar{\phi}^i}{\partial\bar{y}} = \mathcal{O}(\delta) \quad \Rightarrow \quad \bar{n}_k^i = A_k(\bar{x})e^{-z_k\bar{\phi}^i}. \tag{B.8}$$

Applying the electroneutrality condition (and neglecting the term $N_4/N\bar{n}_4^i \approx \mathcal{O}(\delta)$) leads to the following equality

$$(A_0 + A_1)e^{-\bar{\phi}^i} - (A_2 + A_3)e^{\bar{\phi}^i} - \bar{B} - z_X\bar{X} = 0. \tag{B.9}$$

We recall that $z_X\bar{X}$ is spatially homogeneous. The expression for B can be derived using equations (6.14a) and (6.14b). Introducing the following scaling, $K_b = N_4\bar{K}_b$, $K_d = N_3N\bar{K}_d/N_6$ and $C_B = N\bar{C}_B$, from (6.14a) we obtain $\bar{n}_4^i = \bar{n}_6^i/\bar{K}_d\bar{n}_3^i$. Therefore (6.14b) can be written as

$$\bar{B} = \frac{\bar{K}_b\bar{C}_B}{\bar{K}_b+\bar{n}_4^i} = \frac{\bar{K}_b\bar{C}_B\bar{K}_d\bar{n}_3^i}{\bar{K}_b\bar{K}_d\bar{n}_3^i+\bar{n}_6^i} = \frac{\bar{K}_b\bar{C}_B\bar{K}_dA_3e^{\bar{\phi}^i}}{\bar{K}_b\bar{K}_dA_3e^{\bar{\phi}^i}+\bar{n}_6^i}, \tag{B.10}$$

where, for the last equality, we used (B.8). Introducing the notations, $m_1 = \bar{K}_b\bar{C}_B\bar{K}_dA_3$ and $m_2 = \bar{K}_b\bar{K}_dA_3$ and recalling that $\bar{n}_6^i$ is y-independent, we substitute the above expression into (B.9) to obtain an equation for $e^{\bar{\phi}^i}$

$$(A_0+A_1)e^{-\bar{\phi}^i} - (A_2+A_3)e^{\bar{\phi}^i} - \frac{m_1e^{\bar{\phi}^i}}{m_2e^{\bar{\phi}^i}+\bar{n}_6^i} - z_XX = 0, \tag{B.11}$$

which can be transformed into a cubic equation for $e^{\bar{\phi}^i}$ with coefficients that are only dependent on x. This equation admits an analytical solution, with at least one real root (that could be found by Cardano's formula for instance), which depends only on x. This suggests that $\bar{\phi}^i$, and thus all the ions and B, are y-independent.

We note that all the steps from equation (B.6) to (B.11) hold also if one attempts to prove x-independence, as ion fluxes at the apical and basal membranes are also of order δ (see § 5.2.2). However, if a transepithelial CO_2 gradient is present, $\bar{n}_6^i$ in (B.11) would not be x-independent and the equation will no longer have coefficients of just one variable, leading to the presence of x-variability in the cell.

We now represent all the variables in the cell in the following way

$$\bar{n}_k^i = \hat{n}_k^i(\bar{x}) + \mathcal{O}(\delta), \qquad \bar{\phi}^i = \hat{\phi}^i(\bar{x}) + \mathcal{O}(\delta), \tag{B.12}$$

where $\hat{n}_k^i$ and $\hat{\phi}^i$ do not depend on $\bar{y}$. Integrating the equations (6.3a) from δ to $1/2+\delta$ in the $\bar{y}$ -direction we obtain a set of ODEs in the cell in terms of the leading order variables (and using the same notation for leading order variables and exact ones), which at the steady state read

$$\frac{d}{d\bar{x}}\left(\frac{d\bar{n}_k^i}{d\bar{x}} + z_k\bar{n}_k^i\frac{d\bar{\phi}^i}{d\bar{x}}\right) - 2\bar{J}_k^{ig} = 0, \quad k = 0,1,2 \tag{B.13a}$$

$$\frac{D_3}{D}\frac{d}{d\bar{x}}\left(\frac{d\bar{n}_3^i}{d\bar{x}} - \bar{n}_3^i\frac{d\bar{\phi}^i}{d\bar{x}}\right) - 2\bar{J}_3^{ig} - \frac{D_4N_4}{DN}\frac{d}{d\bar{x}}\left(\frac{d\bar{n}_4^i}{d\bar{x}} + \bar{n}_4^i\frac{d\bar{\phi}^i}{d\bar{x}}\right) = 0 \tag{B.13b}$$

$$\frac{D_5N_5}{DN}\frac{d^2\bar{n}_5^i}{d\bar{x}^2} - 2\bar{J}_5^{ig} + \frac{k_hL^2}{DN}\left(\frac{k_dN_6}{k_h}\bar{n}_6^i - N_5\bar{n}_5^i\right) = 0 \tag{B.13c}$$

$$\frac{D_6N_6}{DN}\frac{d^2\bar{n}_6^i}{d\bar{x}^2} - 2\bar{J}_6^{ig} + \frac{D_5N_5}{DN}\frac{d^2\bar{n}_5^i}{d\bar{x}^2} - 2\bar{J}_5^{ig} + \frac{D_3}{D}\frac{d}{d\bar{x}}\left(\frac{d\bar{n}_3^i}{d\bar{x}} - \bar{n}_3^i\frac{d\bar{\phi}^i}{d\bar{x}}\right) - 2\bar{J}_3^{ig} = 0, \tag{B.13d}$$

$$\bar{n}_6^i = \bar{K}_d\bar{n}_3^i\bar{n}_4^i, \tag{B.13e}$$

$$\bar{B} = \frac{\bar{K}_b\bar{C}_B}{\bar{K}_b+\bar{n}_4^i}. \tag{B.13f}$$

This system of eight equations is complemented with membrane boundary conditions at the apical and basal membranes, as in equations (6.5) and (6.6) and electroneutrality condition (6.3b). The y-independence and the validity of the above approximation have been verified with a direct numerical solution in Comsol Multiphysics®.

We note that in the absence of external CO_2 gradient the system may be further simplified to a set of algebraic equations as in § 5.2.2.

B.2 Model simplification: the cleft

The simplification of the model in the cleft derives from its small aspect ratio $\delta = h/L = 0.001$. We rescale the spatial coordinates there in the following way

$$x^* = \bar{x}, \quad y^* = \delta \bar{y}. \tag{B.14}$$

We also introduce a velocity scale in the cleft as $u = U\bar{u}$, $v = \delta U \bar{v}$. We note that the longitudinal velocity U, is $1/\delta$ times larger than in the cell, corresponding to a Péclet number of about 0.1. Thus, Pe$= UL/D \approx \mathcal{O}(1)$, which suggests that we should keep advection in the cleft gap.

We first prove that the variables are y^*-independent at the leading order. In the cleft gap, the electrodiffusion problem is governed by equations (6.3a) for $k \in \{0,1,...,6\}$, which scale as follows

$$\begin{aligned} &\frac{\partial^2 \bar{n}_k^g}{\partial x^{*2}} + z_k \frac{\partial}{\partial x^*}\left(\bar{n}_k^g \frac{\partial \bar{\phi}^g}{\partial x^*}\right) + \frac{1}{\delta^2}\left(\frac{\partial^2 \bar{n}_k^g}{\partial y^{*2}} + z_k \frac{\partial}{\partial y^*}\left(\bar{n}_k^g \frac{\partial \bar{\phi}^g}{\partial y^*}\right)\right) \\ &\qquad -Pe_k\left(\frac{\partial(\bar{u}\bar{n}_k^g)}{\partial x^*} + \frac{\partial(\bar{v}\bar{n}_k^g)}{\partial y^*}\right) + \bar{f}_k = 0, \end{aligned} \tag{B.15}$$

where $\bar{f}_k$ are the dimensionless reaction terms and $\mathrm{Pe}_k = UL/D_k = \mathrm{Pe}\cdot D/D_k$. With the expansion $\bar{n}_k^s = \bar{n}_{k,0}^s + \delta \bar{n}_{k,1}^s + ...$ we write the equations for $k \in \{0,1,2\}$ at the leading order (using the same notation for leading order variables and exact ones)

$$\frac{\partial}{\partial y^*}\left(\frac{\partial \bar{n}_k^g}{\partial y^*} + \bar{n}_k^g \frac{\partial \bar{\phi}^g}{\partial y^*}\right) = 0, \quad \Rightarrow \quad \bar{n}_k^g = A_k(x^*) e^{-z_k \bar{\phi}^g}, \tag{B.16a}$$

where to get the last relation we performed twice an integration with respect to y^* and applied the symmetry condition at $y^* = 0$. Subtracting equation (B.15) for $k = 4$ from (B.15) for $k = 3$ at the leading order we obtain the following equation

$$\frac{\partial}{\partial y^*}\left(\frac{\partial \bar{n}_3^g}{\partial y^*} - \bar{n}_3^g \frac{\partial \bar{\phi}^g}{\partial y^*}\right) - \frac{D_4 N_4}{D_3 N}\frac{\partial}{\partial y^*}\left(\frac{\partial \bar{n}_4^g}{\partial y^*} + \bar{n}_4^g \frac{\partial \bar{\phi}^g}{\partial y^*}\right) = 0, \quad \Rightarrow \quad \bar{n}_3^g = A_3(x^*) e^{\bar{\phi}^g}, \tag{B.16b}$$

where the last expression is obtained by dropping the term of order $D_4 N_4 / D_3 N \approx 10^{-5}$ and integrating twice with respect to y^*. Applying electroneutrality condition (6.3b) leads to

$$(A_0 + A_1) e^{-\bar{\phi}^g} - (A_2 + A_3) e^{\bar{\phi}^g} = 0, \quad \Rightarrow \; e^{2\bar{\phi}^g} = \frac{A_0 + A_1}{A_2 + A_3}, \tag{B.17}$$

proving that $\bar{\phi}^g$ (and therefore n_k^g, $k \in \{0,1,2,3\}$) at the leading order are functions of x^* only.

For $k = 5$, the equation (B.15) reads

$$\frac{\partial^2 \bar{n}_5^g}{\partial y^{*2}} + r_5 \left(\frac{k_d N_6}{k_h N_5} \bar{n}_6^g - \bar{n}_5^g \right) = 0, \tag{B.18}$$

where $r_5 = k_h L^2 \delta^2 / D_5 \approx 10^{-4} \approx \mathcal{O}(\delta)$. At the leading order, we obtain

$$\frac{\partial^2 \bar{n}_5^g}{\partial y^{*2}} = 0, \quad \Rightarrow \quad \bar{n}_5^g = A_5(x^*), \tag{B.19}$$

where the second expression results from a double integration with respect to y^* and the symmetry condition at $y^* = 0$. Summing up equations (B.15) for $k = 4$ and $k = 3$, at the leading order (recalling that $\bar{\phi}^g$ is y^* independent) we obtain

$$\frac{\partial^2 \bar{n}_6^g}{\partial y^{*2}} + \frac{N_4 D_4}{N_6 D_6} \frac{\partial}{\partial y^*} \left(\frac{\partial \bar{n}_4^g}{\partial y^*} \right) + r_6 \left(\frac{k_d N_6}{k_h N_5} \bar{n}_6^g - \bar{n}_5^g \right) = 0, \tag{B.20}$$

where $r_6 = k_h L^2 \delta^2 N_5 / D_6 N_6$. Both coefficients $\frac{N_4 D_4}{N_6 D_6}$ and r_6 are of order $10^{-2} \approx \mathcal{O}(\delta)$, therefore, at the leading order we can neglect them, which leads to the following equation

$$\frac{\partial^2 \bar{n}_6^g}{\partial y^{*2}} = 0, \quad \Rightarrow \quad \bar{n}_6^g = A_6(x^*). \tag{B.21}$$

Finally, the equation (B.15) for $k = 4$, at leading order is the following

$$\frac{\partial}{\partial y^*} \left(\frac{\partial \bar{n}_4^g}{\partial y^*} + \bar{n}_4^g \frac{\partial \bar{\phi}^g}{\partial y^*} \right) + r_4 \left(\bar{n}_6 - \bar{K}_d \bar{n}_3 \bar{n}_4 \right) = 0, \tag{B.22}$$

where $r_4 = k_1 L^2 \delta^2 N_6 / D_4 N_4 \approx \mathcal{O}(1)$. Recalling that $\bar{\phi}^g$ and $\bar{n}_6^g$ are y^* independent, we simplify the equation and integrate it twice with respect to y^* to get

$$\frac{\partial^2 \bar{n}_4^g}{\partial y^{*2}} - \kappa \bar{n}_4 = \hat{\kappa} \quad \Rightarrow \quad \bar{n}_4^g = C_1(x^*) e^{\kappa y^*} + C_2(x^*) e^{-\kappa y^*} - \frac{\hat{\kappa}}{\kappa}, \tag{B.23}$$

where $\kappa = r_4 K_d \bar{n}_3^g$ and $\hat{\kappa} = -r_4 \bar{n}_6^g$. Applying no flux boundary condition at $y^* = 1$ and symmetry condition at $y^* = 0$, we obtain $C_1(x^*) = C_2(x^*) = 0$, implying that $\bar{n}_4^g$ is y^*-independent at the leading order. Furthermore, $\bar{n}_4^g = -\hat{\kappa}/\kappa = \bar{n}_6^g / K_d \bar{n}_3^g$, which means that at the leading order we also can assume that second step of the reaction (6.1) is in equilibrium in the cleft.

Now as we proved y^*-independence of the leading order variables in the cleft, we can integrate the equations across the thickness of the cleft and we keep just the leading order terms. Similarly to what has been implemented in the cell, we assume that H_2CO_3 dissociation is at equilibrium, and work in terms of equations that describe conservation CO_2 (6.15) and conservation of charge (6.16) for the variables in the cleft. These simplifications result into the following dimensionless

system of ODEs and an algebraic equation:

$$\text{(B.24a)}\quad \frac{d}{dx^*}\left(\frac{d\bar{n}_k^g}{dx^*}+z_k\bar{n}_k^g\frac{d\bar{\phi}^g}{dx^*}\right)-\mathrm{Pe}\left(\frac{d\bar{n}_k^g}{dx^*}\bar{q}-\bar{Q}^{ig}\bar{n}_k^g\right)+\frac{\bar{J}_k^{ig}}{\delta}=0,\quad k=0,1,2$$

$$\text{(B.24b)}\quad \frac{D_3}{D}\frac{d}{dx^*}\left(\frac{d\bar{n}_3^g}{dx^*}-n_3^g\frac{d\bar{\phi}^g}{dx^*}\right)-\mathrm{Pe}\left(\frac{d\bar{n}_3^g}{dx^*}\bar{q}-\bar{Q}^{ig}\bar{n}_3^g\right)+\frac{\bar{J}_3^{ig}}{\delta}-$$
$$\frac{D_4}{D}\frac{d}{dx^*}\left(\frac{d\bar{n}_4^g}{dx^*}+\bar{n}_4^g\frac{d\bar{\phi}^g}{dx^*}\right)+\mathrm{Pe}\left(\frac{d\bar{n}_4^g}{dx^*}\bar{q}-\bar{Q}^{ig}\bar{n}_4^g\right)=0,$$

$$\text{(B.24c)}\quad \frac{D_5N_5}{DN}\frac{d^2\bar{n}_5^g}{dx^{*2}}-\mathrm{Pe}\left(\frac{d\bar{n}_5^g}{dx^*}\bar{q}-\bar{Q}^{ig}n_5^g\right)+\frac{\bar{J}_5^{ig}}{\delta}+\frac{k_hL^2}{DN}\left(\frac{k_dN_6}{k_h}\bar{n}_6^g-N_5\bar{n}_5^g\right)=0,$$

$$\text{(B.24d)}\quad \frac{D_6N_6}{DN}\frac{d^2\bar{n}_6^g}{dx^{*2}}-\mathrm{Pe}\left(\frac{d\bar{n}_6^g}{dx^*}\bar{q}-\bar{Q}^{ig}\bar{n}_6^g\right)+\frac{\bar{J}_6^{ig}}{\delta}+\frac{D_5N_5}{DN}\frac{d^2\bar{n}_5^g}{dx^{*2}}-\mathrm{Pe}\left(\frac{d\bar{n}_5^g}{dx^*}\bar{q}-\bar{Q}^{ig}\bar{n}_5^g\right)+\frac{\bar{J}_5^{ig}}{\delta}+$$
$$\frac{D_3}{D}\frac{d}{dx^*}\left(\frac{d\bar{n}_3^g}{dx^*}-n_3^g\frac{d\bar{\phi}^g}{dx^*}\right)-\mathrm{Pe}\left(\frac{d\bar{n}_3^g}{dx^*}\bar{q}-\bar{Q}^{ig}\bar{n}_3^g\right)+\frac{\bar{J}_3^{ig}}{\delta}=0,$$

$$\text{(B.24e)}\quad \bar{n}_6^g=K_d\bar{n}_3^g\bar{n}_4^g.$$

In the above equations we denoted with $\bar{J}_k^{ig}$ the dimensionless lateral flux of species k, so that $J_k^{ig}=DN/L\bar{J}_k^{ig}$, $\bar{Q}^{ig}$ is the dimensionless water flux per unit surface across the lateral membrane, $\bar{Q}^{ig}=Q^{ig}/\delta U=k_m/\delta U\left[RT\left(\sum_{k=0}^6(n_k^i-n_k^g(x))+X+C_B\right)+p(x)\right]$ and $\bar{q}=1/2\int_{-1}^1\bar{u}dy^*$ is the depth-averaged fluid velocity in the cleft.

These equations are subject to the following boundary conditions. At the tight junction, we have a membrane type conditions, that read

$$\text{(B.25a)}\qquad \frac{d\bar{n}_k^g}{dx^*}+z_k\bar{n}_k^g\frac{d\bar{\phi}^g}{dx^*}-\mathrm{Pe}\bar{Q}^{tj}\bar{n}_k^g=\bar{J}_k^{ag},\quad \text{at } x^*=1 \text{ for } k\in\{0,1,...,6\},$$

where the fluxes at the tight junction are given by expressions (6.13) and the advective flux through tight junction $\bar{Q}^{tj}$ is given by the expression $\bar{Q}^{tj}=k_{tj}/U\left(RT\sum_{k=0}^6(n_k^a-n_k^g(L))+p(L)-p_a\right)$. At the boundary with the basal region the conditions are

$$\text{(B.25b)}\qquad \bar{n}_k^g=\bar{n}_k^b,\quad k\in\{0,1,3,4,5,6\},\qquad \bar{\phi}^g=0,\qquad \text{at } x^*=0.$$

To close the system we also impose the electroneutrality condition (6.3b). We note that we require (6.3b) and equilibrium assumptions for the reactions to hold also in the apical and basal regions, so that $n_6^s=K_dn_3^sn_4^s$, $s\in\{a,b\}$.

BIBLIOGRAPHY

World Health Organsation: Blindness and visual impairment. `http://www.who.int/en/news-room/fact-sheets/detail/blindness-and-visual-impairment`. Accessed: 2018-11-04.

O. Abouali, A. Modareszadeh, A. Ghaffarieh, and J. Tu. Investigation of saccadic eye movement effects on the fluid dynamic in the anterior chamber. *J. Biomech. Eng.*, 134(2):021002, Feb. 2012. ISSN 1528-8951. doi: 10.1115/1.4005762. PMID: 22482669.

J. Adijanto, T. Banzon, S. Jalickee, N. S. Wang, and S. S. Miller. Co2-induced ion and fluid transport in human retinal pigment epithelium. *J. Gen. Physiol.*, 133(6):603–622, 2009. doi: 10.1085/jgp.200810169.

A. Alm and S. F. E. Nilsson. Uveoscleral outflow – A review. *Exp. Eye Res.*, 88:760–768, 2009.

J. M. Anderson and C. M. Van Itallie. Physiology and function of the tight junction. *CSH. Perspect. Biol.*, 1(2):a002584, 2009. doi: 10.1101/cshperspect.a002584.

L. P. Ang, H. Higashihara, C. Sotozono, V. A. Shanmuganathan, H. Dua, D. T. Tan, and S. Kinoshita. Argon laser iridotomy-induced bullous keratopathy—a growing problem in japan. *Br. J. Ophthalmol.*, 91(12):1613–1615, 2007.

R. Avtar and R. Srivastava. Modelling aqueous humor outflow through trabecular meshwork. *Appl. Math. Comput.*, 189:734–745, 2007.

R. Avtar, R. Srivastava, and D. Nigam. A mathematical model for solute coupled water transport in the production of aqueous humor. *Appl. Math. Model.*, 32(7):1350–1369, 2008.

G. K. Batchelor. *An Introduction to Fluid Dynamics*. Cambridge University Press, 1967.

W. Becker. Metrics. In R. Wurtz and M. Goldberg, editors, *The neurobiology of saccadic eye movements*. Elsevier Science Publisher BV (Biomedical Division), 1989.

J. A. Beswick and C. McCulloch. Effect of hyaluronidase on the viscosity of the aqueous humour. *Br. J. Ophthamol.*, 40:545–548, 1956.

S. Bialek and S. S. Miller. K+ and cl-transport mechanisms in bovine pigment epithelium that could modulate subretinal space volume and composition. *The Journal of physiology*, 475(3): 401–417, 1994.

A. Bill and C. I. Phillips. Uveoscleral drainage of aqueous humour in human eyes. *Exp. Eye Res.*, 12:275–281, 1971.

P. Blondeaux and G. Vittori. Wall imperfections as a triggering mechanism for stokes-layer

transition. *J. Fluid Mech.*, 264:107–135, 1994.

J. C. Bobrow. Factors influencing cataract formation after Nd: YAG laser peripheral iridotomy. 2008.

A. Bonfiglio, R. Repetto, J. Siggers, and A. Stocchino. Investigation of the motion of a viscous fluid in the vitreous cavity induced by eye rotations and implications for drug delivery. *Phys. Med. Biol.*, 58(6):1969, Mar. 2013. ISSN 0031-9155. doi: 10.1088/0031-9155/58/6/1969.

A. Bonfiglio, A. Lagazzo, R. Repetto, and A. Stocchino. An experimental model of vitreous motion induced by eye rotations. *Eye and Vision*, 2(1):10, 2015.

R. R. Bourne, S. R. Flaxman, T. Braithwaite, M. V. Cicinelli, A. Das, J. B. Jonas, J. Keeffe, J. H. Kempen, J. Leasher, H. Limburg, et al. Magnitude, temporal trends, and projections of the global prevalence of blindness and distance and near vision impairment: a systematic review and meta-analysis. *The Lancet Global Health*, 5(9):e888–e897, 2017.

H. Boushehrian, O. Abouali, K. Jafarpur, A. Ghaffarieh, and G. Ahmadi. Relationship between saccadic eye movements and formation of the Krukenberg's spindle—a CFD study. *Math. Med. Biol.*, 34(3):293–312, 2016.

R. F. Brubaker. Measurement of aqueous flow by fluorophotometry. In *The Glaucomas*. Mosby (St. Louis), 1989.

R. F. Brubaker. Flow of aqueous humor in humans [The Friedenwald Lecture]. *Invest. Ophthalmol. Vis. Sci.*, 32(13):3145–3166, 1991.

C. R. Canning, M. J. Greaney, J. N. Dewynne, and A. Fitt. Fluid flow in the anterior chamber of a human eye. *IMA J. Math. Appl. Med. Biol.*, 19:31–60, 2002.

M. Colombini. Axisymmetric flow within a torsionally oscillating sphere. *Phys. Fluids*, 26(2): 023602, 2014.

S. N. Cox, E. Hay, and A. C. Bird. Treatment of chronic macular edema with acetazolamide. *Arch. Ophthalmol.*, 106(9):1190–1195, 1988.

R. Cukier, C. Fortuin, K. E. Shuler, A. Petschek, and J. Schaibly. Study of the sensitivity of coupled reaction systems to uncertainties in rate coefficients. i theory. *J. Chem. Phys.*, 59(8): 3873–3878, 1973.

R. Cukier, H. Levine, and K. Shuler. Nonlinear sensitivity analysis of multiparameter model systems. *J. Comput. Phys.*, 26(1):1–42, 1978.

A. J. Cunningham and P. Barry. Intraocular pressure-physiology and implications for anaesthetic management. *Can. J. Anaesth.*, 33(2):195–208, 1986.

Z. Dagan, S. Weinbaum, and R. Pfeffer. An infinite-series solution for the creeping motion through an orifice of finite length. *J. Fluid Mech.*, 115:505–523, 1982.

T. David, S. Smye, T. Dabbs, and T. James. A model for the fluid motion of vitreous humour of the human eye during saccadic movement. *Phys. Med. Biol.*, 43:1385–1399, 1998.

N. A. Delamere. Ciliary body and ciliary epithelium. *Advances in organ biology*, 10:127–148, 2005.

J. M. Diamond and W. H. Bossert. Standing-gradient osmotic flow: A mechanism for coupling of water and solute transport in epithelia. *J. Gen. Physiol.*, 50(8):2061–2083, 1967.

H. B. Dick, C. Budo, F. Malecaze, J. L. Güell, A. A. Marinho, R. M. Nuijts, G. P. Luyten, J. L. Menezo, and T. Kohnen. Foldable artiflex phakic intraocular lens for the correction of myopia: two-year follow-up results of a prospective european multicenter study. *Ophthalmology*, 116(4): 671–677, 2009.

S. Dorairaj, J. M. Liebmann, C. Tello, V. Barocas, and R. Ritch. Posterior chamber volume does not change significantly during dilation. *Br. J. Ophthalmol.*, 93:1514–1517, 2009.

M. Dornonville de la Cour. Ion transport in the retinal pigment epithelium. a study with double barrelled ion-selective microelectrodes. *Acta. Ophthalmol. Suppl.*, (209):1, 1993.

M. Dvoriashyna, P. J. O., R. Repetto, and J. H. Tweedy. Mathematical models of aqueous production, flow and drainage. In G. Guidoboni and A. Harris, editors, *Mathematical modeling of ocular fluid dynamics: From theory to clinical applications*. Springer-Birkhauser.

M. Dvoriashyna, R. Repetto, M. R. Romano, and J. H. Tweedy. Aqueous humour flow in the posterior chamber of the eye and its modifications due to pupillary block and iridotomy. *Math. Med. Biol.*, 35:447–467, 2017. doi: 10.1093/imammb/dqx012.

M. Dvoriashyna, A. J. E. Foss, E. A. Gaffney, O. E. Jensen, and R. Repetto. Osmotic and electroosmotic fluid transport across the retinal pigment epithelium: a mathematical model. *J. Theor. Biol.*, 2018.

M. Dvoriashyna, R. Repetto, and J. Tweedy. Oscillatory and steady streaming flow in the anterior chamber of the moving eye. *J. Fluid Mech.*, 863:904–926, 2019.

F. M. Dyka, C. A. May, and R. Enz. Subunits of the epithelial sodium channel family are differentially expressed in the retina of mice with ocular hypertension. *J. Neurochem.*, 94(1): 120–128, 2005.

J. L. Edelman, H. Lin, and S. S. Miller. Acidification stimulates chloride and fluid absorption across frog retinal pigment epithelium. *Am. J. Physiol., Cell Physiol.*, 266(4):C946–C956, 1994.

K. Emi, J. E. Pederson, and C. B. Toris. Hydrostatic pressure of the suprachoroidal space. *Invest. Ophthalmol. Vis. Sci.*, 30(2):233–238, 1989.

C. R. Ethier, R. D. Kamm, B. A. Palaszewski, M. C. Johnson, and T. M. Richardson. Calculation of flow resistance in the juxtacanalicular meshwork. *Invest. Ophthalmol. Vis. Sci.*, 27:1741–1750, 1986.

M. P. Fautsch and D. H. Johnson. Aqueous humor outflow: what do we know? Where will it lead us? *Invest. Ophthalmol. Vis. Sci.*, 47(10):4181–4187, 2006.

J. Fischbarg. On the mechanism of fluid transport across corneal endothelium and epithelia in general. *J. Exp. Zool. A Ecol. Genet. Physiol.*, 300(1):30–40, 2003. doi: 10.1002/jez.a.10306.

J. Fischbarg and F. Diecke. A mathematical model of electrolyte and fluid transport across corneal endothelium. *J. Membr. Biol.*, 203(1):41–56, 2005. doi: 10.1007/s00232-004-0730-7.

J. Fischbarg, F. Diecke, P. Iserovich, and A. Rubashkin. The role of the tight junction in paracel-

lular fluid transport across corneal endothelium. Electro-osmosis as a driving force. *J. Membr. Biol.*, 210(2):117–130, 2006. doi: 10.1007/s00232-005-0850-8.

G. A. Fishman, L. D. Gilbert, R. G. Fiscella, A. E. Kimura, and L. M. Jampol. Acetazolamide for treatment of chronic macular edema in retinitis pigmentosa. *Arch. Ophthalmol.*, 107(10): 1445–1452, 1989.

A. D. Fitt and G. Gonzalez. Fluid mechanics of the human eye: Aqueous humour flow in the anterior chamber. *Bull. Math. Biol.*, 68(1):53–71, 2006.

B. Fleck. How large must an iridotomy be? *Br. J. Ophthalmol.*, 74(10):583–588, 1990.

D. Frambach, J. Valentine, and J. Weiter. Furosemide-sensitive cl transport in bovine retinal pigment epithelium. *Invest. Ophthalmol. Vis. Sci.*, 30(10):2271–2274, 1989.

A. B. Friedland. A hydrodynamic model of acqueous flow in the posterior chamber of the eye. *Bull. Math. Biol.*, 40:223–235, 1978.

D. S. Friedman. Epidemiology of angle-closure glaucoma. *Journal of Current Glaucoma Practice*, 1(1):1–3, 2007.

S. Fujii, R. Gallemore, B. A. Hughes, and R. Steinberg. Direct evidence for a basolateral membrane cl-conductance in toad retinal pigment epithelium. *Am. J. Physiol., Cell Physiol.*, 262(2):C374–C383, 1992.

B. Gabelt and P. Kaufman. Aqueous humor hydrodynamics. *Adler's physiology of the eye; Clinical application. Mosby, St. Louis*, 2003.

R. Gallemore, B. Hughes, and S. Miller. Transport mechanisms in the retinal pigment epithelium. In M. Marmor and T. Wolfensberger, editors, *The Retinal Pigment Epithelium*, pages 103–134. Oxford University Press New York, 1998.

R. P. Gallemore and R. H. Steinberg. Effects of DIDS on the chick retinal pigment epithelium. I. Membrane potentials, apparent resistances, and mechanisms. *J. Neurosci.*, 9(6):1968–1976, 1989.

R. P. Gallemore, B. A. Hughes, and S. S. Miller. Retinal pigment epithelial transport mechanisms and their contributions to the electroretinogram. *Prog. Retin. Eye Res.*, 16(4):509–566, 1997.

N. Gavish and K. Promislow. Dependence of the dielectric constant of electrolyte solutions on ionic concentration: A microfield approach. *Phys. Rev. E*, 94(1):012611, 2016.

S. Ghosal. Fluid mechanics of electroosmotic flow and its effect on band broadening in capillary electrophoresis. *Electrophoresis*, 25(2):214–228, 2004.

S. Hamann. Molecular mechanisms of water transport in the eye. *Int. Rev. Cytol.*, 215:395–431, 2002. doi: 10.1016/S0074-7696(02)15016-9.

H. v. Helmholtz. *Handbuch der physiologischen Optik*. University of Michigan Library, third edition, 1909.

W. Henry. III. experiments on the quantity of gases absorbed by water, at different temperatures, and under different pressures. *Philosophical Transactions of the Royal Society of London*, 93: 29–274, 1803.

J. J. Heys and V. H. Barocas. A Boussinesq model of natural convection in the human eye and formation of krunberg's spindle. *Ann. Biomed. Eng.*, 30:392–401, 2002.

J. J. Heys, V. H. Barocas, and M. J. Taravella. Modeling passive mechanical interaction between aqueous humor and iris. *J. Biomech. Eng.*, 123(6):540–547, 2001.

A. Hill. Solute-solvent coupling in epithelia: a critical examination of the standing-gradient osmotic flow theory. *Proc. R. Soc. Lond.-B Biol. Sci.*, 190(1098):99–114, 1975.

A. Hill. Fluid transport: a guide for the perplexed. *J. Membr. Biol.*, 223(1):1–11, 2008. doi: 10.1007/s00232-007-9085-1.

A. Hill, B. Shachar-Hill, and Y. Shachar-Hill. What are aquaporins for? *J. Membr. Biol.*, 197(1): 1–32, 2004. doi: 10.1007/s00232-003-0639-6.

R. Hu, X. Wang, Y. Wang, and Y. Sun. Occult lens subluxation related to laser peripheral iridotomy: A case report and literature review. *Medicine*, 96(10), 2017.

E. C. Huang and V. H. Barocas. Active iris mechanics and pupillary block: steady-state analysis and comparison with anatomical risk factors. *Ann. Biomed. Eng.*, 32(9):1276–1285, 2004.

B. A. Hughes, S. S. Miller, and T. E. Machen. Effects of cyclic AMP on fluid absorption and ion transport across frog retinal pigment epithelium. Measurements in the open-circuit state. *J. Gen. Physiol.*, 83(6):875–899, 1984.

P. Iserovich, Q. Qin, and K. Petrukhin. DPOFA, a Cl-/HCO3-exchanger antagonist, stimulates fluid absorption across basolateral surface of the retinal pigment epithelium. *BMC ophthalmology*, 11(1):33, 2011.

F. Itel, S. Al-Samir, F. Öberg, M. Chami, M. Kumar, C. T. Supuran, P. M. Deen, W. Meier, K. Hedfalk, G. Gros, et al. CO2 permeability of cell membranes is regulated by membrane cholesterol and protein gas channels. *The FASEB Journal*, 26(12):5182–5191, 2012.

R. Jivrajka, M. C. Shammas, T. Boenzi, M. Swearingen, and H. J. Shammas. Variability of axial length, anterior chamber depth, and lens thickness in the cataractous eye. *J Cataract Refract Surg*, 34(2):289–294, 2008.

D. H. Johnson and M. Johnson. How does nonpenetrating glaucoma surgery work? Aqueous outflow resistance and glaucoma surgery. *J. Glaucoma*, 10:55–67, 2001.

M. Johnson. What controls aqueous humor outflow resistance? *Exp. Eye Res.*, 82(4):545–557, 2006.

M. Johnson, A. Shapiro, C. R. Ethier, and R. D. Kamm. Modulation of outflow resistance by the pores of the inner wall endothelium. *Invest. Ophthalmo. Vis. Sci.*, 33:1670–1675, 1992.

M. C. Johnson and R. D. Kamm. The role of Schlemm's canal in aqueous outflow from the human eye. *Invest. Ophthalmol. Vis. Sci.*., 24(3):320–325, Mar. 1983. ISSN 0146-0404. PMID: 6832907.

K. Juuti-Uusitalo, C. Delporte, F. Grégoire, J. Perret, H. Huhtala, V. Savolainen, S. Nymark, J. Hyttinen, H. Uusitalo, F. Willermain, et al. Aquaporin expression and function in human pluripotent stem cell–derived retinal pigmented epithelial cells. *Invest. Ophthalmol. Vis. Sci.*, 54(5):3510–3519, 2013.

Y. Kaji, T. Oshika, T. Usui, and J. Sakakibara. Effect of shear stress on attachment of corneal endothelial cells in association with corneal endothelial cell loss after laser iridotomy. *Cornea*, 24(8):S55–S58, 2005.

M. Katz and P. Kruger. The human eye as an optical system. *Duane's Ophthalmology. 15th ed. Philadelphia, Pa: Lippincott Williams & Wilkins*, 2009.

P. L. Kaufman, F. H. Adler, L. A. Levin, and A. Alm. *Adler's Physiology of the Eye*. Elsevier Health Sciences, 2011.

J. P. Keener and J. Sneyd. *Mathematical physiology*, volume 1. Springer, 2009.

E. Kenyon, K. Yu, M. La Cour, and S. S. Miller. Lactate transport mechanisms at apical and basolateral membranes of bovine retinal pigment epithelium. *Am. J. Physiol., Cell Physiol.*, 267(6):C1561–C1573, 1994.

J. Kiel, M. Hollingsworth, R. Rao, M. Chen, and H. Reitsamer. Ciliary blood flow and aqueous humor production. *Prog. Retin. Eye Res.*, 30(1):1–17, 2011.

M. Kita and M. Marmor. Retinal adhesive force in living rabbit, cat, and monkey eyes. Normative data and enhancement by mannitol and acetazolamide. *Invest. Ophthalmol. Vis. Sci.*, 33(6): 1879–1882, 1992.

C. C. Klaver, R. C. Wolfs, J. R. Vingerling, A. Hofman, and P. T. de Jong. Age-specific prevalence and causes of blindness and visual impairment in an older population: the rotterdam study. *Arch. Ophthalmol.*, 116(5):653–658, 1998.

H. Kolb. Simple anatomy of the retina by helga kolb. Webvision, 2011. URL `http://webvision.med.utah.edu/book/part-i-foundations/simple-anatomy-of-the-retina/`.

H. Kolb. Gross anatomy of the eye by Helga Kolb. *Webvision*, 2012. URL `https://webvision.med.utah.edu/book/part-i-foundations/gross-anatomy-of-the-ey/`.

G. E. Korte and J. Smith. Carbonic anhydrase type II in regenerating retinal pigment epithelium. A histochemical study in the rabbit. *Experientia*, 49(9):789–791, Sep 1993. ISSN 1420-9071. doi: 10.1007/BF01923549. URL `https://doi.org/10.1007/BF01923549`.

T. A. Krahn and A. M. Weinstein. Acid/base transport in a model of the proximal tubule brush border: impact of carbonic anhydrase. *Am. J. Physiol. Renal Physiol.*, 270(2):F344–F355, 1996. doi: 10.1152/ajprenal.1996.270.2.F344. URL `https://doi.org/10.1152/ajprenal.1996.270.2.F344`. PMID: 8779897.

S. Kusaka, A. Inanobe, A. Fujita, Y. Makino, M. Tanemoto, K. Matsushita, Y. Tano, and Y. Kurachi. Functional Kir7. 1 channels localized at the root of apical processes in rat retinal pigment epithelium. *J. Physiol. (Lond)*, 531(1):27–36, 2001.

Y. H. Kwon, J. H. Fingert, M. H. Kuehn, and W. L. Alward. Primary open-angle glaucoma. *N. Engl. J. Med.*, 360(11):1113–1124, 2009.

M. La Cour. Cl- transport in frog retinal pigment epithelium. *Exp. Eye. Res.*, 54(6):921–931, 1992. doi: 10.1016/0014-4835(92)90156-M.

M. La Cour. The retinal pigment epithelium. *Adler's Physiology of the Eye: Clinical Applications*,

10:348–357, 2003.

V. Lew, H. Ferreira, and T. Moura. The behaviour of transporting epithelial cells. I. Computer analysis of a basic model. *Proc. R. Soc. Lond.-B Biol. Sci.*, 206(1162):53–83, 1979.

H. Li, D. N. Sheppard, and M. J. Hug. Transepithelial electrical measurements with the ussing chamber. *Journal of Cystic Fibrosis*, 3:123–126, 2004.

S. Li, E. Kim, and J. A. Bonanno. Fluid transport by the cornea endothelium is dependent on buffering lactic acid efflux. *Am. J. Physiol., Cell Physiol.*, 311(1):C116–C126, 2016. doi: 10.1152/ajpcell.00095.2016. URL `https://doi.org/10.1152/ajpcell.00095.2016`. PMID: 27225657.

D. Lide, editor. *CRC Handbook of Chemistry and Physics, 77th Edn.* CRC Press Inc., 1996.

J. M. Liebmann and R. Ritch. Laser surgery for angle closure glaucoma. In *Seminars in ophthalmology*, volume 17, pages 84–91. Taylor & Francis, 2002.

L. S. Lim, R. Husain, G. Gazzard, S. K. Seah, and T. Aung. Cataract progression after prophylactic laser peripheral iridotomy: potential implications for the prevention of glaucoma blindness. *Ophthalmology*, 112(8):1355–1359, 2005.

L. S. Lim, C.-L. Ho, L. P. Ang, T. Aung, and D. T. Tan. Inferior corneal decompensation following laser peripheral iridotomy in the superior iris. *Am. J. Ophthalmol.*, 142(1):166–168, 2006.

H. Lin and S. S. Miller. pHi regulation in frog retinal pigment epithelium: two apical membrane mechanisms. *Am. J. Physiol., Cell Physiol.*, 261(1):C132–C142, 1991.

H. Lin, E. Kenyon, and S. Miller. Na-dependent pHi regulatory mechanisms in native human retinal pigment epithelium. *Invest. Ophthalmol. Vis. Sci.*, 33(13):3528–3538, 1992.

G. Lyubimov, I. Moiseeva, and A. Stein. Dynamics of the intraocular fluid: Mathematical model and its main consequences. *Fluid Dynamics*, 42(5):684–694, 2007.

S. Marino, I. B. Hogue, C. J. Ray, and D. E. Kirschner. A methodology for performing global uncertainty and sensitivity analysis in systems biology. *J. Theor. Biol.*, 254(1):178–196, 2008.

M. Marmor. Control of subretinal fluid: experimental and clinical studies. *Eye*, 4(2):340–344, 1990. doi: 10.1038/eye.1990.46.

M. Marmor. Structure, function, and disease of the retinal pigment epithelium. *The Retinal Pigment Epithelium*, pages 3–12, 1998.

M. Marraffa, G. Marchini, A. Pagliarusco, S. Perfetti, A. Toscano, C. Brunelli, R. Tosi, and L. Bonomi. Ultrasound biomicroscopy and corneal endothelium in nd: Yag-laser iridotomy. *Ophthalmic Surgery, Lasers and Imaging Retina*, 26(6):519–523, 1995.

R. Mathias and H. Wang. Local osmosis and isotonic transport. *J. Membr. Biol.*, 208(1):39–53, 2005. doi: 10.1007/s00232-005-0817-9.

R. T. Mathias. Epithelial water transport in a balanced gradient system. *Biophys. J.*, 47(6): 823–836, 1985.

M. A. Matthay, H. G. Folkesson, and A. Verkman. Salt and water transport across alveolar and distal airway epithelia in the adult lung. *Am. J. Physiol. Lung Cell Mol. Physiol.*, 270(4):

L487–L503, 1996.

G. G. Matthews. *Cellular physiology of nerve and muscle*. John Wiley & Sons, 2009.

D. M. Maurice. The Von Sallmann Lecture 1996: an ophthalmological explanation of REM sleep. *Experimental eye research*, 66(2):139–145, 1998.

S. McLaughlin and R. T. Mathias. Electro-osmosis and the reabsorption of fluid in renal proximal tubules. *J. Gen. Physiol.*, 85(5):699–728, 1985.

B. M. Merchant and J. J. Heys. Effects of variable permeability on aqueous humor outflow. *Appl. Math. Comput.*, 196:371–380, 2008.

J. Meskauskas, R. Repetto, and J. H. Siggers. Oscillatory motion of a viscoelastic fluid within a spherical cavity. *J. Fluid Mech.*, 685:1–22, 2011.

S. S. Miller and J. L. Edelman. Active ion transport pathways in the bovine retinal pigment epithelium. *J. Physiol. (Lond)*, 424:283, 1990.

S. S. Miller and R. H. Steinberg. Active transport of ions across frog retinal pigment epithelium. *Exp. Eye. Res.*, 25(3):235–248, 1977. doi: 10.1016/0014-4835(77)90090-2.

S. S. Miller, R. H. Steinberg, and B. Oakley II. The electrogenic sodium pump of the frog retinal pigment epithelium. *J. Membr. Biol.*, 44(3-4):259–279, 1978.

J. G. Milton and A. Longtin. Evaluation of pupil constriction and dilation from cycling measurements. *Vision Res.*, 30(4):515–525, 1990.

S. Modarreszadeh, O. Abouali, A. Ghaffarieh, and G. Ahmadi. Physiology of aqueous humor dynamic in the anterior chamber due to rapid eye movement. *Physiol Behav*, 2014.

Y. Mori and C. Peskin. A numerical method for cellular electrophysiology based on the electrodiffusion equations with internal boundary conditions at membranes. *Comm. App. Math. and Comp. Sci.*, 4:85–134, 2009. doi: 10.2140/camcos.2009.4.85.

Y. Mori, J. Jerome, and C. Peskin. A three-dimensional model of cellular electrical activity. *Bull. Inst. Math. Acad. Sinica*, 2:367–390, 2007.

E. A. Nagelhus, T. M. Mathiisen, A. C. Bateman, F.-M. Haug, O. P. Ottersen, J. H. Grubb, A. Waheed, and W. S. Sly. Carbonic anhydrase xiv is enriched in specific membrane domains of retinal pigment epithelium, müller cells, and astrocytes. *Proceedings of the National Academy of Sciences*, 102(22):8030–8035, 2005.

A. Negi and M. F. Marmor. Quantitative estimation of metabolic transport of subretinal fluid. *Invest. Ophthalmol. Vis. Sci.*, 27(11):1564–1568, 1986.

D. Pascolini and S. P. Mariotti. Global estimates of visual impairment: 2010. *Br. J. Ophthalmol.*, 96(5):614–618, 2012.

C. J. Pavlin, K. Harasiewicz, and F. S. Foster. Ultrasound biomicroscopy of anterior segment structures in normal and glaucomatous eyes. *Am. J. Ophthalmol.*, 113(4):381–389, 1992.

S. Peng, R. A. Adelman, and L. J. Rizzolo. Minimal effects of VEGF and anti-VEGF drugs on the permeability or selectivity of RPE tight junctions. *Invest. Ophthalmol. Vis. Sci.*, 51(6): 3216–3225, 2010. doi: 10.1167/iovs.09-4162.

R. F. Probstein. *Physicochemical hydrodynamics: an introduction*. John Wiley & Sons, 2005.

D. Purves, G. J. Augustine, D. Fitzpatrick, L. C. Katz, A.-S. LaMantia, J. O. McNamara, S. M. Williams, et al. Types of eye movements and their functions. *Neuroscience*, pages 361–390, 2001.

H. A. Quigley and A. T. Broman. The number of people with glaucoma worldwide in 2010 and 2020. *Br. J. Ophthalmol.*, 90(3):262–267, 2006.

R. Quinn and S. Miller. Ion transport mechanisms in native human retinal pigment epithelium. *Invest. Ophthalmol. Vis. Sci.*, 33(13):3513–3527, 1992.

N. Reichhart and O. Strauß. Ion channels and transporters of the retinal pigment epithelium. *Exp. Eye. Res.*, 126:27–37, 2014. doi: 10.1016/j.exer.2014.05.005.

R. Repetto, A. Stocchino, and C. Cafferata. Experimental investigation of vitreous humour motion within a human eye model. *Phys. Med. Biol.*, 50:4729–4743, 2005. doi: 10.1088/0031-9155/50/19/021.

R. Repetto, J. H. Siggers, and A. Stocchino. Steady streaming within a periodically rotating sphere. *J. Fluid Mech.*, 608:71–80, August 2008. doi: 10.1017/S002211200800222X.

R. Repetto, J. H. Siggers, and A. Stocchino. Mathematical model of flow in the vitreous humor induced by saccadic eye rotations: effect of geometry. *Biomech. Model. Mechanobiol.*, 9(1):65–76, 2010. ISSN 1617-7959. doi: 10.1007/s10237-009-0159-0.

R. Repetto, J. O. Pralits, J. H. Siggers, and P. Soleri. Phakic iris-fixated intraocular lens placement in the anterior chamber: effects on aqueous flow. *Invest. Ophthalmol. Vis. Sci.*, 56(5):3061–3068, 2015.

N. Riley. Steady streaming. *Ann. Rev. Fluid Mech.*, 33:43–65, 2001.

L. J. Rizzolo, S. Peng, Y. Luo, and W. Xiao. Integration of tight junctions and claudins with the barrier functions of the retinal pigment epithelium. *Prog. Retin. Eye Res.*, 30(5):296–323, 2011.

A. Rubashkin, P. Iserovich, J. Hernandez, and J. Fischbarg. Epithelial fluid transport: protruding macromolecules and space charges can bring about electro-osmotic coupling at the tight junctions. *J. Membr. Biol.*, 208(3):251–263, 2006. doi: 10.1007/s00232-005-0831-y.

A. R. Rudnicka, S. Mt-Isa, C. G. Owen, D. G. Cook, and D. Ashby. Variations in primary open-angle glaucoma prevalence by age, gender, and race: a bayesian meta-analysis. *Invest. Ophthalmol. Vis. Sci.*, 47(10):4254–4261, 2006.

A. Saltelli, S. Tarantola, and K.-S. Chan. A quantitative model-independent method for global sensitivity analysis of model output. *Technometrics*, 41(1):39–56, 1999.

A. Saltelli, P. Annoni, I. Azzini, F. Campolongo, M. Ratto, and S. Tarantola. Variance based sensitivity analysis of model output. design and estimator for the total sensitivity index. *Comput. Phys. Commun.*, 181(2):259–270, 2010.

A. Samarskiy and E. Nikolaev. Methods for solving grid equations. pages 73–76,154–156,569–577, 1978.

R. A. Sampson. On Stokes' current function. *Phil Trans Roy Soc Lond A*, 182:449–518, 1891.

J. Sanchez, Y. Li, A. Rubashkin, P. Iserovich, Q. Wen, J. Ruberti, R. Smith, D. Rittenband, K. Kuang, F. Diecke, et al. Evidence for a central role for electro-osmosis in fluid transport by corneal endothelium. *J. Membr. Biol.*, 187(1):37–50, 2002.

J. Sanchez, V. Cacace, C. Kusnier, R. Nelson, A. Rubashkin, P. Iserovich, and J. Fischbarg. Net fluorescein flux across corneal endothelium strongly suggests fluid transport is due to electro-osmosis. *J. Membr. Biol.*, 249(4):469–473, 2016.

J. Scott. A finite element model of heat transport in the human eye. *Phys. Med. Biol.*, 33(2):227, 1988.

B. Shachar-Hill and A. E. Hill. Paracellular fluid transport by epithelia. *Int. Rev. Cytol.*, 215: 319–350, 2002. doi: 10.1016/S0074-7696(02)15014-5.

R. K. Sharma and B. Ehinger. Development and structure of the retina. *Adler's Physiology of the Eye: Clinical Applications*, 10:319–347, 2003.

G. Shi, A. Maminishkis, T. Banzon, S. Jalickee, R. Li, J. Hammer, and S. S. Miller. Control of chemokine gradients by the retinal pigment epithelium. *Invest. Ophthalmol. Vis. Sci.*, 49(10): 4620–4630, 2008. doi: 10.1167/iovs.08-1816.

J. H. Siggers and C. R. Ethier. Fluid mechanics of the eye. *Annual Review of Fluid Mechanics*, 44: 347–372, 2012.

A. J. Sillman, W. G. Owen, and H. R. Fernandez. The generation of the late receptor potential: an excitation-inhibition phenomenon. *Vision res.*, 12(9):1519–1531, 1972.

D. M. Silver and H. A. Quigley. Aqueous flow through the iris-lens channel: estimates o the differential pressure between the anterior and the posterior chambers. *J. Glaucoma*, 13(2): 100–107, April 2004.

K. R. Spring. Mechanism of fluid transport by epithelia. *Compr. Physiol.*, 2010. doi: 10.1002/cphy.cp060405.

T. M. Squires and M. Z. Bazant. Induced-charge electro-osmosis. *J. Fluid Mech.*, 509:217–252, 2004.

W. D. Stamer, D. Bok, J. Hu, G. J. Jaffe, and B. S. McKay. Aquaporin-1 channels in human retinal pigment epithelium: role in transepithelial water movement. *Invest. Ophthalmol. Vis. Sci.*, 44 (6):2803–2808, 2003. doi: 10.1167/iovs.03-0001.

O. Strauss. The retinal pigment epithelium. Webvision, 2011. URL `http://webvision.med.utah.edu/book/part-ii-anatomy-and-physiology-of-the-retina/the-retinal-pigment-epithelium/`.

J. Strieter, J. L. Stephenson, L. G. Palmer, and A. M. Weinstein. Volume-activated chloride permeability can mediate cell volume regulation in a mathematical model of a tight epithelium. *J. Gen. Physiol.*, 96(2):319–344, 1990.

M. Szopos, S. Cassani, G. Guidoboni, C. Prud'homme, R. Sacco, B. Siesky, and A. Harris. Mathematical modeling of aqueous humor flow and intraocular pressure under uncertainty: towards individualized glaucoma management. *Journal for Modeling in Ophthalmology*, 1(2):29–39,

2016.

K. Takahashi and Y. Atsumi. Precise measurement of individual rapid eye movements in REM sleep of humans. *Sleep*, 20(9):743–752, 1997.

K.-i. Takahashi, D. B. Dixon, and D. Copenhagen. Modulation of a sustained calcium current by intracellular pH in horizontal cells of fish retina. *J. Gen. Physiol.*, 101(5):695–714, 1993.

E. R. Tamm. The trabecular meshwork outflow pathways: Structural and functional aspects. *Exp. Eye Res.*, 88:648–655, 2009.

P. Tarongoy, C. L. Ho, and D. S. Walton. Angle-closure glaucoma: the role of the lens in the pathogenesis, prevention, and treatment. *Survey of ophthalmology*, 54(2):211–225, 2009.

C. B. Toris, M. E. Yablonski, and Y.-L. W. ad C. B. Camras. Aqueous humor dynamics in the aging human eye. *Am. J, Ophthalmol.*, 127(4):407–412, 1999.

S. Tsuboi. Measurement of the volume flow and hydraulic conductivity across the isolated dog retinal pigment epithelium. *Invest. Ophthalmol. Vis. Sci.*, 28(11):1776–1782, 1987.

S. Türk. Untersuchungen über eine strömung in der vorderen augenkammer. *Gaefes Arch. Ophtalmol.*, 64:481–501, 1906.

J. H. Tweedy, J. O. Pralits, R. Repetto, and P. Soleri. Flow in the anterior chamber of the eye with an implanted iris-fixated artificial lens. *Math. Med. Biol.*, page dqx007, 2017.

G. Van Alphen and S. L. Robinette. The distribution of tissue antigens in the eye. *Acta Ophthalmol.*, 39(6):1029–1039, 1961.

D. D. Van Slyke. On the measurement of buffer values and on the relationship of buffer value to the dissociation constant of the buffer and the concentration and reaction of the buffer solution. *J. Biol. Chem.*, 52(2):525–570, 1922.

A. Villamarin, S. Roy, R. Hasballa, O. Vardoulis, P. Reymond, and N. Stergiopulos. 3D simulation of the aqueous flow in the human eye. *Med. Eng. Phys.*, 34:1462–1470, 2012.

P. X. Wang, V. T. Koh, and S. C. Loon. Laser iridotomy and the corneal endothelium: a systemic review. *Acta Ophthalmol.*, 92(7):604–616, 2014.

R. N. Weinreb and P. T. Khaw. Primary open-angle glaucoma. *The Lancet*, 363(9422):1711–1720, 2004.

A. Weinstein and J. Stephenson. Electrolyte transport across a simple epithelium. steady-state and transient analysis. *Biophys. J.*, 27(2):165–186, 1979.

A. M. Weinstein. A kinetically defined na+/h+ antiporter within a mathematical model of the rat proximal tubule. *J. Gen. Physiol.*, 105(5):617–641, 1995.

A. M. Weinstein. A mathematical model of rat distal convoluted tubule. i. cotransporter function in early dct. *Am. J. Physiol. Renal Physiol.*, 289(4):F699–F720, 2005a.

A. M. Weinstein. A mathematical model of rat distal convoluted tubule. ii. potassium secretion along the connecting segment. *Am. J. Physiol. Renal Physiol.*, 289(4):F721–F741, 2005b.

A. M. Weinstein and E. D. Sontag. Modeling proximal tubule cell homeostasis: tracking changes in luminal flow. *Bull. Math. Biol.*, 71(6):1285–1322, 2009.

A. M. Weinstein and J. L. Stephenson. Models of coupled salt and water transport across leaky epithelia. *J. Gen. Physiol.*, 60(1):1–20, 1981.

T. Weiss. *Cellular Biophysics I. Transport.* MIT Press, Cambridge, Massachusetts, 1996a.

T. Weiss. *Cellular Biophysics II. Electrical Properties.* MIT Press, Cambridge, Massachusetts, 1996b.

S. Wimmers, M. O. Karl, and O. Strauss. Ion channels in the RPE. *Prog. Retin. Eye Res.*, 26(3): 263–301, 2007.

T. J. Wolfensberger, I. Mahieu, J. Jarvis-Evans, M. Boulton, N. D. Carter, A. Nógrádi, E. Hollande, and A. C. Bird. Membrane-bound carbonic anhydrase in human retinal pigment epithelium. *Invest. Ophthalmol. Vis. Sci.*, 35(9):3401–3407, 1994.

T. J. Wolfensberger, R. K. Chiang, A. Takeuchi, and M. F. Marmor. Inhibition of membrane-bound carbonic anhydrase enhances subretinal fluid absorption and retinal adhesiveness. *Graefes Arch. Clin. Exp. Ophthalmol.*, 238(1):76–80, 2000.

C. Wright, M. A. Tawfik, M. Waisbourd, and L. J. Katz. Primary angle-closure glaucoma: an update. *Acta Ophthalmol.*, 94(3):217–225, 2016.

Y. Yamamoto, T. Uno, K. Shisida, L. Xue, A. Shiraishi, X. Zheng, and Y. Ohashi. Demonstration of aqueous streaming through a laser iridotomy window against the corneal endothelium. *Arch. Ophthalmol.*, 124(3):387–393, 2006.

Y. Yamamoto, T. Uno, T. Joko, A. Shiraishi, and Y. Ohashi. Effect of anterior chamber depth on shear stress exerted on corneal endothelial cells by altered aqueous flow after laser iridotomy. *Invest. Ophthalmol. Vis. Sci.*, 51(4):1956–1964, 2010.

E. Yariv. An asymptotic derivation of the thin-debye-layer limit for electrokinetic phenomena. *Chem. Eng. Commun.*, 197(1):3–17, 2009.